Energy Research and Development Division

FINAL PROJECT REPORT

IMPROVING UNDERSTANDING OF REGIONAL AND NEAR-SOURCE AIR QUALITY IMPACTS OF DISTRIBUTED GENERATION SOURCES

Prepared for: California Energy Commission

Prepared by: Department of Mechanical Engineering, University of California, Riverside

OCTOBER 2014

CEC-500-2015-008

Prepared by:

Primary Authors:
Akula Venkatram
Marko Princevac
Sam Pournazeri
Qiguo Jing
Si Tan
Nico Schulte

Department of Mechanical Engineering
University of California, Riverside.
900 University Ave.
Riverside, CA 92521

Contract Number: 500-08-055

Prepared for:

California Energy Commission

Marla Mueller
Contract Manager

Guido Franco
Team Lead

Aleecia Gutierrez
Office Manager
Energy Generation Research Office

Laurie ten Hope
Deputy Director
ENERGY RESEARCH AND DEVELOPMENT DIVISION

Robert P. Oglesby
Executive Director

DISCLAIMER

This report was prepared as the result of work sponsored by the California Energy Commission. It does not necessarily represent the views of the Energy Commission, its employees or the State of California. The Energy Commission, the State of California, its employees, contractors and subcontractors make no warranty, express or implied, and assume no legal liability for the information in this report; nor does any party represent that the uses of this information will not infringe upon privately owned rights. This report has not been approved or disapproved by the California Energy Commission nor has the California Energy Commission passed upon the accuracy or adequacy of the information in this report.

ACKNOWLEDGEMENTS

The California Energy Commission (contract 500-08-055) provided support for the project.

PREFACE

The California Energy Commission Public Interest Energy Research (PIER) Program supports public interest energy research and development that will help improve the quality of life in California by bringing environmentally safe, affordable, and reliable energy services and products to the marketplace.

The PIER Program conducts public interest research, development, and demonstration (RD&D) projects to benefit California.

The PIER Program strives to conduct the most promising public interest energy research by partnering with RD&D entities, including individuals, businesses, utilities, and public or private research institutions.

PIER funding efforts are focused on the following RD&D program areas:

- Buildings End-Use Energy Efficiency
- Energy Innovations Small Grants
- Energy-Related Environmental Research
- Energy Systems Integration
- Environmentally Preferred Advanced Generation
- Industrial/Agricultural/Water End-Use Energy Efficiency
- Renewable Energy Technologies
- Transportation

Improving Understanding of Regional and Near-Source Air Quality Impacts of Distributed Generation Sources is the final report for the Improving Understanding of Regional and Near-Source Air Quality Impacts of Distributed Generation Sources project (contract number 500-08-055) conducted by the Department of Mechanical Engineering, University of California, Riverside. The information from this project contributes to Energy Research and Development Division's Energy-Related Environmental Research Program.

For more information about the Energy Research and Development Division, please visit the Energy Commission's website at www.energy.ca.gov/research/ or contact the Energy Commission at 916-327-1551.

ABSTRACT

This project examined the impact of fossil fuel-based distributed generation on air quality in urban areas, as distributed generation has the potential to meet a significant portion of California's power demand The research team conducted a field study in Palm Springs, California, and a laboratory study to examine the effect of surrounding buildings on plume rise. In general, plume rise increases in the presence of surrounding buildings due to reduced wind speed. However, the ability of dispersion models to predict concentrations in urban areas is limited because buildings near distributed generation units can alter plume rise, which can have a major effect on ground-level concentrations of distributed generation emissions. The team developed a hybrid model that combines long-range and short-range transport models to account for both the regional and local emission contribution of distributed generation units to local air quality. Because conventional, comprehensive dispersion models are computationally expensive and unsuitable for long-term studies, the team developed a more computationally efficient model—the Lagrangian background model—by separating transport and chemistry using the concept of species age (the average age of the emitted species). The Lagrangian background model computes the concentration at a receptor by following the trajectory of an air parcel for the prior 24 hours using surface winds. Chemistry is then simulated using the Generic Reaction Set, an empirical approximation of atmospheric photochemistry. Comparison of model predictions with observations in the South Coast Air Basin and San Joaquin Valley Air Basin show that the model adequately describes the spatial and temporal distribution of nitrogen oxide and nitrogen dioxide concentrations. The impacts of distributed generation units were simulated under a baseline scenario and a hypothetical extra-high penetration scenario in the South Coast Air Basin and San Joaquin Valley Air Basin. Results showed that the total contribution of distributed generation to nitrogen oxide concentration is less than 10 percent under the extra-high penetration scenario, compared to the baseline.

Keywords: distributed generation, hybrid model, Lagrangian background model, plume rise, urban nocturnal boundary layer height, species age

Please use the following citation for this report:

Venkatram, Akula, Sam Pournazeri, Qiguo Jing, Si Tan, and Nico Schulte. (University of California, Riverside). 2013 *Improving Understanding of Regional and Near-Source Air Quality Impacts of Distributed Generation Sources.* California Energy Commission. Publication number: CEC-500-2015-008.

TABLE OF CONTENTS

Acknowledgements i

PREFACE ii

ABSTRACT iii

TABLE OF CONTENTS iv

List of Figures vii

List of Tables xi

EXECUTIVE SUMMARY 1

Methods 2
Results 3
Conclusions 3

CHAPTER 1: Introduction and Objectives 7

CHAPTER 2: Plume Rise and Stable Boundary Layer Height: Field Study 10

2.1 Introduction 10

2.2 Field Study 11

2.2.1 Meteorology 12
2.2.2 Plume Rise 14
2.2.3 Correction Method 15
2.2.4 Field Measurements 16
2.2.5 Results 18
2.2.6 Conclusion 19

2.3 Estimating the Height of the Nocturnal Urban Boundary Layer for Dispersion Applications 21

2.3.1 Introduction 21
2.3.2 Field Study 23
2.3.2.1 Surface Micrometeorology 24
2.3.2.2 Boundary Layer Profiling 26
2.3.3 Analysis of Observations 33
2.3.3.1 Supplementary Field Data 35
2.3.3.2 VTMX Study 35
2.3.3.3 Milan Experiment 36

2.3.3.4 Wangara Data 36
2.3.4 Model Evaluation 36
2.3.4.1 Estimating the Friction Velocity (u_*) 37
2.3.4.2 Field Data Analysis 40
2.3.4.3 Performance of Prognostic Models 42
2.3.4.4 Time-Integrated Friction Velocity Model 45
2.3.5 Conclusions 47
CHAPTER 3: Plume Rise: Laboratory Study 49
3.1 Introduction 49
3.2 Water Channel 49
3.3 Concentration Measurements System 50
3.4 Velocity Measurement System (PIV) 53
3.5 Plume Visualization Technique 53
3.6 Experimental Setup 54
3.7 Upstream Buildings 56
3.8 Downstream Buildings 58
3.9 Upstream and Downstream Buildings 59
3.10 Comparison with the Numerical Plume Rise Model 61
3.11 Summary and Conclusion 63
3.12 Scaling of Urban Plume Rise and Dispersion in Water Channels and Wind Tunnels ... 65
3.12.1 Introduction 65
3.12.2 Flow Similarity 66
3.12.3 Plume Rise Similarity 68
3.12.4 Laboratory Experiment 69
3.12.5 Plume Rise Model 72
3.12.6 Comparison of Models and Experiments 78
3.12.7 Plume Rise Scaling 80
3.12.8 Plume Rise Similarity Sensitivity Study 85
3.12.9 Similarity of Dispersion 91
3.12.10 Summary and Conclusions 94

CHAPTER 4: Impact of Distributed Generation of Electricity Relative to Other Urban Sources **97**

4.1 Introduction 97

4.2 Methods 98

4.2.1 The Lagrangian Background Model 98
4.2.2 The Species Age 100
4.3 Evaluation of the Lagrangian Background Model 101

4.3.1 The South Coast Air Basin Study 101
4.3.2 The San Joaquin Valley Study 115
4.3.3 Comparison of O_3 Time Series 126
4.4 UCI-CIT Model 127

4.5 Generic Reaction Set (GRS) Chemistry 128

4.6 Sensitivity Study 130

4.7 The Air Quality Impact of a DG Deployment Relative to Background Sources in the SoCAB 137

4.7 Conclusions 144

CHAPTER 5: Hybrid Modeling **146**

5.1 The Hybrid Model 146

5.2 Distributed Generation Scenario 150

5.3 Impact of Distributed Generation in the South Coast Air Basin 154

5.4 Impact of Distributed Generation in the San Joaquin Valley 157

5.5 Summary and Conclusions 162

Chapter 6: Conclusions and Recommendations **163**

6.1 Conclusions 163

6.2 Recommendations 165

GLOSSARY **167**

References **170**

APPENDIX A: IMPROVING UNDERSTANDING OF REGIONAL AND NEAR-SOURCE AIR QUALITY IMPACTS OF DISTRIBUTED GENERATION SOURCES A-1

LIST OF FIGURES

Figure 2-1: Location of the Meteorology Stations (Yellow Pins) in Sunrise Park, Palm Springs, California 12

Figure 2-3: Measurement of Plume Rise Associated with the Palm Springs DG 15

Figure 2-7: Normalized Measured Plume Rise 20

Figure 2-8: Location of the Meteorological Station 24

Figure 2-9: Measurements of 15-minute Averaged 25

Figure 2-10: Vertical Profiles 27

Figure 2-11: (a) Schematic of the Method Used for Determination of Nocturnal Boundary Layer Height, and (b) Boundary Layer Height Determination on Temperature Profile Measured During 20:17–20:57 PST on March 9, 2011 28

Figure 2-12: Successive Vertical Profiles of Temperature (°C) 30

Figure 2-13: Nighttime Boundary Layer Parameters vs. Time 34

Figure 2-14: Comparison of Cooling of the Boundary Layer with Integrated Surface Heat Flux 35

Figure 2-18: Measured Boundary Layer Height in the Riverside, VTMX, Milan, and Wangara Field Studies vs. $\int u_* dt$ 42

Figure 2-19: Comparison of AERMOD Stable Boundary Layer Height Model Predictions with Observations from the Riverside Field Study 44

Figure 2-20: Comparison of Predictions by Zilitinkevich et al. (2002) Model with Observations from the Riverside Field Study 45

Figure 2-21: Comparison of the *Time-Integrated Friction Velocity* (eq. 17) Model Predictions with Observation from the Riverside Field Study 46

Figure 2-22: Comparison of the *Time-Integrated Friction Velocity* (eq. 17) Model Predictions with Observation from VTMX Field Study 47

Figure 3-1: (a) Water Channel Schematic; (b) Water Channel Facility at University of California Riverside (LEFM) 50

Figure 3-2: (a) Optical Fiber Sensor and (b) Schematics of the Concentration Measurement System..... 52

Figure 3-3: (a) Sensors Placement in the Water Channel. (b) Laser Setup. (c) Camera Setup..... 52

Figure 3-5: (a) Schematic of the Buildings Configuration. Model of the DG and Surrounding Buildings Situated Upstream (b, e), Downstream (c, f), and both Upstream and Downstream (d, g). Both Single-Story (b, c, d) and Double-Story (e, f, g) Buildings were Investigated..... 55

Figure 3-7 Results from Measurements of Plume Rise (h_p) Associated with a DG with and without Downstream Buildings..... 59

Figure 3-8: Results from Measurements of Plume Rise (h_p) Associated with a DG with and without Upstream/Downstream Buildings..... 60

Figure 3-9: Comparison of the Plume Effective Height (h_e) Observations (blue) with the Numerical Plume Rise Model (red) for Plume Buoyancy of SG = 0.96 61

Figure 3-10: Comparison of the Plume Effective Height (h_e) Observations (blue) with the Numerical Plume Rise Model (red) for Plume Buoyancy of SG = 0.98 62

Figure 3-11: Profiles of Ambient Mean 70

Figure 3-12: Schematic for Plume in a Two-Dimensional Flow 74

Figure 3-13: (a) Schematic of PIV Measurement Setup. (b) Averaged Velocity Field over 180 Images Measured Using PIV System (the dark blue vector lines show the velocity of less than 1 cm/s and the dark red vector lines show the velocity equal/above 5 cm s^{-1}), (c) Versus Normalized Downwind Distance from the DG Building at z = Hb, and (d) Versus Normalized Vertical Distance above the Ground Level Next to the Lee Wall of the Building. 76

Figure 3-14: (a) and (c) Show the Plume Visualization for Modeled DG Source (geometric scaling ratio of 1:100) with Buoyant Emissions of Different Specific Gravity (*SG*): (a) *SG* = 0.98, (c) *SG* = 0.96. (b) and (d) Show Comparisons between the Plume Rise Observations ( ); Briggs (1984) plume rise formulation (red); and numerical plume rise model (blue): (b) *SG* = 0.98, (d) *SG* = 0.96. 79

Figure 3-15: Simulation of Palm Springs DG Plume Rise 89

Figure 3-17: (a) Normalized Ground-Level Concentrations (microseconds per cubic meter, μs/m^3) Associated with the Palm Springs DG (blue) vs. Scaled Ground-Level Concentrations with (black) and without (red) Correction for Turbulent Intensity Discrepancy; (b) Ratio of Scaled to Field Normalized Simulated Concentrations with (blue) and without (red) Correction 93

Figure 4-1: The Lagrangian Background Model 99

Figure 4-2: Gridded NO_x Emissions and Monitoring Stations Located in the South Coast Air Basin, Los Angeles 102

Figure 4-4: Comparison of NO_x and O_3 estimates based on *GRS* and *CBM IV* at stations in the SoCAB 104

Figure 4-5: Locations of 26 SCAQMD Meteorological Stations 105

Figure 4-6: 24-Hour Back-Trajectories of Air Parcels at Two Monitoring Sites on July 31, 2007 106

Figure 4-7: Comparison of modeled and measured monthly averaged NO_x, NO_2, and O_3 concentrations at 21 sites in the SoCAB from January to December 2007 108

Figure 4-8: Monthly averaged NO_x and NO_2 concentrations compared with observations at two sites, in West LA (left panels) and San Bernardino (right panels), in the SoCAB 109

Figure 4-9: Daily maximum O3 (top panels) and NO2 (bottom panels) concentrations compared with observations at two sites, in West LA (left panels) and San Bernardino (right panels), in the SoCAB. 110

Table 4-1: Statistical performance parameter of *LBM* for calendar year 2007 at two sites (West LA and San Bernardino) in the SoCAB 111

Figure 4-10: Monthly averaged daily variation of NO_x and NO_2 compared with observations at two sites, in West LA (left panels) and San Bernardino (right panels), in the SoCAB during two different months. 112

Figure 4-11: Comparison of modeled and measured annually averaged NO_x and NO_2 concentrations at 21 sites in the SoCAB. 113

Figure 4-13: Annual average concentration of the 19 monitoring sites in the SJVAB 118

Figure 4-14: Comparison of modeled daily-average concentrations with the corresponding observed concentrations 120

Figure 4-15: Comparison of modeled daily maximum concentrations with the observed concentrations for sites 5 and 14 from January – December 2005 122

Figure 4-16: Modeled monthly averaged concentration compared with corresponding observed concentration for each month of the year at site 5 and 14. 123

Figure 4-17: Modeled annual averaged daily variation of NO_x, NO_2 and O_3 concentration compared with corresponding observations 125

Figure 4-18: O_3 episodes during September 1 - 4, 2007 in Azusa in the SoCAB (upper panel) and July 14 - 17, 2005 in Fresno in the SJVAB (lower panel). 126

Figure 4-19: Comparison of the UCI-CIT and Lagrangian (UCR) Models 127

Figure 4-22: Hourly Concentration Variation for the Constant Boundary Layer Height Case (left) and the Uniform Emission Distribution Case (right) 134

Figure 4-23: Hourly Concentration Variation for the 48-hour Back Trajectory Case (left) and the 48-hour Back Trajectory and Constant Boundary Layer Height Case (right). 136

Figure 4-24: The Impact of DGs on the Concentrations of NO_x, NO_2, and O_3 under the EHP Scenario 138

Figure 4-25: Maximum Increase/Decrease in Ground-Level Concentrations of NO_x under the EHP Scenario, with CBM IV as the Chemistry Module 139

Figure 4-26: Maximum Increase/Decrease in Ground-Level Concentrations of NO_2 under the EHP Scenario, with CBM IV as the Chemistry Module 140

Figure 4-27: Maximum Increase/Decrease in Ground-Level Concentrations of O_3 under the EHP Scenario, with CBM IV as the Chemistry Module 140

Figure 4-29: The impact of DGs on the Concentrations of NO_x, NO_2, and O_3 under the EHP Scenario, using the GRS Chemistry Set 142

Figure 4-30: Comparison of Different Chemistry Modules (GRS vs. CBM IV) in Predicting the Concentrations of NO_x, NO_2, and O_3 under the Base Scenario 143

Figure 4-31: Comparing NO_x Concentrations of the DG Deployment and the Background Sources. Upper panel: Hourly concentration; lower panel: annually averaged concentration. 144

Figure 5-1: Schematic of the Hybrid Model 146

Figure 5-2: Control Volume Used for the Mass Balance of NOx and Ox within the Plume 147

Figure 5-4: Maximum 72-hr NO_x Ground-Level Concentrations (ppb) 153

Figure 5-5: The Contribution of DGs to the Maximum Increase/Decrease in Ground-Level Concentrations of NO_2 at Each Grid Point 153

Figure 5-6: The Ratio of NO_2 to NOx from Hess and Cope (1989) model 154

Figure 5-7: Maximum Increases/Decreases in Ground-Level Concentrations of NO_x under the EHP Scenario 155

Figure 5-8: Maximum Increase/Decrease in Ground-Level Concentrations of NO_2 under the EHP Scenario 155

Figure 5-9: Maximum Increase/Decrease in Ground-Level Concentrations of O_3 under the EHP Scenario 156

Figure 5-10: Comparison between the Impact on NO_x and NO_2 Predicted by the LBM to those Obtained from the Hybrid Model 156

Figure 5-11: DG Locations for the San Joaquin Valley EHP Scenario (SJV-EHP) 157

Figure 5-12: DG Emissions in the San Joaquin Valley 158

Figure 5-13: Increase or Decrease in Ground-Level 24-hour Maximum NO_x Concentrations under the SJV-EHP Scenario 159

Figure 5-14: Increase or Decrease in Ground-Level 24-hour Maximum NO_2 Concentrations under the SJV-EHP Scenario 160

Figure 5-15: Increase or Decrease in Ground-Level 24-hour Maximum O_3 Concentrations under the SJV-EHP Scenario 161

LIST OF TABLES

Table 2-1: The Distance of Each Camera from the Stack and their Orientation Relative to the North 17

Table 2-2: Stack Properties for Each DG Power Setting 18

Table 2-3: Morphological Parameters (λ_p, λ_f) and Average Building Heights (h_b) Associated with Three Different Urban Areas 23

Table 2-4: Meteorological and Boundary Layer Parameters from 56 Vertical Sounding Data (Different color shading corresponds to measurements at different nights) 31

Table 2-5: Correlation Coefficient (*r*) between the Boundary Layer Height Data and Different Modeling Parameters 42

Table 3-1: Experimental Parameters for Plume Rise Measurements 56

Table 3-2: Experimental Parameters for Plume Rise Measurements 72

Table 3-3: Model Parameters with Scaling Method 1 86

Table 3-4: Model Parameters with Scaling Method 2 87

Table 3-5: Field Parameters 88

Table 3-6: Turbulent Intensities Associated with the Field and Laboratory Model 93

Table 4-1: Statistical performance parameter of *LBM* for calendar year 2007 at two sites (West LA and San Bernardino) in the SoCAB 111

Table 4-2: Statistical Parameter of various air quality models 114

Table 4-3: Statistical performance measures of the *LBM* model for calendar year 2005 at two sites (Bakersfield and Shafter) in SJVAB. 124

Table 4-4: Comparison of m_g and s_g for the Different Cases of the Sensitivity Study 131

Table 5-1: Representative DG Specifications Used to Generate the DG Distribution for EHP Scenarios with a 50-m Resolution 151

EXECUTIVE SUMMARY

Fossil fuel-based distributed generation has the potential to meet a significant portion of increased power demand in California because of the following advantages:

(1) Reduction in electricity transmission losses because distributed generation units are located in the area they service

(2) Flexibility in size tailored to local power demand

(3) Increase in efficiency and decrease in emissions by replacing boilers with Combined Heat and Power systems

The main disadvantage of distributed generation is that emissions from distributed generation units can affect the air quality in local populated areas.

Several studies have examined the impact of distributed generation on air quality at urban and regional scales. One such study (Allison and Lents, J. Energy Policy, 30 (2002), 737-752) found that realistic distributed generation scenarios were likely to lead to net increases in emissions in urban areas. However, their analysis focused on aggregated emissions and did not relate these emission changes to air quality impacts. Another group (Rodriguez et al., Atmos. Environ., 40(2006), 5508-5521) performed a detailed examination of the impact of distributed generation emissions on ambient concentrations of both primary and secondary pollutants in the South Coast Air Basin using a regional grid model. The results of that study show that distributed generation penetration, amounting to as much as 20 percent of energy growth until 2010, results in the total increase of primary pollutants of less than 1 percent with respect to the baseline. Furthermore, distributed generation penetration has little effect on secondary pollutants such as ozone and concentrations of particulate matter 2.5 microns or less in size. However, that study did not provide results on the impact of primary distributed generation emissions on spatial scales of less than 5 kilometers (km) because the comprehensive air quality model uses a 5 km by 5 km grid resolution. The short-range impact of distributed generation units relative to central generating stations was addressed in a previous study (Improving Understanding of Regional and Near-Source Air Quality Impacts of Distributed Generation Sources; Appendix A), where the AERMOD atmospheric dispersion model was used to estimate the impact of distributed generation units on nitrogen oxide (NOx) concentrations within a few kilometers from the distributed generation emission point. The major conclusion from the study was that distributed generation units would reduce maximum NOx concentrations by a factor of four relative to central generating stations generating the same amount of power. This study did not address the chemistry associated with the conversion of nitrogen monoxide (NO) to nitrogen dioxide (NO_2) or the calculation of a model to estimate the relative impact of other sources of NOx in the domain of interest.

This report describes results from the research that extend the work described above. This study focused on two recommendations from the earlier study, funded by the California Energy Commission:

- Examine the impact of multiple buildings on plume rise and dispersion. Such situations are important because of the regulatory concern with risks posed by emissions of toxics in urban areas.
- Develop models to address concentrations at scales ranging from a few meters to hundreds of kilometers by combining large-scale grid models with short-range dispersion models, such as AERMOD.

Methods

A field study and a laboratory study were conducted to examine the impact of urban buildings on plume rise. In November 2010, a field study was conducted in Palm Springs, California, to study plume rise from a distributed generation unit with a stack height of 9.3 meters (m). Smoke oil was injected into the stack to produce a thick white smoke visible to the naked eye, and cameras were used to measure the plume rise. A method was developed to measure plume rise when the wind direction was not perpendicular to the camera lens orientation.

The laboratory study was conducted in the water channel facility at the University of California, Riverside, Laboratory for Environmental Flow Modeling, to understand the effect of nearby buildings on plume rise. A distributed generation building similar to the Palm Springs distributed generation unit ($L \times W \times H$ = 15 m × 15 m × 7 m) with a stack height of 9.3 m was modeled in the water channel at a scale of 1:100. Arrays of buildings (two rows and three columns) of two different heights (single- and double-story, with heights of 100 millimeters (mm) and 200 mm, respectively) were created and were situated upstream and downstream of the distributed generation building. A florescent dye injected into the stack enabled the research team to visualize and quantify plume rise using a variety of building configurations.

The use of a comprehensive photochemical model, the University of California, Irvine-California Institute of Technology model, was explored to estimate the background concentrations of pollutants required to estimate the local impact of distributed generators. The computational resources required to run the University of California, Irvine-California Institute of Technology model became impractical for annual simulations and sensitivity studies, so a computationally efficient background model, referred to as the Lagrangian background model, was developed to compute the concentrations at a receptor by following the history of a 5 km by 5 km air parcel that reaches a receptor of interest every hour. The history of the air parcel was traced back 24 hours through back trajectories calculated using surface winds measured at meteorological stations. Emissions were injected into the box and mixed through its volume as the box moved over the urban area. The photochemistry and transport processes were split using the concept of *species age*. The species age is the average effective age (the effective age of a molecule is the time taken for the molecule to travel from source to receptor) of the species within the box. The species age decreases as fresh emissions are added to the box and increases as the box travels along the trajectory. Then, the chemical transformation of this species is estimated by reacting it with other species in a box with initial concentrations corresponding to those in the absence of chemistry. The time period for chemical calculations is specified by the end time corresponding to the time of

interest and a start time, which is the end time minus the species age. The model was evaluated with data from the South Coast Air Basin and the San Joaquin Valley.

A hybrid model was then developed by combining the background model with the local dispersion model, AERMOD. A method was developed to combine the background concentrations of NO, NO_2, and ozone with the local AERMOD predictions, which accounts for entrainment of the background species into the plumes emitted from local sources. The concentrations of NO, NO_2 and ozone were estimated under an emission scenario for the South Coast Air Basin and the San Joaquin Valley. The research team ran both a "base" scenario for the South Coast Air Basin in 2010 and a hypothetical scenario in which distributed generation accounts for 20 percent of the increased power demand from 2002 to 2010 in the South Coast Air Basin (extra-high penetration scenario). They also ran a "base" scenario for the San Joaquin Valley and a hypothetical scenario in which distributed generation accounts for 45 percent of the increased power demand of the San Joaquin Valley from 2007 to 2030.

Results

This research shows that fossil fuel-based distributed generation of electricity has a relatively small impact on local air quality, and is thus a viable alternative to conventional centralized generation of electricity. This information can be used to improve air quality and mitigate adverse health impacts associated with air pollution from power generation in California.

Specific results from the study are:

- Estimates of hourly and annually averaged near-source concentrations of primary and secondary pollutants associated with distributed generation penetration scenarios in the South Coast and the San Joaquin Valley developed by the University of California, Irvine.
- A computationally efficient model to compute concentrations of NO, NO_2, and ozone over regional scales of 10 to 100 km.
- A hybrid model that combines concentrations from the background model with a short-range dispersion model such as AERMOD
- A method to measure plume rise in urban settings using visualization and photographs of the plume.

Conclusions

The study resulted in the following major conclusions:

1. The Briggs plume rise prediction, an analytical plume rise model used in dispersion models such as AERMOD, was in good agreement with the observations from the field study, which shows that the relatively sparse and small buildings surrounding the distributed generation do not have significant impact on plume rise. The low wind speeds in Palm Springs allow the plume to rise high relative to the stack,

avoiding possible trapping by the updrafts/downdrafts caused by distributed generation and surrounding buildings.

2. The results from laboratory measurements show that, in most cases, the presence of surrounding buildings increases the plume rise because buildings reduce the wind speed close to the stack and induce updrafts in the region where the plume tends to rise. However, the plume rise is reduced by increasing the height of the downstream buildings.

3. Evaluations with measurements made in the South Coast Air Basin during 2007 and in the San Joaquin Valley indicate that the Lagrangian background model can provide adequate descriptions of the spatial and temporal behavior of NO_x and NO_2. Model estimates of maximum hourly ozone concentrations are unbiased relative to observations, but the 95 percent confidence interval of the ratios of observed-to-estimated concentrations is over a factor of two. A comparison of the background model with the University of California, Irvine-California Institute of Technology model shows that the model predicts higher concentrations, and the variation of ozone concentrations predicted by the model is larger than that of the Lagrangian background model.

4. A sensitivity study of the Lagrangian background model shows that the model is not sensitive to the wind speed and direction. This is because the trajectory, modified by changing the wind speed and direction, still passes through grid squares with emissions that are similar to those of the unmodified trajectory. The model sensitivity to wind speed and direction must depend on the emission distribution because the function of the trajectories is to select the grid squares from which emissions contribute to the predicted concentrations. If the emission distribution within the San Joaquin Valley were less homogeneous, then the model would likely be more sensitive to the wind speed and direction.

5. This study also validates the researchers' choice of the surface winds, rather than the upper air winds, for calculating the trajectories in the San Joaquin Valley and the South Coast Air Basin because the model estimates are not very sensitive to the wind speed in these domains.

6. The model is also not sensitive to the time period over which the back-trajectory is calculated. This is due to the boundary layer height variation over a 24-hour period; when the boundary layer collapses at dusk the pollutant mass above the nighttime boundary layer height is lost, which reduces the total mass that the model accumulates over a 24-hour period and limits the concentration increase over time periods greater than 24 hours.

7. The most important factor of the Lagrangian background model is the emission distribution. The model is also sensitive to the boundary layer height formulation, which is important to produce adequate estimates of the hourly concentration variation.

8. Increasing the species age causes the model to overestimate NO_2 and ozone. This, along with the comparison with observations, shows that the researchers' formulation of the species age accurately represents the chemical processes and is useful for decoupling the transport and chemical processes of the model.

9. The contribution of fossil fuel-baseddistributed generation units to the ground-level concentrations of NO_x, NO_2, and ozone in the South Coast Air Basin is less than 10 percent of the base concentrations. Under the extra-high penetration scenario the maximum increase in NO_2 is about 10 parts per billion and the maximum decrease in ozone is about 8 parts per billion. The reason for this low impact is the relatively small increase in the total emission associated with distributed generation units under the extra-high penetration scenario. Similar results were found when comparing the base and extra-high penetration scenarios for the San Joaquin Valley. In the San Joaquin Valley the maximum increase in NO_2 and ozone are both about 1 part per billion, relative to the base concentrations of about 30 and 60 parts per billion, respectively. The maximum NO_2 change occurs near Stockton and Bakersfield, where most of the distributed generation emissions are located.

CHAPTER 1:

Introduction and Objectives

Several studies have examined the impact of fossil fuel-based distributed generation (DG) on air quality at urban and regional scales. Allison and Lents (2002) examined the tradeoff between the increase in emissions associated with urban DG emissions and the decrease in emissions by replacing heating plants with waste heat generated from DG plants. They found that realistic DG scenarios were likely to lead to net increases in emissions in urban areas. Their relatively simple analysis focused on aggregated emissions and did not relate these emission changes to air quality.

Heath et al. (2006) examined the air quality impact of DG units relative to central generating stations. They found that the air quality impact of DG units, quantified in terms of intake factors, could be several times that of central generating (CG) stations because (1) the ground-level concentrations from the elevated emissions of a CG plant are much smaller than those associated with the near surface emissions from DG units, such as microturbines, and (2) CG plants are likely to be located far from urban centers, while DG units are located in urban areas close to energy consumers. These conclusions are based on a simple Gaussian model applied to idealized emission scenarios that do not account for existing emissions. Thus, the results from Heath et al. (2006) do not directly address the impact of DG emissions on ambient concentrations under realistic emission scenarios.

Carreras-Sospedra et al. (2004, 2008) have performed a detailed examination of the impact of DG emissions on ambient concentrations of both primary and secondary pollutants in the South Coast Air Basin (SoCAB). A major part of their effort was the construction of detailed emission inventories for the year 2010. These inventories accounted for growth in energy demand as well as likely DG penetration scenarios. The DG emissions were spatially allocated in the SoCAB using demographic and land-use information. The air quality impacts of DG were examined by running a comprehensive photochemical model using these emission scenarios as inputs. Because DG emissions contribute less than 3 percent to the total projected nitrogen oxide (NO_x) emissions in SoCAB, and less to the voltaic organic compound (VOC) emissions, ambient concentrations of ozone (O_3), nitrogen dioxide (NO_2), and particulate matter (PM) are changed by relatively small amounts. The maximum concentrations show almost no change, while the largest changes of about 5 percent occur during nighttime conditions. These results show that DG penetration, amounting to as much as 20 percent of energy growth until 2010, has little effect on secondary pollutants such as O_3 concentrations and concentrations of particulate matter smaller with a diameter smaller than 2.5 microns ($PM_{2.5}$). However, this study did not provide results on the impact of primary DG emissions on scales of less than 5 kilometers (km) because the comprehensive air quality model uses a 5 km by 5 km grid resolution. Thus, emissions are instantaneously mixed through a box that is 5 km by 5 km by the mixed layer height. While this approximation might be valid for estimating secondary pollutants, it cannot provide realistic concentration estimates of primary pollutants at neighborhood scales of meters to kilometers.

Over the past years, methods have been developed to estimate the air quality impact at source-receptor distances of hundreds of meters (Venkatram 2008; Venkatram at al. 2004a) within urban areas. These methods are currently being evaluated with field observations of concentrations due to distributed generators.

A realistic assessment of the air quality impact of urban sources such as DGs requires a model that can estimate concentrations at the required scale of interest. In principle, an Eulerian grid model could satisfy this requirement if the grid size was small enough, but such a model would be impractical from a computational viewpoint. Furthermore, at scales of meters, dispersion parameterizations in grid-based models are inadequate for resolving the horizontal and vertical structure of plumes.

A potential solution is to combine models for regional- and local-scale transport: the regional transport model, such as that used by Carreras-Sospedra et al. (2004), provides the background concentrations of primary and secondary pollutants, and the local-scale model provides concentrations resolved at scales of tens of meters. Such an approach has been used by Stein et al. (2007) to examine the impact of urban sources of benzene in greater Houston. The Community Modeling and Analysis System (CMAS) model was used to model primary and secondary pollutant concentrations over a 36 km by 36 km region covered with a 1 km square grid. AERMOD, an atmospheric dispersion model, was used to resolve concentrations at scales of tens of meters. Estimates from the two models were combined at a selected receptor using the following approach. First, the Community Multiscale Air Quality (CMAQ) model was run by zeroing out the emissions in the grid corresponding to the receptor. The resulting concentration constituted the background in the grid square. Then, AERMOD was run with the missing emissions to compute the concentration at the receptor, which was then added to the CMAQ "background" value to yield the total concentration at the receptor. It turned out that the concentrations computed using this "hybridization" procedure compared slightly better with observations than did concentrations from either CMAQ or AERMOD individually.

Isakov et al. (2007) used a slightly modified approach in modeling fine-scale features of formaldehyde and benzene in the greater Philadelphia area. In this case, the local-scale contribution was parameterized as the difference between the concentration predicted by the local-scale model, and the average of the local-scale estimates over the CMAQ grid in which the receptor was located. The local-scale model only considered primary emissions of benzene and formaldehyde; chemistry was neglected.

This project examined two models to estimate regional-scale concentrations (1) the UCT-CIT Eulerian Model, and (2) a computationally efficient Lagrangian background model (LBM). The hybrid model was constructed by combining concentrations from the regional model with short range concentrations from AERMOD (Cimorelli et al. 2005). This project also evaluated the applicability of the plume rise equations in AERMOD to small sources, such as gas-fired generators.

The objectives of this project were to:

1. Develop and evaluate a model that improves upon current models of plume rise from near-surface sources, such as distributed generators.
2. Incorporate an improved plume rise model into the local-scale model, and evaluate this model with data from field studies.
3. Develop a hybrid model that combines concentration estimates from regional- and local-scale models.
4. Apply the hybrid model to the South Coast and the San Joaquin Valley air basins, to demonstrate its capability in estimating the air quality impact of potential distributed generation of electricity in these regions.

The following sections describe the results from research conducted to achieve the preceding objectives.

CHAPTER 2:

Plume Rise and Stable Boundary Layer Height: Field Study

2.1 Introduction

Ground-level concentrations of pollutants emitted from a stack are extremely sensitive to plume rise. Since the 1950s, many studies have been made in an attempt to provide accurate numerical and analytical models to predict plume rise from large centralized power plants (Halliday 1968) or sources located far away from urban environments with stack heights of 200 to 300 meters (m) (Fay 1973). In 1963 the Tennessee Valley Authority (TVA) initiated a comprehensive plume rise study with relatively tall stacks (about 150 m) during stable, neutral, and slightly unstable conditions (Carpenter et al. 1968). The analysis of the data obtained from that field study revealed that wind speed and stack heat emission rate are the most significant parameters determining the plume rise from large power generating stations.

Halliday (1968) carried out field measurements of plume rise from a 76.3 m stack to verify plume rise equations developed by Priestly (1956), Bosanquet (1957), and Lucas et al. (1963). They measured the plume rise by taking photographs of the plume. The disadvantage of Halliday's (1968) plume rise measuring technique was that plume rise could only be correctly measured when the wind direction was perpendicular to the camera lens orientation. Hence, for cases when the wind direction was not perpendicular to the camera orientation, this technique did not give accurate results. In other studies, Hamilton (1967) and Bacci et al. (1974) also measured plume rise using the *LI*ght *D*etection *A*nd *R*anging (LIDAR) technique. They related their data to the meteorological variables and power station operating conditions and showed that the plume rise measurements were in agreement with the models developed by Lucas et al. (1963) and Briggs (1969).

The ability to explain the concentrations associated with a low-level buoyant source through a model, such as AERMOD (Cimorelli et al. 2005), is limited (Jing et al. 2010). One of the reasons for this limitation can be the formulation of plume rise. In AERMOD, the plume rise formulation (Weil 1988; Briggs 1984) is designed primarily for elevated emissions from large power plants where it neglects building effects, as well as the effects of the variation of meteorological parameters with height that govern the plume rise for near-surface DG sources. Distributed generation resources commonly deploy heat recovery to increase the efficiency during power generation. This heat recovery lowers the exhaust gas temperature, which results in lower plume rise. The lower plume will be much more affected by surrounding buildings. This further increase the uncertainty of simple models (e.g., Weil, 1988; Briggs 1984) in predicting the plume rise associated with DGs, since they have no capability to incorporate building effects.

None of the past and current studies have focused on plume rise from low-level buoyant sources. Furthermore, none of them have studied the effects of buildings on plume rise. Hence, this study was motivated by the need for a better understanding of the plume rise from low-level buoyant sources in urban areas and reliable models to predict it. As the first step towards satisfying this need, a field study was conducted in Palm Springs, California, USA. Plume rise from a DG located in Sunrise Park was measured using a new plume rise photography method where, unlike the previous photography methods applied by Halliday (1968) and Bringfelt (1968), plume rise was correctly measured even if the wind direction was not perpendicular to the camera lens orientation.

Results from the field study are highly dependent on the site meteorological conditions, and it would be difficult to extrapolate the plume rise results from the Palm Springs study to other urban settings. Also, conducting field studies for various wind conditions at different sites would be prohibitively expensive. For these reasons, in addition to the field study, a systematic laboratory investigation was done, and plume rise under several different upstream and downstream building geometries was measured in the water channel facility at the University of California (UC), Riverside. Field measurements are explained in Section 2.2, followed by the laboratory and numerical study in Chapter 0.

The impact of DG on NO_2 concentrations is largest during the night, when NO emissions react with background O_3 to produce NO_2 in the absence of photolysis, and the shallow stable boundary layer limits dispersion. The understanding of dispersion during nighttime conditions is limited, in part because there is not a generally applicable model of the stable boundary layer height. Even less is known about the nighttime boundary layer height in urban environments, which is particularly important to estimate DG impact, so the researchers conducted a field study to measure the height of the nocturnal urban boundary layer. The field study and a comparison with several models of boundary layer height are explained in Section 2.3.

2.2 Field Study

In November 2010, a field study was conducted in Palm Springs, California, USA. In this study, the plume rise from a DG, located in Sunrise Park, with a stack height of 9.3 m and stack diameter of 0.3 m, was measured under different source conditions. Sunrise Park is located in the central area of Palm Springs, close to the downtown, between Ramon Road and E. Baristo Road. This park consists of 38 acres of grassy area and is surrounded by a residential area with mostly single-story (≈ 5–7 m height) buildings and 10–15 m tall palm trees. The site has an approximate roughness length of z_0 = 0.5 m; zero plane displacement height of d_h = 2.5 m ($d_h = 5z_0$ based on Britter and Hanna 2003); Bowen ratio of Bo = 1.5; and surface albedo of al = 0.22. These surface parameters correspond to those recommended by the South Coast Air Quality Management District (SCAQMD). They were obtained by applying AERSURFACE (EPA 2008), a program developed by the U.S. Environmental Protection Agency (U.S. EPA) to the Palm Springs urban area (SCAQMD 2009). The DG was surrounded by Palm Spring swim center (a single story $L \times W \times H$ = 50 m × 30 m × 7 m building) to the south, a baseball stadium to the north-east, and a playground to the west.

The plume rise measurements were accompanied with basic meteorological measurements, which are described next.

Figure 2-1: Location of the Meteorology Stations (Yellow Pins) in Sunrise Park, Palm Springs, California

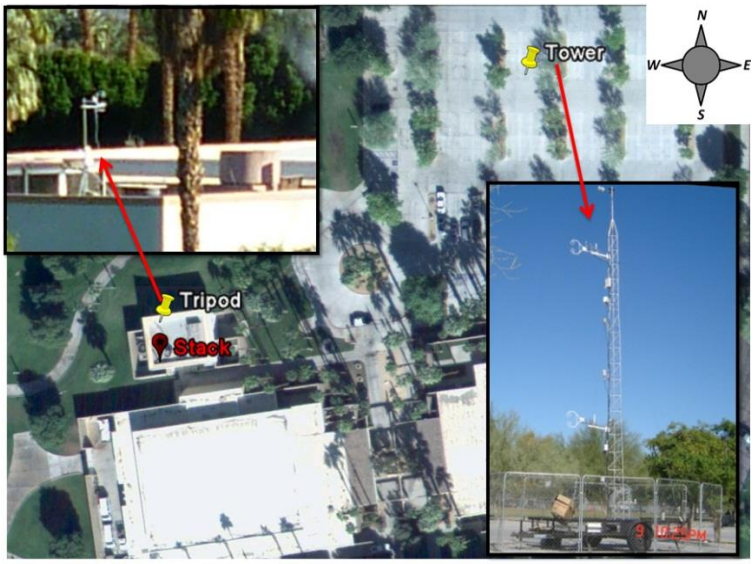

The aerial picture was produced using Google Earth.

2.2.1 Meteorology

Two meteorological stations were set up: a tower (with two sonic anemometers at 3 m and 8 m above ground level) and a tripod (with a sonic anemometer at approximately 4 m above the rooftop of the DG, i.e., 11 m from the ground). Figure 2-1 shows the locations of these two stations. The tower was set up on the parking lot of Sunrise Park within 100 m of the DG facility, and the tripod was set up on the roof of the DG building. Three components of wind speed and the ambient virtual temperature were measured by sonic anemometers at the rate of 10 samples per second. Using these measurements, mean and turbulent wind speeds and surface heat flux were calculated and averaged over periods of 15 minutes (9,000 samples).

Figure 2-2 shows the meteorology measured from November 7 to November 10 from the sonic anemometer located on the roof of the DG at 11 m from the ground. The data show that wind speeds are less than 1 meter per second (m s^{-1}) for most of the days. This makes Palm Springs a low wind speed case compared to other urban areas, where wind speeds mostly exceed 3 m s^{-1} during the day (Allwine et al. 2006; Venkatram et al. 2004b; Rotach et al. 2004). The wind direction were variable, vertical turbulent velocities (Figure 2-2d) were approximately 0.25 m s^{-1}, and lateral turbulent velocities (Figure 2-2c) were generally higher, around 0.5 m s^{-1}. The site in Sunrise Park has relatively high turbulent intensities of about 25 percent in the vertical direction and about 50 percent in the horizontal direction. In addition, as the wind direction changes substantially (Figure 2-2b), plume meandering can play a major role in the dispersion of pollutants released from the DG.

Figure 2-2: Meteorology Measurements (a) Wind Speed U (m s-1), (b) Wind Direction, (c) Lateral Turbulent Velocity σ_v (m s-1), (d) Vertical Turbulent Velocity σ_w (m s-1), and (e) Sensible Heat Flux $\rho C_p \overline{w'T'}$ (W m-2) (green dots show the meteorology at the time of the plume rise measurements on November 2009 from 1400 to 1500 PST).

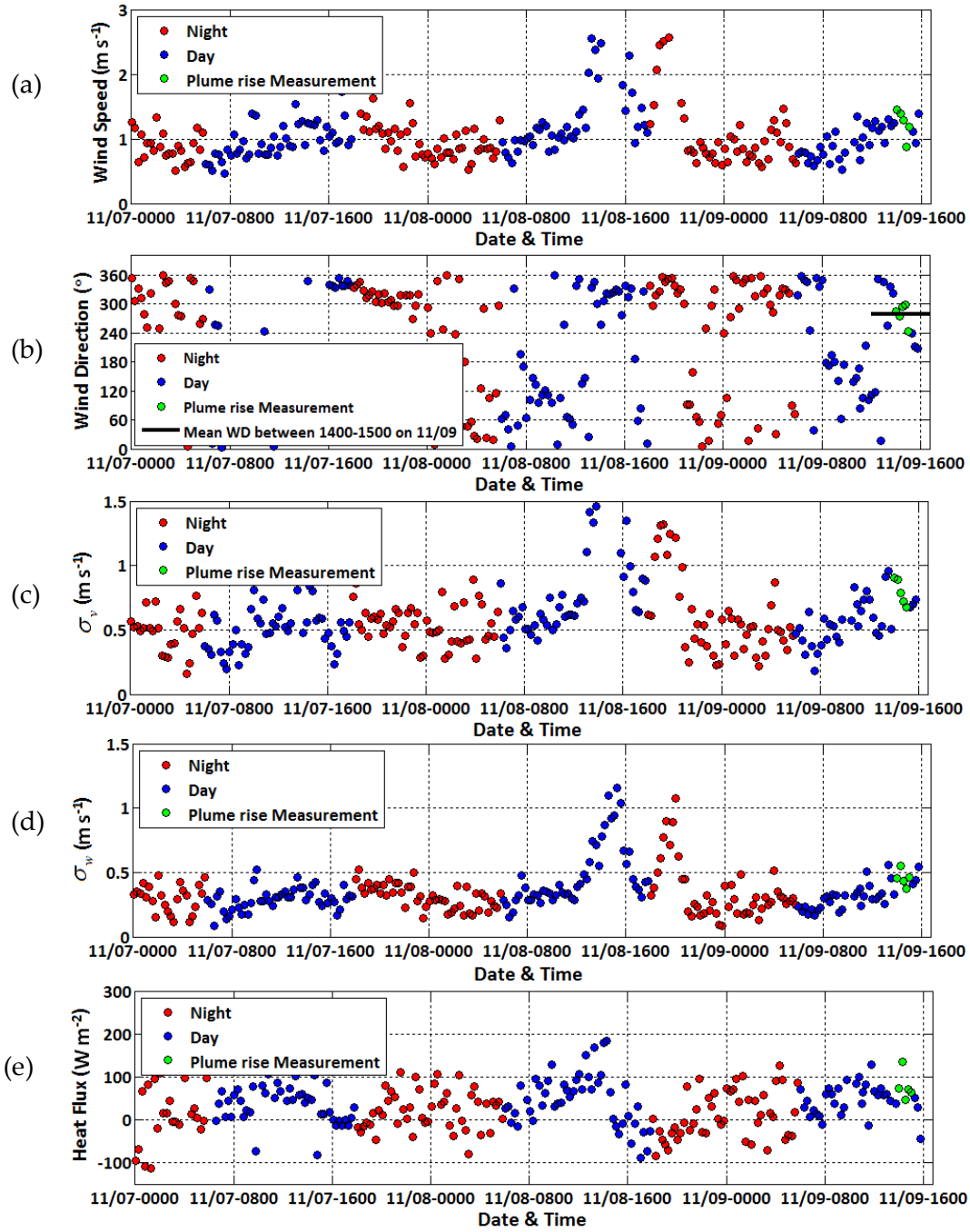

A comparison between data from different sonics showed that there is no significant spatial variation of micrometeorology between the roof of the DG and the tower site. In addition, it has been observed that wind direction does not change substantially with height up to 11 m from the ground.

2.2.2 Plume Rise

In order to visualize the plume released from the DG, smoke oil (Super*Dri® Aviation Smoke Oil) was injected into the stack four meters below the stack exit to allow for oil evaporation and mixing. This produced a thick white smoke visible to the naked eye. Consecutive images of the plume were taken from different locations close to the stack using commercial digital cameras (Figure 2-3a). The plume images were averaged over five minute periods, and the background image (an image that was taken from the same location when there was no visible plume exiting the stack) was subtracted from the averaged images (Figure 2-3b). After the contrast enhancement, only the region of the highest smoke concentration (i.e., the plume centerlines) remained on the image. The height from the stack of the line passing through the center of this region (the green line in (Figure 2-3b) represents the average plume rise, i.e., averaged location of the plume centerlines. The horizontal and vertical distances (L) of the plume centerline can be calculated as,

$$L = L_{image}\left(H_{s-field} \big/ H_{s-image} \right) \tag{2-1}$$

where L_{image} is the distance (horizontal or vertical) of the plume centerline measured on the averaged image; $H_{s-field}$ and $H_{s-image}$ are the height of the stack in the field and the image, respectively. However, it needs to be noted that the calculation of the plume centerline height from such an image is only accurate when the plume direction (i.e., wind direction) is perpendicular to the camera lens orientation. Therefore, for the cases where the wind direction was not perpendicular to the camera orientation, corrections were made to calculate the correct plume rise. The following section describes the correction method for the discrepancy in wind direction and camera orientation.

Figure 2-3: Measurement of Plume Rise Associated with the Palm Springs DG

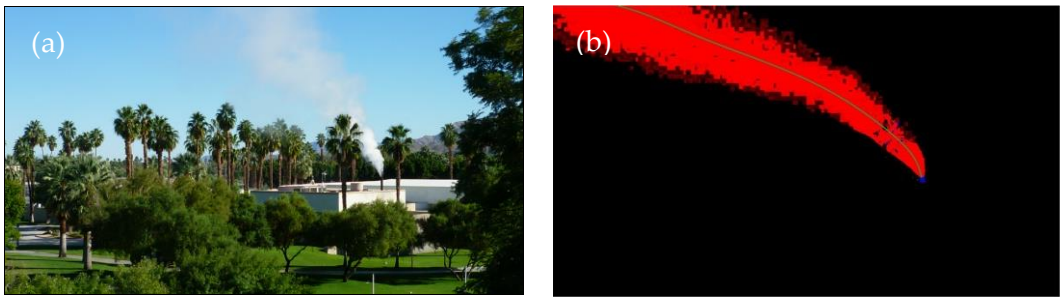

(a) Example of an instantaneous photograph of the plume released from the DG, and (b) The averaged image of the plume with the background subtracted and contrast enhanced. This is considered as the region of the plume centerlines. The mean plume centerline is shown as a green line.

2.2.3 Correction Method

Figure 2-4 gives the schematic used for the correction method. The plume centerline plane (the brown line in Figure 2-4) in general does not overlap with a plane that is normal to the camera orientation and passes through the stack (*Normal Plane* in Figure 2-4). The plume centerline plane deviates from the *Normal Plane* by an angle θ_1; the camera is located at a distance D_{stack} from the stack; X_m is the downwind distance of the plume centerline calculated from the averaged plume images through equation 2-1 assuming that plume direction is perpendicular to the camera lens orientation; L_{cam} is the distance of the camera to the *Normal Plane*; λ is the angle between the *Normal Plane* and the line connecting the stack to the camera. The corrected plume centerline downwind distance X_{real} can be calculated as follows:

$$X_{real} = X_m\left(\cos(\theta_1) + \sin(\theta_1)\tan(\theta_3)\right) \tag{2-2}$$

where $\theta_3 = \theta_1 + \theta_2$, and

$$\theta_2 = \tan^{-1}\left(\frac{X_m - X_{centre}}{L_{cam}}\right) \tag{2-3}$$

where X_{center} is the distance in the field from the stack to the center of the image and

$$L_{cam} = D_{stack}\sin(\lambda). \tag{2-4}$$

Figure 2-4: Schematic Used for the Correction Technique for the Case When the Plume Centerline (Brown Line —) Is Deviated from the Normal Plane of the Camera Lens (Blue Line —).

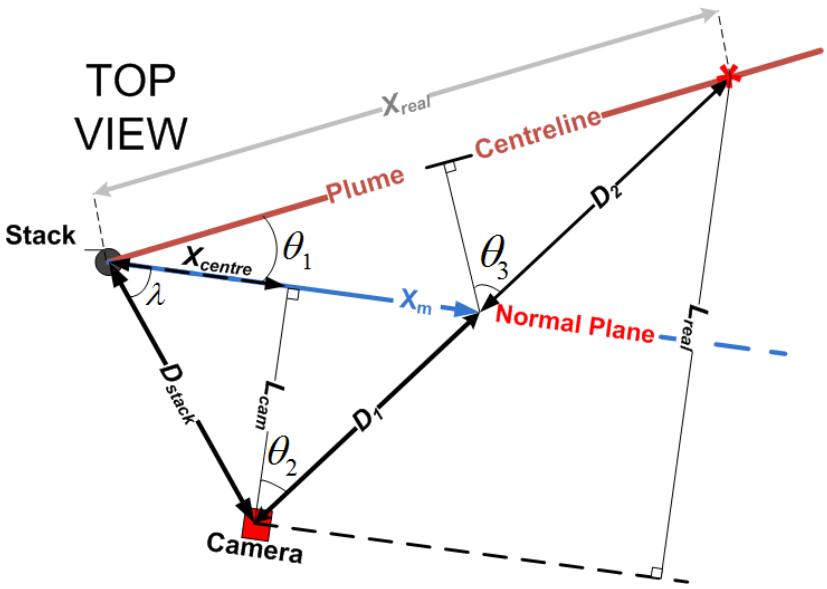

Assuming that plume rise measured from the averaged image is Z_m, the corrected plume rise Z_{real} is calculated as follows,

$$Z_{real} = Z_m \left(L_{real} / L_{cam} \right) \tag{2-5}$$

where $L_{real} = L_{cam} + X_{real} \sin(\theta_1)$.

By utilizing this method, the numerical value for plume rise was corrected for all wind directions measured by sonic anemometers located at the roof of the DG. This method cannot incorporate the change in the wind direction with height. Since the measurement of the plume rise was limited to 35 m from the ground, and the wind direction measurements at three different heights (up to 11 m) did not differ significantly, the researchers assumed that there was no significant variation in wind direction over the observed plume.

2.2.4 Field Measurements

Plume rise measurements were conducted on November 9, 2010. Figure 2-5 shows the wind speed and direction measured one hour before the experiment (13:00) until one hour after the experiment (16:00). It can be seen that the wind direction is mostly towards the east; however, its deviation from the mean is relatively large. Therefore, most of the cases needed correction.

Figure 2-5: (a) Wind Speed and (b) Wind Direction

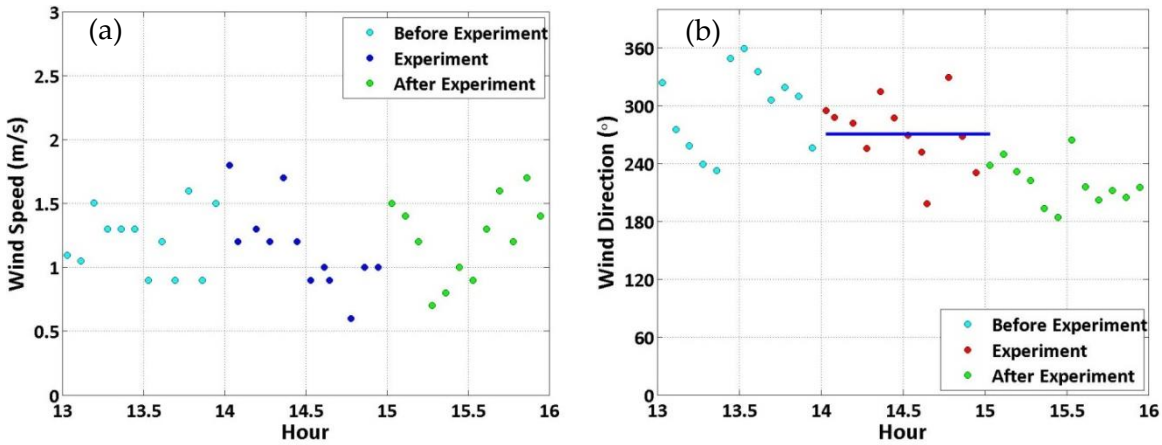

Measured from 13:00 to 16:00 on November 9, 2010, During Plume Rise Measurements

Plume rise data were gathered by five cameras at different locations relative to the stack (Figure 2-6), in order to have full coverage of the plume under different wind angles. The orientation of each camera and their distance from the stack are shown in Table 2-1.

Table 2-1: The Distance of Each Camera from the Stack and their Orientation Relative to the North

Camera	Distance from Stack (m)	Camera Orientation from North
CAM 1	119	125°
CAM 2	67	100°
CAM 3	67	35°
CAM 4	67	65°
CAM 5	34	275°

Images were captured at the rate of approximately one image per second. Experiments were conducted for two power outputs of the DG. By changing the power output of the DG, the stack exit velocity changed. Since the heat recovery was not modified, due to the need of the community center, the exhaust temperature also changed for each power setting. The stack exit velocity and exhaust temperature were measured using a pitot tube and a k-type thermocouple, respectively. Table 2-2 shows the details of the parameters involved in each DG power setting. For each DG power setting, the average plume rise was measured in intervals of five minutes and was compared with the Briggs (1984) plume rise formulation described in previous chapters.

Figure 2-6: The Location of the Five Cameras (blue pins) with Respect to the Location of the Stack (red pin).

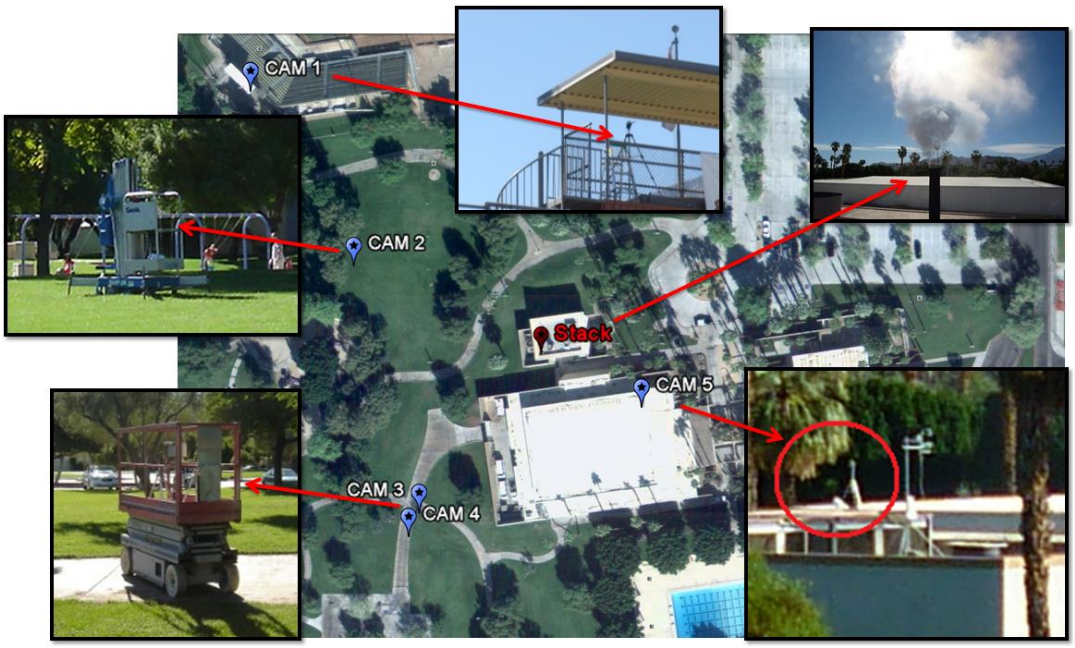

The aerial picture was produced using Google Earth.

Table 2-2: Stack Properties for Each DG Power Setting

Stage #	Time Interval	Stack Exit Temperature	Stack Exit Velocity (m s^{-1})	DG Output (kW)
1	1400–1420	248.5°C	15.4	600
2	1425–1440	210.7°C	9.5	300

kW = kilowatts

2.2.5 Results

The results of plume rise measurement and uncertainties associated with them were compared with the Briggs (1984) formulation, as shown in Figure 2-7. Here, the uncertainties, σ, were obtained by calculating the standard deviation of the height of plume centerlines from the averaged and contrasted plume images (e.g., Figure 2-3b). The measured wind speed at the roof of the DG building (11 m from the ground) was employed in predicting the plume rise. It can be seen that, for most of the cases, the predictions made by utilizing the Briggs plume rise model are in good agreement with the observations from the field experiment. Although the experimental uncertainties are relatively higher than the differences between the observations and predictions, in most cases it can be seen that

plume rise is slightly over-predicted close to the stack, and is under-predicted by the Briggs formulation further downwind. The primary reasons for these differences are likely the lower wind speed at the stack exit (z = 9.3 m) and the effect of the ambient turbulence on the plume rise at larger downwind distances. Lower wind speed allows the plume to rise higher near the stack, and ambient turbulence suppresses the plume rise at larger distances. Although these effects can slightly modify the plume rise behavior, the Briggs formulation appears to perform reasonably well in predicting plume rise.

As it was shown in Figure 2-2a, Palm Springs was dominated by low wind speeds with a mean value of approximately 1 m s^{-1} and a maximum of 1.5 m s^{-1} for most of the days. This allowed the plume to rise relatively high, making the effect of nearby buildings on the plume rise non-existent. Also, because the urban morphology of Palm Springs consists of mostly low-rise (single-story) buildings, approximately the same height as that of the DG, it is not expected for the plume to be affected by complex flows caused by buildings (e.g., updrafts and downdrafts) in the region where it tends to rise.

2.2.6 Conclusion

Distributed generation units are highly efficient as they customarily deploy heat recovery, thus providing both electricity and heating/cooling to nearby facilities. This heat recovery decreases the exhaust temperature, which leads to a lower plume rise that can result in higher ground-level concentrations. Therefore, realistic modeling of plume rise from DGs plays a major role in determining the ground-level concentrations associated with these sources. In this study, laboratory and field measurements have been conducted to investigate the plume rise associated with these low-level buoyant sources under different meteorological conditions and surrounding building geometries.

This chapter describes the field study conducted in November of 2010, where the plume rise associated with a DG located at Palm Springs, California, was measured. Meteorological parameters, such as the mean and turbulent wind speeds, and the sensible heat flux, were measured using sonic anemometers. On November 9, plume rise was measured for a 40-minute period (1400–1440). The measured plume rise was compared with the Briggs (1984) plume rise model. The Briggs plume rise prediction was in good agreement with the observations from the field study, which shows that the relatively sparse and small buildings surrounding the DG do not have significant impact on plume rise. The low wind speeds in Palm Springs allow the plume to rise high relative to the stack, avoiding possible trapping by the updrafts/downdrafts caused by DG and surrounding buildings. As the plume rises higher, the effects of the buildings on plume rise become smaller.

Figure 2-7: Normalized Measured Plume Rise

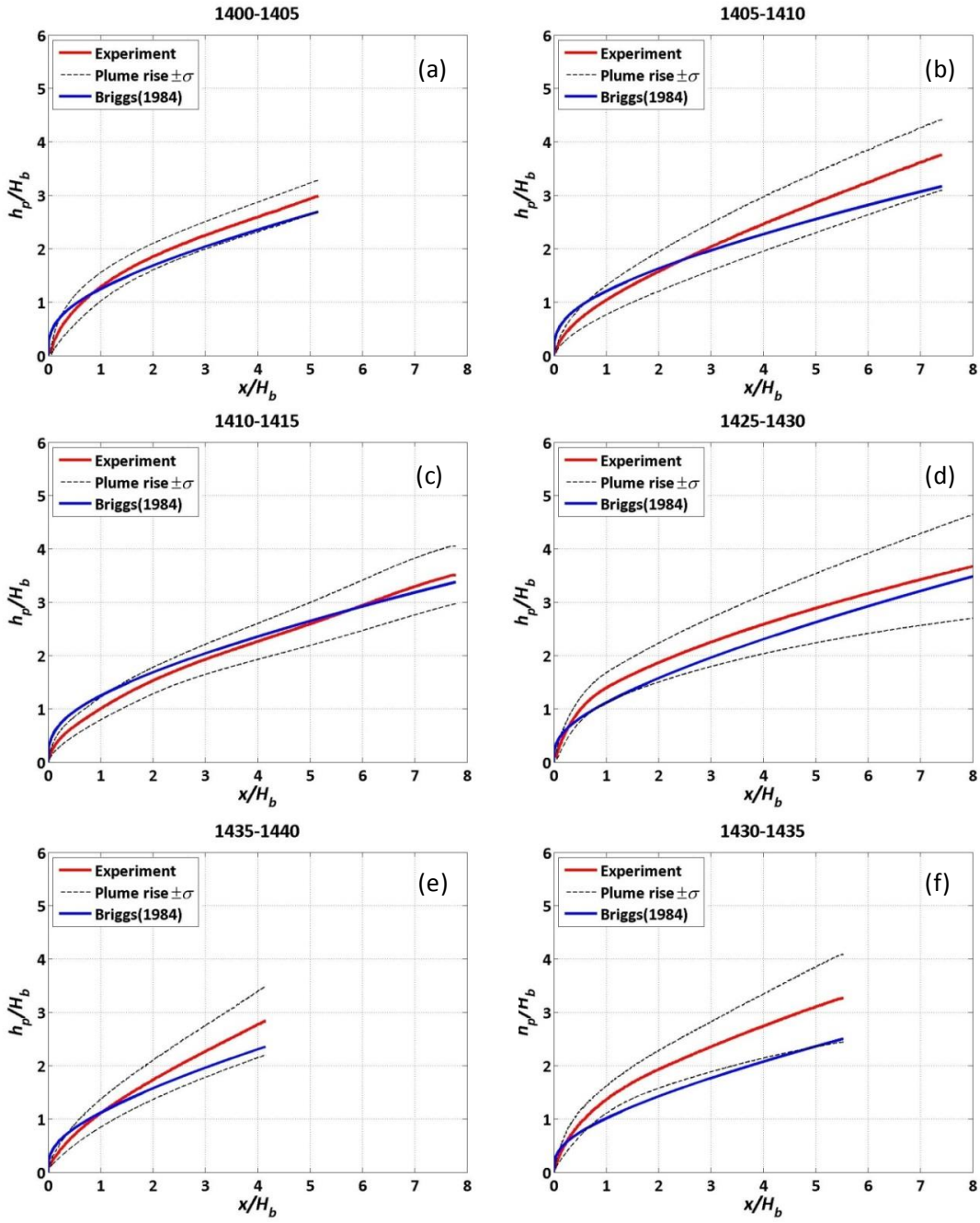

(red ▬) vs. Briggs (1984) Plume Rise Model (blue ▬) for Time Intervals of (a) 1400–1405, (b) 1405–1410, (c) 1410–1415, (d) 1425–1430, (e) 1430–1435, and (f) 1435–1440 (Plume rise, h_p, and distance x, are normalized with respect to building height H_b = 7 m). The error bars for measured centerline ($h_p \pm \sigma$) are also shown as a black dashed (----) line. Both the error lines and the plume centerline are smoothed

Conducting different field tests in order to examine the effect of various urban geometry and meteorology is prohibitively time consuming and expensive. Also, preparation for field

measurements includes proper permit seeking, and there are not many DG owners willing to allow plume visualization from their DG stacks. Therefore, in order to have a better understanding of plume rise in the presence of upstream and downstream obstacles near the source under more controlled stack and wind conditions, a laboratory study was done. Unlike the Palm Springs field study, where a low wind condition was considered; in the laboratory study, the researchers examined the plume rise under relatively high wind speeds. The laboratory study is described in Section 0.

2.3 Estimating the Height of the Nocturnal Urban Boundary Layer for Dispersion Applications[1]

2.3.1 Introduction

In the Palm Springs field study conducted in July 2008, the highest concentrations occurred during the night, even though the emissions were highly buoyant (Jing 2011). The ability to explain these concentrations through a model, such as AERMOD (Cimorelli et al. 2005), was limited by the uncertainty in describing the structure of the stable boundary layer (SBL) over an urban area. Thus the researchers initiated the following study to address the need for a model to estimate ground-level concentrations associated with emissions from low-level buoyant sources, such as distributed power generators.

The height of the atmospheric boundary layer (ABL) is highly variable with time and ranges from tens of meters at night to thousands of meters during daytime (Stull 1988). One of the main characteristics of the ABL is the presence of relatively high turbulence near the ground. Pollutants emitted in this layer are dispersed in both a horizontal and vertical direction as a result of turbulence and eventually become well mixed throughout this layer. As a result of this mixing, the height of this layer can strongly influence the ground-level concentrations, especially during nighttime when the boundary layer is relatively shallow.

Characteristics of ABL are well described in the literature, and there are several textbooks (Arya 1988; Stull 1988; Sorbjan 1989; Garratt 1992; Kaimal and Finnigan 1994) that provide detailed descriptions on its mean and turbulent structure. Here the team mentions some basic characteristics of ABL related to the scope of this study.

It has been found that the ABL becomes stably stratified during nighttime, due to surface cooling (Stull 1988). As a result of this, turbulence is suppressed due to stability damping. In urban areas, presence of roughness elements can generate high levels of mechanical turbulence, which can overcome the damping effect of stable air. Due to this turbulence, two different regions can be distinguished within the boundary layer (Seibert et al. 2000). The first region is a layer with periodic and relatively strong turbulence that extends from the ground, and the second region is an outer layer with sporadic and relatively weak

[1] Reprinted from Pournazeri, S., A. Venkatram, M. Princevac, S. Tan, and N. Schulte. 2012. "Estimating the height of the nocturnal urban boundary layer for dispersion applications." *Atmospheric Environment* 54: 611–623, Copyright 2012, with permission from Elsevier.

turbulence. Since in air pollution dispersion, regions with relatively high turbulence are of interest, the height of the first layer is taken as the boundary layer height (Seibert et al. 1998).

Many studies are also focused on the parameterizing of the nighttime boundary layer height using surface-based meteorology (Hanna 1969; Zilitinkevich 1972; Etling and Wippermann 1975; Venkatram 1980; Arya 1981; Mahrt 1981a; Nieuwstadt 1984; Koracin and Berkowicz 1988). Hanna (1969) examined several methods for predicting the boundary layer thickness. It has been shown that models by Lettau (1962) and Blackadar (1962), which use the surface observations; works only for very-near-neutral conditions and have extremely poor performance under highly stable conditions. It has also been shown that the formulation of boundary layer height by Laikhtman (1961) can approximate the observations very well. However, in order to run this model, meteorological information along the boundary layer is needed. Zilitinkevich (1972) has proposed a diagnostic formulation for predicting the boundary layer height using similarity consideration and scaling arguments. Venkatram (1980) has empirically shown that in the absence of any information regarding surface heat flux, boundary layer height can be predicted as $h = 2300u_*^{3/2}$. Following the Taylor (1931) classical theory, assuming that the turbulence production vanishes if the bulk/gradient Richardson number (*Ri*) exceeds a critical value of Ri_{cr}, Mahrt (1981a), Holstag et al. (1990), and Nieuwstadt and Tennekes (1981) proposed several diagnostic equations for predicting the equilibrium nocturnal boundary layer height.

Due to the unsteady behavior of the nocturnal boundary layer (Zilitinkevich and Baklanov 2002), high accuracy cannot be expected from the above-mentioned diagnostic equations. Therefore, assuming that actual boundary layer height tends to adjust to the equilibrium boundary layer height[2] with a time response of τ_{SBL}, several prognostic equations were proposed (Deardorff 1972; Zilitinkevich et al. 2002). A review paper by Seibert et al. (2000) indicates that although these models show some skill in explaining selected data sets, they lack general applicability. This situation is more severe for the nocturnal boundary layer over an urban area, where heat fluxes can be positive while the upwind rural areas are stable. A report by Baklanov et al. (2006) concludes that one-dimensional models developed for horizontally homogeneous conditions have limited applicability to urban conditions. In principle, two- or three-dimensional boundary layer models should be able to provide better estimates of boundary layer heights. However, evaluation against observations has not yet confirmed this.

There is a need for a method to estimate the height of the SBL for dispersion applications in urban areas. All of the studies to date indicate that diagnostic equations that ignore the history of the boundary layer provide poor estimates of the boundary layer height. This study focuses on one-dimensional prognostic models for the height of the SBL. As pointed out by Siebert et al. (2000), there is a paucity of the time-resolved data required to test these models. Thus, it was necessary to conduct a field study to provide the required information.

[2] The equilibrium height h_e is often parameterized using one of the diagnostic equations given above.

Because this field study covers only two nights, the research team supplements the data with the relatively small data sets that are currently available.

Section 0 describes the field study; Section 0 presents analyses of the observations; Section 0 describes the supplementary field data from Vertical Transport and Mixing (VTMX), Milan, and Wangara experiments; Section 0 discusses evaluation of diagnostic and prognostic models that are employed to describe data; and Section 0 describes the resulting conclusions.

2.3.2 Field Study

The field study was conducted in Riverside, California, in March 2011 in the grassy area next to the parking lot of the College of Engineering's Center for Environmental Research and Technology (CE-CERT). This site is located in a low-density urban area surrounded by sparse trees, bushes, and one-story buildings that do not vary much in height. The degree of urbanization of this area can be characterized in terms of the plan area fraction (λ_p), which is the ratio of the plan area of the roughness elements to the total lot area, and the frontal area fraction (λ_f), which is the ratio of the frontal area of roughness elements to the total lot area. Table 2-3 compares approximate values of the average building height (h_b), plan area fraction (λ_p), and frontal area fraction (λ_f) associated with the Riverside urban area with those from a high-rise settlement urban area such as Los Angeles downtown (near the 6th St. /Grand Ave. intersection), and a low-density settlement such as Anaheim (near the Harbor Blvd. /Lampson Ave. intersection) obtained from Boarnet et al. (2009).

Table 2-3: Morphological Parameters (λ_p, λ_f) and Average Building Heights (h_b) Associated with Three Different Urban Areas

City	Type	h_b (m)	λ_p	λ_f
Riverside	low-rise settlement	4	0.3	0.1
Los Angeles	high-rise settlement	42	0.36	0.47
Anaheim	low-density settlement	4	0.26	0.12

Meteorological measurements were made over the period starting at noon on March 9, 2011, and extending to noon, March 11, 2011, under clear skies and low winds. Surface micrometeorological variables were measured using a sonic anemometer placed at a height of 3.4 m above the ground. The sonic was located at a distance of about 25 m towards the north of a building (L × W × H = 62 m × 20 m × 5 m). A tethersonde was used to measure vertical profiles of temperature, wind speed, and humidity up to height of 500 m. The locations of the instrumentation are shown in Figure 2-8.

Figure 2-8: Location of the Meteorological Station

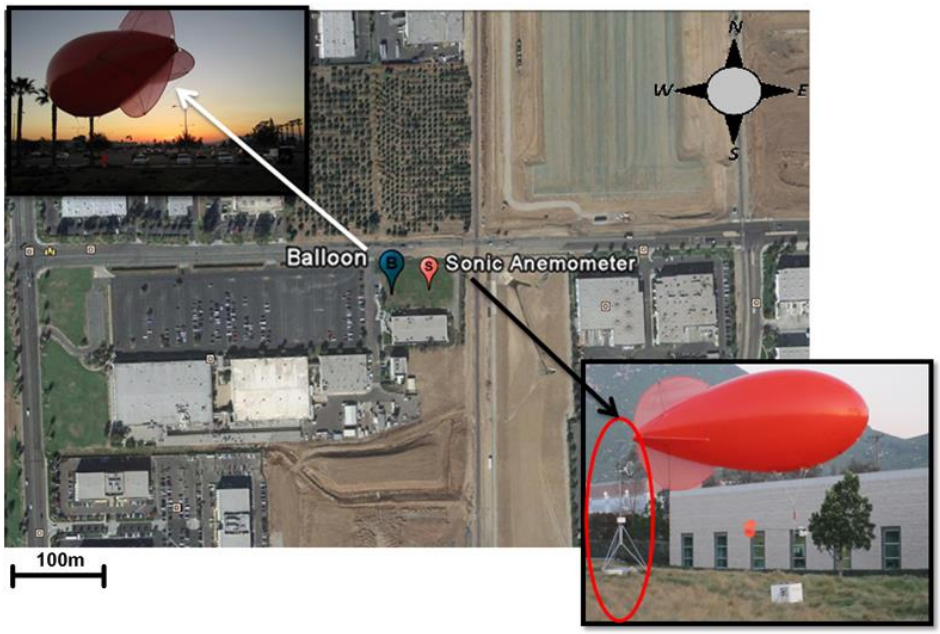

(red pin) and Tethered Balloon (blue pin) at the College of Engineering - Center for Environmental Research and Technology (CE-CERT), Riverside, California.

The aerial picture was produced using Google Earth.

2.3.2.1 Surface Micrometeorology

Three components of wind speed and virtual temperature were measured using a Campbell Scientific CSAT3 sonic anemometer located at 3.4 m above the ground, at the sampling rate of 10 hertz (Hz). These measurements were processed to obtain mean and turbulent wind speeds and surface heat fluxes averaged over 15-minute periods. Figure 2-9 shows the results from these measurements.

Figure 2-9: Measurements of 15-minute Averaged

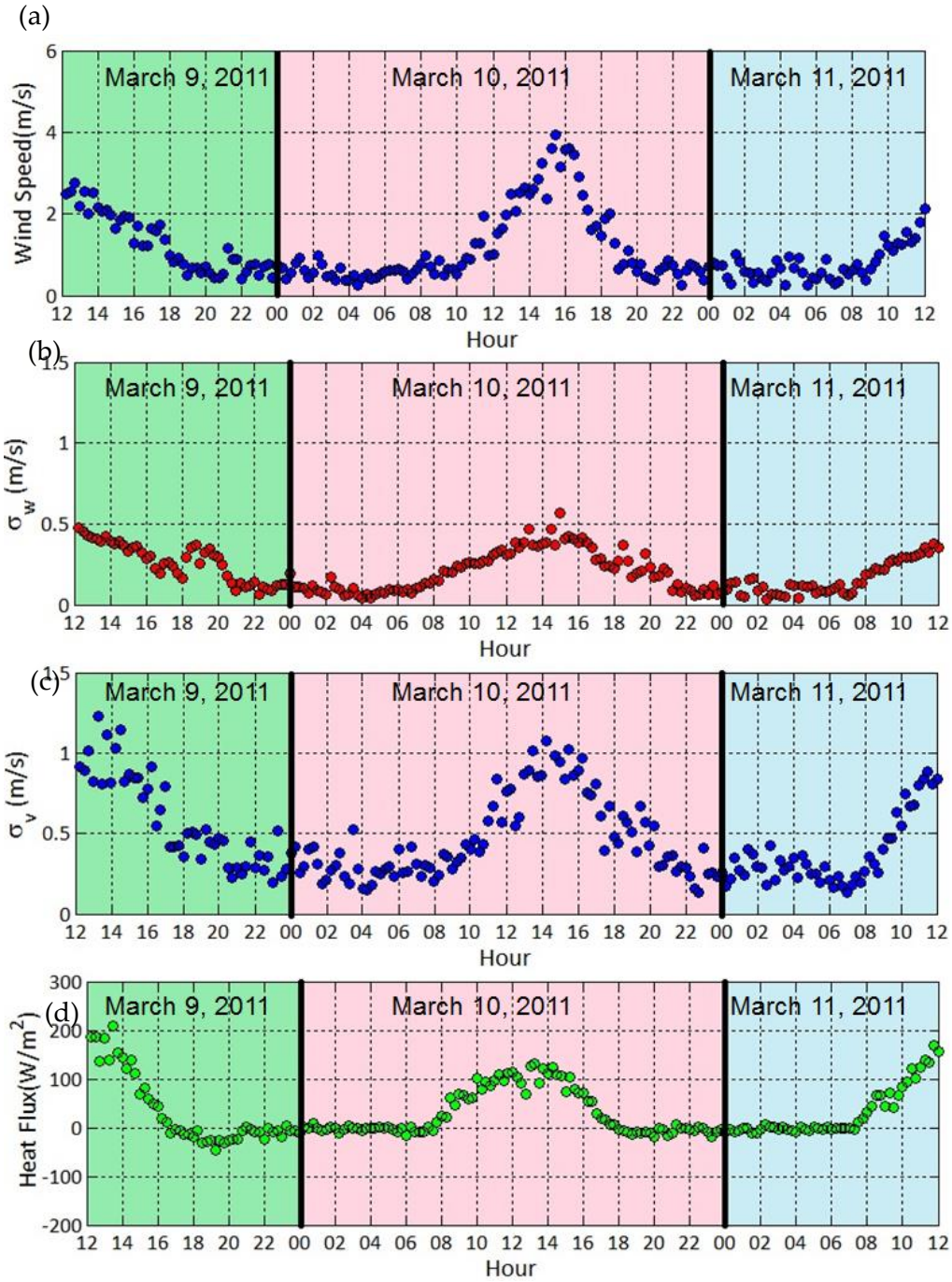

(a) Wind Speed *U* (meters per second, ms^{-1}); (b) Vertical Turbulent Velocity σ_w (ms^{-1}); (c) Lateral Turbulent Velocity σ_v (ms^{-1}); and (d) Surface Sensible Heat Flux $\rho C_p \overline{w'T'}$ (watts per square meter, Wm^{-2}).

The near-surface wind speeds are less than 1 ms^{-1} during most of the nighttime. Vertical turbulent velocities are approximately 0.15 ms^{-1} during nighttime and increase to a maximum of 0.5 ms^{-1} during daytime. Lateral turbulent velocities are less than 0.3 ms^{-1} during nighttime, with a maximum of about 1 ms^{-1} during the daytime. This translates into

turbulent intensities of about 20 percent in the vertical direction and about 50 percent in the horizontal direction. The near-surface sensible heat flux ($\rho C_p \overline{w' T_v'}$, where ρ is the air density, C_p is the specific heat of air, and $\overline{w' T_v'}$ is the correlation of fluctuations of vertical velocity w and virtual temperature T_v), reaches a maximum of about 200 Wm^{-2} at noon and approaches to zero during nighttime.

2.3.2.2 Boundary Layer Profiling

Vertical profiles of temperature, relative humidity, and wind speed along the Riverside urban boundary layer were obtained up to 500 m above ground level using a Vaisala tethersonde system. The measurements were made during three nights. Data from the first night were used to check out the instrumentation. The main field experiments were conducted on two consecutive nights (March 9–11) starting at 18:00 PST to 6:00 PST of the following morning. Data from these nights were used in the modeling described in sections 2.3.4.3 and2.3.4.4. The tethered balloon was raised periodically up to a height of 500 m and lowered to the ground within 20 minutes. This resulted in two profiles of boundary layer parameters per hour.

Selected results from these measurements (Figure 2-10) show that the urban boundary layer over Riverside, California, was stably stratified throughout the three nights of the field study. The absolute temperature gradient (Figure 2-10 a, b) was positive near the surface and became negative far from the ground. The potential temperature gradient (Figure 2-10 c, d) was about 8°C/100 m near the ground and approached zero in the upper part of the boundary layer. The potential temperature of the upper part of the boundary layer remained almost constant (~25°C), while the surface temperature decreased with time. Therefore, assuming a well-mixed temperature profile at the time of sunset, the temperature difference over the depth of the boundary layer can be estimated from the variation of the near-surface temperature after sunset. This approach can be used to estimate the temperature gradient across the boundary layer, which is a critical input to dispersion models, such as AERMOD.

Figure 2-10: Vertical Profiles

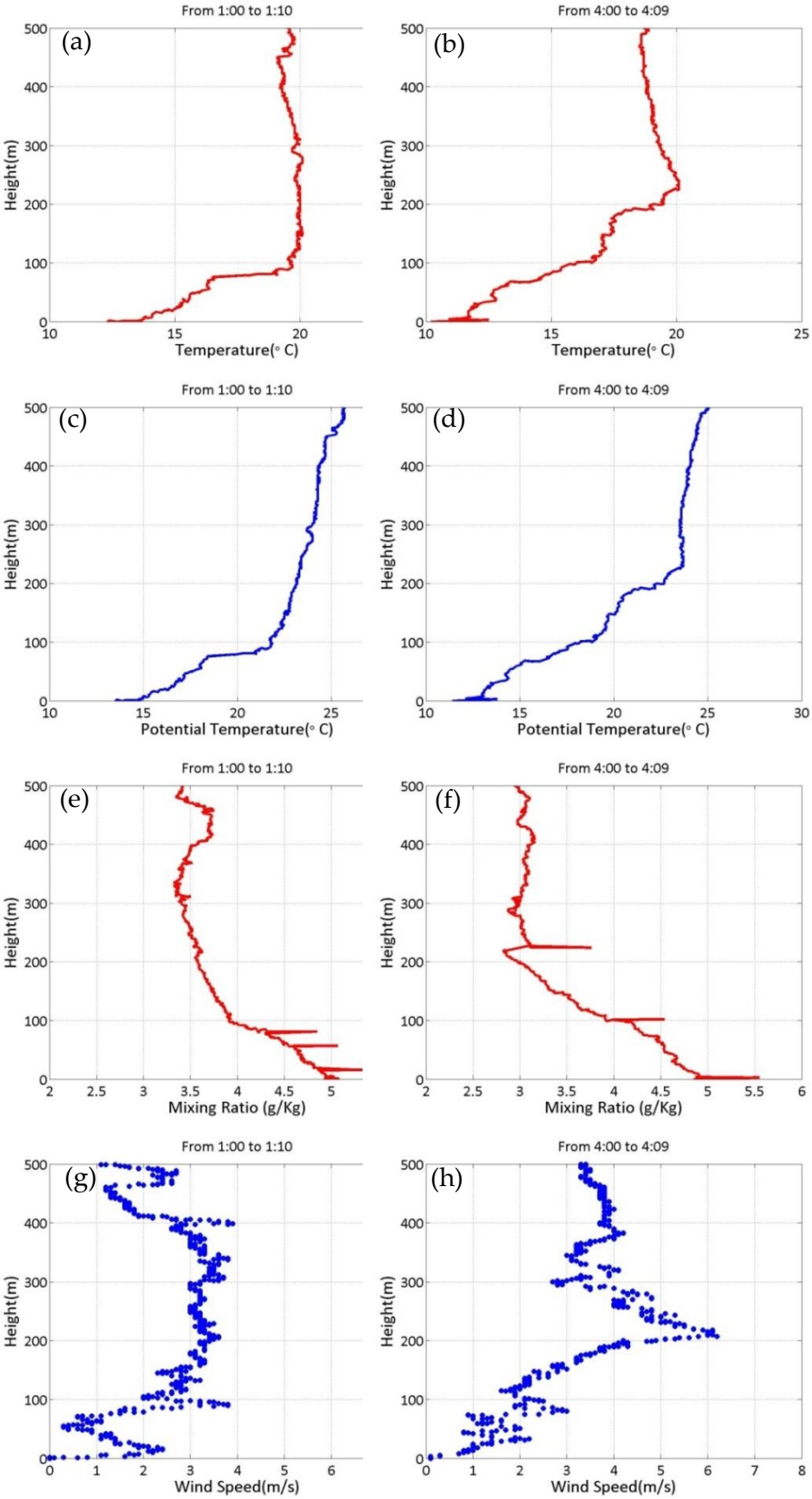

(a) (b) Temperature (°C); (c) (d) Potential Temperature (°C); (e) (f) Mixing Ratio (grams per kilogram, g/kg); and (g) (h) Wind Speed (ms^{-1}) at 1:00 and 4:00 PST on March 10, 2011

In describing the vertical profiles, the research team tentatively identifies the top of the stable boundary layer as the height at which the absolute temperature gradient becomes negative. The authors will provide a more precise definition later.

Figure 2-10 e, f show that the mixing ratio decreases with height from the ground and the gradient approaches zero at the top of the boundary layer. The vertical profile of wind speed (Figure 2-10 g, h) shows the presence of wind shear across the boundary layer, in which the wind speed reaches a maximum of 6 ms^{-1} at the boundary layer height (Figure 2-10 h). There is a suggestion of a low-level jet at the top of the boundary layer.

In the absence of turbulence measurements as a function of height, the height of the nocturnal boundary layer has to be inferred from profiles of mean temperature and wind speed. There is little consensus on the method for this indirect estimation, as evidenced in many different definitions of the boundary layer height found in literature. Seibert et al. (1998) summarized the most popular algorithms used to determinate the nocturnal boundary layer height from vertical sounding data.

The usefulness of some of the methods was examined. Cuxart et al. (2006), Garratt (1982, 1992), and Mahrt et al. (1982) suggest using the value of the gradient Richardson number to estimate the height of the stable boundary layer in mesoscale numerical models. When applied to the field data, this approach left too much room for interpretation to be useful.

In this study, the team found it convenient to use the definition proposed by Yu (1978), which assumes that the height of the nocturnal boundary layer (*h*) is the height at which $\partial T / \partial z = 0$. Figure 2-11 illustrates this method, which, in most cases, allowed an unambiguous identification of the boundary layer height. The team's assumption that this height represents the vertical extent of mixing is supported by the observation that it often coincided with the height at which the water vapor mixing ratio gradient approached zero and the velocity gradient changed sign.

Figure 2-11: (a) Schematic of the Method Used for Determination of Nocturnal Boundary Layer Height, and (b) Boundary Layer Height Determination on Temperature Profile Measured During 20:17–20:57 PST on March 9, 2011

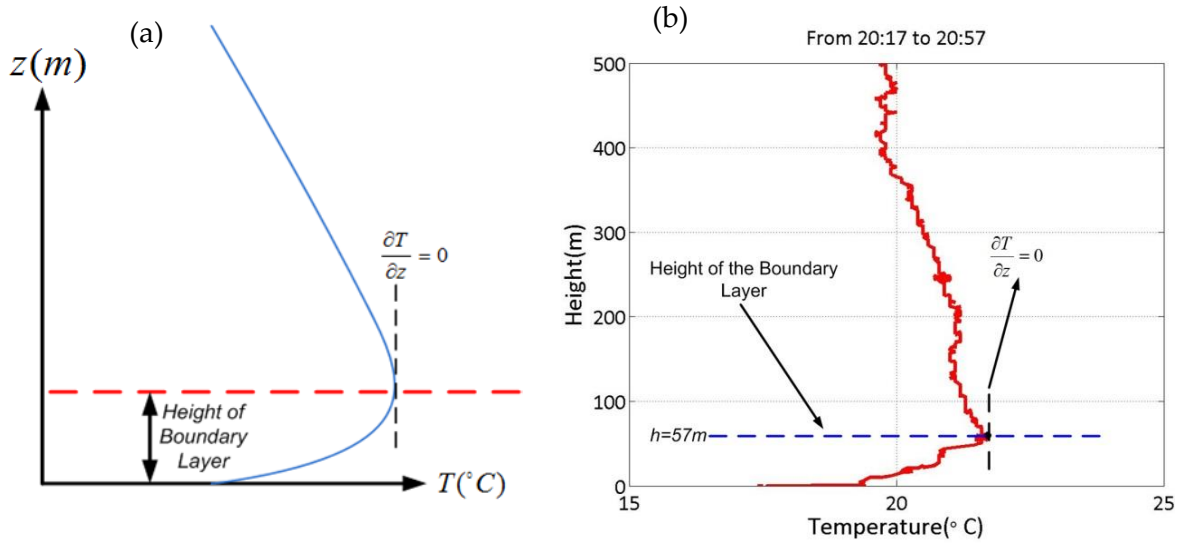

Boundary layer heights for the 56 profiles from the vertical sounding data were obtained based on this definition. The research team also estimated the boundary layer height using an approach suggested by Melgarejo and Deardorff (1974). They defined *h* as the height to which significant cooling can be recognized, which is determined by superimposing vertical profiles of potential temperature at successive time intervals. Selected results from this comparison are shown in Figure 2-11. As can be seen, for most of the cases, significant cooling (the area between the two profiles) occurs just below the height at which $\partial T / \partial z$ of the second profile approaches zero. Because the two different definitions yield similar results, the researchers used the more convenient method based on the criterion, $\partial T / \partial z = 0$ to estimate the boundary layer heights for the 56 profiles from the vertical sounding data. Table 2-4 presents the relevant boundary layer parameters associated with these profiles: boundary layer height (*h*), wind velocity, and potential temperature difference across the boundary layer (ΔU, $\Delta \theta$).

Figure 2-12: Successive Vertical Profiles of Temperature (°C)

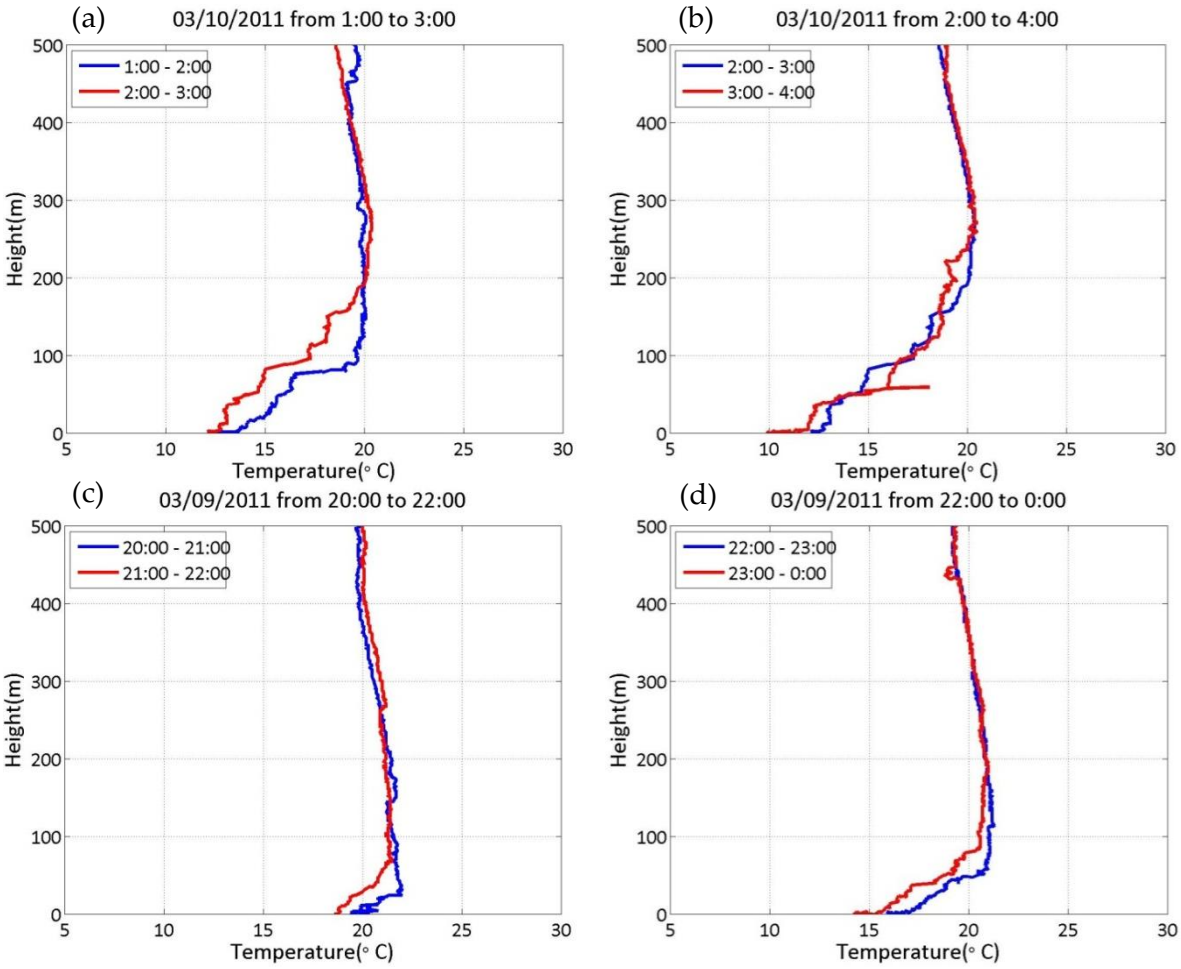

(a) from 20:00 to 22:00; (b) from 22:00 to 00:00; (c) from 1:00 to 3:00; and (d) from 2:00 to 4:00

Table 2-4: Meteorological and Boundary Layer Parameters from 56 Vertical Sounding Data (Different color shading corresponds to measurements at different nights)

Profile Number	Day of Year	Boundary Layer Height *h* (m)	u_* (ms^{-1})	U (ms^{-1})	Heat Flux (Wm^{-2})	L_{M-O} (m)	$\Delta\theta$ (°C)	ΔU (ms^{-1})	T_0 (K)
1*	60.793	33	0.14	0.54	-11.25	16.22	1.60	1.10	287.7
2*	60.803	26	0.09	0.56	-9.10	6.38	1.80	1.50	287.2
3*	60.814	15	0.12	0.59	0.47	-269.69	1.90	1.40	287.2
4*	60.823	36	0.10	0.74	3.76	-22.05	1.90	2.80	286.8
5*	60.875	25	0.26	0.75	-26.17	50.59	2.00	1.10	285.8
6*	60.887	39	0.23	0.84	-20.00	44.79	2.90	3.20	284.5
7*	60.917	24	0.46	1.01	-91.14	75.37	0.80	3.90	285.1
8*	60.926	24	0.47	1.19	-90.82	85.39	1.40	2.70	284.2
9	68.761	26	0.22	0.81	-6.49	125.94	0.70	2.20	297.6
10	68.772	22	0.27	0.93	-32.38	47.30	1.77	2.80	295.5
11	68.785	30	0.16	0.50	-25.09	13.24	1.43	2.70	296.0
12	68.799	27	0.25	0.67	-45.08	26.88	1.60	2.10	295.1
13	68.833	37	0.21	0.70	-25.20	26.76	2.90	4.40	293.6
14	68.845	57	0.15	0.56	-23.60	10.82	4.60	1.10	291.6
15	68.876	73	0.09	0.53	1.04	-56.34	3.60	1.80	292.7
16	68.882	74	0.11	1.16	-3.19	33.68	4.43	2.30	291.9
17	68.917	66	0.13	0.41	-22.89	6.90	5.67	2.40	290.1
18	68.926	60	0.01	0.60	-1.59	0.11	7.63	1.60	288.2
19	68.960	84	0.12	0.50	-19.18	6.07	7.07	1.90	288.4
20	68.976	88	0.04	0.70	4.37	-1.12	5.93	3.30	288.2
21	69.001	109	0.06	0.73	-10.85	1.31	6.00	3.20	288.5
22	69.007	113	0.10	0.69	2.02	-34.10	6.67	3.00	286.9
23	69.042	76	0.11	0.79	-2.30	46.07	5.87	2.40	286.5
24	69.046	96	0.08	0.93	-6.99	4.61	6.77	2.30	286.9
25	69.083	200	0.03	0.55	-0.34	4.29	10.03	4.10	286.3
26	69.091	218	0.09	0.99	-10.70	4.78	10.30	2.30	285.2
27	69.128	231	0.05	0.49	-1.60	7.37	12.10	4.60	284.1
28	69.135	258	0.07	0.38	-1.07	20.07	12.00	5.10	285.2
29	69.167	234	0.02	0.39	-0.30	1.38	12.27	6.10	284.4
30	69.173	204	0.07	0.51	-0.66	34.91	11.27	4.80	285.0

Profile Number	Day of Year	Boundary Layer Height *h* (m)	u_* (ms^{-1})	U (ms^{-1})	Heat Flux (Wm^{-2})	L_{M-O} (m)	$\Delta\theta$ (°C)	ΔU (ms^{-1})	T_0 (K)
31	69.208	212	0.02	0.54	1.35	-0.24	11.30	4.30	284.7
32	69.214	215	0.06	0.42	-4.21	4.24	11.30	3.80	284.8
33	69.750	11	0.13	1.46	-2.85	62.46	0.60	0.70	296.0
34	69.758	5	0.17	1.89	-5.33	67.29	0.10	0.60	295.6
35	69.792	12	0.10	0.64	-8.65	8.73	0.40	0.90	295.1
36	69.799	24	0.18	0.77	-12.37	34.02	1.00	2.70	293.1
37	69.833	38	0.18	0.59	-18.71	23.35	1.73	2.40	292.4
38	69.839	45	0.14	0.76	-0.41	482.91	2.93	3.70	291.0
39	69.875	39	0.16	0.38	-11.06	27.86	2.93	2.80	290.8
40	69.881	31	0.10	0.61	5.45	-14.77	3.60	0.80	290.0
41	69.917	43	0.12	0.73	-2.53	53.02	4.40	1.50	289.2
42	69.923	81	0.07	0.52	-6.35	3.74	3.97	1.10	289.3
43	69.958	50	0.11	0.77	-9.25	10.74	5.57	1.00	286.9
44	69.965	93	0.10	0.71	-18.25	4.46	5.60	1.60	286.9
45	70.006	98	0.10	0.70	-7.87	10.71	3.90	3.10	287.9
46	70.013	81	0.07	0.79	-3.90	7.62	5.17	2.30	286.9
47	70.043	88	0.06	0.44	-1.32	10.61	5.30	2.30	286.8
48	70.050	119	0.03	0.30	-1.12	1.04	5.53	1.90	286.4
49	70.084	110	0.05	0.60	-3.10	2.94	5.20	2.10	286.4
50	70.091	100	0.10	0.54	5.37	-12.74	5.23	2.50	285.4
51	70.126	93	0.05	0.42	-2.92	2.57	5.17	3.10	285.0
52	70.132	99	0.02	0.35	1.82	-0.50	5.60	1.60	284.8
53	70.167	171	0.11	0.68	-7.75	13.31	6.87	2.80	284.7
54	70.173	113	0.04	0.27	1.35	-2.85	3.63	0.90	284.8
55	70.208	261	0.11	0.92	1.42	-62.95	8.77	3.50	285.1
56	70.213	233	0.06	0.54	-2.00	8.30	8.67	1.80	284.4

* Data from a test field study conducted in March 1, 2011, at the same location, from 19:00–22:00 PST.

Table 2-4 also presents surface-based (z = 3.4 m) meteorological parameters such as mean wind speed (U), friction velocity (u_*), ground sensible heat flux, surface temperature (T_0), and Monin-Obukhov length (L_{M-O}) averaged over 15 minutes prior to each profiling time.

The time corresponding to each profile is shown in terms of Day of Year (DOY), where the DOY of 68 represents March 9, and the DOY of 70 represents March 11.

The data show that the nocturnal boundary layer height (top of the surface inversion) ranges from ~10 m after sunset (18:00 PST) to ~260 m before sunrise (6:00 PST). Note that the surface wind speed is less than 1 ms^{-1} during most of the soundings. The surface heat flux is negative most of the time, and its magnitude varies from approximately -30 Wm^{-2} after sunset (18:00 PST) up to approximately -1 Wm^{-2} before sunrise (6:00 PST).

2.3.3 Analysis of Observations

Figure 2-13 shows the variation with time from sunset of some broad features of the nocturnal boundary layer. Figure 2-13a indicates that boundary layer height (*h*) varies almost linearly with time ($h \propto t^{0.9}$) from sunset. Figure 2-13b shows that the temperature difference across the boundary layer increases with time ($\Delta\theta \propto t^{0.8}$); the near surface temperature decreases, while the temperature at the top of the boundary layer remains almost constant.

Because both temperature difference across the boundary layer ($\Delta\theta$) and height of the boundary layer (*h*) increase with time, the mean potential temperature gradient ($\Delta\theta / h$) shows little variation and has a mean value of about 0.062 Kelvin per meter (Figure 2-13c). Figure 2-13d reveals that the velocity difference across the boundary layer (ΔU) does not have any trend with time from sunset, and it ranges from 1 to 5 m s^{-1}.

Figure 2-13: Nighttime Boundary Layer Parameters vs. Time

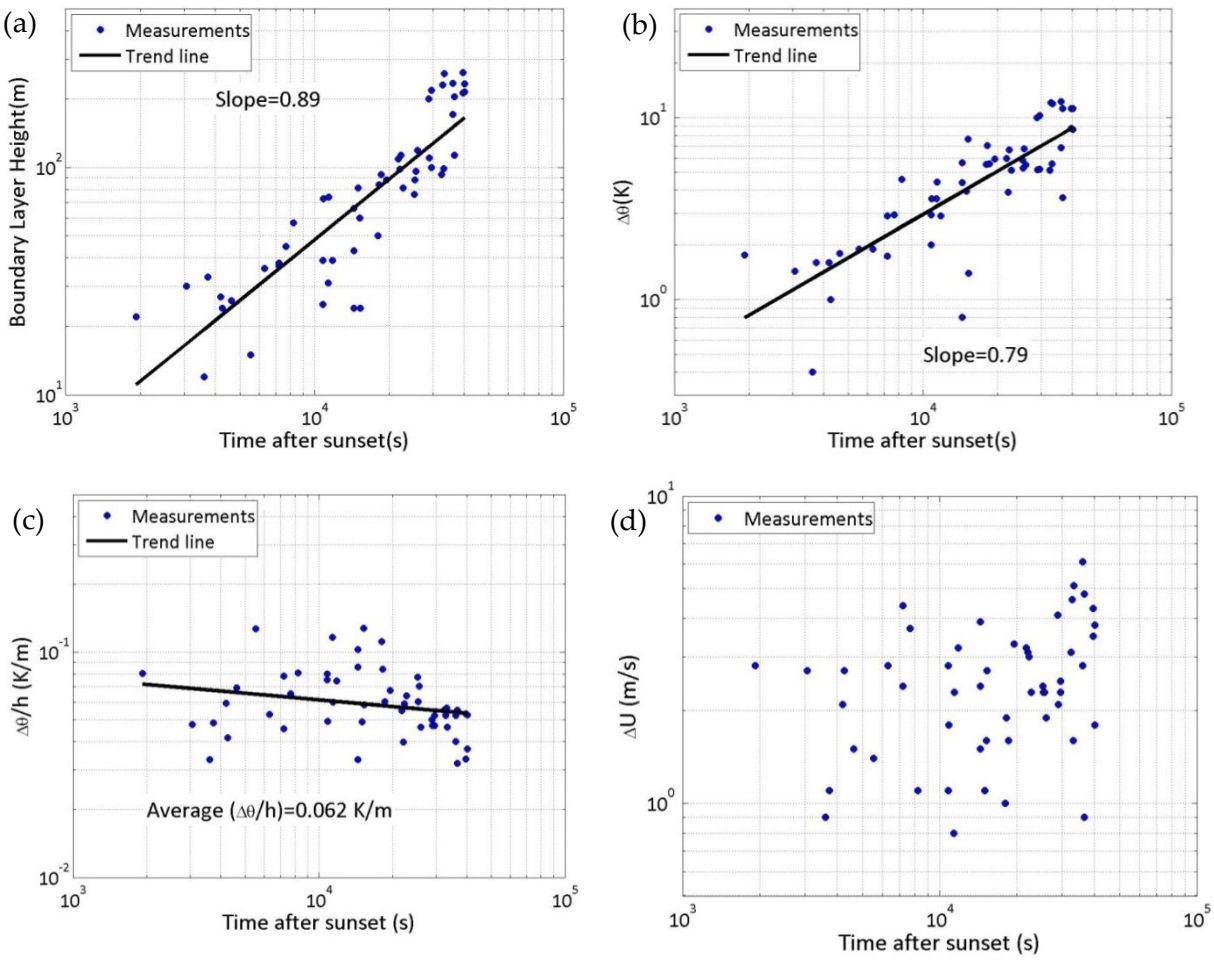

(a) Boundary Layer Height (*h*); (b) Temperature Difference across Boundary Layer ($\Delta\theta$); (c) Mean Potential Temperature Gradient across Boundary Layer ($\Delta\theta/h$); and (d) Velocity Difference across Boundary Layer (ΔU). Data from all nights are included.

Yamada (1979) and Stull (1983) have developed prognostic models for the height of the nighttime boundary layer by equating the energy loss in the boundary layer to the integrated downward surface heat flux. The team tested the usefulness of this approach by comparing the cooling of the boundary layer,

$$Boundary\ Layer\ Heat\ Loss = \rho C_p \int_0^{h(t)} [\theta(z,t) - \theta(z,t_0)]dz\,, \qquad (2\text{-}6)$$

where t_0 is the time of sunset, to the integrated downward surface heat flux at the surface.

$$Integrated\ \ downward\ surface\ heat\ flux = \rho C_p \int_{t_0}^{t} \overline{w'T'}dt\ . \qquad (2\text{-}7)$$

Figure 2-14: Comparison of Cooling of the Boundary Layer with Integrated Surface Heat Flux

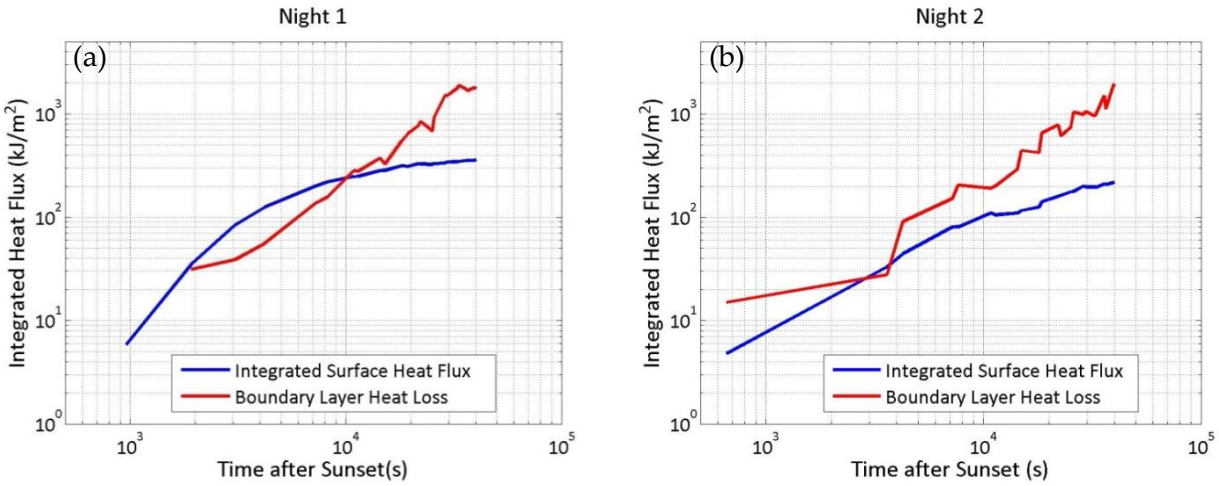

(a) Night 1 on March 9, 2011 and (b) Night 2 on March 10, 2011

kJ/m^2 = kilojoules per square meter

Figure 2-14 indicates that there are substantial differences between the boundary layer cooling and the integrated surface heat flux, which cannot be explained in terms of radiative cooling or heating. Therefore, an estimate of the boundary layer height based on equality between these two energy terms cannot be justified in this case. For this reason, the team focused on methods that assume that the boundary layer height corresponds to the upward diffusion of shear-generated turbulence at the surface. The most well-known methods are based on that proposed by Zilitinkevich (1972). Some of these are evaluated in Section 2.3.4.

2.3.3.1 Supplementary Field Data

The Riverside data was supplemented with data sets from three field studies. The Milan data corresponds to urban conditions, the VTMX data set was obtained in a suburban area, and the Wangara data set corresponds to rural conditions. The rationale for choosing the Wangara data set is to ensure that if the model works in an urban setting, it should also do so in the simpler rural setting of Wangara. These field studies are briefly described next.

2.3.3.2 VTMX Study

The Vertical Transport and Mixing (VTMX) field study was conducted during October 2000 in the Salt Lake Valley, Utah. The main goal of this field study was to investigate the transport and mixing processes under (nocturnal) stable conditions. The site was equipped with a variety of meteorological instruments, such as sonic anemometers and tethersondes, in order to measure three-dimensional wind speed as well as vertical temperature profile. More details of the field campaign can be found in Doran et al. (2002). Data used in this study were collected by the Environmental Fluid Dynamics group at Arizona State University. These data covered six different nights; however, data from first three nights were insufficient to be used in the team's analysis, and only data from last three nights (October 14, 16 and 17) were used.

2.3.3.3 Milan Experiment

The Milan experiment (Lena and Desiato 1999) took place in the area of Milan, Italy, in the northwest part of Po Valley from May to August 1996. Profiles of wind speed and temperature were measured using a Doppler SODAR (SOnic Detection And Ranging) and a Radio Acoustic Sounding System (RASS). The measurement site was located at a distance of about 8 km from the center of Milan, which according to Lena and Desiato (1999) is a typical urban environment. In this study, boundary layer heights were determined through the (1) height of the low-level jets (h_u); (2) height of the surface inversion ($h_{\theta g}$); (3) height of the elevated inversion ($h_{\theta e}$); and (4) depth of the adiabatic layer ($h_{\theta a}$). Lena and Desiato (1999) compare the values of mixing heights derived from the wind (h_u) and temperature profiles (h_θ) with predictions from 10 different mixing height algorithms. Results showed that the h_u values provide the best correlation with model estimates. Assuming that the models are based on data that reflect the vertical extent of mixing, they conclude that the h_u values are good indicators of boundary layer height. They also find that the heights of the surface-based inversion layer ($h_{\theta g}$) are close to that of h_u values. This supports the team's use of the height of the surface-based inversion as a measure of boundary height in the analysis of the Riverside data.

2.3.3.4 Wangara Data

The Wangara boundary layer experiment was conducted in July and August 1967 at Hay, New South Wales, Australia (Clarke et al. 1971) to describe characteristics of the atmospheric boundary layer (Hess et al. 1981). During this experiment, 5,000 balloon ascents were used to obtain temperature profiles up to 2,000 m from the surface every three hours (nighttime data are available for 18:00, 21:00, 00:00, 3:00, and 6:00) with the resolution of 50 m in the first 1,000 m and 100 m after that. Horizontal wind speed was also measured at three different heights: 2, 4, and 8 m from the ground. Surface meteorological data from this experiment were analyzed by Melgarejo and Deardorff (1974) to obtain the surface friction velocities (u_*) and Monin-Obukhov lengths ($L_{M\text{-}O}$). The data analysis by Melgarejo and Deardorff was limited to cases where no frontal systems existed within 500 km from Hay. These data are available in Yu (1978).

2.3.4 Model Evaluation

This study focused on prognostic models that are based on surface variables, and thus can provide inputs to the current generation of dispersion models, such as AERMOD. The boundary layer height in most of these models is controlled by the surface friction velocity, u_*. The team applied these models assuming that the appropriate friction velocity corresponds to the inertial sublayer (ISL), which lies above the roughness sublayer (RSL). The ISL refers to the layer that is about one to three times the average building height, where the flow can be considered to be in equilibrium with the underlying rough surface. The RSL lies below the ISL, and corresponds to the lowest layer that is governed by the spatially averaged properties of the urban surface. Fluxes of momentum, energy, and moisture vary with height in the RSL. The shear stress (and local friction velocity) reach a maximum at the bottom of the ISL. Rotach (1993) proposes an empirical formula for the variation of the friction velocity with height in the RSL. In principle, this formula can be used to relate a friction velocity measured within the RSL to its maximum in the ISL. Because such

measurements are not made routinely, it is useful to examine the possibility of estimating the friction velocity in the RSL from routine surface meteorological measurements.

2.3.4.1 Estimating the Friction Velocity (u_*)

We compare the observed values of friction velocity with estimates obtained by fitting the Monin-Obukhov similarity theory (MOST) wind speed profile (Businger 1973) to the measured mean wind speed (U) and Monin-Obukhov length (L_{M-O}),

$$u_* = \kappa U_{ref}\left[\ln\left(\frac{z_{ref}-d_h}{z_0}\right)-\psi\left(\frac{z_{ref}-d_h}{L_{M-O}}\right)\right]^{-1} \tag{2-8}$$

where κ is von Karman constant, U_{ref} is the mean wind speed measured at reference height (z_{ref}), d_h is the zero plane displacement which is taken as $d_h = 5z_0$ (Britter and Hanna 2003), z_0 is aerodynamic roughness length, and

$$\psi\left(\frac{z}{L_{M-O}}\right) = -4.7\frac{z}{L_{M-O}}\,. \tag{2-9}$$

Because the surface heat flux is not measured routinely, it is useful to estimate the surface friction velocity using an approach (Venkatram 1980; Qian and Venkatram 2011) that assumes that the temperature scale $\theta_* = -\overline{w'T_v'}/u_*$ varies little with time and has a value of about 0.08 K, which might be site specific. The variation of θ_* and u_* shown in Figure 2-15 indicates that θ_* varies about a mean value of about 0.053 K, while u_* shows a decreasing trend with time throughout the night. The team used $\theta_* = 0.053K$ in this analysis to be consistent with the measurements, although a value of 0.08 K yields very similar results.

Figure 2-15: Variation of (a) Surface Layer Temperature Scale ($\theta_* = -\overline{w'T_v'}/u_*$) and (b) Friction Velocity (u_*) with Time

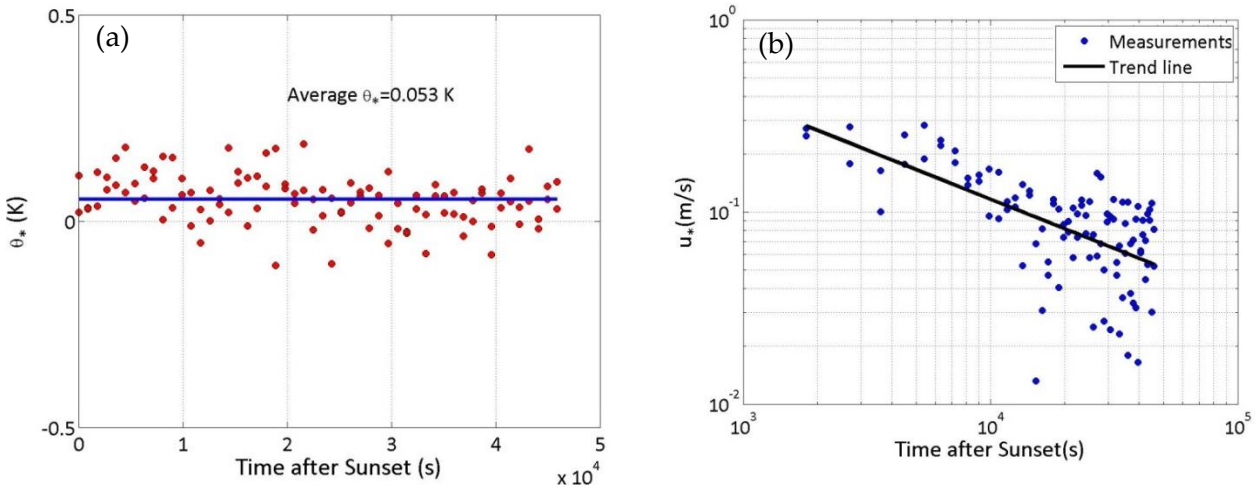

15-minute averaged data from all nights are used

The performance of the SBL models evaluated in this study are measured through the statistics, m_g and s_g, which are the geometric mean and standard deviation of the ratios of the observed to estimated u_*, respectively (Venkatram 2008). Deviation of m_g from unity indicates whether the model is over predicting or under predicting and expresses the bias of the model estimates. The standard deviation, s_g measures the spread of the observations about the model estimate, and s_g^2 is approximately the 95 percent confidence interval for the ratio of observed values to predicted values.

Performance statistics m_g and s_g are defined as,

$$m_g = \exp\left(\langle \varepsilon_m \rangle\right) \tag{2-10}$$

$$s_g = \exp\left(std\left[\varepsilon_m\right]\right) \tag{2-11}$$

where $\langle\ \rangle$ represents the mean, std is the standard deviation, and ε_m can be expressed as

$$\varepsilon_m = \ln\left(u_{*o}\right) - \ln\left(u_{*p}\right) \tag{2-12}$$

where subscripts o and p represent the predicted and observed values, respectively.

The roughness length is derived by treating z_0 as a parameter that provides the best fit between the observed u_* and that estimated from the mean wind speed with MOST. The team finds that $z_0 = 0.3$ m yields the results shown in Figure 2-16a, which indicates that the values of u_* based on MOST and measured heat fluxes are within a factor of two of the observed values. The values of m_g and s_g indicate that the bias is about 13 percent and the 95 percent confidence interval for the ratio of predicted to observed u_* is about 2.75.

Figure 2-16: Comparison of Nighttime Observed vs. Predicted u_*

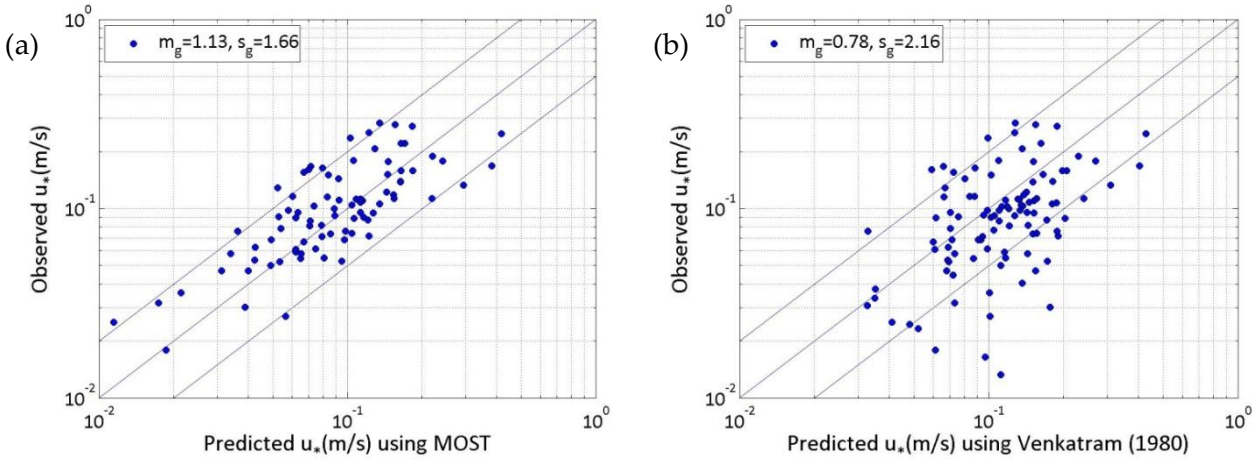

(a) MOST, Using Measured Wind Speed and Sensible Surface Heat Flux and (b) Venkatram (1980), Using only Measured Wind Speed. Data from all nights are included.

Figure 2-16b shows that the estimates of u_* based on a constant $\theta_* = 0.053K$ compare well with observations (bias of 22 percent and 95 percent confidence interval of 4.66), although the scatter is larger than those based on the measured heat fluxes.

As mentioned earlier, observations made by Rotach (1993) suggest that the Reynold's stress, $\overline{u'w'}$, increases with height within the RSL before reaching its maximum value in the ISL. The team can estimate the value of u_* in the ISL using Rotach's (2001) profile for the variation of the surface friction with height in the RSL,

$$u_{*ISL} = \frac{u_*(z_{ref})}{\left[\sin\left(\frac{\pi}{2}Z\right)\right]^{a/b}} \tag{2-13}$$

where a = 1.28 and b = 3.0 are empirical constants and

$$Z = \frac{z_{ref} - d_h}{h_{RSL} - d_h} \tag{2-14}$$

Where h_{RSL} is the height of the RSL. The team takes h_{RSL} to be the average building height in the urban area, $h_b = 4m$. The models described in sections 2.3.4.3 and 2.3.4.4 use u_{*ISL} to predict the SBL height.

2.3.4.2 Field Data Analysis

Before describing the performance of prognostic models, the research team examines the relationship between the measured boundary layer heights and the variables used in diagnostic models, which are based on data from relatively homogeneous rural terrain. Some of these models assume that the SBL height is proportional to the neutral length scale, u_* / f (Arya 1981; Mahrt et al. 1982) where f is the coriolis parameter. Another popular length scale is $(u_* L_{M-O} / f)^{1/2}$ (Zilitinkevich 1972; Arya 1981; Mahrt et al. 1982). Other models assume that the boundary layer height is proportional to the near-surface wind speed (Nieuwstadt 1984; Benkley and Schulmann 1979). Steeneveld et al. (2007) finds that the SBL height is proportional to u_* / N, where N is the Brunt-Vaisala frequency of the temperature profile above the stable boundary layer.

Figure 2-17a shows that, except for the Milan data, the SBL heights show little correlation with u_*. Figure 2-17b, and Figure 2-17c indicates similar results for the correlation between the urban SBL height and $(u_* L_{M-O})^{1/2}$ and surface wind speed (U), respectively. The usefulness of u_* / N was not evaluated, because the potential temperature gradient above the boundary layer was essentially zero in the Riverside and VTMX experiments, and was not available for Milan studies.

As a prelude to the examination of prognostic models, the team examined the relationship between the boundary layer height and the time integral of friction velocity, $\int u_* dt$ which is a measure of the height over which the surface shear stress exerts its influence after sunset. Figure 2-18 indicates that SBL height correlates well with the time integral of friction velocity for the Riverside and VTMX data sets; the correlation is lower for the Wangara data

and is poor for the Milan data. Table 2-5 indicates that this integral provides a better description of the SBL height than the variables used in diagnostic models.

Figure 2-17: Measured Boundary Layer Height in Riverside, VTMX, Milan, and Wangara Feld Studies vs. (a) Friction Velocity (*u*$_*$), (b) $(u_* L_{M-O})^{1/2}$, and (c) Wind Speed (*U*)

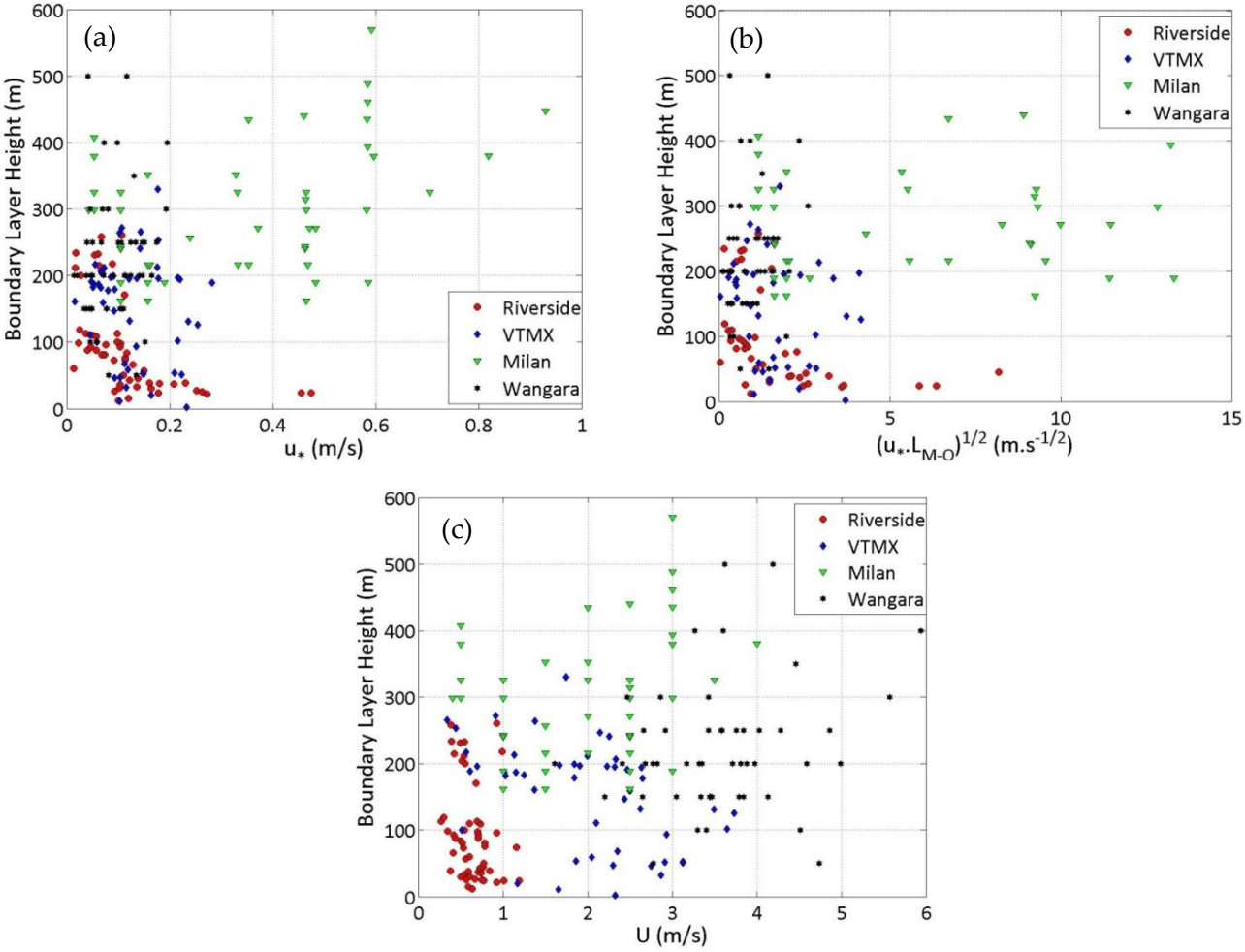

Figure 2-18: Measured Boundary Layer Height in the Riverside, VTMX, Milan, and Wangara Field Studies vs. $\int u_* dt$.

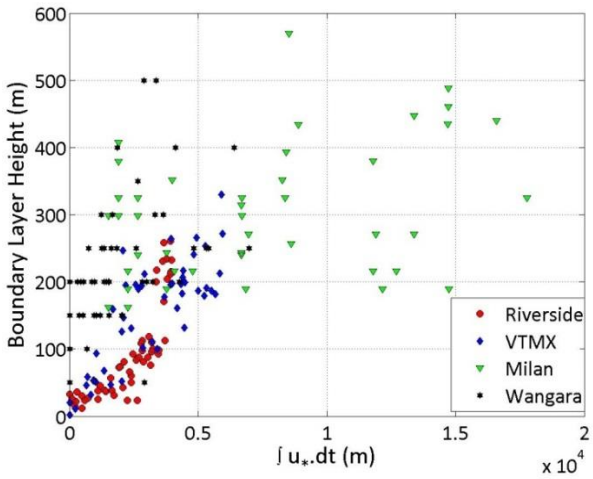

Table 2-5 shows a summary of the correlation coefficients (*r*) of different parameters explained above with the field data.

Table 2-5: Correlation Coefficient (*r*) between the Boundary Layer Height Data and Different Modeling Parameters

Field Data	$\int u_* dt$	u_*	$(u_* L_{M-O})^{1/2}$	U
Riverside	0.82	-0.51	-0.45	-0.25
VTMX	0.82	-0.14	-0.21	-0.44
Milan	0.26	0.38	0.42	0.34
Wangara	0.5	0.18	0.18	0.21

2.3.4.3 Performance of Prognostic Models

This section examines the performance of a class of prognostic models that simulate the time variation of the SBL height by relaxing the height towards an equilibrium height using the equation,

$$\frac{dh}{dt} = -\frac{(h - h_E)}{\tau} \qquad (2\text{-}15)$$

where h_E is the equilibrium height corresponding to a diagnostic model, and τ is a relaxation time scale. The team investigated two versions of this formulation. AERMOD (Cimorelli et al. 2005), a dispersion model that is recommended for U.S. regulatory applications, uses an

equilibrium boundary layer height (Venkatram 1980) that is based on the Zilitinkevich (1972) formulation, $\left(u_* L_{M-O} / f\right)^{1/2}$:

$$h_E = 2300\ u_*^{3/2}. \tag{2-16}$$

The relaxation time scale τ is formulated as,

$$\tau = \frac{h}{2u_*} \tag{2-17}$$

This roughly corresponds to the time taken for changes at the surface to be transmitted to the top of the boundary layer.

The model proposed by Zilitinkevich et al. (2002) predicts that the boundary layer height in the absence of the large-scale vertical velocity approaches an equilibrium height given by:

$$h_E = \frac{C_R u_*}{|f|}\left\{1 + \frac{C_R^{\ 2} u_* \left(1 + C_{uN}.Fi\right)}{C_s^{\ 2} |f| L_{M-O}}\right\}^{-1/2} \tag{2-18}$$

where $C_R = 0.4$, $C_{uN} = 0.25$ and $C_s = 0.74$ are empirical constants and *Fi* is inverse Froude number given by,

$$Fi = \frac{L_{M-O} N}{u_*} \tag{2-19}$$

where $N = \left[g\left(\partial\theta/\partial z\right)/T_0\right]^{1/2}$ is the free flow Brunt-Vaisala frequency above the SBL.

The relaxation time scale, τ, is given by,

$$\tau = \frac{1}{C_E |f|} \tag{2-20}$$

where $C_E = 1$ is an empirical dimensionless constant.

We integrate equation (2-15) through the numerical approximation,

$$h(t + \Delta t) = h(t) e^{(-\Delta t/\tau)} + h_E(t + \Delta t)\left[1 - e^{(-\Delta t/\tau)}\right] \tag{2-21}$$

where *t* is the time from sunset.

Figure 2-19 indicates that AERMOD predictions show variations, governed by the surface friction velocity, that are not reflected in the observations. The model overestimates the boundary layer height during the first four hours of the night (due to large u_*) and tends to underestimate it after that. Evaluation of this model using predicted and observed u_* yield similar results.

Figure 2-19: Comparison of AERMOD Stable Boundary Layer Height Model Predictions with Observations from the Riverside Field Study

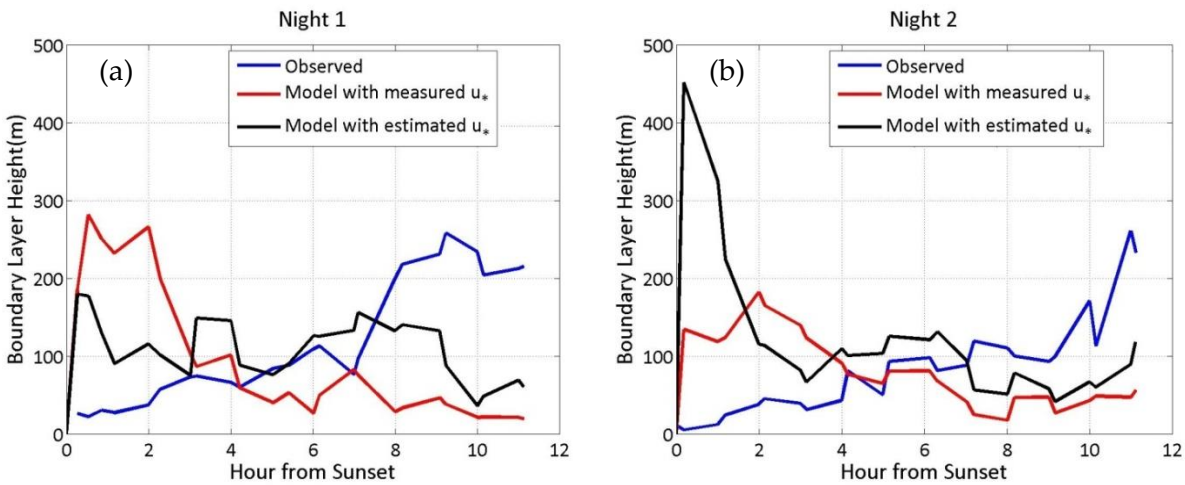

(a) Night 1 and (b) Night 2

Figure 2-20 indicates that the Zilitinkevich et al. (2002) model predictions are of the right order of magnitude, but they do not vary significantly with time; they range from 30 m up to 160 m throughout the night, while the observed values show larger variation. Predicted values of boundary layer height using estimated u_* and L_{M-O} (Venkatram 1980) are relatively higher than those based on the measured u_* and L_{M-O}.

Figure 2-20: Comparison of Predictions by Zilitinkevich et al. (2002) Model with Observations from the Riverside Field Study

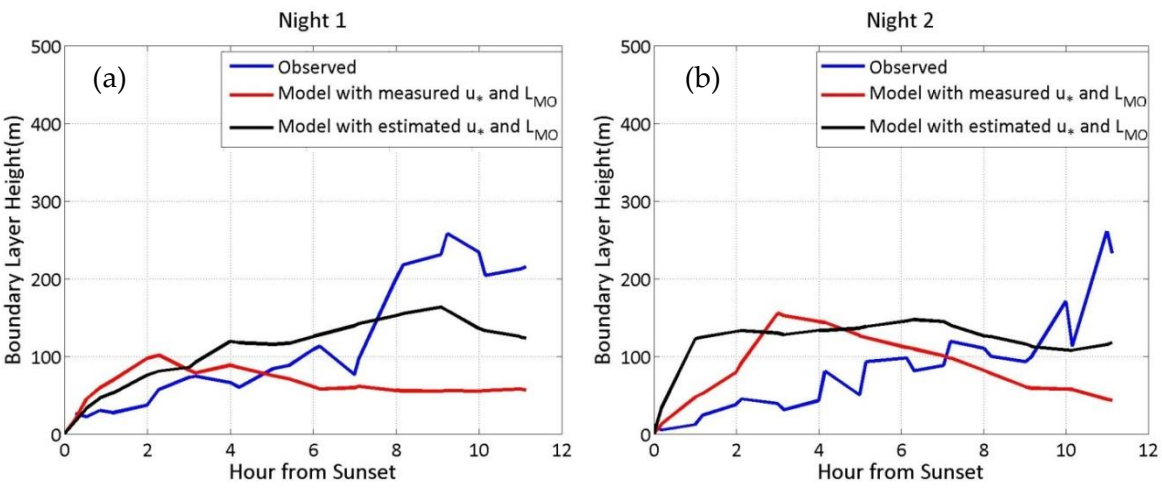

(a) Night 1 and (b) Night 2

2.3.4.4 Time-Integrated Friction Velocity Model

The analysis performed in Section 0 suggests the simple model,

$$\frac{dh}{dt} = \alpha u_* , \qquad (2\text{-}22)$$

which is based on that proposed by Deardorff (1972) (see Yu 1978), which unlike equation 2-22, ensures that the boundary layer height starts to decrease with time once it exceeds an equilibrium height of $0.35u_*/f$. The empirical constant α in Deardorff (1972) is 0.025.The team finds that $\alpha = 0.04$ provided the best fit between the observed boundary layer heights and model estimates. Figure 2-21 shows that this model performed adequately in predicting the boundary layer height for both nights in Riverside, except that there was slight overestimation in the second night. In addition, Figure 2-21 reveals that using the u_* predicted from the measurements of surface mean wind speed at one level, the model performs reasonably well in predicting the boundary layer height.

Figure 2-21: Comparison of the *Time-Integrated Friction Velocity* (eq. 17) Model Predictions with Observation from the Riverside Field Study

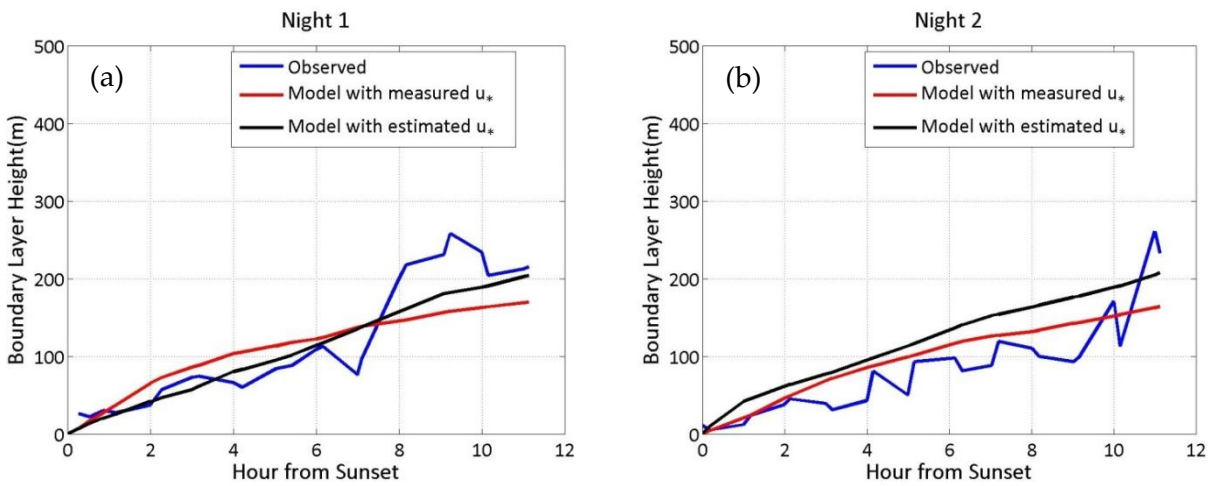

(a) Night 1 and (b) Night 2

This model has also been evaluated with data from VTMX and Wangara field experiments, as shown in Figure 2-22. Boundary layer heights are predicted from 18:00 local time for both VTMX and Wangara field data. Mahrt (1981b) argues that turbulence did not break down completely at sunset during the Wangara experiment, and that the minimum boundary layer height was about 125 m. This initial value was used in the team's simulations.

As seen in Figure 2-22a–c, the model performed adequately for the first two nights of the VTMX experiment but slightly underestimated the boundary layer height on the third night. The evaluation of the model with Wangara data is shown in a scatter plot (Figure 2-22d), since the data are associated with 16 different nights. Evaluation of the model with Wangara data shows that over 90 percent of the data lies within a factor of two of the observed values. There is a bias of 4 percent with the 95 percent confidence interval for the ratio of observed values to predicted values of 2.3. This shows that although the vertical (~50 m) and temporal (~3 hr) resolution of data is low, this model performed well in predicting the boundary layer height in the Wangara field experiment using the estimated friction velocities from Melgarejo and Deardorff (1974).

Figure 2-22: Comparison of the *Time-Integrated Friction Velocity* (eq. 17) Model Predictions with Observation from VTMX Field Study

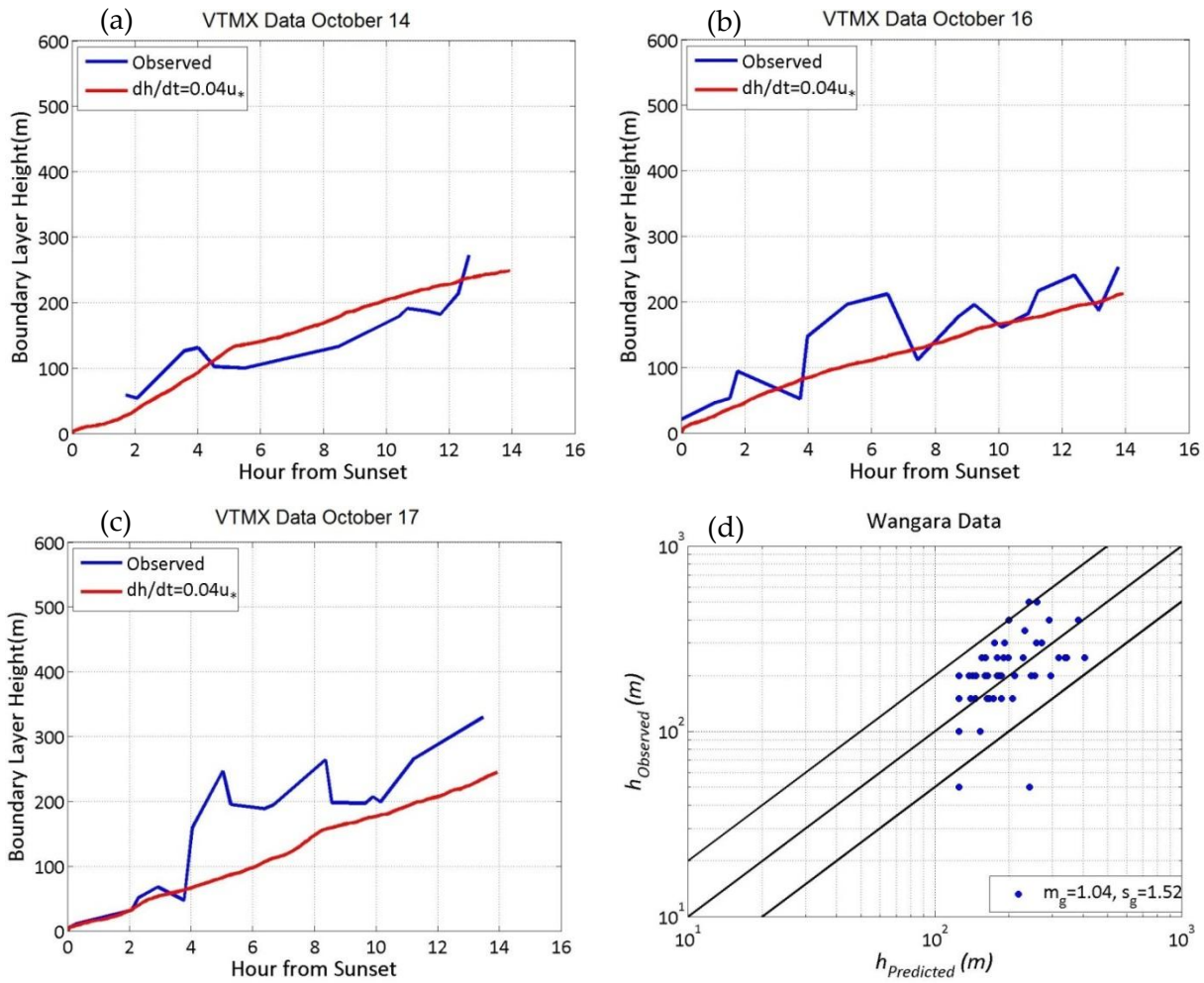

(a) October 14; (b) October 16; (c) October 17, and with (d) Wangara field experiment data

As seen in Figure 2-21 and Figure 2-22, the time-integrated friction velocity model follows the boundary layer height for the first four to eight hours after sunset but underestimates the boundary layer height at the end of the night due to the rapid increase of the SBL height starting from midnight. Mahrt (1998) suggests that this rapid increase in boundary layer height is related to the presence of a nocturnal jet (this is clearly illustrated in Figure 2-10h at $z \approx 200$ m), which represents an elevated source of turbulence. This source of turbulence can dominate surface shear generation in governing the growth of the SBL. The simple model based on the surface friction velocity cannot account for this elevated source of turbulence.

2.3.5 Conclusions

Our analysis of data from three field studies conducted in urban areas confirms earlier results that diagnostic models of the SBL provide poor estimates of the height of the SBL. One-dimensional prognostic models also fare poorly in estimating the SBL height. These results are not unexpected in view of the spatial inhomogeneity of the urban surface. Under these circumstances, it is still necessary to estimate the stable boundary layer height for

diffusion applications. the team's analysis indicates that observed boundary layer height correlates best with the $\int u_* dt$, where time is counted from sunset; the constant multiplying the integral might be site specific. Note that this relationship also implies that the boundary layer height is correlated with the integrated surface heat flux (Yamada 1979; Stull 1983) only because the heat flux is correlated with the surface friction velocity. An estimate of the boundary layer height based on the integrated surface friction velocity has practical value because the surface friction velocity can be estimated from a measured surface wind speed, and an estimate of the surface roughness length.

CHAPTER 3:

Plume Rise: Laboratory Study

3.1 Introduction

Simulated flows and emissions in water channels are the most efficient ways of studying plume motion, due to the relative simplicity of generating stably stratified flows and making visualizations using fluorescent dyes (Contini and Robins 2001; Arya and Lape 1990). Examples of such applications can be found in Hunter (1992), Ohba et al. (1990), Snyder (1985), and Hoult and Weil (1972), and will not be discussed here. The laboratory study explained in this report was conducted through a series of experiments in the water channel facility at University of California Riverside, Laboratory for Environmental Flow Modeling (LEFM). The main focus was to investigate the air quality impact of buoyant emissions from DGs under different building configurations and meteorological conditions.

The laboratory study to understand the effect of nearby buildings (upstream and downstream) on the plume rise was conducted in a custom-designed water channel, which is described in Section 3.2. Methods of scaling urban plume rise and dispersion in water channels is explained in Section 3.12. Also examined was the performance of the numerical plume rise model explained in Section 3.12.5, which accounts for the effect of surrounding buildings on plume rise. That examination used measurements from the laboratory study.

3.2 Water Channel

A custom-designed circulating water channel with a test section that is 1.5 m long, 1 m wide, and 0.5 m deep (see the schematic in Figure 3-1a and a photograph in Figure 3-1b) was utilized for the experiments. The channel is located in the LEFM. Water is circulated through the channel test section using a 15 kW axial pump that produces a maximum mean velocity of 0.5 m s^{-1} in the test section. A variable-frequency controller allows flow control with a resolution of 1/100 Hz (from 0 to 60 Hz). Flow conditioning is achieved with the profiled honeycombs and the custom-built perforated screens. The perforated screens are used to generate desired inflow velocity profiles as a part of the flow conditioning. The channel flow is steady and becomes fully developed before reaching the test section. The channel has flow control capability to maintain desired velocity profile starting from the classical logarithmic to the linear profile. As needed, the channel can also maintain well -defined jets at a desired height. Simulating flow and dispersion in such laboratory facility requires that the correct scaling techniques be used. These scaling methods will be explained in more detail in the next chapter.

Figure 3-1: (a) Water Channel Schematic; (b) Water Channel Facility at University of California Riverside (LEFM)

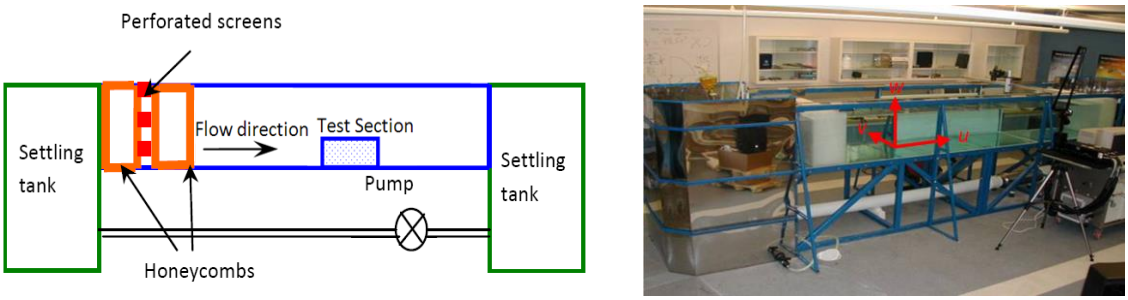

(a) (b)

3.3 Concentration Measurements System

The existing concentration measurements system, the planar laser-induced fluorescence (PLIF) system, is one of the most powerful techniques to measure the tracer concentrations in water channels. The principle of this technique is relatively old and well addressed in literature (e.g., Pringsheim 1949; Kychakoff et al. 1984; Hanson 1988). This system consisted of a 400 mJ Nd-YAG laser (Big Sky Laser Technologies Inc.) producing a 532 nanometer (nm) wavelength laser beam with the frequency of up to 15 Hz as the radiation source, laser pulse synchronizer (TSI Inc.), high-resolution (1600 x 1192) POWERVIEW 2M CCD camera (TSI Inc.), and 575–585 nm light filter. Rhodamine 6G was used as a tracer dye. The basic equation that relates the induced fluorescence intensity, I_f, with the fluorescent dye concentration is defined by Guilbault (1973) as

$$I_f = 2.3\,\Phi\, I_0\, \varepsilon\, b\, c, \tag{3-1}$$

where the quantum efficiency Φ is the ratio between the energy that is emitted to that which is absorbed, I_0 represents the light intensity, ε is the molar absorptivity, b is the absorption path length, and c is the concentration of the fluorescent dye.

The PLIF results were found to be reliable for the far field concentrations, but the measurements were biased high close to the source because of several PLIF measurement difficulties: (1) light reflection from the water channel bottom face, which is especially pronounced when the goal is to measure near-surface concentrations; (2) laser light attenuation by varying plume intensity outside of the region of interest; (3) self-illumination, which is very pronounced when extreme concentration gradients are present, like in the case of near-source measurements of ground-level concentrations for elevated release (here ground-level concentrations near the stack can be four orders of magnitude less than at the nearby elevated source); and (4) averaging time, which is a problem of the recirculating nature of the tank. Once dye recirculates back to the test section of the water channel, the

background concentration becomes comparable to the ground-level concentration. For these reasons the team decided to keep PLIF for plume spread and far field concentration measurements and to conduct near-source measurements using a different technique.

To overcome the PLIF deficiencies the team tried several methods, including placing thin, non-reflective enclosures in the region of interest to avoid self-illumination and laser light attenuation. These met with limited success and will not be discussed here. The satisfactory solution was finally designed by implementing 750 micrometer (μm) unjacketed plastic optical fibers. Conducting the laser beam through a short optical fiber prevented attenuation and allowed us to direct the beam to a point, to avoid light reflection and self-illumination. Several sensors were placed in the background for real-time corrections of the background concentrations to allow for a longer averaging time. Each sensor consisted of two optical fibers: one for delivery of a laser beam and a second for delivering fluorescent light to the charge coupled device (CCD) camera. It has been experimentally shown that the best arrangement for the fibers in the sensor is when the fibers are adjusted at an angle of 26° to each other (Kulchin et al. 2007).

Figure 3 2a shows a sensor photo, and a schematic of the setup is shown in Figure 3 2b. The laser beam is focused on a bundle of optical fibers. Each fiber guides laser light to the location of interest. Light from the fluorescent dye at the sensor location is then conducted to the camera via a second pair of fibers, referred here as *return fibers.* Return fibers are sparsely fixed in front of a CCD camera at predetermined location so that all fibers are recorded at the same image without interference. A filter is placed in front of the camera to prevent any laser light reaching the CCD. Each sensor has to be individually calibrated. By utilizing this system, the team sacrificed the whole-plane PLIF measurements and replaced them with numerous point measurements. This is not a big disadvantage; sensors are inexpensive and small enough not to disturb the flow, so many of them can be placed in desired region. In addition, light intensities from all of the sensors are collected to a single image, so processing is relatively simple. Figure 3 3 shows the experiment setups for the sensors, camera, and laser.

Figure 3-2: (a) Optical Fiber Sensor and (b) Schematics of the Concentration Measurement System

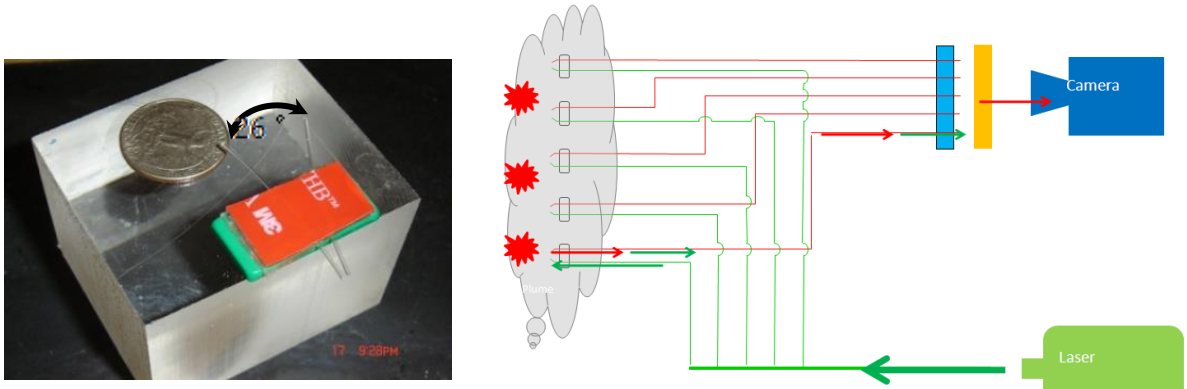

(a) (b)

Green fibers are emitting fibers and red fibers are receiving fibers

Figure 3-3: (a) Sensors Placement in the Water Channel. (b) Laser Setup. (c) Camera Setup.

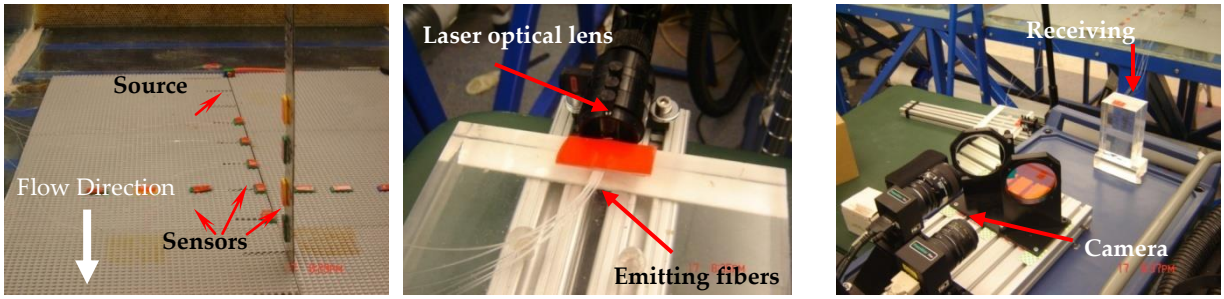

(a) (b) (c)

There are a variety of fluorescent substances available (Berlman 1971); however, not all are suitable for the team's application. The fluorescent dye suitable for this application should have the following properties: (1) solubility in water, (2) absorption and emission spectra in the range of the applicability of the devices, and (3) a high resistance to photo bleaching. Among the commonly used tracer dyes, Rhodamine B was the most suitable tracer dye for this specific application. Rhodamine B ($C_{28}H_{31}ClN_2O_3$) is a water-soluble (up to 50 g/L) fluorescent dye that has the absorption spectrum of 460 nm–590 nm along with the emission spectrum of 550 nm–680 nm with the maximum emission intensity occurring at 590 nm. There have been several different results reported for the concentration-intensity linearity limit of Rhodamine B. Guilbault (1973) stated that only when less than 5 percent of the exciting light is absorbed by the fluorescent dye, a linear response can be achieved from the Rhodamine B. This occurs for concentration less than 30 mg/L (Walker 1987). Arcoumanis et al. (1990) show that the concentration should be less than 0.08 mg/L for a linear response. However, Houcine et al. (1996) reported a concentration of less than 40 μg/L. Kassaro and Mungal (1997) show that the linear response is only available for concentration up to

9.57 mg/L. Therefore, prior to proceeding to the measurements, this uncertainty in the linearity of light intensity and concentration made us investigate the linear behavior of Rhodamine B. According to the team's results, Rhodamine B shows a linear concentration-intensity behavior up to 10 mg/L.

3.4 Velocity Measurement System (PIV)

The velocity field is measured by TSI's Particle Image Velocimetry (PIV) system. This system consists of 400 mJ Nd-YAG laser (Big Sky Laser Technologies Inc.) producing a 532-nm wavelength laser beam with the frequency of 1 HZ, which is expanded into a laser sheet using sheet forming optics, a laser pulse synchronizer (TSI Inc.), and a PowerView Plus 2M and 11M camera. Pliolite Ultra 100 particles are used as seeding particles in the water channel. To measure the fluid's velocity, at least two separate exposures must be recorded. This typically involves producing a pair of laser pulses which are recorded onto a pair of camera frames. The frames are then split in a large number of interrogation areas, often called tiles. Through image processing it is then possible to calculate a displacement vector for each tile. This displacement is converted to a velocity using the time step between consecutive images (in the team's case $\Delta t = 1.2ms$). Insight 3G (TSI Inc.) software is used for data collection and image processing. The PIV measurement technique is well established and widely used for fluid flow investigations (Adrian 1988, 1991, 1997; Prasad et al. 1992).

3.5 Plume Visualization Technique

Plume rise in the water channel has been measured through the plume visualization technique. This simple technique consisted of a commercial camera (Sony 4.1MP Cyber shot) located on a tripod and a light source illuminating the test section. Using the manual option by adjusting the lens aperture and/or shutter speed, the team achieved the desired exposure. Fluorescent dye, Uranine, is used as the visualizing dye, as it has high light intensity in the range of visible light. Therefore, plume visualization can be achieved by releasing the tracer dye from the source and capturing the long exposure image for 30 seconds. This technique gives us a plume-averaged visualization image that can be used to measure the plume rise under different meteorological conditions and building geometries. Figure 3-4 shows two examples of the plume visualization images that were produced using this technique.

Figure 3-4: Plume Visualization

(a) (b)

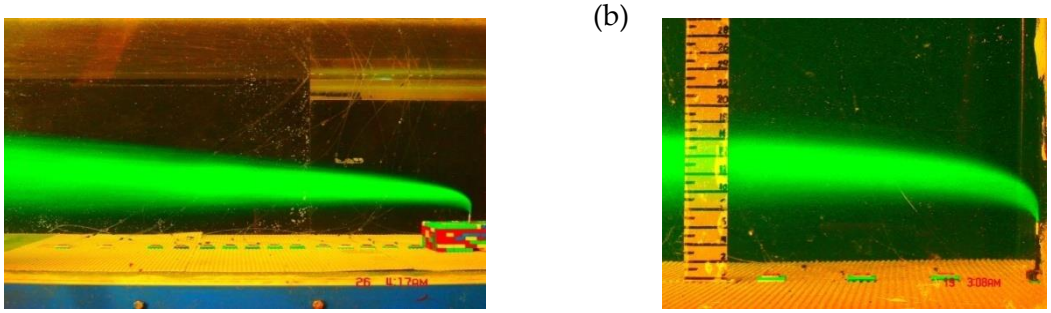

(a) Palm Springs DG Model; (b) Single-Stack Non-Buoyant Release

Section 3.12 will explain appropriate methodologies to scale real-world dispersion problems in this water channel facility and translate the concentration and plume rise results obtained from the laboratory measurements to those from the field for evaluation and comparison.

3.6 Experimental Setup

To investigate plume rise associated with DGs, a DG building similar to Palm Springs DG (L × W × H = 15 m × 15 m × 7 m) with stack height of 9.3 m and stack diameter of 0.3 m (with the stack in the middle of the building) was modeled in the water channel at a scale of 1:100. Note that the laboratory study shown in this study does not represent the scaled problem from the Palm Springs field study, except for the geometry. To observe the effect of surrounding buildings on plume rise, arrays of buildings (2 rows and 3 columns) of two different heights (single and double story, with the heights of H_{single} = 100 mm and H_{double} = 200 mm, respectively) were created using Lego blocks. They were situated as follows: (1) upstream of the DG building; (2) downstream of the DG building; and (3) upstream and downstream of the DG building (Figure 3-5). The upstream and downstream building arrays were located at a distance of 150 mm from the upwind and downwind side of the DG building, respectively. the team are aware that the building configurations used in the laboratory study do not necessarily resemble a typical urban environment. However, since a hot plume rises above the urban canopy in a relatively short distance from the stack, its rise would be mainly affected by the nearby buildings rather than the overall urban geometry. the team should note that the background micrometeorology that governs the plume rise near the stack is surely dependent to the urban morphology. The influence of urban morphology on the upwind micrometeorology in urban areas has been widely explained in the literature (e.g., Venkatram and Princevac 2008; Princevac and Venkatram 2007; Luhar et al. 2006) and will not be discussed here.

Figure 3-5: (a) Schematic of the Buildings Configuration. Model of the DG and Surrounding Buildings Situated Upstream (b, e), Downstream (c, f), and both Upstream and Downstream (d, g). Both Single-Story (b, c, d) and Double-Story (e, f, g) Buildings were Investigated.

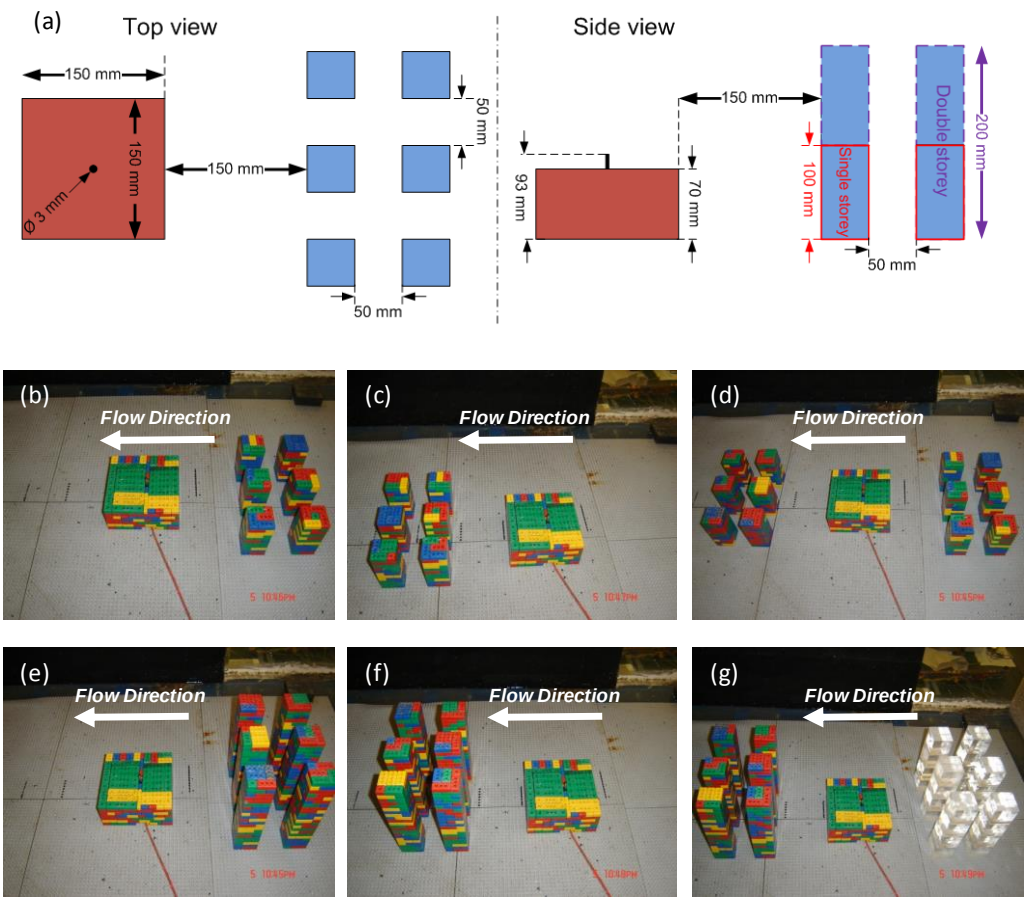

Different tracer buoyancies were achieved by using different mixtures of alcohol and water and expressed as specific gravity (*SG*). Plume rise was measured under two different buoyancies (*SG* = 0.98 and 0.96). These plume buoyancies were selected in order to observe how plume rise affected by buildings changes with an increase in buoyancy (buoyancy associated with a tracer of *SG* = 0.96 is equivalent to two times that of a tracer with *SG* = 0.98, since the buoyancy is proportional to 1-*SG*).

As explained in Section 3.12, in scaling the free stream velocity, the most important consideration is to satisfy the Reynolds number independence criteria. Following Yee et al. (2006) and Snyder (1981), in order to satisfy this criteria, the reference Reynolds number (*Re*), based on the free stream velocity (v_∞) and characteristics building frontal length scale, H_b^* (length scale based on the obstacle frontal area; $H_b^* = (WH)^{1/2}$) should be larger than 4,000. In the water channel, this is obtained for velocities larger than 3.9 centimeters per second (cm s^{-1}). Therefore, to scale the field velocity of 3–4 m s^{-1}, a velocity scale of 3:200 was used. This velocity scale was selected to have sufficiently fast flow to satisfy *Re* independence

criteria and at the same time to be slow enough to allow for accurate measurements of plume rise. Using this velocity scale, average stack exit velocity of 12.5 m s^{-1} in the field were scaled and modeled in the lab. Table 3-1 shows the details of the experimental conditions.

Table 3-1: Experimental Parameters for Plume Rise Measurements

Parameters	Value
Free stream horizontal velocity (v_∞)	4.5 cm s^{-1}
Diameter of the stack (D)	3 mm
Stack exit velocity (V_s)	19 cm s^{-1}
Roughness length of Lego blocks (z_0)	≈ 0.6 mm
Plume specific gravity (SG)	0.96 nd 0.98

3.7 Upstream Buildings

Figure 3-6 shows the results of the flow and plume rise measurements when buildings (of two different heights) are situated upstream of the DG building. It can be seen from Figure 3-6 a-b that upstream buildings increase the plume rise, compared to the case where no buildings are present. Figure 3-6 a-b also shows that an increase in the height of the upstream buildings further increases the plume rise. This effect can be explained through the flow measurements (Figure 3-6 c-e) associated with these three cases (the DG-only building, single-story upstream buildings, and double-story upstream buildings). From Figure 3-6 c-e, it can be inferred that the presence of upstream buildings increases the flow resistance and induces a low wind speed condition near the DG building, which allows the plume to rise higher. The increase in the height of the upstream buildings decreases the wind speed in a larger region above the DG, which enables the plume to rise much higher.

However, as can be seen from Figure 3-6 b, the rate of plume rise in the presence of upstream buildings (especially for the case of double-story upstream buildings) is slower compared to the case of an isolated DG without any surrounding buildings. This suppression of the plume rise is due to the higher levels of turbulence caused by the upstream buildings. This higher turbulence leads to enhanced entrainment of ambient fluid and causes the plume to level off. In addition to the above-mentioned observations, Figure 3-6 also shows that an increase in the buoyancy from $SG = 0.98$ to $SG = 0.96$ reduces the discrepancy between the plume rise measurements under the three different conditions; since the effect due to buildings becomes smaller as the plume rises higher.

Figure 3-6: Results from Measurements of Plume Rise (h_p) Associated with a DG with and without Upstream Buildings

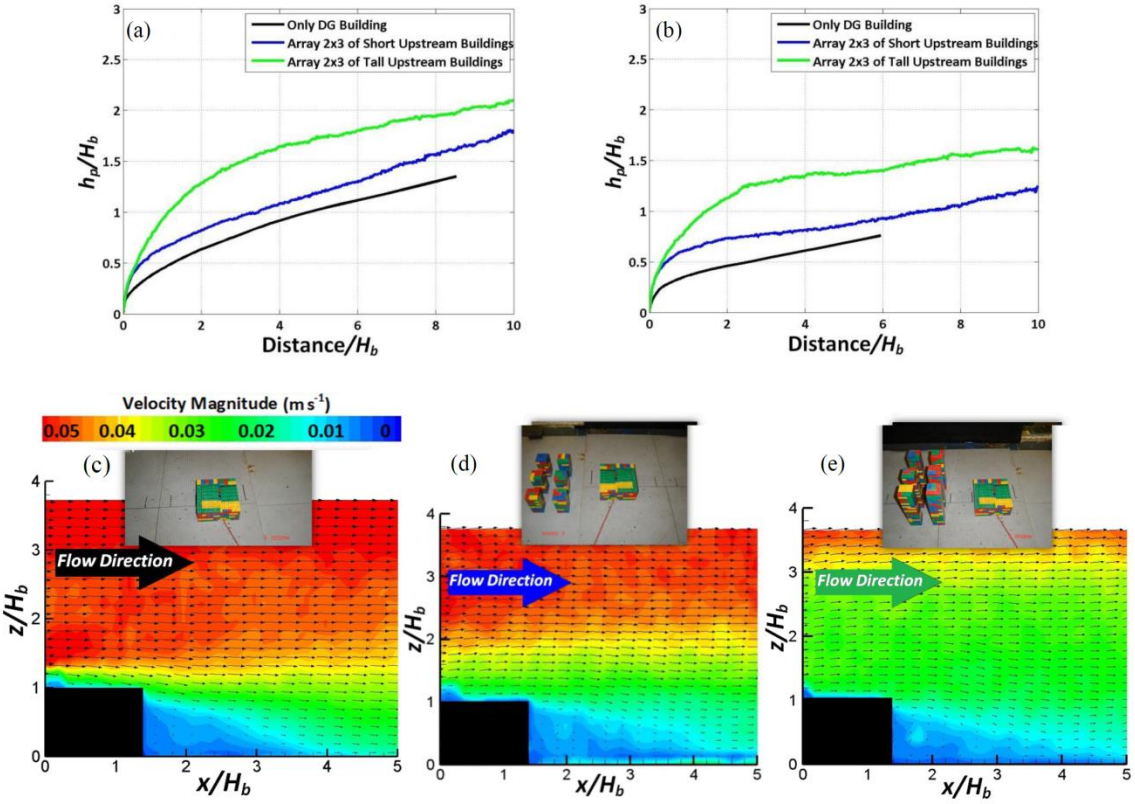

(a) *SG* = 0.96 and (b) *SG* = 0.98 (distances in horizontal and vertical directions are normalized with respect to the height of the DG model building H_b = 0.07 m). Flow measurements associated with (c) the DG building only, (d) the DG building with single-story upstream buildings, and (e) the DG building with double-story upstream buildings (the blue vector lines show the velocity of less than 0.01 m s^{-1}, and the dark red vector lines show the velocity equal/above 0.05 m s^{-1} corresponding to approximate velocity of 3.5 m s^{-1} in the field).

3.8 Downstream Buildings

Figure 3-7 shows the results from the measurement of flow and plume rise when the buildings are situated downstream of DG building.

From Figure 3-7 a-b it can be seen that single-story (short) downstream buildings with the height approximately the same as that of the stack height increase the plume rise, compared to a scenario where there are no surrounding buildings. However, by increasing the height of the downstream buildings, the plume rise is reduced. As in the previous case, flow measurements are used to explain the observations (Figure 3-7c-e).

Figure 3-7 c-e shows that the presence of single-story downstream buildings lowers the wind speed. In addition, these buildings reduce the downdrafts induced by the DG building, and instead create slight updrafts in the vicinity of the DG. Due to these two effects, the plume rises higher when single-story downstream buildings are present. However, the effect of buildings on plume rise is significantly different when the height of the downstream buildings is doubled. As the flow approaches the double-story downstream buildings, flow above the stagnation point passes over the buildings and produces an updraft; but most of the flow is deflected towards the ground and produces a strong downdraft (Figure 3-7 e). This effect has also been studied by Oke (1987) where he mentioned that the stagnation point occurs at approximately 2/3 height of the building while a result from the team's flow measurements in Figure 3-7 e shows this stagnation height as the 3/4 of the building height. For the presented analysis the exact stagnation height is not crucial. Depending whether the plume approaches the updraft above the stagnation height of the downstream building or the downdraft below this height, it can rise higher or lower.

In the case of the team's laboratory study, due to the low buoyancy and high wind speeds, the plume could not reach above the stagnation height and pass over the downstream buildings. Therefore, the plume approached the region where it was dominated by downdrafts, which resulted in lower plume rise. This effect became more apparent when the buoyancy was decreased from $SG = 0.96$ to $SG = 0.98$. The plume rise associated with the double-story downstream buildings became even slightly lower than for the case when no surrounding buildings were present. Since the plume passes through the array of downstream buildings, no accurate plume rise measurements were possible in the vicinity of these buildings (discontinuity in the green line in Figures 3-7 a-b).

Figure 3-7 Results from Measurements of Plume Rise (h_p) Associated with a DG with and without Downstream Buildings

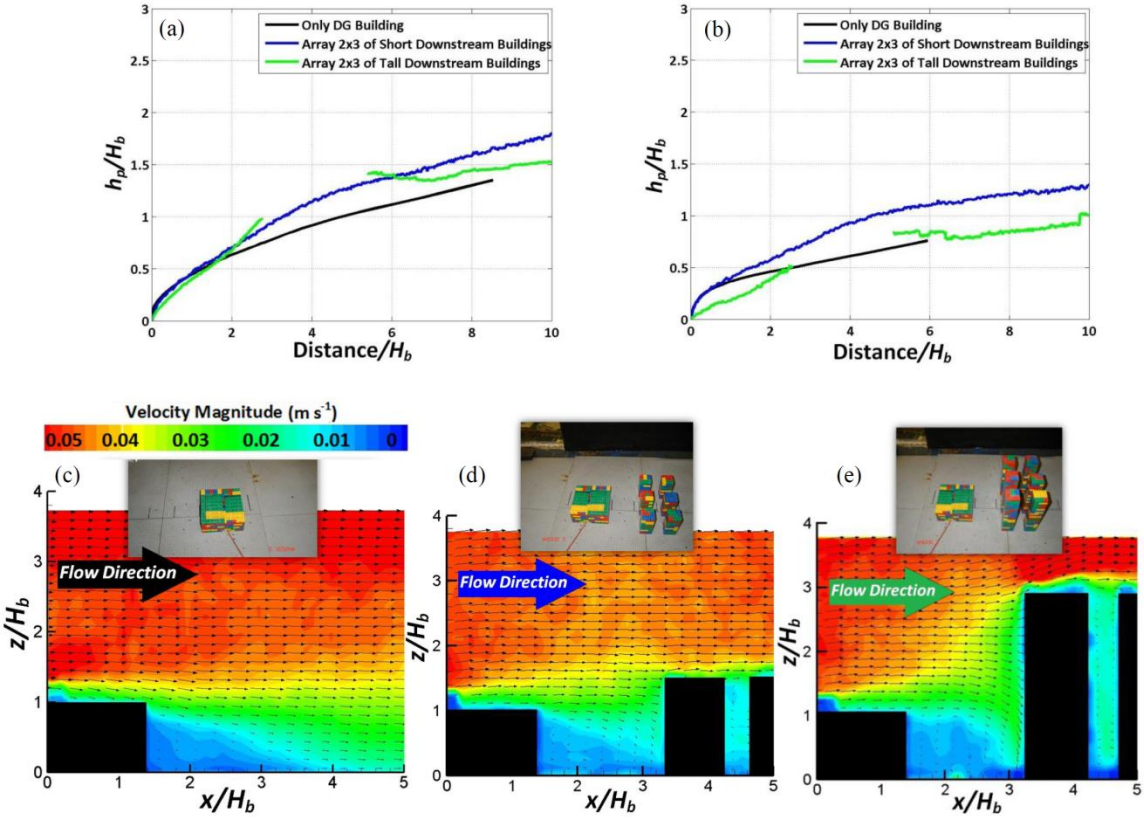

(a) *SG* = 0.96 (b) *SG* = 0.98 (Since for the case of tall, double-story, downstream buildings, plume passes through the buildings, no measurements of plume rise were available in this region. This explains the discontinuity of the green line). Flow measurements associated with (c) the DG-only building, (d) the DG building with single-story downstream buildings, and (e) the DG building with double-story downstream buildings.

3.9 Upstream and Downstream Buildings

Figure 3-8 shows the results from the flow and plume rise measurements when both upstream and downstream buildings were present. From Figure 3-8 a-b, it can be observed that a combination of both upstream and downstream buildings cause the plume to rise higher; this increase in plume rise becomes larger when the height of the buildings is doubled. As in the previous cases, flow measurements were used to explain the observed effects.

As shown in Figure 3-8 d, in the case of the single-story buildings, the upstream buildings slightly reduce the wind speed. In addition, the downstream buildings reduce the downdrafts caused by the DG building. The reduced wind speeds and weaker downdrafts cause the plume to rise higher. In the case of the double-story buildings (Figure 3-8 e), the

upstream buildings significantly reduce the wind speed close to the stack. This allows the plume to rise relatively high within a short distance from the stack.

Unlike the case where only downstream buildings were present, the plume reaches above the stagnation height of the downstream buildings, where updrafts help the plume to rise higher. Because of these two complementary effects (lower wind speed and updrafts), plume rises the most when both double-story upstream and downstream buildings are present. It is interesting to note that in the case of the double-story upstream and downstream buildings, plume rise does not change significantly when buoyancy is increased from $SG = 0.98$ to $SG = 0.96$, as the plume rise is dominated by the stack momentum and updrafts induced by the downstream buildings in close vicinity of the DG building. In addition, these buildings increase the ambient turbulence, which dominates the entrainment of ambient air into the plume and causes the plume to rise slower at larger distances from the stack.

Figure 3-8: Results from Measurements of Plume Rise (h_p) Associated with a DG with and without Upstream/Downstream Buildings

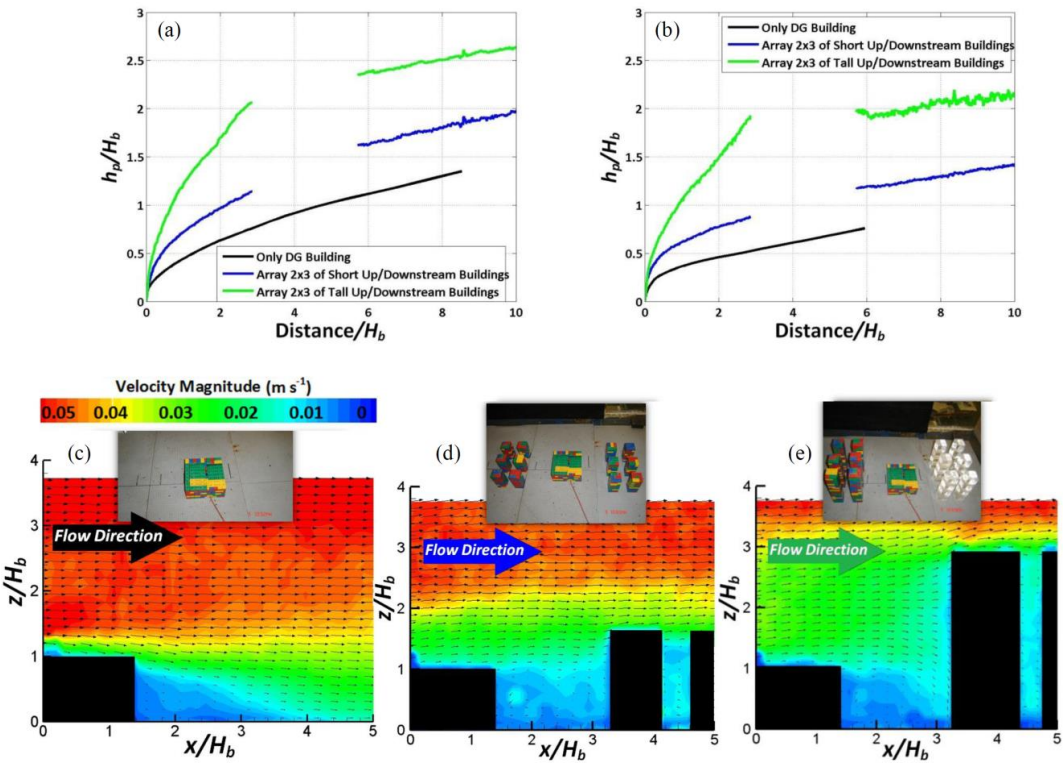

(a) SG = 0.96 and (b) SG = 0.98. Flow measurements associated with (c) only the DG building, (d) the DG building with single-story upstream and downstream buildings, and (e) the DG building with double-story upstream and downstream buildings.

3.10 Comparison with the Numerical Plume Rise Model

The results from the plume rise measurements discussed in the previous section have also been compared with the numerical plume rise model, which is explained in Section 3.12.5.

Figure 3-9: Comparison of the Plume Effective Height (h_e) Observations (blue) with the Numerical Plume Rise Model (red) for Plume Buoyancy of SG = 0.96

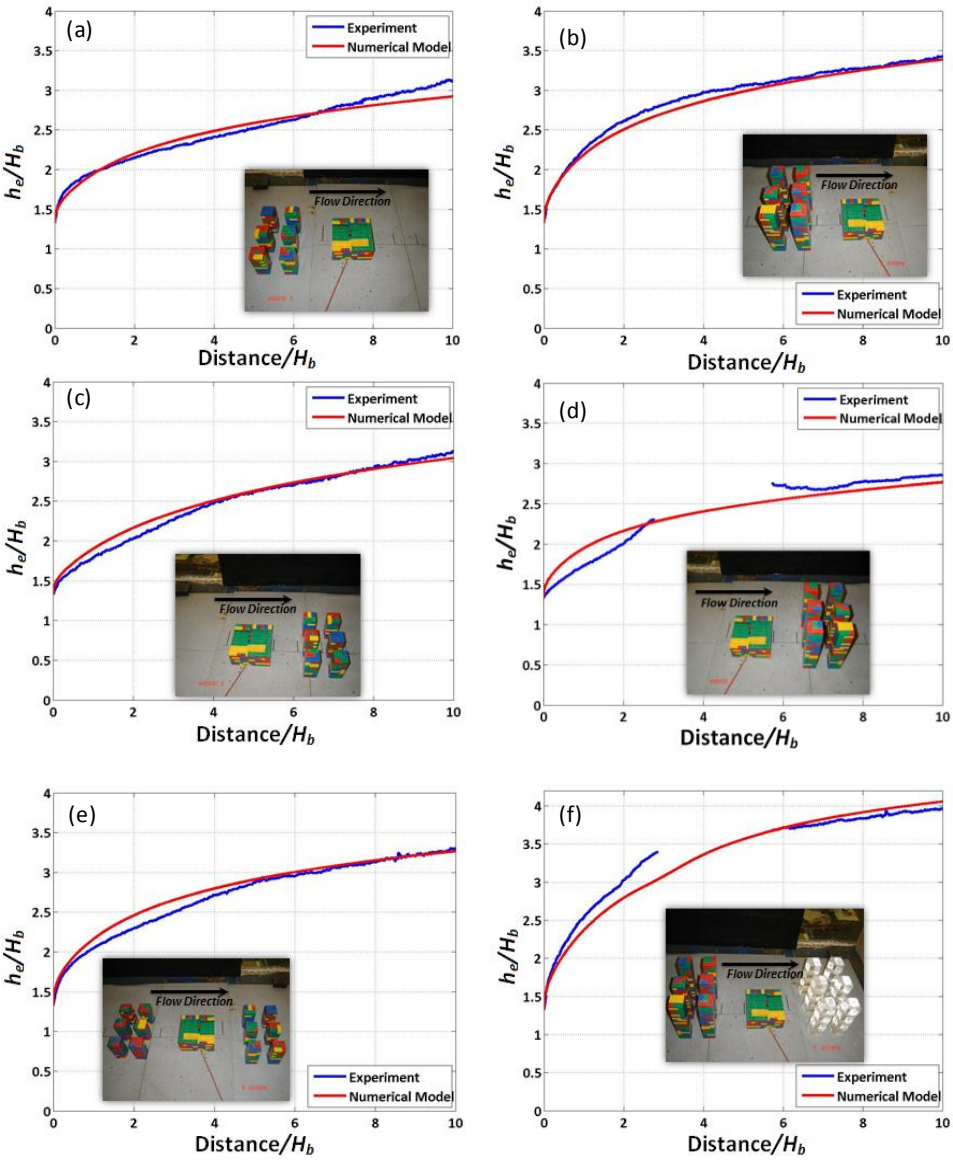

Comparisons were done for cases (a) with an upstream single-story buildings array; (b) with an upstream double-story building array; (c) with a downstream single-story building array; (d) with a downstream double- story building array; (e) with upstream and downstream single-story building arrays; and (f) with upstream and downstream double-story building arrays. Distances in horizontal and vertical directions are normalized with respect to the height of the DG model building H_b = 0.07 m.

Figure 3-10: Comparison of the Plume Effective Height (h_e) Observations (blue) with the Numerical Plume Rise Model (red) for Plume Buoyancy of SG = 0.98

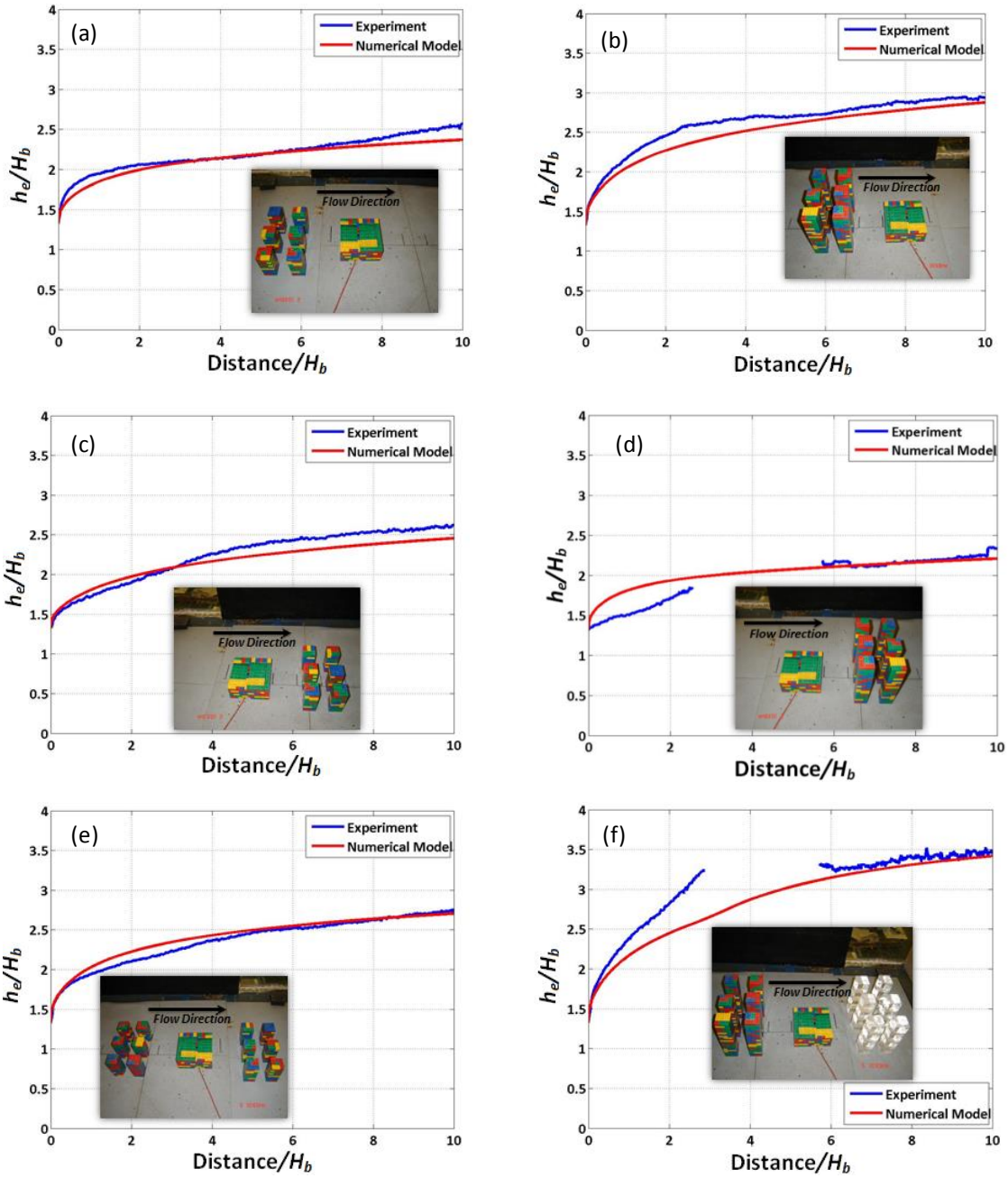

Comparisons were done for cases (a) with an upstream single-story buildings array; (b) with an upstream double-story building array; (c) with a downstream single-story building array; (d) with a downstream double- story building array; (e) with upstream and downstream single-story building arrays; and (f) with upstream and downstream double-story building arrays. Distances in horizontal and vertical directions are normalized with respect to the height of the DG model building H_b = 0.07 m.

In Section 3.12 this model is evaluated for a scenario where only the DG building is present. In this section, using the flow measurements shown in the previous section, the plume effective height ($h_e = h_p + H_s$) associated with the DG model under different surrounding building geometries has been predicted and compared with the plume effective height measured in the laboratory (Figure 3-19 and Figure 3-10).

Figure 3-9 shows the results where the plume specific gravity is *SG* = 0.96. The results from a model comparison under the buoyancy of *SG* = 0.98 are given inFigure 3-10. It can be seen from Figure 3-9 that the numerical plume rise model performs reasonably well in predicting the plume rise, as it accounts for the flow modifications induced by the surrounding buildings. The same results have also been obtained for the plume buoyancy of *SG* = 0.98 (Figure 3-10). The downside of this model is that it requires measured flow velocities as inputs, and these are not usually available. However, even when the full flow field data is not available, linear interpolation of limited available flow data points can be sufficient to construct the required inputs for this model, although the results might not be as accurate as if the detailed flow velocities were available. For the complex flow conditions that include updrafts, downdrafts, and regions of increased and decreased flow velocities, one cannot expect a simple plume rise formulation to perform satisfactorily. This plume rise model can be easily implemented in an urban Computational Fluid Dynamics (CFD) model for accurate calculations of the plume height.

3.11 Summary and Conclusion

Distributed generation units are highly efficient, as they customarily deploy heat recovery, thus providing both electricity and heating/cooling to nearby facilities. This heat recovery decreases the exhaust temperature, which leads to a lower plume rise that can result in higher ground-level concentrations. Therefore, realistic modeling of plume rise from DGs plays a major role in determining the ground-level concentrations associated with these sources. In this study, laboratory and field measurements were conducted to investigate the plume rise associated with these low-level buoyant sources under different meteorological conditions and surrounding building geometries.

Results from the Palm Springs field study described in Chapter 2 are specific to the site and cannot be extrapolated to other settings. In addition, Palm Spring represented a low-wind case that might not be necessarily a general case in urban environments. To have a more generalized understanding of the plume rise affected by buildings, experiments under relatively high wind conditions are required. Since conducting multiple field studies are prohibitively expensive and time consuming, laboratory simulation would be the most efficient way of studying such a problem. Accordingly, this chapter described the water channel simulations that were conducted to observe the effects of nearby buildings (upstream and downstream) on plume rise under relatively high wind speeds (≈ 3 to 4 m s^{-1}). Plume rise from a DG model was measured under different surrounding geometries and source conditions. Arrays of buildings (2 rows, each with 3 buildings) of two different heights (single- and double-story) were created and situated upwind and downwind of the

DG building (Figure 3-5). Due to the lack of complexity of these building geometries, they do not necessarily represent a typical urban environment, and the plume rise measurements demonstrate a first order sensitivity of the plume to surrounding buildings rather than an urban effect. However, it needs to be noted that due to the relatively high momentums and buoyancies, such plumes tends to rise rapidly close to the source. As a result, they are only affected by the updrafts/downdrafts of the buildings within relatively short distances from the stack, and not further. Conversely, the upwind meteorology that governs the plume rise near the stack is surely dependent to the urban morphology and is not limited to nearby buildings.

The results from laboratory measurements show that, in most cases, the presence of surrounding buildings increases the plume rise as buildings reduce the wind speed close to the stack and induce updrafts in the region where the plume tends to rise. As mentioned earlier, these results do not declare the urban influence on plume rise; however, they provide very useful data for analyzing the plume rise in urban areas where geometries are significantly complex.

The results from the plume rise measurements in the laboratory were compared with the results from the numerical plume rise model explained in Section 3.12.5. Using the flow measurements explained in this chapter, plume rise associated with each laboratory case study was predicted and compared with the measured plume rise experiments conducted in the water channel. It was observed that this model is able to accurately predict the plume rise as it can account for the effect of surrounding buildings. To apply this plume rise model to the field case, measurements of building caused flows are needed. However, with the significant improvement in CFD models throughout the past decade, the future work will be to combine this plume rise model with a CFD model and evaluate it with field measurements.

3.12 Scaling of Urban Plume Rise and Dispersion in Water Channels and Wind Tunnels[3]

3.12.1 Introduction

Site-specific results of field studies and their high dependency to meteorological conditions lead to the conclusion that much of today's understanding on dispersion of urban releases results from laboratory modeling in water channels and wind tunnels (Macdonald et al. 1998; Contini and Robins 2001; Yee et al. 2006; Klein et al. 2011). Correct modeling of atmospheric dispersion in these laboratory setups requires correct scaling of the physical properties relevant to mean flow, plume rise, and turbulent dispersion.

Various scaling methods for laboratory modeling have been explained in previous studies. Kobus and Abraham (1980) defined the proper scaling laws for hydraulic modeling through dimensional analysis. Hughes (1993) addressed the similarity criteria for laboratory physical modeling of real problems in coastal engineering. He derived the similitude criteria required for scaling the hydrodynamic phenomena through the non-dimensionalized equations of motion and conservation of mass. Snyder (1981) explained atmospheric flow similarity through matching the dimensionless parameters involved in the physics of the flow.

Similarity criteria for the atmospheric boundary layer have been investigated by:

- Snyder (1972) and Plate (1999) for neutrally stable atmosphere
- Meroney et al. (1975) and Avissar et al. (1990) for stably stratified atmospheric conditions
- Rau et al. (1991), Poreh et al. (1991), Meroney and Melbourne (1992), and (Meroney 1998) for convective boundary layers.

Snyder (1981) summarized a variety of techniques used to simulate the plume rise associated with buoyant emissions at various fluid modeling facilities where different scaling parameters such as Froude number, initial velocity ratio, and initial density ratio were matched to achieve the minimum possible scaling effect. Robins (1980), Obasaju and Robins (1998), and Robins (2003) also investigated the applicability of various plume-rise scaling techniques for laboratory modeling of atmospheric dispersion. They compared the performance of these techniques in simulating the plume rise from isolated stacks. Their analysis showed that results from different combinations of plume rise similarity criteria derived from Briggs (1984) formulations are in agreement with results from a plume-rise field study (Hamilton 1967) that took place downwind of the Tilbury and Northfleet power station resembling an isolated stack with undisturbed flow.

---

[3] Reprinted from Pournazeri, S, M. Princevac, and A. Venkatram. "Scaling of building affected plume rise and dispersion in water channels and wind tunnels—Revisit of an old problem." *Journal of Wind Engineering and Industrial Aerodynamics* 103: 16–30, Copyright (2012), with permission from Elsevier.

Obasaju and Robins (1998) also investigated the effectiveness of scaling techniques applied to building-affected plume dispersion problems. They studied the effect of different scaling methods on the ground-level concentrations rather than on the plume rise itself. Accordingly, Robins (2003) validated these scaling techniques with data from a buoyant tracer field study conducted in the vicinity of the Hinkley Point A nuclear power station building. In addition, Robins (1980) and Snyder (1981) explained the scaling of dispersion through non-dimensionalization of concentration (C) with respect to wind speed (v), stack height (H_s), and source emission rate (Q). Meroney (1982, 1986a, 1986b, 1987) has also explained the similarity criteria, limitations, and constraints involved with the fluid modeling of dense gas cloud dispersion.

Following these results, a complete set of scaling laws associated with similarity of flow, plume rise, and dispersion may be attained. Since some of these similarity criteria need to be relaxed and distorted in order to obtain feasible laboratory parameters, their applicability must be investigated. These relaxed criteria have been evaluated for the dispersion and plume rise from tall isolated stacks where the effect of surrounding buildings can be neglected (Robins 1980; Meroney 1986a, 1986b; Obasaju and Robins 1998). However, their performance is unknown for laboratory modeling of dispersion from low-level buoyant sources in urban areas where surrounding buildings can significantly influence plume behavior. Although, as mentioned earlier, there are studies (Obasaju and Robins 1998; Robins 2003) on evaluating the plume scaling techniques for plumes affected by buildings. However, these studies focused on the ground-level concentrations, which depend on both plume spreads and plume trajectory, and they did not explicitly illustrate the impact of scaling distortion on different parameters (e.g., plume rise) involved in dispersion process of a buoyant plume. Therefore, in order to have a detailed understanding on the laboratory scaling of the dispersion from such sources, there is a need to investigate the impact of different scaling methods on dispersion parameters individually.

Motivated by this need, a systematic laboratory study has been performed, and appropriate scaling methods for urban dispersion are presented. The correct scaling of the atmospheric dispersion problems in wind tunnels and water channels requires similarity of (1) mean flow, (2) plume rise, and (3) turbulence-governed plume spreads with appropriate boundary conditions. The following sections discuss the scaling laws relevant to each of these three similarities. Section 3.12.2 gives details of scaling the flow in water channel and wind tunnels. Details of plume rise similarity are explained in Section 3.12.3. Laboratory setup and experiments used to investigate plume rise are explained in Section 3.12.4. Section 3.12.5 briefly explains the widely used Briggs (1984) plume rise model and introduces a new model that accounts for building influence on the plume rise. Plume rise model evaluation with experiments is shown in Section 3.12.6, followed by a plume rise scaling method in Section 3.12.7. Sensitivity study of the proposed technique under urban conditions is given in Section 3.12.8. Concentration scaling methods are explained in Section 3.12.9. Finally, a summary and conclusions are given in Section 3.12.10.

3.12.2 Flow Similarity

A good foundation for this analysis is the work done by Snyder (1981), where the similarity criteria for flow modeling are described. Starting with the full conservation equations of

mass, momentum, and energy, non-dimensionalizing them by characteristic length *L*, velocity *v*, angular velocity Ω_R, reference density ρ_R, and reference temperature T_R, four dimensionless parameters—Reynolds (*Re*), Rossby (*Ro*), Peclet (*Pe*), and densimetric Froude (Fr_d) number—were created (Snyder 1981).

1. $Re = UL/\nu$ is the Reynolds number representing the ratio between inertial and viscous forces, where ν is the fluid kinematic viscosity

2. $Ro = U/L\Omega_r$ is the Rossby number representing the ratio between inertial and Coriolis effects

3. $Pe = UL/K$ is the Peclet number, defined to be the rate of advection of heat by the flow to the rate of diffusion of heat, *K*, and it can be written as the product of *Re* and Prandtl number, $Pr = \nu/\alpha$, where α is the thermal diffusivity, i.e., $Pe = RePr$

4. $Fr = U/(g\,L\,\Delta T/T_0)^{1/2}$ $Fr = U/\left(\frac{gL\Delta T}{T_0}\right)^{1/2}$ is the Froude number, showing the ratio of inertial and buoyancy forces. Here ΔT is temperature difference, T_0 is reference temperature, and *g* is gravitational acceleration.

Satisfying these four dimensionless numbers with appropriate boundary conditions will result in similar flow characteristics for the model and the field. However, duplicating all these dimensionless numbers is impossible; thus, some of them must be relaxed at the expense of satisfying the others. For practicality, for scales less than 5 km (Mery 1969), Ro similarity can be neglected as the Coriolis effect is relatively small and results in significantly large Ro. Townsend (1956) has also shown that in the absence of Coriolis and thermal effects, turbulent structure of flow is similar for all sufficiently high *Re*, except for very small-scale turbulent structures with sizes comparable to Kolmogorov-length scale. In terms of scaling the dispersion of elevated releases, Reynolds independency has to be satisfied for both the ambient flow and the efflux from the stack. Sustaining the *Re* independency at the stack exit will be further explained in Section 3.12.7.

Since Pe is expressed as the product of the *Re* and Prandtl (*Pr*) number, for sufficiently high *Re* numbers, the flow is also independent of Pe number. This independence is easier to achieve in a water channel than a wind tunnel, since the *Pr* of water (≈ 7) at room temperature is nearly one order of magnitude larger than *Pr* of air (≈ 0.7). This leaves us with

Fr as the only parameter left to be matched to achieve dynamic flow similarity, which is not very difficult.

In addition to the above-mentioned similarity criteria, specifying the correct boundary conditions is necessary for correct flow scaling. Due to the no-slip condition at the solid boundaries, flow velocity and all of its moments are zero at the boundaries. Hence, satisfying the geometrical similarity by reproduction of associated obstacles, buildings, etc. (undistorted replicas), would be necessary to satisfy the velocity boundary condition (Snyder 1972, 1981). Jensen (1958) has suggested that geometrical details with sizes smaller than the roughness length (z_0) have very little effect on the overall flow. Therefore, geometric similarity is only required for geometries larger than the height of the roughness length, and is not necessary for the details below this scale.

Flow adjacent to smooth boundaries is not *Re* independent and is dominated by viscous stresses. The presence of surface irregularities larger than the thickness of the viscous sub-layer induces a flow resistance, which is caused by the pressure gradient across the obstacle and not the viscous stresses (Snyder 1981). This feature allows the flow to be *Re* independent. Since atmospheric flows are always turbulent, over-roughening of the laboratory surface might be necessary to satisfy the *Re* independence criterion and produce turbulent flows near all surfaces.

In addition to geometrical similarity, atmospheric boundary conditions, such as (1) surface temperature distribution; (2) upstream distribution of mean and turbulent (*rms*) velocities; (3) upstream distribution of mean and turbulent (*rms*) temperatures; (4) mixing layer height; and (5) near-zero pressure gradient aloft the boundary layer should also be satisfied in order to achieve full similarity of atmospheric flow in the laboratory scales (Meroney 1998). Details of atmospheric boundary layer simulations can be found in Snyder (1972), Meroney et al. (1975), and Meroney (1998). The following section describes the criteria involved in the similarity of plume rise.

3.12.3 Plume Rise Similarity

Plume rise plays an important role in determining the ground-level concentrations associated with low-level buoyant sources. Realistic modeling of plume rise is critical for DG sources because one way of increasing the efficiency of a DG is by capturing the waste heat from its exhaust, which results in reduced plume rise and increased ground-level concentrations. Formulation of plume rise in current dispersion models such as AERMOD (Cimorelli et al. 2005) is designed primarily for elevated emissions from large power plants (Briggs 1984; Weil 1988), and does not account for the effects of multiple surrounding buildings on buoyant emissions from low-level sources, where updrafts and downdrafts induced by buildings have significant effects. Some of the modern dispersion models such as AERMOD-PRIME (Schulman et al. 2000) and ADMS (Carruthers et al. 1994) include effects of vertical wind shear and streamline ascent and descent on plume rise and dispersion near buildings.

These models have been extensively evaluated using different wind tunnel and field data sets (Robins et al. 1997a; Carruthers et al. 1999; Schulmann et al. 2000). Although the

building effect modules in these models (Robins et al. 1997b; Schulman et al. 2000; Robins and McHugh 2001) are designed to be generic, they compute the dispersion and plume rise from sources near isolated large buildings or an effective building representing a group of closely spaced blocks, which is not always the case in urban areas. Hence, they do not describe the plume rise within complex urban morphology, which requires information on the flow field affected by surrounding buildings near the stack. In order to clarify these effects, a systematic laboratory study was conducted in the water channel facility described in Section 3.12.4.

3.12.4 Laboratory Experiment

Using the PIV system, flow velocities in the water channel for the pump frequency of 17.5 Hz were measured. Profiles of the mean horizontal (v) and vertical (w) velocities, together with their standard deviations (σ_v and σ_w) and the shear stress (τ), are shown inFigure 3-11.

Figure 3-11: Profiles of Ambient Mean

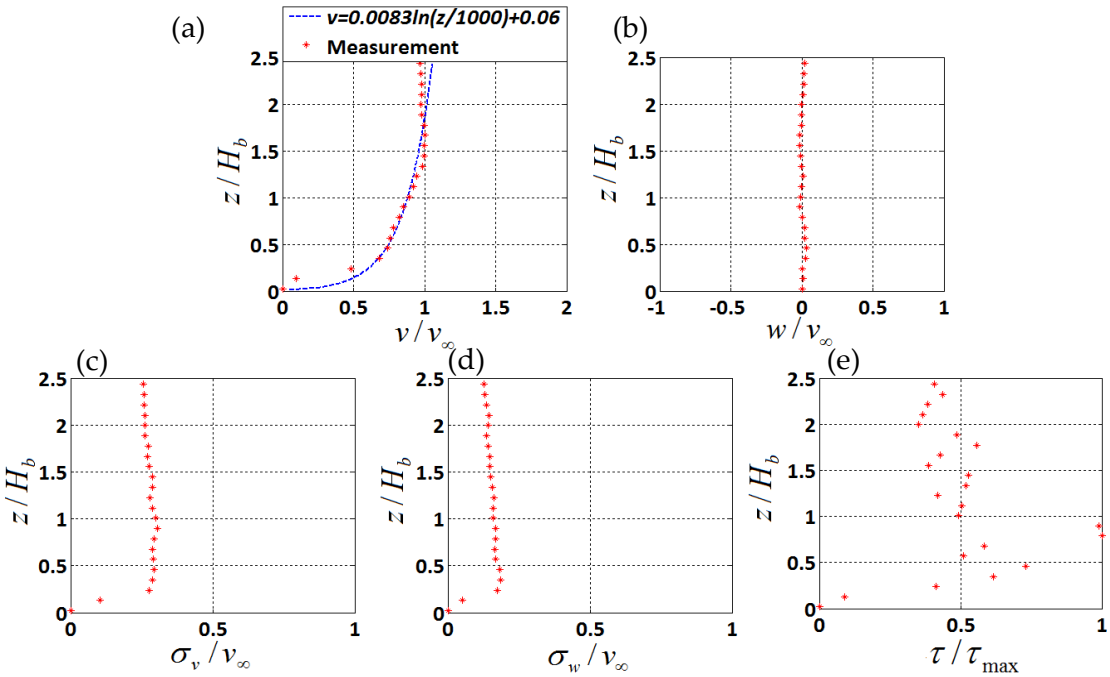

(a) Horizontal v (m/s) and (b) Vertical w (m/s) Velocities; Standard Deviations of (c) Horizontal σ_v (m/s) and (d) Vertical σ_w (m s^{-1}) Velocities; and (d) Mean Shear Stress τ (newtons per square meter, Nm^{-2}). Dashed blue line represents the logarithmic wind profile. Vertical distance z and velocities are normalized with respect to building height H_b = 0.07 m and free stream horizontal velocity (v_∞= 0.045 ms^{-1}). Shear stress (τ) is normalized with respect to the maximum shear stress of $\tau_{\max} = 0.03\, Nm^{-2}$.

Distances, velocities, and shear stresses are normalized with respect to building height (H_b = 0.07 m), horizontal free stream velocity (v_∞ = 0.045 m s^{-1}), and maximum shear stress of $\tau_{\max} = 0.03\, N\, m^{-2}$, respectively. It can be seen that the vertical profile of horizontal wind speed matches well with the logarithmic wind profile, especially for heights up to 2.5 H_b. Vertical profiles of standard deviation of horizontal and vertical velocities (σ_v and σ_w) and the shear stress (τ) are maintained almost constant with a slight peak at 0.5H_b from the ground.

To investigate plume rise associated with low-level buoyant sources, a DG building from Palm Springs, California (L × W × H =$15\,m \times 15\,m \times 7\,m$) with stack height ($H_s$) of 9.3 m above ground level (2.3 m above roof level) was modeled in the water channel at a scale of 1:100. It should be mentioned that the laboratory study shown in this chapter does not represent the scaled problem from the Palm Springs field study (Jing et al. 2010), except for the DG geometry. In this set of laboratory experiments, the field wind speeds of ≈ 3 m s^{-1} and stack exit velocity of

≈ 12.5 m s^{-1} were simulated in the water channel. The reference Reynolds number, based on the free stream velocity (v_∞) and characteristics building frontal length scale, H_b^* (length scale based on the obstacle frontal area; $H_b^* = (WH)^{1/2}$) was $Re = 4600$, which is sufficient to satisfy Reynolds number independency criteria of $Re \approx 4{,}000$ (Halitsky 1968; Fackrell and Pearce 1981; Snyder 1981; Yee et al. 2006). However, a study by Robert Meroney and David Neff at Colorado State university (private communication) showed that this criteria ($Re \approx 4{,}000$) is limited only to flow around cubical buildings oriented perpendicular to the wind direction and sources located in the near wake of the building. Given the complexities involved with flow around different building shapes and orientations, they suggested $Re \geq 15{,}000$ for model simulations. Since in this study the team are utilizing a cubical building oriented normal to the flow direction, the team consider that the $Re \geq 4{,}000$ is sufficient to satisfy Reynolds number independency criteria. In addition, the Lego blocks with sufficiently rough surfaces help the flow to become Reynolds number independent.

A fluorescent dye, Uranine, is used as the tracer dye for plume visualizations because of its high light sensitivity in the range of visible light. Uranine has a very low molecular diffusivity; hence, the corresponding Schmidt number is relatively large ($Sc \approx 2{,}000$). Due to high Re, turbulence will be the leading mechanism in dispersing the tracer dye, and the molecular diffusivity will serve as a smoothing mechanism for small-scale concentration discontinuities (Snyder 1972). Therefore, due to the turbulent nature of the flow, the matching of Sc number to the field is not required. Desired plume buoyancies are achieved by mixing the tracer dye with water and alcohol (specific gravity $SG = 0.8$). Another way to simulate buoyant emissions would be to use an inverted experimental setup and release a salt-water solution at the top of the channel (e.g., Contini and Robins 2001, 2004). Images of the dyed plume were captured using long exposure imaging. This technique gives us averaged plume behavior, which is used to measure the plume rise under different buoyancies, flow conditions, and building geometries. Experiments were repeated for at least three times and in several instances up to four and five times. The root mean squared error (Contini et al. 2011; RMSE = $\sqrt{\sum\left(h_p - \overline{h_p}\right)^2 / N}$, where h_p and $\overline{h_p}$ are the observed and mean values of plume rise, respectively, and N is the number of data points) was less than 5 percent of the mean plume rise for all of the experiments.

Plume rise has been measured under two different buoyancies ($SG = 0.98$ and 0.96). These plume buoyancies were selected in order to observe how a major increase in buoyancy can alter the effect of buildings on plume rise (buoyancy associated with tracer of $SG = 0.96$ is equivalent to two times that of a tracer with $SG = 0.98$, since the buoyancy is proportional to $1-SG$). Table 3-2 shows the details of the experimental conditions.

Table 3-2: Experimental Parameters for Plume Rise Measurements

Parameters	Value
Free stream horizontal velocity (v_∞)	0.045 m s^{-1}
Re (based on H_b^*)	4,600
Internal Diameter of the stack (*D*)	3×10^{-3} m
Stack exit velocity (V_s)	0.19 m s^{-1}
Stack exit Reynolds number (Re_s)	570
Average vertical turbulent velocity (σ_w)	0.0056 m s^{-1}
Vertical turbulent intensity of flow ($I_z = \sigma_w/v$)	~0.12-0.14
Surface friction velocity (u_*)	0.0034 m s^{-1}
Roughness length of Lego blocks (z_0)	~6×10^{-4} m
Plume specific gravity (*SG*)	0.96 and 0.98

Next, these plume rise measurements were compared with Briggs' (1984) plume rise equation and a numerical plume rise model, which are explained next.

3.12.5 Plume Rise Model

The Briggs (1984) plume rise model,

$$h_p = \left(\frac{3}{2\beta^2} \frac{F_b x^2}{v^3} + \frac{3}{\beta^2} \frac{F_m x}{v^2} \right)^{1/3}, \qquad (3\text{-}2)$$

was derived by solving the mass, momentum and energy conservation equations analytically, assuming a bent-over plume released in a neutrally stratified atmosphere with a constant horizontal wind speed (*v*), where no updrafts and downdrafts exist. Due to the vigorous mixing that occurs in the daytime urban boundary layer, the potential temperature gradient just above the roof level is close to zero (Cermak et al. 1995). Thus, the neutral stability assumption for simulating the daytime plume rise using Briggs (1984) is mostly valid. Here $\beta \sim 0.6$ (Hoult and Weil 1972) is the entrainment parameter; F_b and F_m are the buoyancy and momentum flux parameters, respectively, expressed as,

$$F_b = g b_0^2 V_s \left(\frac{T_p - T_0}{T_p} \right) \quad \text{, or} \quad F_b = g b_0^2 V_s \left(\frac{T_p - T_a}{T_p} \right)$$

(0-1)

$$F_m = b_0{}^2 V_s^2 \left(\frac{T_p}{T_0} \right), \quad \text{or} \quad F_m = b_0{}^2 V_s^2 \left(\frac{T_p}{T_a} \right)$$

(0-2)

where b_0 is the radius of the stack, V_s is the stack exit velocity, T_p is the temperature of the exhaust plume, and T_a is the ambient temperature. Although widely used, this simple model has no capability to incorporate building influence.

As explained earlier, plume rise and dispersion modules in AERMOD-PRIME (Schulman et al. 2000; Cimorelli et al. 2005) and ADMS (Carruthers et al. 1994; Robins et al. 2005) can only account for the effects of isolated buildings and do not describe the plume rise within complex urban morphology (Pournazeri et al. 2012a). To account for the effects of complex flows induced by surrounding buildings on the plume rise, a numerical plume rise model has been developed. The starting point of this model is the plume rise governing equations by Hoult et al. (1969), where the plume is assumed to be slender and continuous with a circular cross section and uniform properties within the plume (Contini et al. 2011). These equations are the modified version of the plume rise model by Morton et al. (1956), where the classical theory of the Boussinesq plume was established. These governing equations were derived for the case of horizontal wind speed only. Therefore, modifying these equations and re-deriving them, by assuming that wind speed has both vertical and horizontal components, allows us to account for the effect of updrafts/downdrafts induced by buildings. Similar concepts to account for building effects are used in the ADMS (Robins et al. 1997a) and AERMOD-PRIME (Schulman et al. 2000) building modules. Figure 3-12 shows schematics of the plume rise and the parameters involved.

Figure 3-12: Schematic for Plume in a Two-Dimensional Flow

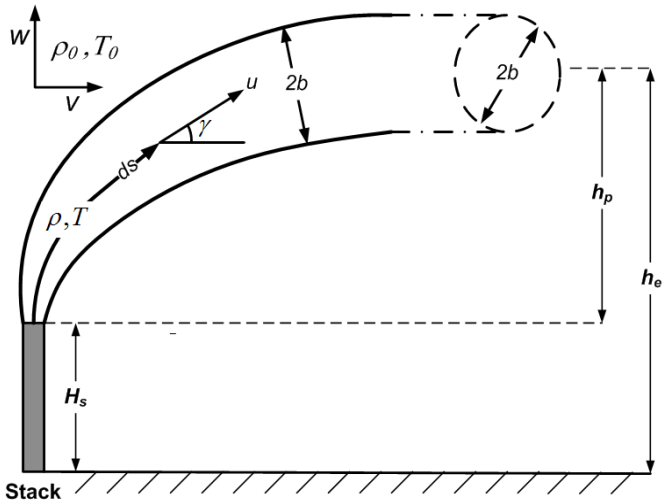

Here, *u* is the velocity of the plume along its centerline, *v* and *w* are the horizontal and vertical ambient velocities, *s* is along the centerline coordinate, γ is the plume centerline inclination, *b* is the averaged plume radius, ρ is the plume density, *T* is the plume absolute temperature, H_s is the height of the stack, h_p is the plume rise, and h_e is the actual plume height.

The modified governing equations are:

Conservation of mass flux

$$\frac{d}{ds}(\pi b^2 u\rho) = 2\pi b\rho_0\left[\alpha\left|u - v\cos(\gamma) - w\sin(\gamma)\right| + \beta\left|v\sin(\gamma) - w\cos(\gamma)\right|\right]$$

(0-3)

Conservation of momentum flux: along the plume centerline

$$\frac{d}{ds}(\pi b^2 u^2\rho) = \left(v\cos(\gamma) + w\sin(\gamma)\right)\frac{d}{ds}(\pi b^2 u\rho) + (\rho_0 - \rho)\pi b^2 g\sin(\gamma)$$

(0-4)

Conservation of momentum flux: normal to the plume centerline

$$\pi b^2 u^2\rho\frac{d\gamma}{ds} = -\left(v\sin(\gamma) - w\cos(\gamma)\right)\frac{d}{ds}(\pi b^2 u\rho) + (\rho_0 - \rho)\pi b^2 g\cos(\gamma)$$

(0-5)

Conservation of buoyancy flux

$$\frac{d}{ds}(\pi b^2 u(\rho - \rho_0)g) = -\pi b^2 u\rho_0\left(\frac{g}{\theta_a}\frac{d\theta_a}{dz}\right)\sin(\gamma)$$

(0-6)

where ρ is the plume density, ρ_0 is the density of the ambient air, u is the velocity of the plume centerline, v and w are the horizontal and vertical ambient velocities, θ is the plume centerline inclination, and θ_a is the ambient potential temperature. As reported by Hoult and Weil (1972), the entrainment coefficients $\beta = 0.6$ and $\alpha = 0.11$ are independent of plume parameters for a fully turbulent plume. Contini et al. (2011) showed that the entrainment coefficient α, corresponding to the horizontal velocity difference between the plume and ambient flow, does not have significant impact on the performance of this model. One needs to keep in mind that these governing equations are derived based on assumptions (such as Boussinesq plume), which might not be necessarily valid for all different plume conditions (e.g., dense gas plumes).

After solving equations 3-5 through 3-8 numerically for b, u, ρ, and θ as function of s (distance on the plume centerline), the plume rise h_p and distance x associated with it can be calculated as

$$h_p = \int_0^s \sin(\gamma) ds \tag{3-9}$$

$$x = \int_0^s \cos(\gamma) ds \tag{3-10}$$

In this model, the influence of updrafts and downdrafts induced by buildings on the plume rise is taken into account through the measured velocity (v and w) field (Figure 3-13b). Velocity field was measured at the centerline of the building without the plume in place (see the schematic in Figure 3-13a).

Figure 3-13: (a) Schematic of PIV Measurement Setup. (b) Averaged Velocity Field over 180 Images Measured Using PIV System (the dark blue vector lines show the velocity of less than 1 cm/s and the dark red vector lines show the velocity equal/above 5 cm s^{-1}), (c) Versus Normalized Downwind Distance from the DG Building at z = Hb, and (d) Versus Normalized Vertical Distance above the Ground Level Next to the Lee Wall of the Building.

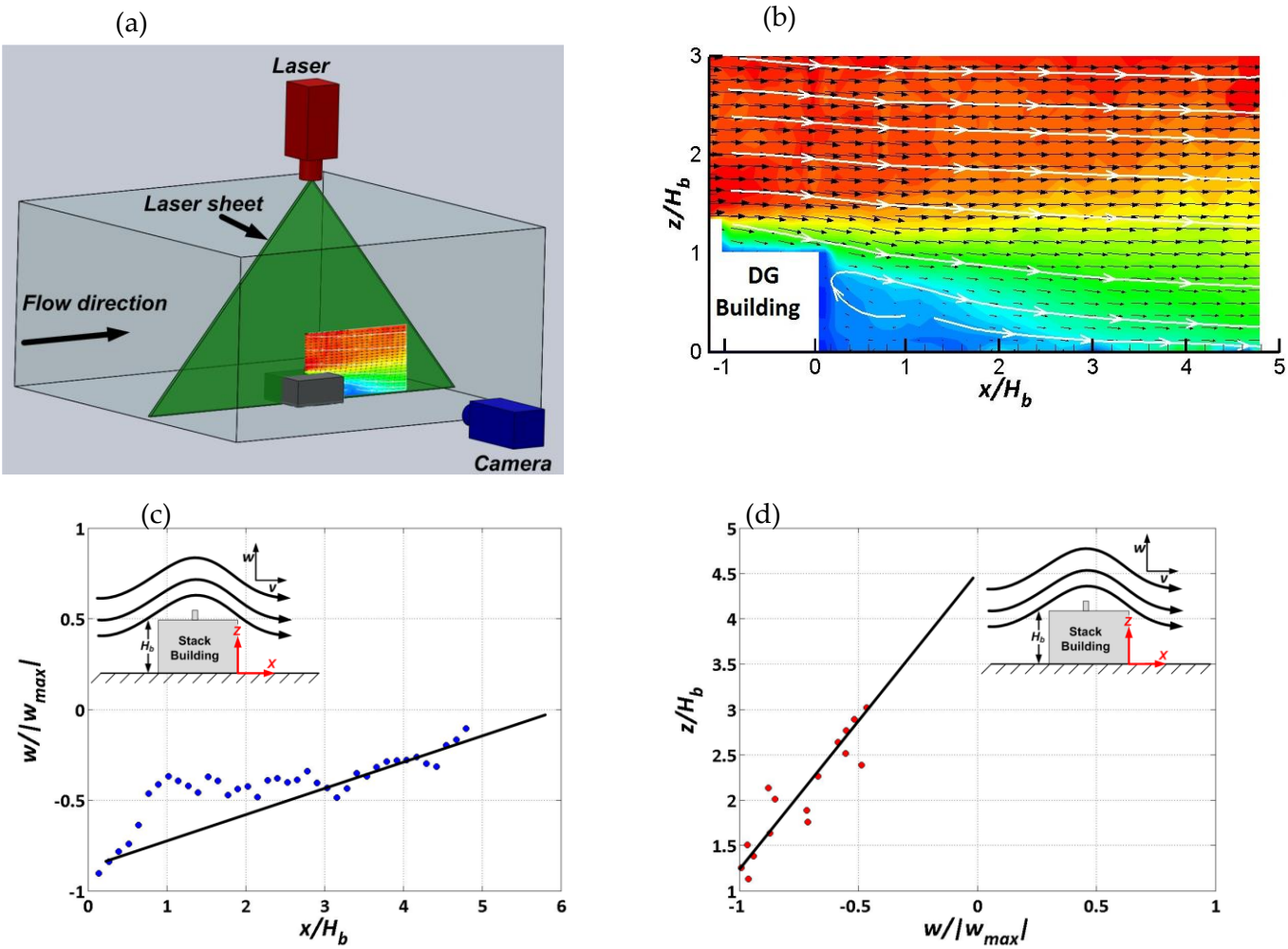

Streamlines are calculated using a commercial plotting software package (TECPLOT 10). This software plots the streamlines by interpolating the velocity between the grid points. Normalized measured downdraft velocity, w/|wmax| (wmax = 4.5×10^{-3} ms^{-1} is the maximum downdraft velocity, measured at the lee wall of the building at z = Hb, where Hb is the building height) is presented

The reference wind speed is v_∞= 0.045 ms^{-1}.

For these experiments, due to relatively high ambient velocity, the flow perturbation by the plume was not significant. In addition, since the team modeled the DG using Lego blocks with relatively large roughness length of ≈ 0.6 mm, the flow at the rooftop is highly perturbed, and once separated at the leading edge, it quickly re-attaches. Furthermore, the presence of a 3 mm diameter stack on the rooftop further contributes to the flow perturbation and causes the separated flow to re-attach rapidly. In another study (Princevac et al. 2010), PIV measurements of flow around modeled buildings made of highly polished acrylic cubes do show separation, starting from the leading edge of the building rooftop. Figure 3-13 c-d shows the downdraft velocities measured downstream and above the DG model in the water channel. From Figure 3-13 c-d, it can be assumed that downdraft velocity decays almost linearly to zero within approximately 6 building heights (H_b) downwind of the building and 3.5 H_b above the rooftop of the building. In addition, due to the solid surface boundary condition, downdraft velocity becomes zero at the ground level ($z = 0$). This is modeled as

$$w(x,z) = w_{\max}\left[1-\left|\frac{z-H_b}{\lambda_1 H_b}\right|\right].\left[1-\frac{x}{\lambda_2 H_b}\right] \text{ for } x \le \lambda_2 H_b \text{ and } z \le (\lambda_1+1)H_b \quad , \qquad (3\text{-}11)$$

where $\lambda_1 = 3.5$, $\lambda_2 = 6$, and $w_{\max} = -4.5\times10^{-3}$ (m s^{-1}) is the maximum downdraft velocity which occurs on the lee wall of the building ($x = 0$) near the rooftop ($z = H_b$). Note that equation 3-11 describes the downdraft velocity for the particular case considered in this study and might not apply to all building configurations and wind directions. However, similar interpolation for the downdraft velocity can be made for other building and flow conditions.

In addition to the above-mentioned properties, this model also accounts for the effect of ambient turbulence. It is assumed that, at large distances where the entrainment due to the horizontal and vertical velocity difference between plume and ambient becomes relatively small, the entrainment process is dominated by the plume growth due to ambient turbulence (Schulman et al. 2000). As per Schulman et al. (2000), this effect can be modeled as

$$\frac{d}{ds}(\pi b^2 u\rho) = \max\left[\frac{d}{ds}(\pi b^2 u\rho)_{entrainment}\,,\, 2\pi b\rho_0 v\left(\frac{db}{ds}\right)_{amb.\ \text{turb.}}\right], \qquad (3\text{-}12)$$

where

$$\left(\frac{db}{ds}\right)_{amb.\ \text{turb.}} = \sqrt{\frac{\pi}{2}}\frac{\sigma_w}{v}. \qquad (3\text{-}13)$$

This effect is negligible for distances close to the stack with relatively small turbulent intensities (σ_w/v). However, in cases with relatively high turbulent intensities, ambient turbulence can reduce the plume rise at large distances.

3.12.6 Comparison of Models and Experiments

Figure 3-14 shows the comparison between Briggs' (1984) plume rise formulation (equation 3-2) and the numerical solution of equations 3-5 through 3-8 (with vertical velocity given by equation3-11), together with the results from the plume rise measurements in the water channel Figure 3-14a and Figure 3-14c show the recorded averaged plume. Plume rise was measured by determining the location of the plume centerline in these images. As can be seen in Figure 3-14b and Figure 3-14d, Briggs' (1984) formulation tends to overestimate the plume rise, as it cannot account for the downdraft velocities induced in the near-wake region of the building. This causes the plume to rise more slowly even though the maximum downdraft velocity is relatively small ($|w_{max}/v| \sim 0.1$, where v is the horizontal wind speed measured at $z = H_b$ at the lee wall of the building). As shown in Figure 3-13, downdraft velocity decays with height from the rooftop of the building. Therefore, the higher the plume rises, the less effect downdrafts have on plume rise. This effect can be observed in Figure 3-14 as the buoyancy is increased from $SG = 0.98$ to $SG = 0.96$, the discrepancy between plume rise predicted by Briggs (1984) and measured plume rise becomes smaller.

Figure 3-14: (a) and (c) Show the Plume Visualization for Modeled DG Source (geometric scaling ratio of 1:100) with Buoyant Emissions of Different Specific Gravity (*SG*): (a) *SG* = 0.98, (c) *SG* = 0.96. (b) and (d) Show Comparisons between the Plume Rise Observations (▲); Briggs (1984) plume rise formulation (red—); and numerical plume rise model (blue—): (b) *SG* = 0.98, (d) *SG* = 0.96.

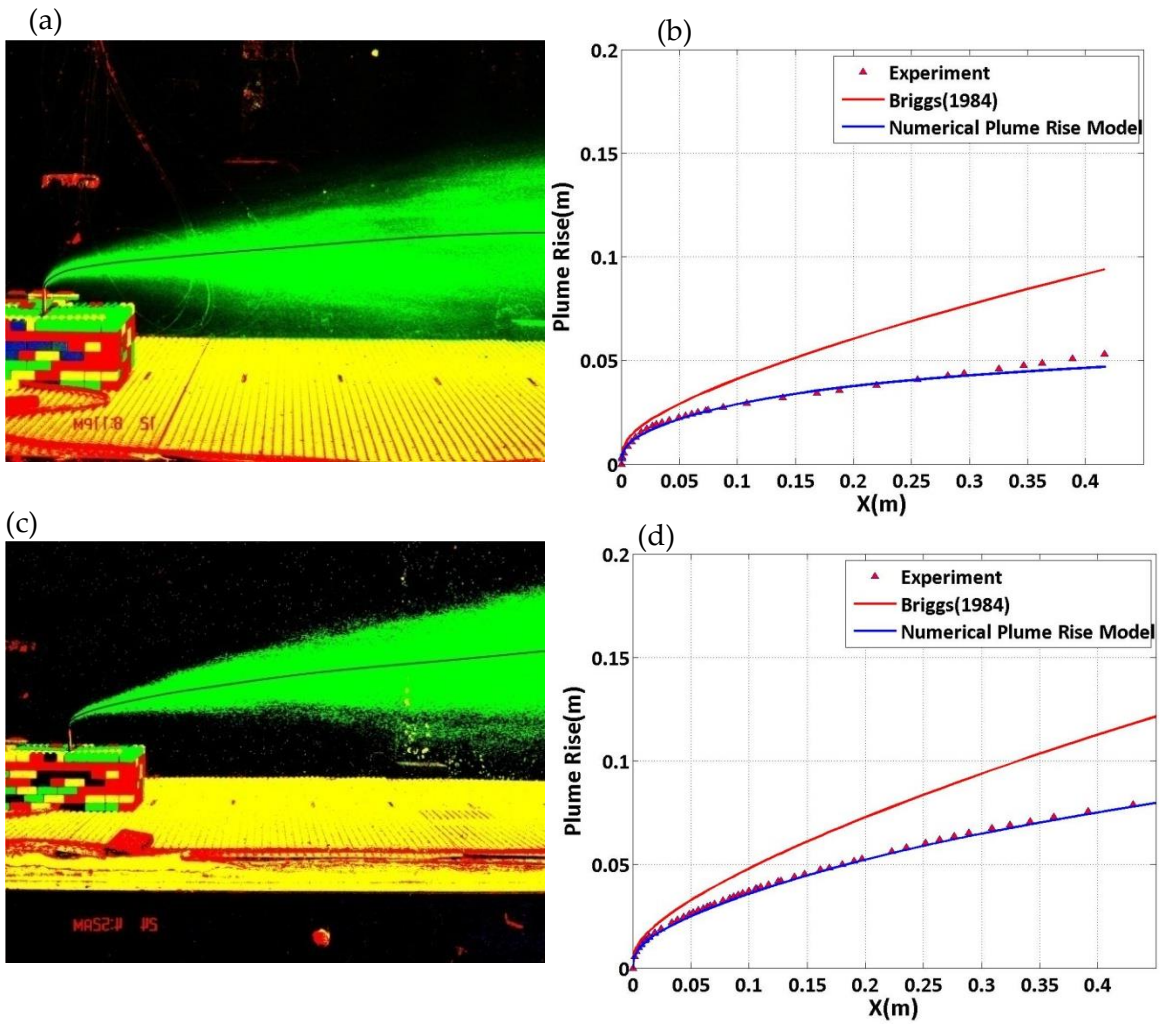

However, by accounting for flow modifications induced by the building in a vertical direction, the numerical plume rise model produces an accurate prediction of the plume rise in the water channel. Although the flow downstream of the building is three-dimensional, flow features in a lateral direction do not influence the plume rise significantly. Thus, accounting only for the flow in horizontal (along the stream) and vertical direction is sufficient to predict the plume rise. These results show the performance of the model at distances close to the stack, but do not provide a description of model performance at large distances from the stack, where the variation of wind speed and plume parameters become significant along the plume width and depth.

Different plume rise scaling methods are described in the next section.

3.12.7 Plume Rise Scaling

There are several scaling methods of plume rise explained in the literature (Isyumov and Tanaka 1979; Robins 1980; Snyder 1981; Obasaju and Robins 1998; Robins 2003) that are derived from the mass, momentum, and energy conservation laws. Robins (1980) and Obasaju and Robins (1998) evaluated different plume rise scaling methods for isolated stacks and concluded that by relaxing the initial density ratio and matching the non-dimensional buoyancy and momentum flux parameters, plume rise can be accurately scaled from the field to the laboratory. However, all these methods were only evaluated for plume rise from isolated stacks where the effect of surrounding buildings can be neglected, but the team has already shown that plume rise is significantly affected by updrafts and downdrafts caused by the surrounding buildings. Therefore, using the plume rise governing equations that account for the building effects, the team reconstructed the complete scaling method. These equations (3-5 through 3-8) are now used to develop appropriate scaling.

Non-dimensionalizing equations (3-5 through 3-8) with respect to ambient density ρ_0, ambient velocity v, and stack radius b_0 results in

$$\frac{d}{ds^*}(\pi b^{*2}u^*\rho^*) = 2\pi b^*\left[\alpha\left|u^* - \cos(\gamma) - \left(\frac{w}{v}\right)\sin(\gamma)\right| + \beta\left|\sin(\gamma) - \left(\frac{w}{v}\right)\cos(\gamma)\right|\right] \tag{3-14}$$

$$\frac{d}{ds^*}(\pi b^{*2}u^{*2}\rho^*) = \left(\cos(\gamma) + \left(\frac{w}{v}\right)\sin(\gamma)\right)\frac{d}{ds^*}(\pi b^{*2}u^*\rho^*) + \frac{gb_0}{v^2}(1-\rho^*)\pi b^{*2}\sin(\gamma) \tag{3-15}$$

$$\pi b^{*2}u^{*2}\rho^*\frac{d\gamma}{ds^*} = -\left(\sin(\gamma) - \left(\frac{w}{v}\right)\cos(\gamma)\right)\frac{d}{ds^*}(\pi b^{*2}u^*\rho^*) + \frac{gb_0}{v^2}(1-\rho^*)\pi b^{*2}\cos(\gamma)$$

$$\pi b^{*2}u^{*2}\rho^*\frac{d\theta}{ds^*} - \left(\sin(\theta) - \left(\frac{w}{v}\right)\cos(\theta)\right)\frac{d}{ds^*}\left(\pi b^{*2}u^*\rho^*\right) = \frac{gb_0}{v^2}\left(1-\rho^*\right)\pi b^{*2}\cos(\theta) \tag{3-16}$$

$$\frac{d}{ds^*}(\pi b^{*2}u^*(\rho^*-1)) = -\pi b^{*2}u^*\left(\frac{1}{\theta_a}\frac{d\theta_a}{dz^*}\right)\sin(\gamma), \tag{3-17}$$

where $b^* = b/b_0$, $u^* = u/v$, $\rho^* = \rho/\rho_0$, $s^* = s/b_0$, $z^* = z/b_0$.

Three dimensionless numbers appeared in the non-dimensionalized governing equations (3-14 through 3-17). Except for the ratio between the vertical and horizontal velocities (w/v), all of the other parameters can also be found by non-dimensionalizing the plume rise governing equations in Hoult et al. (1969). Although detailed description of these dimensionless parameters can be found in the literature, the team briefly discuss them here.

The first dimensionless parameter is $1/\theta_a \cdot (d\theta_a/dz^*)$, which is a measure of the background atmospheric stability, and needs to be matched in both model and field. Following the similarity of flow and atmospheric boundary layer described in Section 3.12.2, this parameter is matched automatically for stable and convective boundary layers. For the neutral atmospheric stability condition, this parameter is equal to zero in both the model and field. The second dimensionless parameter is the ratio between the vertical and horizontal velocities (w/v). Per the flow similarity explained in the previous section, by satisfying the Reynolds independence criterion and applying correct boundary conditions, the ratio of the vertical velocity to the horizontal velocity at all locations will be automatically matched in the model and field. The third dimensionless parameter is gb_0/v^2, which is half the inversed square of the Froude number ($v/\sqrt{gD}$, where $D = 2b_0$). To match this single parameter in the model and field, the velocity scale ratio should be equal to the square root of the geometrical scaling ratio.

As also discussed by Meroney (1986b), and Robins (2003), even for cases where wind speeds (v) in the field are relatively high (≈ 5 ms^{-1}), a typical geometrical scaling ratio, such as 1:400, would yield exceptionally low flow velocities in the model (in this case ≈ 0.25 ms^{-1}), which are not easy to manage in wind tunnels. These low-flow velocities introduce difficulties concerning the *Re* independency criteria (Meroney 1986b). In the water channel, due to the higher flow control capabilities, matching the Froude number is not difficult in most cases. Since kinematic viscosity (ν) of water at room temperature (≈10^{-6} $m^2 s^{-1}$) is approximately 10 times smaller than that of air (≈10^{-5} $m^2 s^{-1}$), it is easier to satisfy the *Re* independency criteria in a water channel, even under low-flow velocities.

In addition to the Froude number, the similarity of initial conditions at the stack exit should also be satisfied by matching the initial magnitudes of b^*, u^* and ρ^*, in the model and field. As the magnitude of b at the stack exit is equal to b_0, b^* will be unity at the stack exit in both the field and model, which means that the initial value of b^* is automatically matched. This leaves us with matching the initial values of u^* and ρ^* at the stack exit.

At the stack exit, u^* is equal to the ratio of the stack exit velocity V_s to the ambient velocity v (V_s/v), characterizing the jet (momentum) behavior of the plume. This behavior has been the subject of numerous theoretical and laboratory studies. Hoult and Weil (1972) have defined $R = V_s / v$ as the speed ratio in order to define the region of the plume governed by the initial momentum. Davidson and Slawson (1967) have shown that for distances x where $R << g(\Delta\rho/\rho_0)(x/v^2)$ ($\Delta\rho = \rho_0 - \rho_p$, where ρ_p is the exhaust plume density), the effect of

initial momentum can be neglected and plume rise becomes buoyancy dominated. Barilla (1968) has shown that for $R \leq 2$ in non-buoyant plumes and $R \leq 1$ in buoyant plumes, the entrapment of plume in the cavity produced by the stack or buildings (known as downwash) may occur. The downwash effect has also been investigated by Fay et al. (1970), and it has been observed that in industrial chimneys this effect happens for $R \leq 1.25$ (Hoult and Weil 1972). Wind tunnel simulation by Snyder and Lawson (1991) has also shown that downwash occurs for $R \leq 1.5$ when *Re* is smaller than critical Reynolds number of $Re_c = 2 \times 10^5$ and happens for $R \leq 1.1$ when $Re \geq Re_c$. Therefore, different values of speed ratio would yield different near source plume behavior.

The initial value of ρ^* is equal to the ratio of the exhaust plume density ρ_p to ambient density ρ_0, presenting a measure of the non-Boussinesq effect. Non-Boussinesq effects arise when the difference between the plume density and ambient density at the source is significantly large compared to the reference (ambient) density ρ_0 (Carlotti and Hunt 2005). This effect may have a significant impact on the shape of the plume over a distance z_s above the source, as the entrainment velocity is a function of the plume to ambient density ratio (Ricou and Spalding 1961). This distance (z_s) may be as large as 0.3 m for smoke plumes produced by small fires in buildings ($T \sim 400^\circ C$) and extends to several kilometers in large volcanic eruptions ($T \sim 2{,}200^\circ C$) (Woods 1997). Since temperatures are usually within $150 - 500^\circ C$ in the team's case, the non-Boussinesq effects would not play a major role, except very close to the source, and the motion will quickly converge to that of the Boussinesq plume.

As a result, three scaling factors associated with plume rise can be expressed as

$$\left(\frac{gb_0}{v^2}\right)_m = \left(\frac{gb_0}{v^2}\right)_f \tag{3-18}$$

$$\left(\frac{V_s}{v}\right)_m = \left(\frac{V_s}{v}\right)_f \tag{3-19}$$

$$\left(\frac{\rho_p}{\rho_0}\right)_m = \left(\frac{\rho_p}{\rho_0}\right)_f, \tag{3-20}$$

where the subscripts m and f denote model and field, respectively.

Satisfying the above-mentioned parameters will result in correct similarity of plume rise. These parameters were also reported by Isyumov and Tanaka (1979), Robins (1980), Snyder (1981), and several other studies, as required criteria for accurate scaling of near/far field plumes.

Following equations 3-18 through 3-20 and satisfying the geometric similarity (required for similarity of the flow) as,

$$\left(\frac{H_s}{b_o}\right)_f = \left(\frac{H_s}{b_o}\right)_m, \qquad (3\text{-}21)$$

laboratory plume rise can be scaled back to the field through equation (3-22, which is obtained by non-dimensionalizing equations (3-9 and (3-10 with respect to stack height (H_s) as

$$\left(\frac{h_p(x^*)}{b_o}\right)_m = \left(\frac{h_p(x^*)}{b_o}\right)_f, \qquad (3\text{-}22)$$

where h_p is the plume rise and x^* is the dimensionless distance from the source ($x^* = x/H_s$ $x^* = x/b_0$).

As explained in Section 3.12.4, in the water channel, plume buoyancies are achieved by mixing the tracer dye with water ($SG = 1$) and alcohol ($SG = 0.8$); thus, the maximum achievable buoyancy is associated with the mixture of dye with pure alcohol ($SG = 0.8$). Therefore, in addition to difficulties associated with satisfying the Froude number criteria, for very hot plumes with temperatures (T_p) higher than 460 K (i.e., $\rho_p/\rho_a \leq 0.8$), it becomes difficult to satisfy the density condition (equation) in the water channel. Further increases in buoyancy, up to $SG = 0.76$ can be achieved by using heated alcohol (at a boiling temperature of $T = 65°C$). It is also possible to use salty water in the water channel, and by injecting heated alcohol achieve $SG = 0.74$ (for salty water of $\rho_0 = 1.025$ kg m^{-3}), which is a 30 percent increase in buoyancy (1-SG) compared to that of pure alcohol at room temperature (SG = 0.8). However, since a buoyancy increase of 75 percent (for T_p = 460 K) to 250 percent (for T_p = 1,000 K) is required, this is not large enough. Additionally, this would introduce additional uncertainty (heat loss from the hot alcohol during its pumping from the beaker to the source inside the water channel) and risk causing corrosion due to the water salt mixture in the channel. Similar to Robins (1980), in order to achieve similarity for the case of high buoyancy and low ambient velocity, the team relaxes the Froude number and define a similarity

criteria where the team matchs the initial values of $gb_0/v^2(1-\rho^*)$ $gb_0(1-\rho^*)/v^2$ (this parameter appears in equations 3-15 and 3-16 in the model and the field. This parameter is half the inversed square of the densimetric Froude number ($v/\sqrt{g'D}$ where $g'=g\Delta\rho/\rho_0$). Therefore, this similarity can be expressed as,

$$\left(\frac{gb_0}{v^2}\frac{\Delta\rho}{\rho_0}\right)_m=\left(\frac{gb_0}{v^2}\frac{\Delta\rho}{\rho_0}\right)_f, \qquad (3\text{-}23)$$

where $\Delta\rho=\rho_a-\rho_p$.

Although not necessarily needed, keeping a constant velocity scaling ratio (due to the constraints imposed by the *Re* independency criteria and water channel flow control capabilities) and matching the densimetric Froude number with a higher density ratio (ρ_p/ρ_a) in the model than that in the field, yield to a larger stack diameter ($D = 2b_0$) for the model. Consequently, the Reynolds number associated with stack becomes larger compared to the case when the density ratio (ρ_p/ρ_a) in the model and field is the same. This feature allows us to choose the density ratio in the model such that the stack Reynolds number meets the Reynolds independence criterion, which states that as long as the plume is in turbulent regime at the stack exit, plume behavior is independent of the Reynolds number (Snyder 1981). Snyder (1981) reported that for buoyant plumes, the critical Reynolds number $Re = 200$, based on stack diameter, is sufficient for formation of a fully turbulent plume at the stack exit. In addition, using a higher density ratio (ρ_p/ρ_a) yields larger ratio of Peclet (based on mass diffusion) to Richardson number ($v^3/g'K_m$, where K_m is the molecular diffusivity of the tracer), which reduces the microscopic diffusion effects (Meroney 1986b). As reported by Meroney (1986b), this ratio should be larger than 1,500 for accurate simulations.

As mentioned earlier, many studies such as Robins (1980), Arya and Lape (1990), and Obasaju and Robins (1998) have used similar criteria to the densimetric Froude number as a proper scaling method in the characterization of the buoyant plume rise.

Matching this similarity criterion (equation 3-23) in the model and field would lead to satisfying the initial condition on the righthand side of conservation of momentum flux equations (equations 3-15 and 3-16), where the buoyancy force term appears. However, it would change the initial value of ρ^* on the left hand side of equations 3-14 through 3-17. Several studies by Meroney (1982, 1986a, 1986b) on wind tunnel simulation of dense gas

dispersion suggested that distorting the initial value of ρ^* in order to allow for more convenient flow velocities in the model can delay the time of arrival and departure of the model plume. Neff and Meroney (1981) have also observed that under distorted density conditions, the cloud of dense gas moves slower compared to the undistorted model. However, it needs to be mentioned that these limitations are specific to emissions heavier than air and might not necessarily hold for buoyant emissions described in this study, since the source effects persists over much longer times in dense gas plumes than in buoyant plumes. The effect of this distortion has also been investigated for plume rise from isolated tall stacks by comparing plume rise results from wind tunnel simulations (with distorted density condition) with field results (Robins 1980) and Briggs (1984) plume rise predictions (Obasaju and Robins 1998). Thus, there is a need to examine the performance of this scaling method under buoyant emissions affected by buildings. Robins (2003) illustrated the performance of similar scaling methods on building-affected plumes by investigating the ground-level concentrations. Since the plume rise is one of the major parameters that affect the ground-level concentrations, this study focused on plume rise rather than directly on concentrations. The sensitivity of plume rise to the scaling distortion is investigated next.

3.12.8 Plume Rise Similarity Sensitivity Study

To investigate the sensitivity of the plume-rise scaling method shown in the previous section, plume rise from the 650 kW distributed power generator in Palm Springs, California, was simulated using the numerical plume rise model described in Section 3.12.5. As mentioned previously, DGs are highly efficient because they recover heat from their coolant and exhaust, providing both electricity and heating/cooling to the neighborhood. Thus, for the Palm Springs DG, depending on how much heat is recovered from the exhaust, the exhaust temperature may differ between 460 K (~75 percent heat recovery) and 800 K (~20 percent heat recovery). Therefore, in this study the team has chosen four different stack temperatures, ranging from 460 K to 800 K. According to Jing et al. (2010), typical average wind speed in the Palm Springs urban area (from a sonic anemometer located at Sunrise Park in Palm Springs, on the rooftop of the DG at 11 m from the ground) is $v_f \approx 1$ m s^{-1}. Note that the sensitivity analysis presented in this section is separate from the laboratory study shown in sections 3.12.4 through 3.12.6.

By selecting $v_m = 0.045$ m s^{-1} $v_m = 0.045 m/s$ (with a velocity scaling ratio of 1:22.5), the plume rise from the Palm Springs DG has been scaled through:

1. *Scaling method 1*, by matching the Froude number (equation 3-18), initial velocity ratio (equation 3-19) and initial density ratio (equation 3-20); and
2. *Scaling method 2*, by matching the densimetric Froude number (equation 3-23), initial velocity ratio (equation 3-19) and choosing $\left(\rho_p/\rho_a\right)_m = 0.9$.

Each of these scaling methods results in a set of model parameters that include internal stack diameter (D), stack exit velocity (V_s), and plume initial density (ρ_P). These parameters (Table 3-3 and Table 3-4) are then used as the inputs to the numerical plume rise model, and the plume rise associated with each set of model parameters is calculated and then scaled to the field through equation 3-21. In addition to the results from the scaling methods, plume rise associated with the Palm Springs DG is also calculated directly from the field (non-scaled) parameters (Table 3-3). The results of these simulations are shown and compared (Figure 3-15), and stack parameters corresponding to the field and each of the scaling methods are given in Table 3-3 through Table 3-5.

Table 3-3: Model Parameters with Scaling Method 1

Model Parameters Scaling with $\left(\rho_p/\rho_0\right)_m = \left(\rho_p/\rho_0\right)_f$	**Case 1**	**Case2**	**Case 3**	**Case 4**
Inside diameter of stack (D)	0.6 mm	0.6 mm	0.6 mm	0.6 mm
Stack height (H_s)	18.6 mm	18.6 mm	18.6 mm	18.6 mm
Geometrical scaling ratio	1:500	1:500	1:500	1:500
Reference flow velocity (v_∞)	0.045 m s^{-1}	0.045 m s^{-1}	0.045 m s^{-1}	0.045 m s^{-1}
ρ_p/ρ_0	0.6522	0.5	0.4286	0.3750
gb_0/v_∞^2	1.47	1.47	1.47	1.47
V_s/v_∞	11	11	11	11
$\frac{gb_0}{v_\infty^2}\frac{\Delta\rho}{\rho_0}$	0.5118	0.7358	0.8408	0.9197

Table 3-4: Model Parameters with Scaling Method 2

Model Parameters Scaling with $\left(\rho_p / \rho_0\right)_m = 0.96$	**Case 1**	**Case2**	**Case 3**	**Case 4**
Inside diameter of stack (*D*)	5.2 mm	7.6 mm	8.6 mm	9.4 mm
Stack height (H_s)	16.1 cm	23.5 cm	26.6 cm	29.1 cm
Geometrical scaling ratio	1:58	1:40	1:35	1:32
Reference flow velocity (v_∞)	0.045 m s^{-1}	0.045 m s^{-1}	0.045 m s^{-1}	0.045 m s^{-1}
ρ_p / ρ_0	0.96	0.96	0.96	0.96
$gb_0/v^2)$	12.8	18.4	21	23
V_s / v_∞	11	11	11	11
$\frac{gb_0}{v_\infty^2}\frac{\Delta\rho}{\rho_0}$	0.5118	0.7358	0.8408	0.9197

Table 3-5: Field Parameters

Field Parameters	Case 1	Case2	Case 3	Case 4
Stack exit plume temperature	460 K	600 K	700 K	800 K
Inside diameter of stack (*D*)	0.3 m	0.3 m	0.3 m	0.3 m
Stack height (H_s)	9.3 m	9.3 m	9.3 m	9.3 m
Reference wind speed (v_∞)	1 m s^{-1}	1 m s^{-1}	1 m s^{-1}	1 m s^{-1}
ρ_p / ρ_0	0.6522	0.5	0.4286	0.3750
$gb_0/v^2)\ gb_0 / v_\infty^2$	1.4715	1.4715	1.4715	1.4715
V_s / v_∞	11	11	11	11
$\frac{gb_0}{v_\infty^2} \frac{\Delta\rho}{\rho_0}$	0.5118	0.7358	0.8408	0.9197

As the actual plume height (h_e) is the key factor for determining the ground-level concentrations rather than plume rise itself, in these simulations, plume rise is shown in terms of actual plume height h_e, where

$$h_e = H_s + h_p. \tag{3-24}$$

Following equations (3-21), (3-22), and (3-24), plume actual height associated with the model can be scaled to the field through the equation (3-25) as,

$$\left(\frac{h_e}{H_s}\right)_m = \left(\frac{h_e}{H_s}\right)_f. \tag{3-25}$$

Figure 3-15 shows the results from the simulations of plume rise at four different stack exit temperatures using parameters associated with (1) *Field* (Table 3-5), (2) *Scaling method 1* (Table 3-3), and (3) *Scaling method 2* (Table 3-4).

Figure 3-15: Simulation of Palm Springs DG Plume Rise

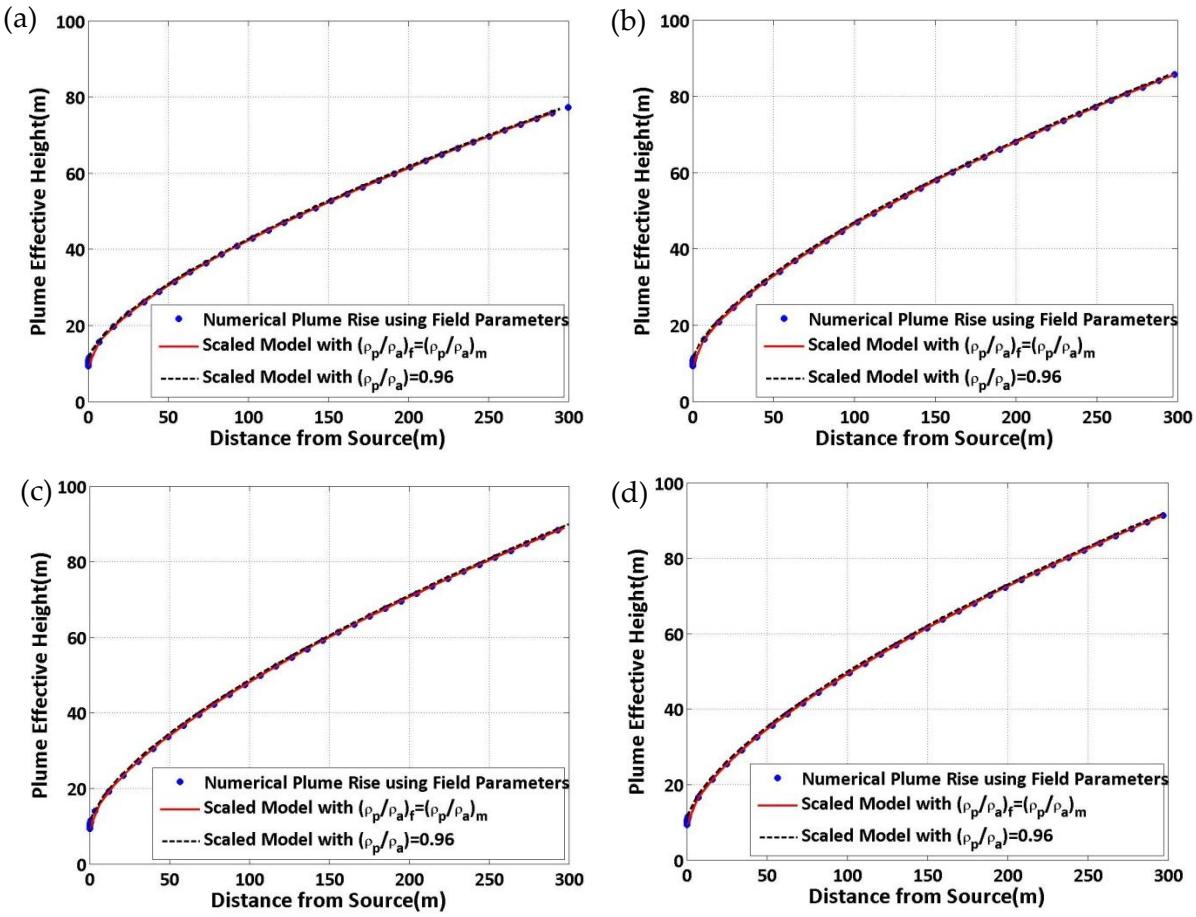

As can be seen figure 3-15, plume actual height associated with *Scaling method 2* (scaling using the densimetric Froude number) yields almost identical results compared with the field simulation. To clarify the accuracy of *Scaling method 2* under urban conditions, the errors associated with this method have been calculated as

$$\%\,error = \left| \frac{h_e(Field) - h_e(Scaling\ method\ 2)}{h_e(Field)} \right| \times 100\% \quad , \qquad (3\text{-}26)$$

where $h_e(Field)$ is the plume actual height calculated using the field parameters (Table 3-4) and h_e *(Scaling method 2)* is the scaled plume actual height calculated using parameters associated with *Scaling method 2* (Table 3-4). These errors are shown in Figure 3-16.

Figure 3-16: Actual Calculated Plume Height Errors Associated with Distorting the Initial Density Condition in the Plume Rise Scaling Method Using the Densimetric Froude Number vs. Distance from the Stack at Four Different Stack Exit Temperatures Ranging from 460 K–800 K.

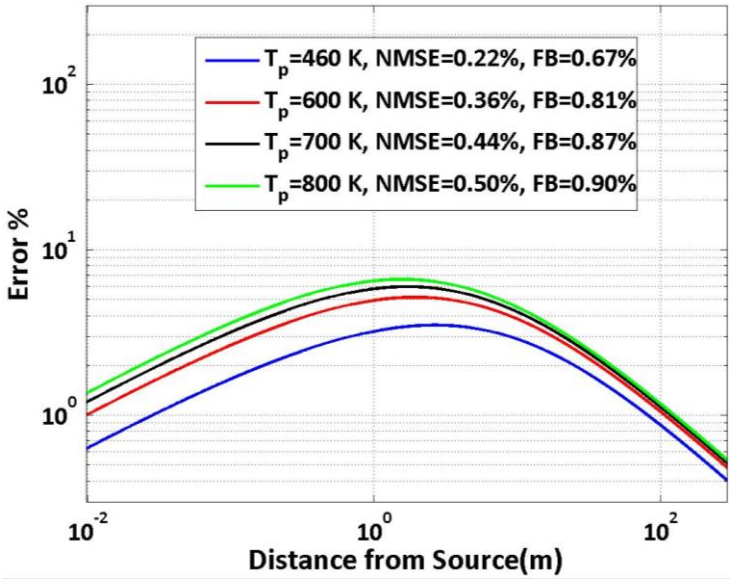

In addition to these errors, the performance of *Scaling method 2* is also investigated through the normalized mean square error (NSME) and fractional bias (FB), which are the standard methods for comparing field, model, and numerical predictions. These methods are explicitly discussed in the Model Validation Kit (MVK) package (Olesen 2005; Contini et al. 2011).

Figure 3-16 shows that the maximum error occurs at a distance of 2 m from the stack and ranges from 3.5 percent (at T_p = 460 K) up to 7 percent (at T_p = 800 K). The error reduces to less than 1 percent at distance of 120 m from the stack. In addition, the maximum NSME and FB are associated with T_p = 800 K, and are equal to 0.5 percent and 0.9 percent, respectively. This shows that, similar to isolated stacks, scaling using densimetric Froude number (*Scaling method 2*) is also accurate (over the range of parameters considered) under urban conditions even though it is not satisfying the initial value of ρ^*. Also, results from *Scaling method 2* show larger values ($\geq$ 5.2 mm) of the model stack diameter (Table 3-4) than those obtained from *Scaling method 1* (Table 3-3) since the velocity scaling ratio remained constant (1:22.5) for both scaling methods. A small stack diameter yields a lower stack Reynolds number, which might lead to a laminar plume. This will not satisfy the Reynolds independency, resulting in non-similar plume motion close to the stack. Therefore, larger stack diameters (such as those given by *Scaling method 2*) are more desirable in laboratory modeling. In addition, small stack diameters ($\leq 1\,\mathrm{mm}$) are more difficult to fabricate due to manufacturing limitations, and are more prone to clogging.

3.12.9 Similarity of Dispersion

Although the Gaussian dispersion model (Sutton 1947) might not necessarily explain the dispersion of pollutants in the urban boundary layer, due to its simplicity, it is used as the main framework for the urban pollution dispersion purposes (e.g., in the U.S. EPA regulatory model AERMOD). Therefore, the team based the team's dispersion similarity on this model:

$$\frac{C(x,y,z)}{Q} = \frac{1}{2\pi\sigma_y\sigma_z U}\exp\left(-\frac{y^2}{2\sigma_y{}^2}\right)\left[\exp\left(-\frac{(z-h_e(x))^2}{2\sigma_z{}^2}\right)+\exp\left(-\frac{(z+h_e(x))^2}{2\sigma_z{}^2}\right)\right]$$

$$\frac{C(x,y,z)}{Q} = \frac{1}{2\pi\sigma_y\sigma_z U}\exp\left(-\frac{y^2}{2\sigma_y^2}\right)\left[\exp\left(-\frac{(z-h_e(x))^2}{2\sigma_z^2}\right)+\exp\left(-\frac{(z+h_e(x))^2}{2\sigma_z^2}\right)\right] \quad (3\text{-}27)$$

where C is the concentration, σ_y and σ_z are the plume spreads in the horizontal and vertical directions, respectively, at distance x from the source; U is the ambient velocity at the plume height; h_e is the actual height of the plume defined in the previous section; and Q is the pollutant mass emission rate. This model will perform well for cases where the plume can rise above the wake of the stack building and is not trapped in the recirculation region downwind. Due to the typically low wind speeds in urban areas and relatively high buoyancy and momentum of the exhaust plumes, urban plumes rise rapidly near the stack and in most cases escape the wake of the stack buildings.

The Gaussian dispersion model can be re-written in terms of dimensionless parameters as,

$$C = \frac{Q}{2\pi H_s{}^2 v\sqrt{(I_y{}^2 x^{*2}+\sigma_b^{*2})(I_z{}^2 x^{*2}+\sigma_b^{*2})}}\exp\left(-\frac{y^{*2}}{2(I_y{}^2 x^{*2}+\sigma_b^{*2})}\right)$$
$$\left[\exp\left(-\frac{(z^*-h_e{}^*(x))^2}{2(I_z{}^2 x^{*2}+\sigma_b^{*2})}\right)+\exp\left(-\frac{(z^*+h_e{}^*(x))^2}{2(I_z{}^2 x^{*2}+\sigma_b^{*2})}\right)\right] \quad (3\text{-}28)$$

where x^*, y^*, and z^* are dimensionless spatial coordinates; and h_e^* is the dimensionless actual height of the plume, which is defined as,

$$h_e^* = \frac{h_p+H_s}{b_o}. \quad (3\text{-}29)$$

The dimensionless buoyancy-induced dispersion (σ_b^*) can also be defined as,

$$\sigma_b^* = \frac{0.4}{\sqrt{2}}\left(h_e^* - 1\right) \quad . \tag{3-30}$$

As most of the studies involved with the dispersion of pollutants are focused on the ground-level concentrations, the team simplifies the Gaussian dispersion model to calculate only the downstream ground-level concentration as,

$$C(x^*,0,0) = \frac{Q}{\pi v H_s^{\,2}\sqrt{(I_y^{\,2}x^{*2} + \sigma_b^{*2})(I_z^{\,2}x^{*2} + \sigma_b^{*2})}} \exp\left(-\frac{h_e^{\,*}(x)^2}{2(I_z^{\,2}x^{*2} + \sigma_b^{*2})}\right) . \tag{3-31}$$

The dimensionless ground-level concentration becomes

$$C^*(x^*) = C(x^*)\frac{H_s^{\,2} v\sqrt{(I_y^{\,2}x^{*2} + \sigma_b^{*2})(I_z^{\,2}x^{*2} + \sigma_b^{*2})}}{Q} \exp\left(\frac{h_e^*(x^*)^2}{2(I_z^{\,2}x^{*2} + \sigma_b^{*2})}\right) , \tag{3-32}$$

and can be used to convert concentration levels from laboratory to field scale.

If the turbulent intensities, I_y and I_z, are the same for both the field and model, then equation (3-32) reduces to the non-dimensional concentration proposed by Robins (1980) and Snyder (1981) as,

$$d^*(x^*) = \frac{1}{4} d(x^*) D^2 U \quad , \tag{3-33}$$

since I_y, I_z, and the exponential term cancel out. In cases where the full flow similarity is achieved such that the turbulent intensities are the same in both field and model, equation 3-33 can be used to scale the concentration levels from laboratory to the field and vice versa. However, this condition is not likely to occur in water channels, as the turbulent intensities are not easy to control and are often different from those in the field. Turbulent intensities are difficult to control since their magnitudes are very sensitive to the adjustment of flow conditioners, as well as to the roughness elements used in the water channels. Turbulent intensities in the water channels are typically within 10 to 30precent, while in urban areas they range from 20 percent on windy days to more than 100 percent during low-wind (< 1 m s^{-1}) conditions. Therefore, a correction (equation 3-32) to account for the discrepancy in the turbulent intensities is often required. To clarify the effect of this correction method, ground-level concentrations associated with the Palm Springs DG were predicted using the Gaussian dispersion model and compared with those predicted using the scaled model with and without correction for discrepancy in turbulent intensities. Average turbulent intensities associated with the field (Jing et al. 2010) and laboratory model are listed in Table 3-6.

Using the field stack parameters in Table 3-5 and scaled stack parameters corresponding to *Scaling method 2* (scaling using densimetric Froude number) in Table 3-4, assuming T_p = 460 K, ground-level concentrations in the field and model are predicted through the Gaussian dispersion model (equation 3-27).

Table 3-6: Turbulent Intensities Associated with the Field and Laboratory Model

	I_y	I_z
Field*	0.5	0.3
Laboratory model	0.2	0.12

*Field data are provided by Jing et al. (2010), obtained from a sonic anemometer located on the rooftop of the DG, at 11 m from the ground, in Sunrise Park at Palm Springs, California, averaged over the period of July 15, 2008 to July 21, 2008.

The predicted ground-level concentrations in the laboratory model were then scaled back to the field with and without correction for discrepancy in turbulent intensities through equations 3-32 and 3-33, respectively. These concentrations are shown in terms of normalized concentration, d, defined as,

$$d = C/Q \quad (3\text{-}34)$$

Figure 3-17 shows the results from these simulations and the ratio of concentrations associated with the field to the scaled concentrations (d_{Scaled}/d_{Field}) with and without correction..

Figure 3-17: (a) Normalized Ground-Level Concentrations (microseconds per cubic meter, μs/m^3) Associated with the Palm Springs DG (blue_) vs. Scaled Ground-Level Concentrations with (black_) and without (red_) Correction for Turbulent Intensity Discrepancy; (b) Ratio of Scaled to Field Normalized Simulated Concentrations with (blue_) and without (red_) Correction

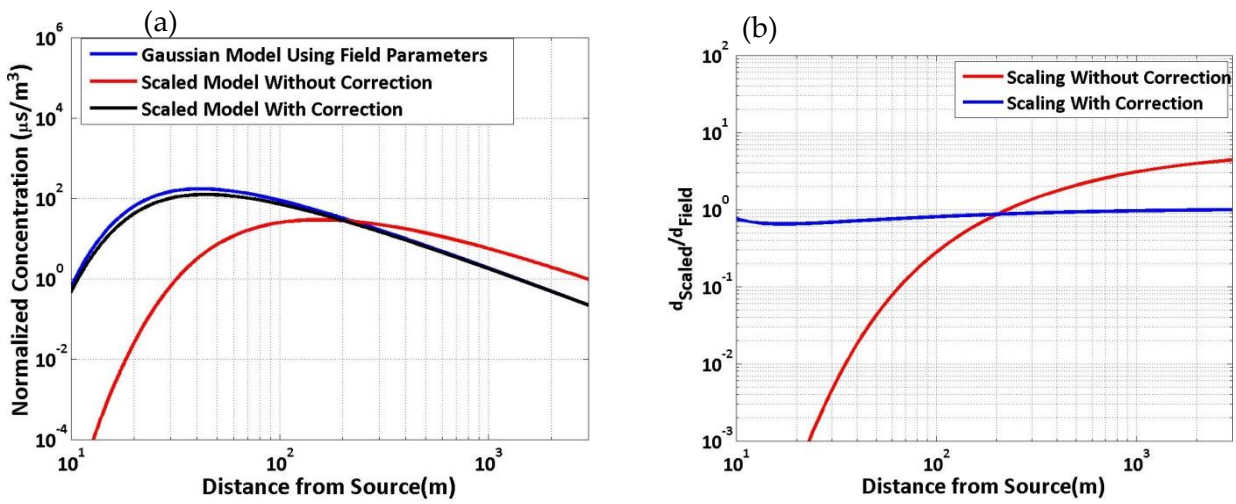

Figure 3-17a shows that the scaled ground-level concentration (d_{Scaled}), corrected for the difference in turbulent intensities of the model and field, is almost identical to the ground-level concentration predicted using field parameters (d_{Field}), since plume spread is mostly dominated by the ambient turbulence. The minimum scaled to field normalized concentration ratio (d_{Scaled}/d_{Field}) associated with this scaling is about 0.6 near to the source (~15 m) and becomes almost unity for distances larger than 100 m (Figure 3-17b). This discrepancy between scaled and field concentration (at distances of $x \leq 100\,m$) results from the errors (~3.5 percent) due to the plume rise scaling (scaling using the densimetric Froude number and relaxing the initial density ratio), explained in the previous section, which significantly affects ground-level concentrations very close to the source and becomes negligible at larger distances $(x \geq 100\,m)$. However, when no correction has been made, there is a large discrepancy between field predictions and scaled model predictions (Figure 3-17a); also, the scaled to field normalized concentration ratio (d_{Scaled}/d_{Field}) is less than 10^{-3} at 20 m from the source and increase to 5 at 3 km from the source (Figure 3-17b). Therefore, it may be concluded that neglecting the above-mentioned correction in laboratory dispersion studies, where turbulent intensities differ from those in the field, may lead to significant errors. However, this simple correction can be of great help in modeling real-world dispersion problems in the laboratory without a need to match the turbulent intensities.

Following these procedures gives a proper scaling of the flow, plume rise, and dispersion for problems involving buoyant releases from low-level sources in urban areas.

3.12.10 Summary and Conclusions

The rapid growth of urbanization in recent decades has forced the air quality modelers to focus on the air quality impact of pollutants released within the urban canopy. Although numerous field studies have been performed, results of these field measurements are always specific to the site geometry, and thus are difficult to extrapolate meaningfully to other settings. For these reasons, laboratory modeling inside water channels or wind tunnels is expected to provide major contributions. For these measurements to be applicable to real cases, correct methods for scaling of flow, plume rise, and turbulence-governed plume spread are needed.

The first part of this study explains the scaling of the flow. Flow similarity has been explained by Snyder (1981) through non-dimensionalizing the equations of motion. This yields four dimensionless parameters. As the urban flow length scales are less than 5 km, the Coriolis effect can be neglected; thus, there is no need to match the Rossby number. As long as the Reynolds number is sufficiently high, the large-scale flow features are similar and independent from the Reynolds number (Townsend 1956). This approach for high Reynolds number automatically satisfies the Peclet number in both the model and field. Therefore, the only dimensionless parameter that must be matched is the densimetric Froude number, which accounts for buoyancy effects in the flow. The geometric similarity is also required to satisfy the velocity boundary conditions.

The second part of the study describes the scaling of plume rise and dispersion in urban areas. Based on the observation from plume rise measurements in the water channel, it has been shown that plume rise of pollutants released inside urban areas is highly sensitive to the updrafts and downdrafts induced by the surrounding buildings. Consequently, the plume rise formulation of Briggs (1984) is unable to reproduce results accurately, since it does not account for the streamline ascents and descents. A plume rise model based on the conservation equations of mass, momentum, and buoyancy flux has been developed which accounts for the flow velocity in both vertical and horizontal (along the stream) directions. Providing the measured flow field in the vicinity of the source, stack exit velocity (V_s), and plume buoyancy (σ_p) as input variables, this model has been evaluated with data from the water channel experiments and the results show that this numerical model is able to accurately predict the plume rise affected by flow modifications caused by buildings. The downside of this model is that it requires measured flow velocities as inputs, which are not usually available. However, even when the full flow field data is not available, linear interpolation of limited available flow data points can be sufficient to construct the required inputs for this model. For practical applications, this plume rise model can be easily implemented in an urban CFD model for accurate calculations of the plume height.

Next, non-dimensionalization of the plume rise governing equations and satisfying the boundary conditions at the source yields dimensionless parameters such as Froude number (gb_0 / v^2), velocity ratio (V_s / v), and density ratio (ρ_p / ρ_0) that must be matched between the model and the field to ensure the correct scaling. These parameters are the same as those discussed in the literature for scaling plume rise from tall isolated stacks. It has been shown that among the dimensionless parameters involved in the scaling process, it would be difficult to match the Froude number in wind tunnels (over a considerable range of atmospheric wind speeds) since it implies significantly low-flow velocities. These velocities create difficulties satisfying the *Re* independency criteria and are not easy to control. In addition to Froude number, matching initial (stack exit) dimensionless density (ρ_p / ρ_0) in the laboratory model and the field is challenging in the water channels, due to the limitations on the density of the tracer that can be used. By relaxing these dimensionless parameters and matching the densimetric Froude number for the plume in the laboratory model and field, plume rise can be scaled from the field to the laboratory.

The performance of this method and similar scaling methods has been evaluated in previous studies (e.g., Robins 1980) for tall isolated stacks. In this study, results from this scaling technique and the original scaling have been compared for an urban case. It has been shown that scaling using the densimetric Froude number is relatively accurate, and the model stack dimensions derived from this scaling method (under a constant velocity scaling ratio) result in higher stack *Re,* which makes it easier to achieve *Re*-independent plume motion at the stack exit. In addition, larger model stack diameters may be sometimes easier to manufacture, and they will be less prone to clogging by particles used for PIV measurements.

In this study, the errors associated with scaling of a low wind speed urban condition under four different stack exit temperatures were investigated; thus, the analysis does not necessarily hold for all urban condition (e.g., higher wind speeds and stack exit temperatures). Furthermore, the validation of this scaling technique was accomplished using the numerical plume rise model explained in Section 3.12.5. As explained earlier, this model was developed based on different assumptions, which might not be valid under certain source conditions. For example, the entrainment relationship in this model does not account for the density difference between the plume and ambient air and thus, it does not necessarily hold for conditions where large density differences are used. Therefore, results from this analysis are not necessarily generic to all source conditions. In addition, according to Meroney (1982, 1986a, 1986b), scaling using densimetric Froude number might have a significant impact on time-scale ratios especially for the dense gas plume dispersion problem. Therefore, further investigation is needed to address the generality of this scaling method for all urban conditions and its impacts on averaging time.

Following the correct scaling of flow and plume rise, concentration is scaled through the Gaussian dispersion model for the case where turbulent intensities in the laboratory and field are not the same. If the turbulent intensities are matched, then there is no need for the Gaussian formulation, and concentration is directly scaled through the non-dimensional concentration proposed by Robins (1980) and Snyder (1981). Although the Gaussian model does not account for all of the urban dispersion effects, it can be considered as an appropriate framework for correcting the scaling distortions (different turbulent intensities in the laboratory and the field). This scaling method will allow experimental investigators to correctly model real-world problems associated with air quality in urban areas inside water channels and wind tunnels, where conditions are more controllable and geometry can be easily adjusted.

CHAPTER 4:

Impact of Distributed Generation of Electricity Relative to Other Urban Sources[4]

4.1 Introduction

The air quality in an urban area is affected by a large number of sources, such as vehicles, distributed over the urban area. Thus, the contribution of sources within meters from an urban receptor might be comparable to that of sources outside the local area of interest. In principle, an air quality model can be used to estimate the contributions of all the urban sources to concentrations at a receptor. However, the large number and variety of sources in an urban area necessitates computational resources that can become impractical even with current computers, especially when it is necessary to conduct sensitivity studies over long averaging times. The current approach to this problem is to use models applicable to several scales, so that sources at different distances from the area of interest can be treated with different levels of source aggregation.

The concentration at a receptor has three components: (1) a regional contribution computed from a long-range transport model with a grid spacing of the order of tens of kilometers, (2) an urban "background" contribution from sources aggregated over kilometer-sized grids, and (3) a local contribution from models that estimate concentrations at meters from a receptor (See Brandt et al. 2003 for an example).

This chapter focuses on a model that estimates urban "background" concentrations of NO_x, NO_2, and O_3, averaged over a scale on the order of kilometers. In a normal numerical solution to the mass conservation equation, transport and chemistry are treated simultaneously or as processes that follow each other within a numerical time step. This coupling treatment is adopted in most grid models, such as CMAQ (Byun and Schere 2006) and UCI-CIT (Carreras et al. 2004). The chemistry module in these grid models, however, occupies a large portion of computing time, and their application becomes a computational burden if concentrations are required over a year. The simple urban background model (UBM) developed by Berkowicz (2000) addresses this problem through two simplifications: a straight line steady dispersion model and chemistry based on photostationarity neglecting the role of hydrocarbons. The model presented here is intermediate between comprehensive photochemical models and the simple UBM. It treats unsteady meteorological conditions with trajectories that reflect space and time varying winds, and it reduces the computational requirements of photochemical models by separating transport and chemistry using a

[4] Reprinted from Pournazeri, S., Tan, S., Schulte, N., Jing, Q., and Venkatram, A. A computationally efficient model for estimating background concentrations of NO_x, NO_2, and O_3. *Environmental Modelling & Software* 52: 19–37

method described in Venkatram et al. (1998). The model is evaluated with data from measurements made in Los Angeles (CARB 2011).

4.2 Methods

We suggest reducing the computational requirement of the grid model by separating transport and chemistry. The uncoupled grid model presented in this chapter replace the coupled processes of transport and chemistry by first performing the transport and then performing chemistry over a time interval corresponding to the age associated with transport. The transport is based on a receptor-based Lagrangian background model (LBM) in which back trajectories are used to trace the history of a moving box arriving at a receptor. The chemical species emitted into the box are first transported without accounting for chemistry. However, each species is associated with an effective age in addition to concentrations. The species are then allowed to react in a box over a time corresponding to the maximum of the ages of the species that arrive at the receptor. The photochemical model used to produce ozone concentrations in this chapter is the Carbon Bond IV mechanism (CBM IV) (Gery et al. 1989), in which the VOCs are assumed to be a mixture typical of ambient measurements made in Los Angeles; the VOCs are distributed among eight surrogate species and one inert species.

4.2.1 The Lagrangian Background Model

The model described here is similar to the Lagrangian model used in Europe to estimate long-range transport of sulfur (Eliassen and Saltbones, 1983). It estimates the concentration of a pollutant by tracing the history of the air parcel associated with the concentration at the receptor of concern at a specified time. Back trajectories are calculated in 1-hour time steps using the hourly averaged wind speed (at 10 m above the ground level), and wind direction from the meteorological station closest to the receptor. Each trajectory is extended backwards in time for 24 hours, which assumes that sources beyond this travel time make a negligible contribution to concentrations at the receptor. This assumption was evaluated using sensitivity studies. To facilitate the use of the model, meteorological inputs are taken directly from the surface input files used by AERMOD (Cimorelli et al., 2005) which are generated by the AERMOD meteorological preprocessor (AERMET). In a single layer model, the choice of the height of the wind used to compute trajectories is arbitrary; the choice of the 10 m wind is justified a posteriori through comparison of model estimates with observations.

The air parcel has horizontal dimensions of the grid square used to represent emissions of NO_x and *VOC* (Volatile Organic Compounds) over the domain. The height of the air parcel corresponds to the local mixed layer height. Emissions are injected into the box and mixed through its volume as the box moves over the urban area, which is described with a gridded emission inventory of NO_x and VOC. To ensure pollutants are well mixed, the team carefully choose a time step which is higher than the mixing time scale given by

$\sqrt{2/\pi}\, z_i/\sigma_w$. For the meteorological conditions used in the study for the SoCAB, this

mixing time scale has a maximum value of about 0.9 h. Therefore, the team can use a time step $\Delta t = 1$h to trace back the history of the box for 24 hours. The concentrations are stepped from the (i-1)th to the ith time step through

$$C_i = C_{i-1} \min\left(\frac{z_{i-1}}{z_i}, 1\right) \exp(-v_d \Delta t / z_i) + \frac{\Delta m_i}{z_i} \exp(-(v_d/2)\Delta t / z_i), \qquad (4\text{-}1)$$

where z_i is the mixed layer height, and v_d is the deposition velocity. The team assumes that the deposition velocity of newly emitted pollutants is half of the velocity of those transported from the previous step. The minimum term on the right-hand side of the equation ensures that the concentration does not increase when the mixed layer decreases during a time step.

The mass of pollutant injected per unit surface area of the air parcel is $\Delta m_i = q_i(\vec{r})\Delta t$, where $q_i(\vec{r})$ is the emission density at the location of the parcel, $\vec{r}$, and Δt is the time step of the trajectory calculate. Figure 4-1 illustrates the described LBM.

Figure 4-1: The Lagrangian Background Model

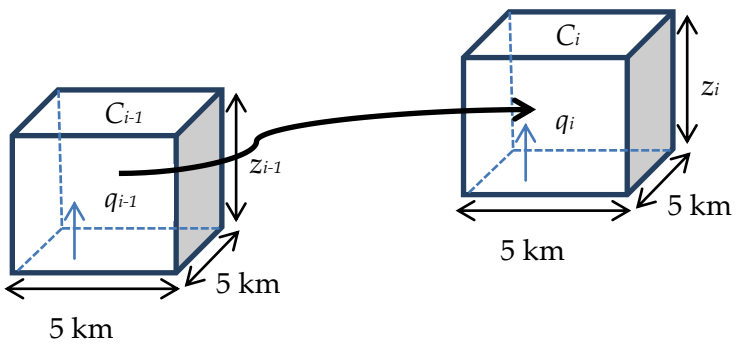

Used to Calculate Concentrations at a Receptor

The incremental concentration, ΔC_i, during the last hour of the air parcel's path is computed with a steady-state dispersion model (Venkatram and Cimorelli 2007) that accounts for incomplete vertical mixing,

$$\Delta C_i = \sqrt{2/\pi} \ln(1 + \sigma_w R/(Uh)) q_i / \sigma_w, \qquad (4\text{-}2)$$

where R is half of the grid length, U is the mean wind speed, h is the initial vertical spread of surface emissions, and σ_w is the standard deviation of the vertical velocity fluctuations.

When the pollutant is well mixed through the boundary layer during the last time step before the parcel reaches the receptor, the equation is modified,

$$\Delta C_i = \sqrt{2/\pi}\ln\left(\sqrt{2/\pi}\, z_i/h\right) q_i/\sigma_w + q_i(R - R_m)/(Uz_i) \quad , \qquad (4\text{-}3)$$

where R_m is a critical-length scale that determines if the pollutants are well mixed.

4.2.2 The Species Age

The concept of species age is best illustrated by Venkatram et al. (1994, 1998). The effective age of a molecule is the time taken for the molecule to travel from source to receptor. Considering a case in which a source emits NO_x, and the wind speed is u_i, the team can simply calculate the age of the molecules at a distance x_i from the source as x_i/u_i. This simple case can be generalized to more complex wind flows by formulating a conservation equation for species age. The formulation is best understood by examining each of the processes that determine the aging of molecules enclosed within a control volume. The underlying concept is that an average age can be associated for each of the species in a grid volume.

The differential equation for the age, A, of a species can be formulated by considering the following: (1) The age of material in a control volume increases with time if nothing is emitted into the box; (2) The average age decreases when new material is emitted into the volume; and (3) Transport of material into and out of the volume changes the age.

Consider a box in which the mass per unit surface area of certain species changes from $m(t)$ to $m(t+\Delta t)$ and the age changes from $A(t)$ to $A(t+\Delta t)$ in the time interval Δt. The age $A(t+\Delta t)$ is determined by the ages of material that follow into the box and by aging of the material that is already in the box. Then the conservation of age for a box with dimensions, Δx_i, along the coordinate direction, i, can be written as

$$A(t+\Delta t)m(t+\Delta t) = m(t)(A(t)+\Delta t) - \frac{\Delta(u_i mA)}{\Delta x_i}\Delta t \quad . \qquad (4\text{-}4)$$

The first term on the right-hand side of equation 4-4 refers to the aging of the material in the box during the interval Δt, and the second term corresponds to the contribution of the material transported into the box at a rate $u_i m$ by the instantaneous velocity, u_i. If the team defines $\phi \equiv Am$, the differential corresponding to equation 4-4 can be written as

$$\frac{D\varphi}{Dt} = \frac{\partial\varphi}{\partial t} + \frac{\partial(u_i\varphi)}{\partial x_i} = m \quad , \qquad (4\text{-}5)$$

where the left-hand side is the Lagrangian derivative defined along the trajectory of the box moving with a velocity u_i.

If there are no emissions along the trajectory, the mass density of certain species will remain constant, and the team can integrate equation 4-5 to obtain $\phi = mt$, which leads to the

conclusion that the species age is equal to the travel time along the box trajectory, $A(t) = t$.

Considering a new case, in which the mass density increases linearly with time as a result of emissions, $m(t) = \alpha t$, where α is a constant, substituting this mass into equation 4-5 and integrating yields the result that the age is one-half of the travel time, $A(t) = t/2$. This result is consistent with the idea that new emissions reduce the average age of the species associated with the moving box. Thus, the ages can be computed from the $(i\text{-}1)^{th}$ to the ith time step through a numerical version of equation (4-5)

$$\varphi(i) - \varphi(i-1) = \Delta t\,(m_i + m_{i-1})/2 = m_i \Delta t - \Delta m_i \cdot (\Delta t/2), \qquad (4\text{-}6)$$

which can be rearranged as

$$A_i = A_{i-1}(1 - \Delta m_i/m_i) + \Delta t(1 - \Delta m_i/(2m_i)). \qquad (4\text{-}7)$$

In the absence of fresh emissions, that is $\Delta m_i = 0$, the team obtains the expected result: $A_i = A_{i-1} + \Delta t$. Note that fresh emissions always decrease the effective age of the species within the parcel, that is, $A_i < A_{i-1} + \Delta t$.

Then, the chemical transformation of this species is estimated by reacting it with other species in a box with initial concentrations corresponding to those in the absence of chemistry. The time period for chemical calculations is specified by the end time corresponding to the time of interest and a start time, which is the end time minus the species age. The chemical calculation is performed over the maximum of the ages of the species in the air parcel. The chemistry accounts for the variation of photolysis rates with time of day.

4.3 Evaluation of the Lagrangian Background Model

4.3.1 The South Coast Air Basin Study

We used LBM to estimate NO_x, NO_2, and O_3 concentrations in the SoCAB at the monitors depicted in Figure 4-2, maintained by the South Coast Air Quality Management District (SCAQMD). Figure 4-3 shows the daily average NO_x and *VOC* emissions at the 994, 5km×5km grids used by Samuelsen et al. (2005) for the SoCAB emission inventory. These emissions are projected into the future considering the growth in population, industrial and commercial activity, vehicle miles traveled, and other factors. This inventory includes stationary point and nonpoint, non-road mobile, mobile, biogenic, and geogenic emission sources as required by Consolidated Emissions Reporting Rule (CERR, 2002). The team assumed that the diurnal variation of NO_x emissions corresponds to traffic volume, shown in the right panel of Figure 4-2. Figure 4-3 shows the daily (24-hr) averaged NO_x and *VOC* emissions in the SoCAB. As seen in Figure 4-3, the maximum NO_x emissions occur near the

port of Long Beach where ships, trucks, trains, and cargo-handling equipment emits about 48 tons of NO_x per day (http://www.polb.com). In addition, high levels of NO_x and *VOC* emissions occur near the city of Ontario where highway 10 and 60 as well as the Ontario international airport are the main contributors.

The transport model was run with surface meteorological data corresponding to 2007, measured at 21 meteorological stations operated by the SCAQMD. Model estimates are compared with NO_x concentrations measured at 21 monitoring stations numbered in the left panel of Figure 4-2. First, the team compared the results from the *LBM* that incorporates *GRS* chemistry with those from the *LBM* with the more complete Carbon Bond Model IV (*CBM IV*) mechanism. In the *CBM IV* chemistry module, the volatile organic compounds (*VOC*) are taken to be a mixture typical of ambient measurements made in Los Angeles: the *VOC* is distributed among eight surrogate species and one inert species. In these simulations, background ozone is taken to be 20 ppb.

We compared the monthly averaged concentrations of NO_x and O_3 from the two models at the 21 receptors located in SoCAB. Figure 4-4 indicates that estimates of concentrations obtained from *GRS* and *CBM IV* follow the 1:1 line, except at small concentrations, where *CBM IV* predicts higher concentrations than *GRS*. The maximum bias between the estimates from *GRS* and *CBM IV* is 7%. Figure 4-4 shows that the models predict similar diurnal variations of hourly NO_x while O_3 estimates based on *GRS* are slightly lower than those from *CBM IV*.

Figure 4-2: Gridded NO_x Emissions and Monitoring Stations Located in the South Coast Air Basin, Los Angeles

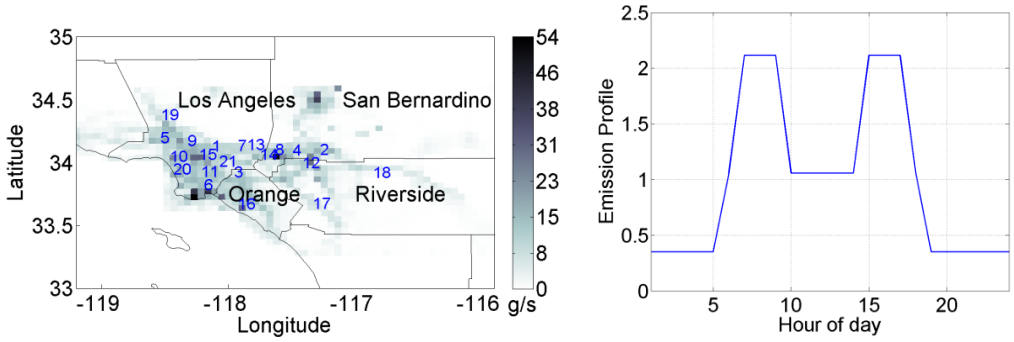

The right panel shows the assumed temporal profile of NO_x emissions.

Figure 4-3: Daily average *NO_x* (left panel) and *VOC* (right panel) emissions (g s^{-1}) in SoCAB

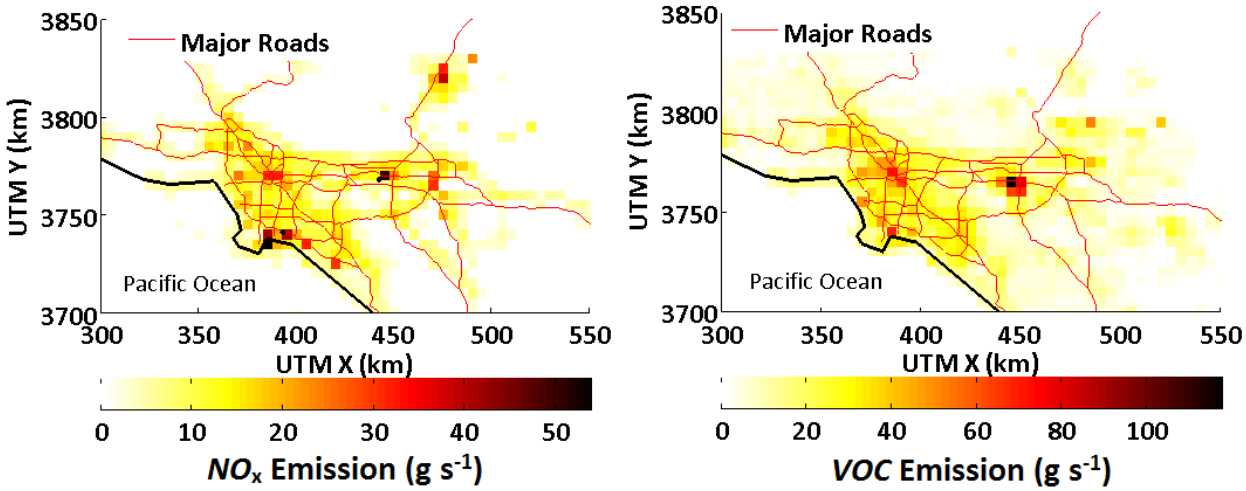

from Samuelsen et al. (2005).

Figure 4-4: Comparison of *NO_x* and *O_3* estimates based on *GRS* and *CBM IV* at stations in the SoCAB

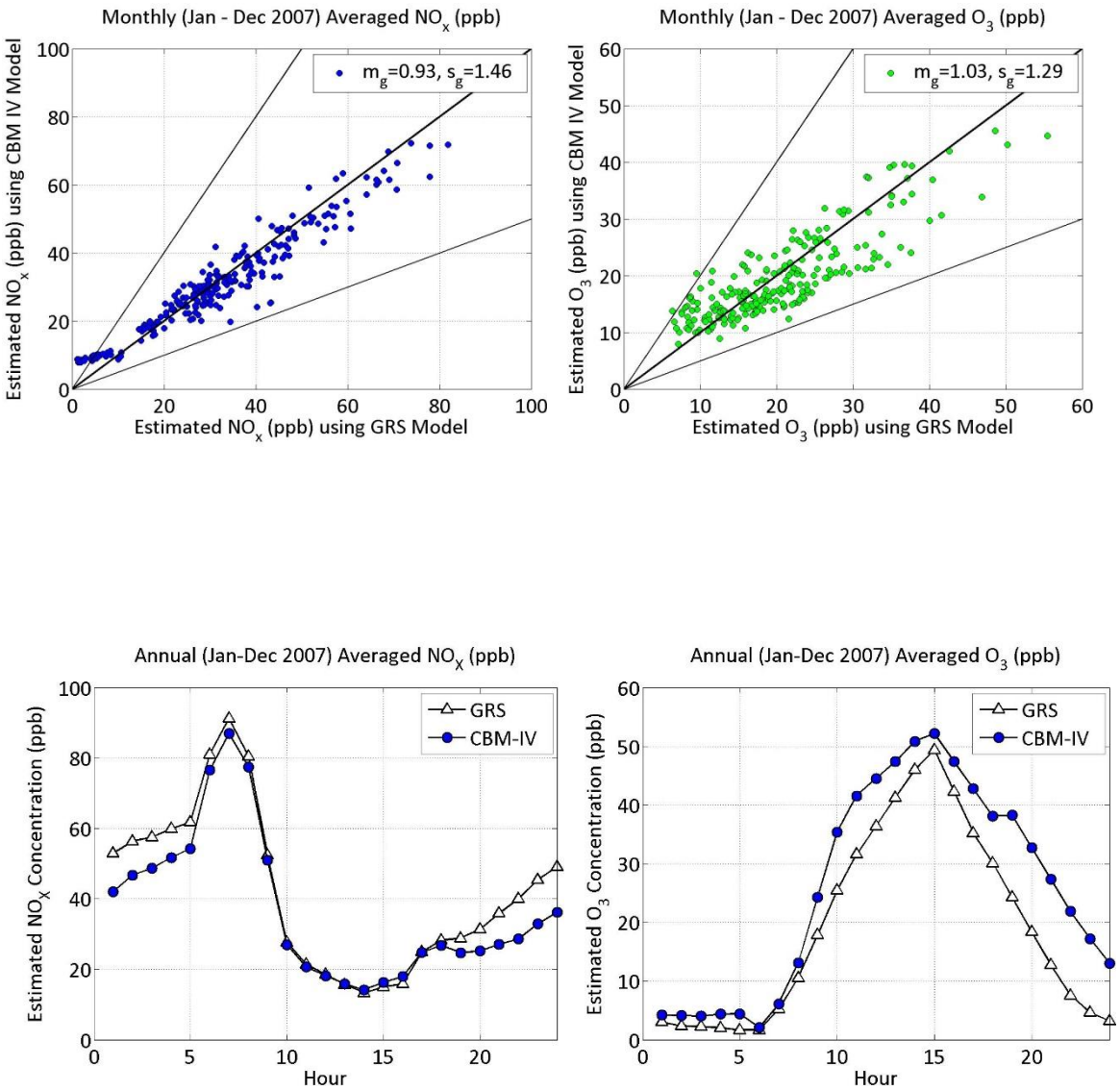

The upper panels show the monthly averaged *NO_x* and *O_3* concentrations and the lower panels show daily variations of *NO_x* and *O_3* concentrations at the San Bernardino monitoring station from January to December 2007

Figure 4-5: Locations of 26 SCAQMD Meteorological Stations

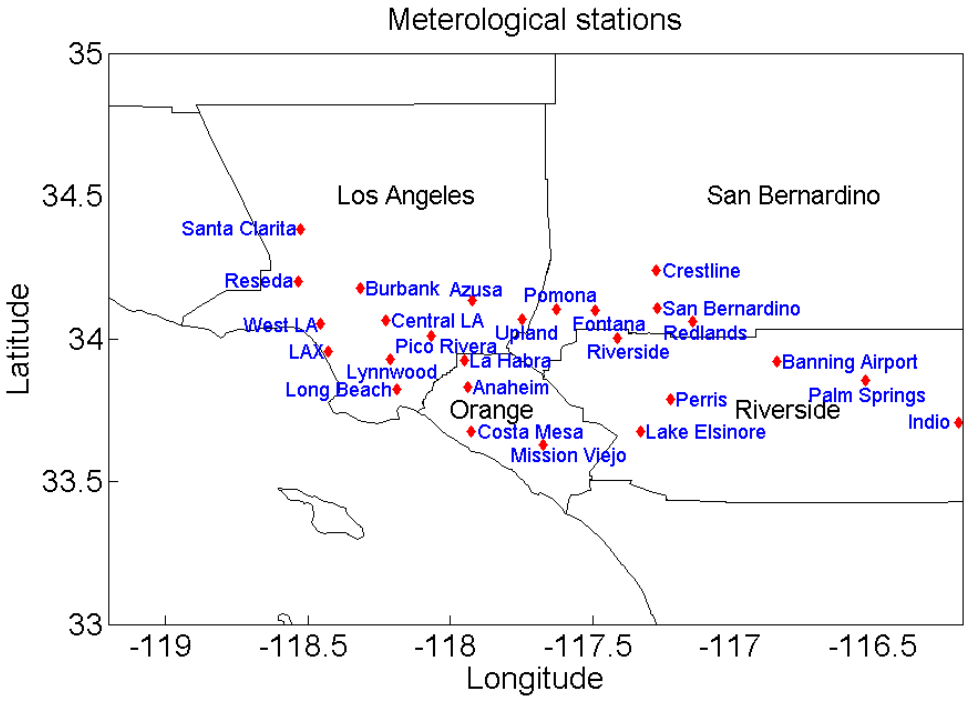

Figure 4-6 shows typical 24-hour back-trajectories of air parcels at two monitoring sites on July 31, 2007. The back trajectory is calculated using the available meteorological station in the SoCAB (Figure 4-5). One site is near the Fontana meteorological station. The southwestern mean winds originate from the Pacific Ocean, cross the shoreline, blow over Orange County, and arrive at the monitoring site. The other site is located near the La Habra meteorological station. The winds originate again from the Pacific Ocean. The southern mean winds blow across the shoreline and arrive at the monitoring station. As the air passes along the mean wind trajectories to the monitoring sites urban pollutants are emitted into the atmosphere, mixed with ambient air, subjected to atmospheric photochemistry processes, and transported by the mean wind. Using the back trajectory, the concentration of NO_x at each monitoring station was predicted.

Figure 4-6: 24-Hour Back-Trajectories of Air Parcels at Two Monitoring Sites on July 31, 2007

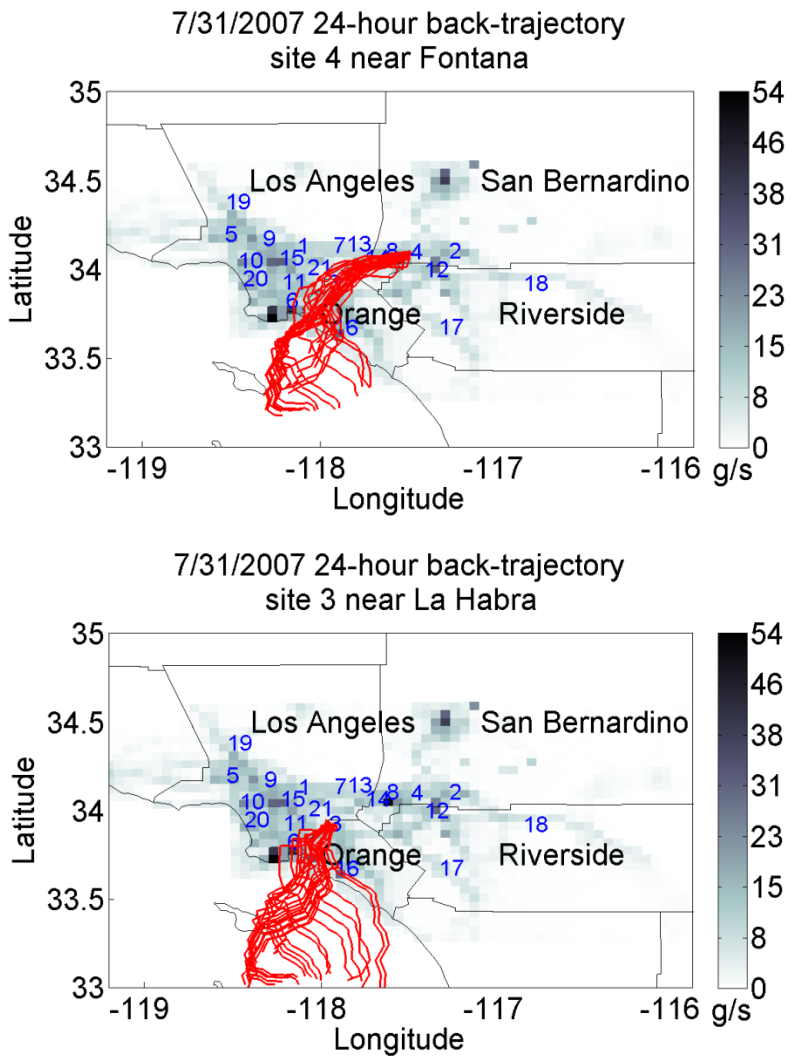

We examined the performance of *UBM* (Berkowicz, 2000) and *LBM* in describing the monthly (January - December 2007) averaged background concentrations of NO_x, NO_2, and O_3 over 21 receptors (Figure 4-7). Model performance is described in terms of the geometric mean and standard deviation, m_g, s_g, of the ratio of the estimated to the observed concentrations (Venkatram, 2008). *FAC*2 refers to the fraction of the model estimates within a factor of two of the corresponding observations. The values of normalized mean bias (*NMB*) and normalized mean error (*NME*) are also provided so that the results may be compared with the evaluation studies found in the literature. The formulas used to compute *NMB* and *NME* are

$$NMB[\%] = \frac{\sum(c_{pi} - c_{oi})}{\sum c_{oi}} \times 100 \qquad (4)$$

$$NME[\%] = \frac{\sum|C_{pi} - C_{oi}|}{\sum C_{oi}} \times 100 \quad (5)$$

where C_{pi} is the 'ith' predicted concentration and C_{oi} is the corresponding observed concentration.

We see that *UBM* overestimates NO_x (top left panel) and NO_2 (middle left panel) concentrations while it provides relatively unbiased estimates of the O_3 (bottom left panel) concentrations as indicated by the value of m_g close to unity (~0.78). Figure 4-7 shows that *LBM* provides unbiased estimates of concentrations: all the NO_x and NO_2 estimates are within a factor of two of the observations with a 4 - 13% bias. O_3 concentrations from both models show similar comparisons with observations. One of the reasons for the poor performance of *UBM* in estimating the NO_x concentration for this specific case study could be the domain size. *UBM* is designed to provide urban background concentrations for domains with an area of about 50 km × 50 km, in which straight-line trajectories are a reasonable approximation. The computational domain used in this study covers a region of about 400 km × 150 km. For such large domains, Brandt et al. (2000a,b, 2001a,b,c,d) developed a coupled system that consists of an Eulerian model, DEOM (Danish Eulerian Operational Model) for air pollution forecasts at a regional scale (grid resolution of 50 km × 50 km), which is combined with the *UBM* model (Berkowicz, 2000) at a 2×2 km^2 grid resolution. The output from *UBM* is fed into the operational street pollution model (OSPM)(Berkowicz, 1999) to estimate street level pollution concentrations at a resolution of meters. This air pollution modeling system yields results that compare favorably with measurements from the Danish urban monitoring network (Brandt et al., 2001c, 2003). The correlation coefficients (r^2) between model estimates and observations of *NO*, NO_2 and *CO* range from 0.72 to 0.96 and the maximum bias is a few ppb.

Figure 4-7: Comparison of modeled and measured monthly averaged NO_x, NO_2, and O_3 concentrations at 21 sites in the SoCAB from January to December 2007

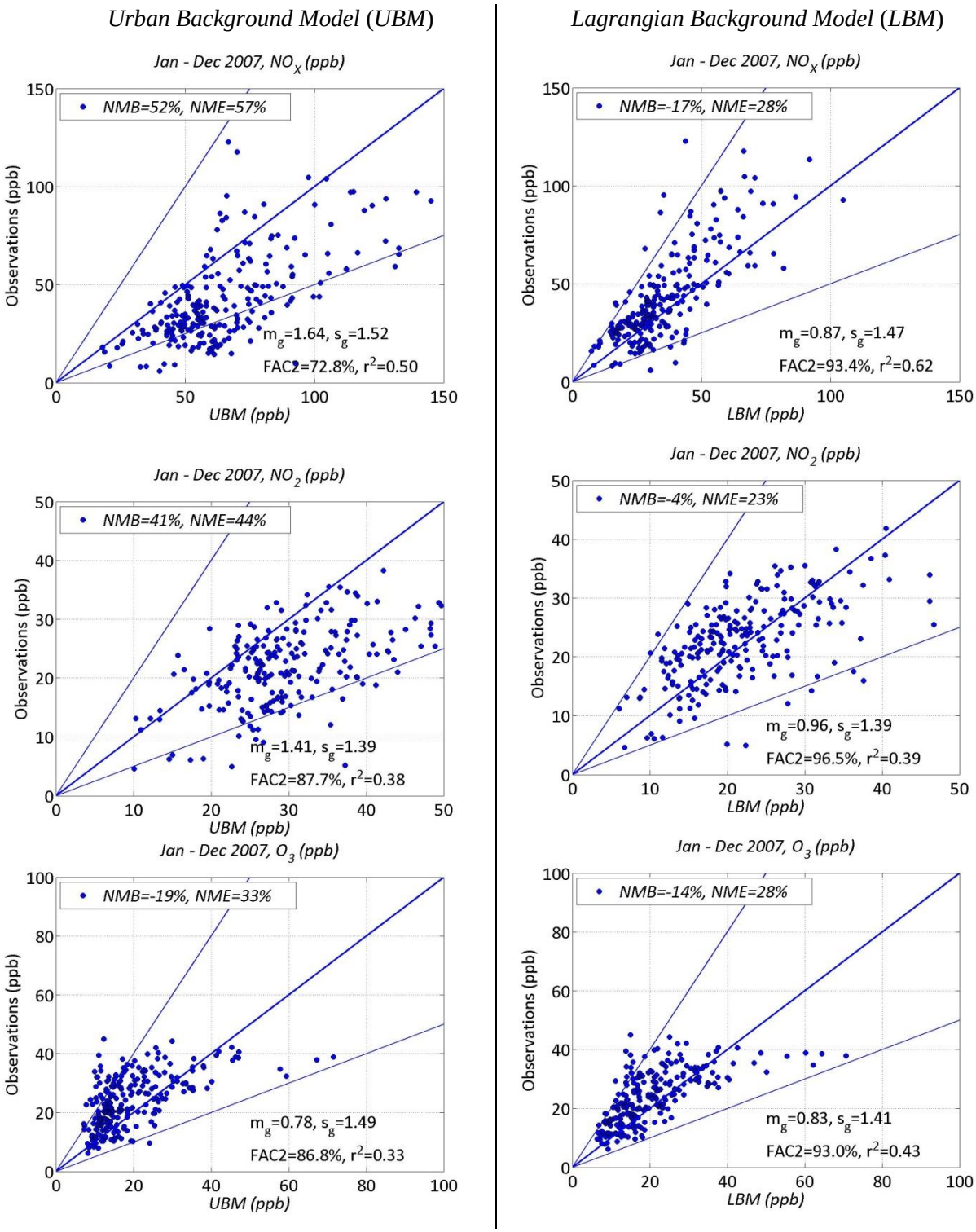

Left panels correspond to *UBM* and right panels to *LBM*.

Next the team examined the performance of *LBM* in estimating NO_2 and NO_x concentrations at two sites, one in the west and the other in the east of the Los Angeles basin, which is downwind of the major sources of ozone precursors. The top two panels of Figure 4-8 show

that the modeled NO_2 and NO_x concentrations, averaged over a month, are correlated well with the corresponding observations. However, the model underestimates NO_2 during the winter months at the San Bernardino site. The discrepancies between model estimates and observations during the winter months could be related to the uncertainty in predicting the stable boundary layer height as described in Pournazeri et al. (2012b).

Figure 4-8: Monthly averaged NO_x and NO_2 concentrations compared with observations at two sites, in West LA (left panels) and San Bernardino (right panels), in the SoCAB.

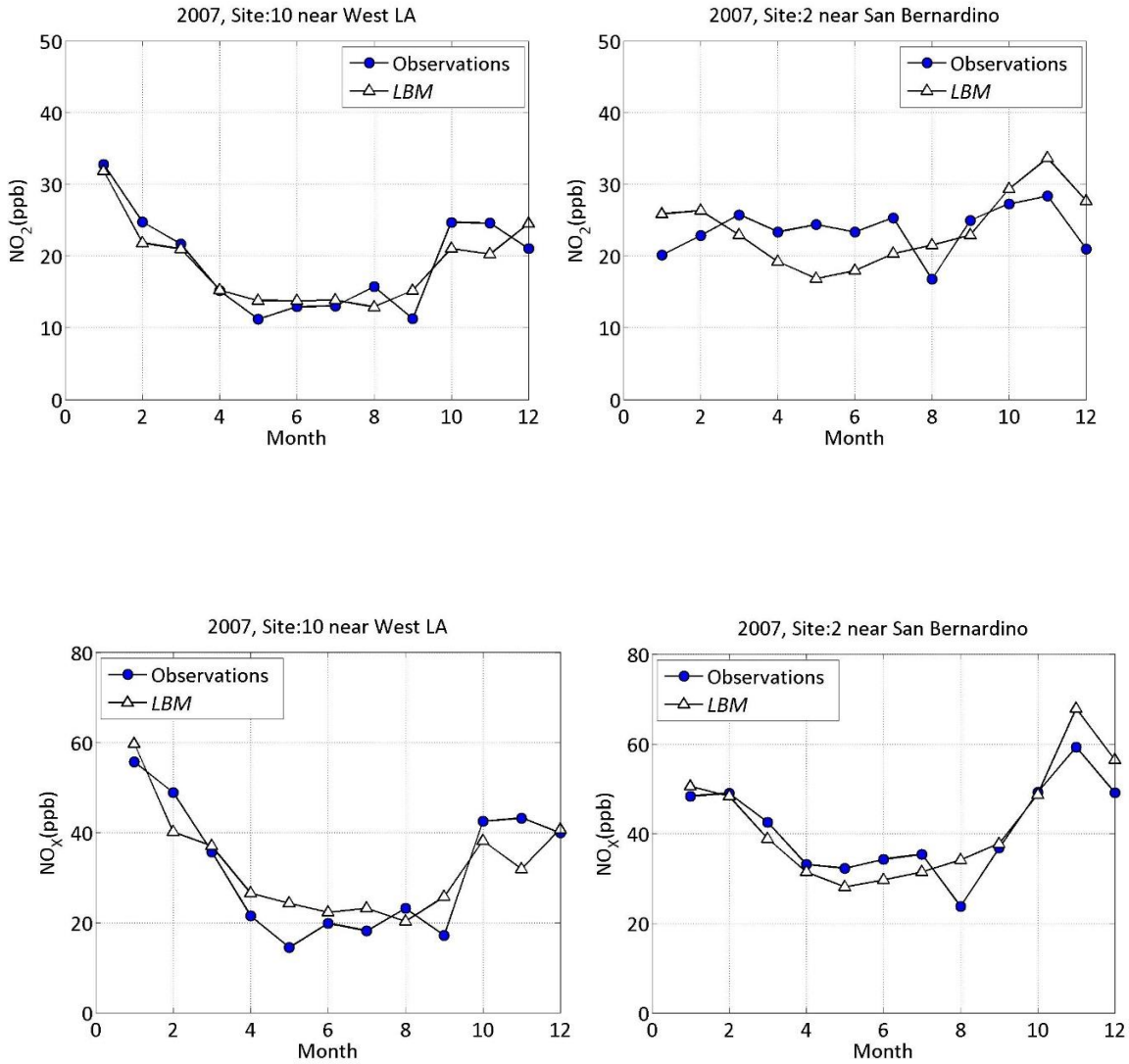

Figure 4-9 compares the modeled and observed maximum daily O_3 (top panels) and NO_2 (bottom panels) concentrations at these stations. Statistics of the model performance reveal that the bias, as indicated by m_g, ranges from 10 to 20%, and the scatter (95% confidence interval for the ratio of predicted to observed concentrations) is less than 2.56. More than 87% of the estimated values are within a factor of two of the observations. The performance of *LBM* in estimating the background concentrations of O_3 and NO_2 in the SoCAB is

expressed in terms of the statistical parameters *NMB*, *NME*, and the correlation coefficient r^2 (Table 4-1).

Figure 4-9: Daily maximum O3 (top panels) and NO2 (bottom panels) concentrations compared with observations at two sites, in West LA (left panels) and San Bernardino (right panels), in the SoCAB.

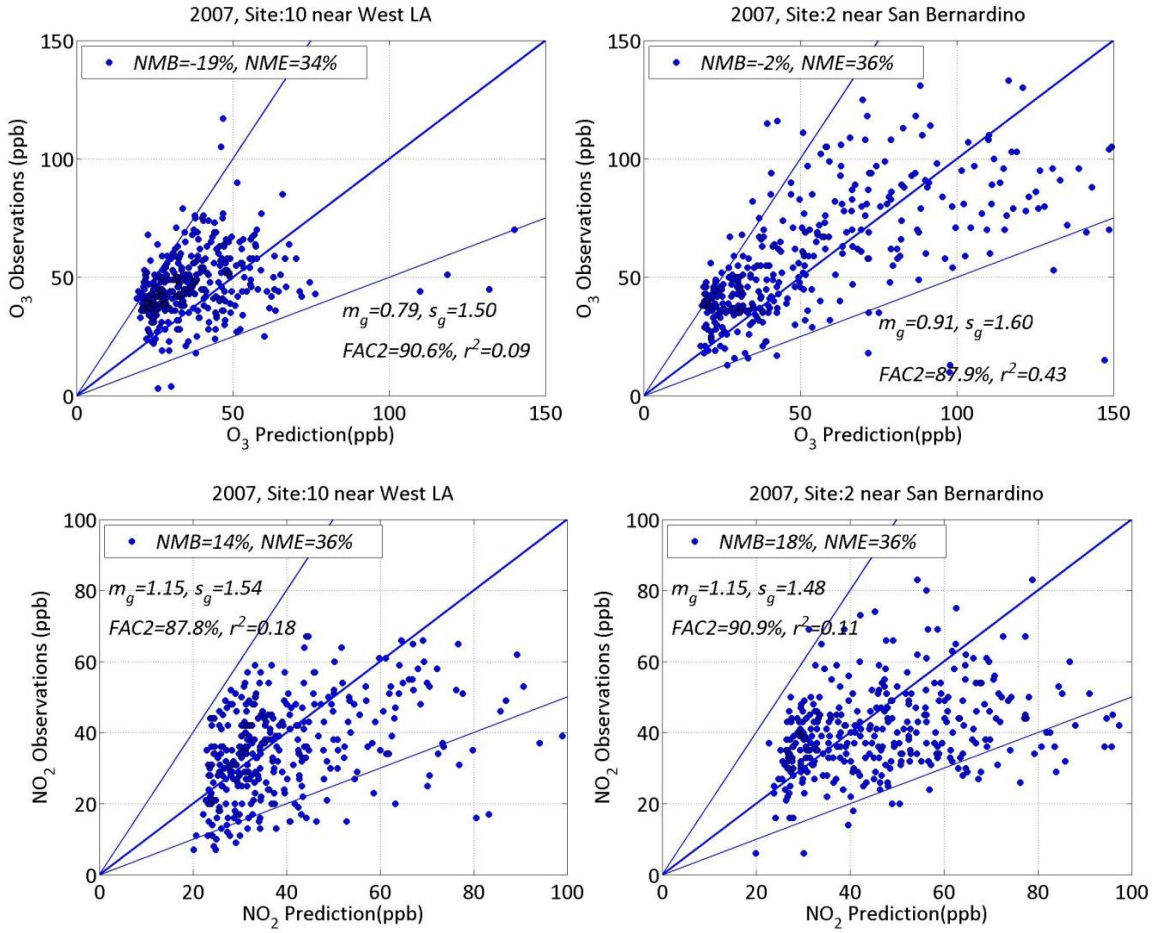

Table 4-1: Statistical performance parameter of *LBM* for calendar year 2007 at two sites (West LA and San Bernardino) in the SoCAB

Species		NMB [a] (%)		NME [b] (%)		r^2	
		W LA[1]	SB[2]	W LA	SB	W LA	SB
NO_2	Daily Max	14	18	36	36	0.18	0.11
	Monthly Averaged	-2	0	27	31	0.64	0.37
O_3	Daily Max	-19	-2	34	36	0.09	0.43
	Monthly Averaged	-44	-24	48	27	0.57	0.92

a: Normalized Mean Bias

b: Normalized Mean Error

1W LA:West LA

2SB: San Bernardino

Figure 4-10 shows the daily variation of NO_x and NO_2 concentrations averaged over March and September in the SoCAB compared with model estimates. The team sees that the model overestimates NO_2 and NO_x concentrations in the early morning hours at the San Bernardino site. This might be related to the uncertainty in estimating the mixed layer height and the possibility of NO_2 dry deposition during these hours. It could also be associated with the assumed temporal profile of NO_x emissions. Figure 4-11 indicates that the model provides a satisfactory description of the spatial variation of the concentrations of these species across the 21 stations in the SoCAB.

Figure 4-10: Monthly averaged daily variation of NO_x and NO_2 compared with observations at two sites, in West LA (left panels) and San Bernardino (right panels), in the SoCAB during two different months.

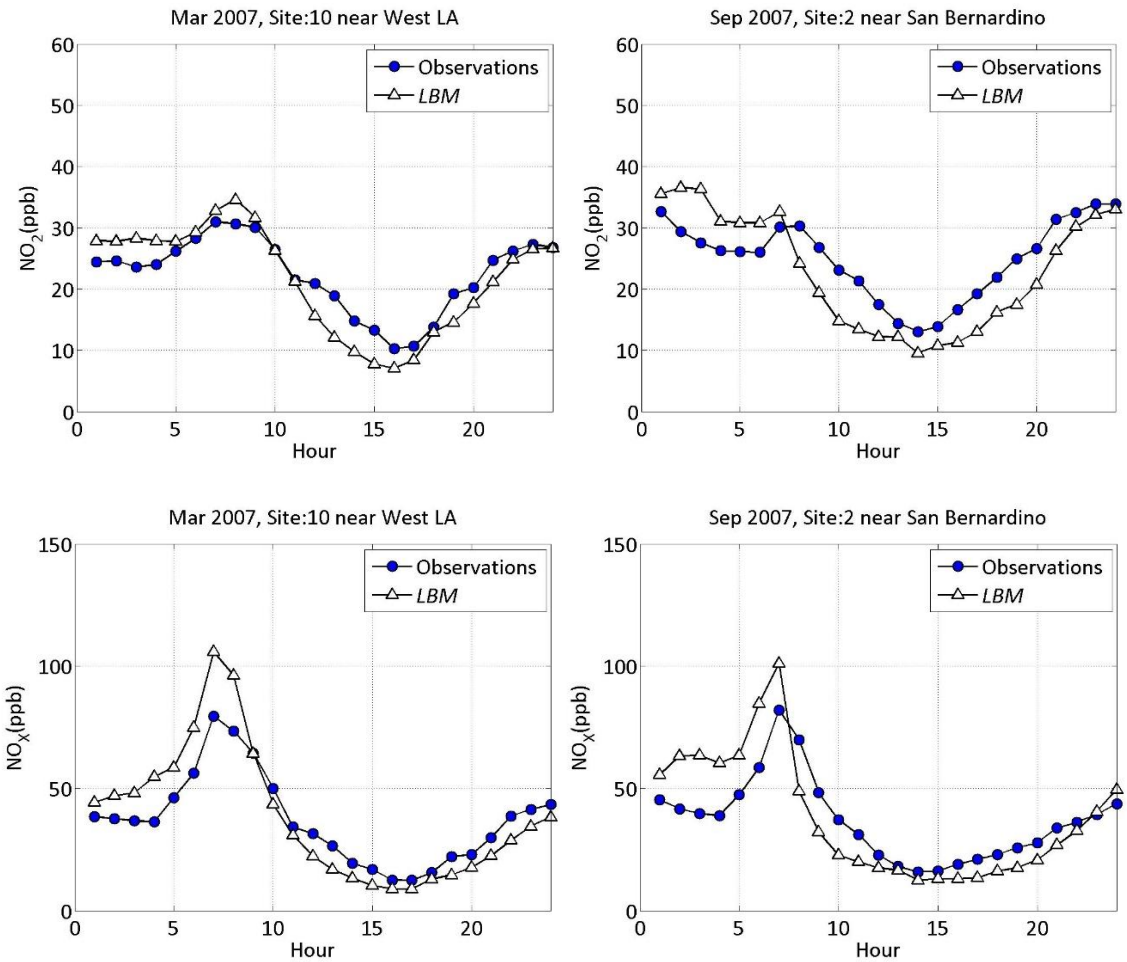

Figure 4-11: Comparison of modeled and measured annually averaged NO_x and NO_2 concentrations at 21 sites in the SoCAB.

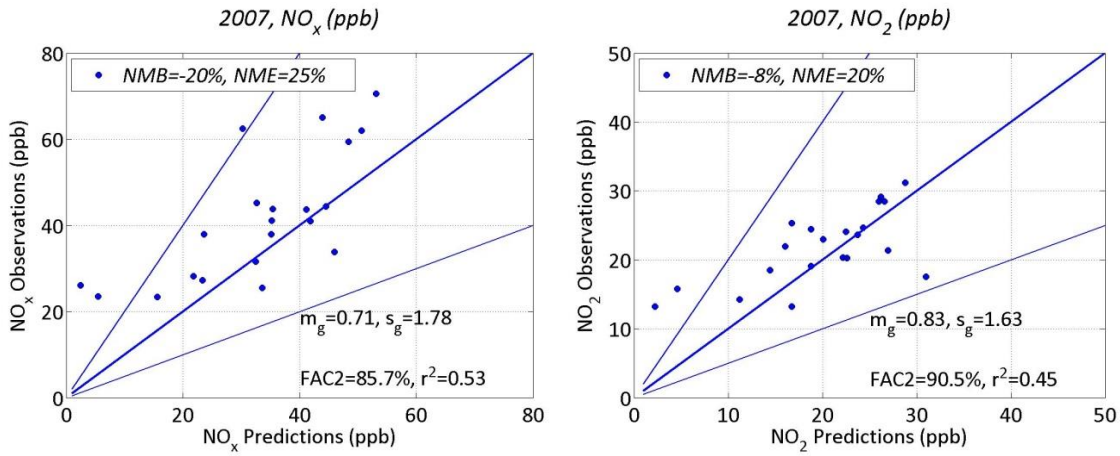

How do the performance measures of *LBM* compare with those of more comprehensive models such as *CMAQ*? Table 4-2 compares the performance of *LBM* with those of comprehensive models.

Table 4-2: Statistical Parameter of various air quality models

Study	Region/Database	Species	Model	Data Type	Simulation Period	NMB [a] (%)	NME [b] (%)	r^2
Eder and Yu (2006)	IMPROVE, STN, CASTNET,ARI	O_3	CMAQ [1]	Daily Maximum of 1-hr average	April–September, 2001	4.0	18.3	0.46
Liu et al (2010)	Eastern China	NO_2	CMAQ [2]	Monthly average of daily	Jan, Apr, Jul, and Oct 2008	-6.5~-32.0 [d]	47.1~66.6 [d]	0.09~0.36[d]
Liu et al (2010)	Eastern China	O_3	CMAQ [2]	Daily maximum of 1-hr average	Jan, Apr, Jul, and Oct 2008	1.1~12.0 [d]	16.9~36.6 [d]	0.5~0.7
McNair et al (1996)	Southern California, US	NO_2	CIT Airshed[3]	1-hr Average	June 25th, 1987	--	69 [c]	0.1
McNair et al (1996)	Southern California, US	NO_2	CIT Airshed[3]	1-hr Average	August 28th, 1987	--	44 [c]	0.52
McNair et al (1996)	Southern California, US	O_3	CIT Airshed[3]	1-hr Average	June 25th 1987	--	38 [c]	0.83
McNair et al (1996)	Southern California, US	O_3	CIT Airshed[3]	1-hr Average	August 25th 1987	--	29 [c]	0.82
Smyth et al (2006)	Vancouver, Canada	O_3	CMAQ [4]	Daily maximum of 1-hr average	August 9th - 20th2001	-2.2	24.3	--
Vijayaraghavan et al (2006)	Central California, US	O_3	CMAQ [5]	1-hr Average	Jul 30th - Aug 1st 2000	-3.9~-61.1 [e]	15.5~61.1 [f]	--
Zhang et al (2009)	IMPROVE, STN, CASTNET,	O3	CMAQ [1]	Daily maximum of 1-hr average	2001	0.1~ -11.6	19.8~20.5	--

a: Normalized Mean Bias

b: Normalized Mean Error

c: Normalized Gross Error

d: Based on surface concentrations using 36 km horizontal grid spacing

e: Normalized Bias

f: Normalized Error

1: 36 km horizontal resolution

2: Nested 12 km horizontal resolution within 36 km outer grid

3: 5 km horizontal resolution

4: Nested 4 km horizontal resolution within 12 km outer grid

5: 4 km horizontal resolution

AIRS-AQS:Aerometric Information Retrieval System-Air Quality Subsystem. Contains 1161 sites located primarily in cities and towns in the U.S.

CASTNET: Clean Air Status and Trends Network. Contains 83 sites located primarily in remote/rural areas in the U.S.

IMPROVE: Interagency Monitoring of Protected Visual Environments. Contains 134 sites located primarily in remote areas in the western U.S.

NADP: National Acid Deposition Program. Contains 250 sites nationwide in the U.S.

SEARCH: Southeastern Aerosol Research and Characterization. Contains 8 sites located in the urban/suburban areas in the southeastern U.S.

STN: Speciated Trends Network. Contains 139 sites in urban areas in the U.S.

Eder and Yu (2006) compared a full year of concentrations from *CMAQ* simulations to data from four nationwide monitoring networks (*IMPROVE, STN,CASTNET, and ARIS-AQS*) in the United States. *CMAQ*'s performance at estimating criteria pollutants and particulate matter (*PM*) concentrations varies significantly. Estimates of 1-hr and 8-hr peak O_3 concentrations compare well with data, with correlation coefficients, r^2, of 0.46 and 0.47 respectively. However, *CMAQ* does not show comparable performance in estimating nitrate (NO_3^-) concentrations with r^2 ranging from 0.13 to 0.38. *CMAQ* (Smyth et al., 2006) captures the spatial and temporal distribution of O_3 concentrations measured during the *Pacific 2001* experiment (Li, 2004). Liu et al (2010) applied *CMAQ* to study the formation and seasonal variations of major pollutants such as SO_2, NO_2, and PM_{10} in China during January, April, July, and October of 2008. The predicted surface NO_2 concentrations were significantly smaller than the corresponding observed concentrations for all four months, and the mixing ratios of the maximum O_3 concentration in January and July are over-predicted. Vijayaraghavan et al. (2006) evaluated *CMAQ*'s performance against an episode from the Central California Ozone Study (CCOS) in July and August 2000. This study found that *CMAQ* underestimates 1-hr O_3 concentrations. Zhang et al. (2009) conducted a comprehensive study to evaluate *CMAQ*'s ability to reproduce the long-term variation of pollutants such as O_3. The study compared results from a *CMAQ* simulation of a full year to both ground-based and satellite measurements; the normalized mean bias ranges from 11% to 0.1% for the annual maximum 1-hr O_3 mixing ratio (Zhang et al., 2009).

The California Institute of Technology (*CIT*) Airshed model is another comprehensive air quality model that is widely used (Cohan et al., 2008; Ensberg et al., 2010; Carreras-Sospedra et al., 2010) for regional air quality studies in Southern California. McNair et al. (1996) evaluated the *CIT Airshed* model against the Southern California Air Quality Study (SCAQS)(Lawson, 1990) database and concluded that the *CIT Airshed* model is able to predict the diurnal variation of the reactive species and the transport of the relatively non-reactive species.

A comparison between the values listed in Table 4-1 and those of Table 4-2 shows that the performance of *LBM* is comparable to that of complex models such as *CMAQ* and *CIT Airshed*. The *NMB* is less than 45% and the *NME* is within 25 – 50%.

4.3.2 The San Joaquin Valley Study

The SJVAB is one of the 15 air basins located in California, USA. The SJVAB has an area of approximately 60,900 square kilometers and is surrounded by the Coastal Range Mountains to the west, the Sierra Nevada Mountains to the east, the Transverse Range Mountains to the south, and the Sacramento Valley to the north. These mountain ranges give the Valley a bowl-shaped topography that retains air pollutants generated by the activities of the Valley's three million residents and their two million vehicles. The presence of two major highways, CA 99 and Interstate 5, adds high vehicular emissions to the existing NO_x emissions in the valley. The San Joaquin Valley does not meet the 2008 8-hour averaged ozone national ambient air quality standards (NAAQS) of 75 ppb (Jin et al., 2011). The California Air Resources Board (*CARB*) has proposed a new state implementation (SIP) plan to attain the 1997 80 ppb 8-hour averaged ozone NAAQS in the San Joaquin Valley by June 15, 2024 (CARB, 2007).

Several studies have been conducted to examine the formation of ozone and particulate matter in the SJVAB (See Table 2 for relevant studies). Here the team describes the results from the application of LBM to the SJVAB for the year 2005. The emission inventory, provided by Samuelsen et al. (2010), consists of an 80×89 grid of 4 × 4 km squares (Figure 4-12). Since the total NO_x emission in this inventory was slightly different from that reported by *CARB* as the official inventory for the year of 2005, the team scaled this inventory to match the 594.6 tons per day of total NO_x emission in the SJVAB as reported by *CARB* (http://www.arb.ca.gov/ei/emissiondata.htm). High emissions occur primarily along major roads such as Interstate 5 and Highway 99, and at large cities such as Fresno and Bakersfield. The background ozone concentration is taken to be 30 ppb, and the *VOC* concentration is assumed to be a multiple of the NO_x concentration:

$$[VOC] = [NO_x] \times Ratio + [VOC]_{Background} \tag{6}$$

where the ratio is taken to be 6. This ratio is consistent with measurments of VOC/NOx ratios measured in the Los Angeles basin (Fujita et al., 2003). The team then add a background *VOC* concentration of 40 ppbC for the simulation of NO_x, NO_2, and O_3 in the SJVAB. This value is consistent with the minimum daily averaged concentrations of non-methane hydrocarbons *(NMHC)* in the SJVAB reported by the Air Quality and Meteorological Information System (*AQMIS*) of the CARB for the year, 2005 (http://www.arb.ca.gov/aqmis2/aqmis2.php).

There are 28 ambient monitoring sites in the San Joaquin Valley study domain as shown in Figure 9. The red dots indicate the location of the 28 sites and the white numbers are the corresponding site numbers. The team simulated the concentrations at the 21 monitoring sites that are located in the valley. The 2005 hourly NO_2, NO_x, and O_3 data at the 21 sites were obtained from the *CARB* website (CARB, 2012). Sites 9 and 11 were excluded from this evaluation study because the concentrations were overestimated by a large amount and the evaluation at these two sites is not representative of the model performance. The reason for this overestimation might be due to the uncertainties in the gridded emission inventory. Both sites 9 and 11 are located in the suburbs of Fresno and Bakersfield and might have much lower emissions than that indicated by the gridded emission inventory. Wind speeds and directions measured at 11 meteorological stations in the SJVAB were used to compute back trajectories. The *GRS* mechanism was used to model the chemical processes.

Figure 4-12: Daily average NO_x emission in the San Joaquin Valley in 2005

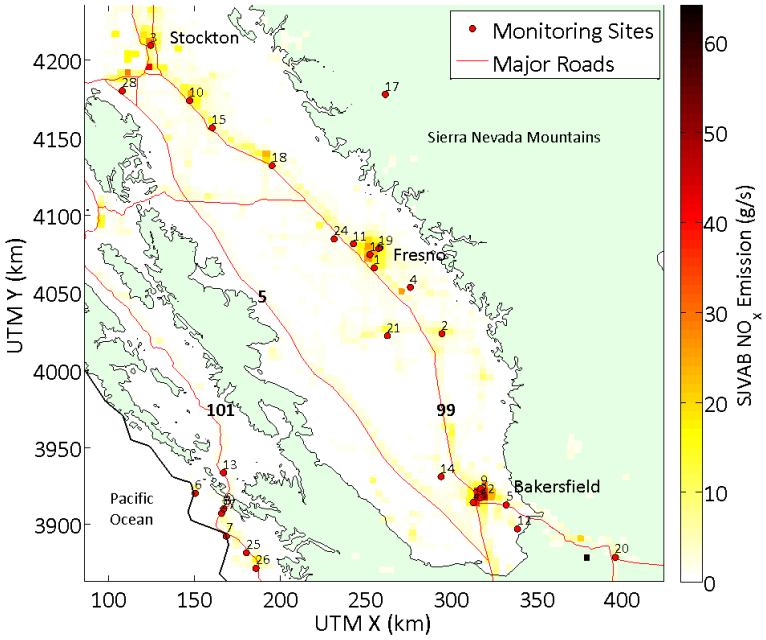

Red dots indicate monitoring site locations, and the numbers are the corresponding site numbers. Note: Emissions from Highway 101 are excluded in the simulations.

Figure 4-13 shows model performance in describing annually averaged 1-hr NO_x, NO_2, and O_3 concentrations of 19 monitoring sites in the San Joaquin Valley. More than 85% of the modeled NO_x and 90 % of the NO_2 concentrations are within a factor of two of the corresponding observed concentrations. The predicted annually averaged 1-hr O_3 concentrations for all 19 monitoring sites are within a factor of two of observations.

Figure 4-13: Annual average concentration of the 19 monitoring sites in the SJVAB

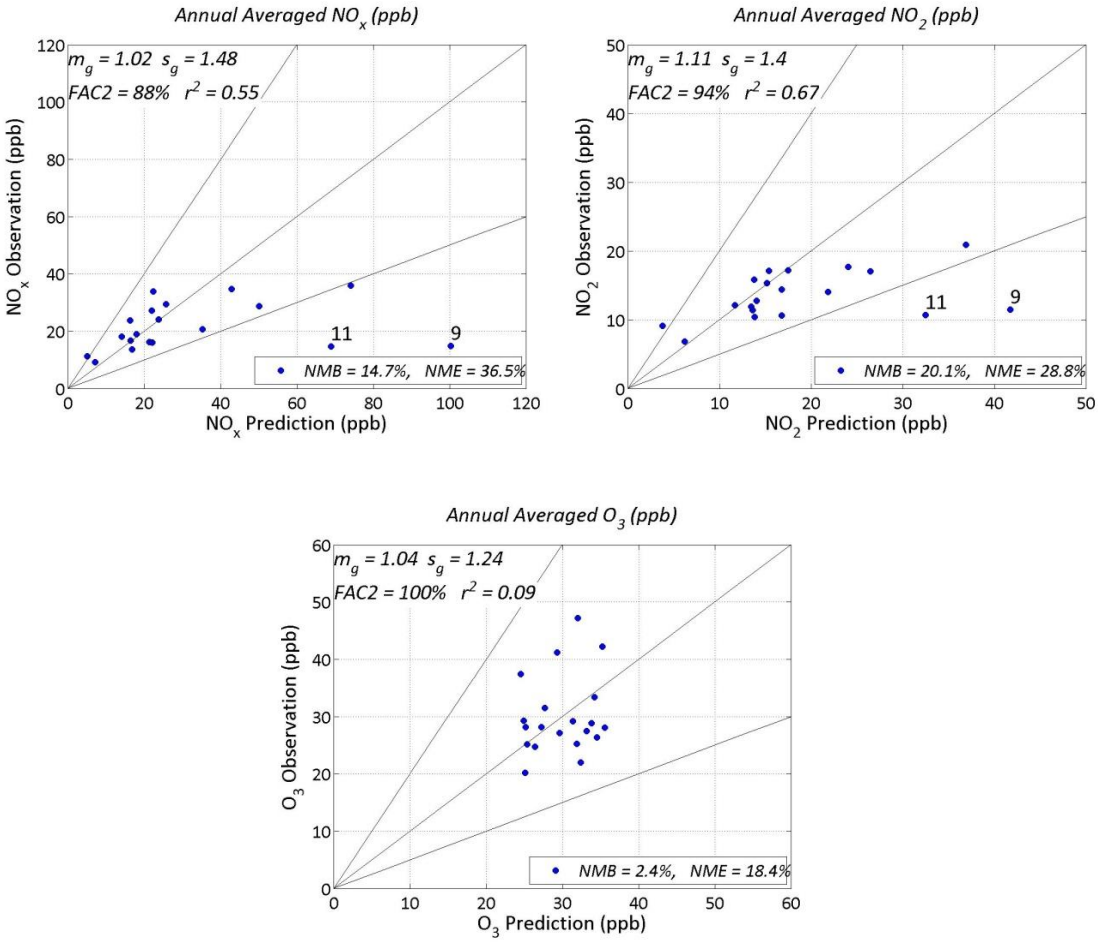

Upper left panel: NO_x. Upper right panel: NO_2. Lower panel: O_3. Note: Statistics shown are calculated excluding site 9 and 11.

Figure 4-13 shows that *LBM* provides a good description of the spatial variation of NO_x and NO_2 at regional scales; the correlation coefficients (r^2) are 0.55 and 0.67, respectively. Figure 4-13 also indicates that the observed annual averaged O_3 in the SJVAB varies over a narrow range (20 - 30 ppb), except for stations 12, 17, and 20 (the relative standard deviation of the observed O_3 concentrations is about 12%). This suggests that the annual averaged O_3 is mostly driven by the background O_3, and that the high ozone events are relatively infrequent. With m_g close to unity (=1.02, 1.11, and 1.04 for NO_x, NO_2 and O_3, respectively), the model shows little or no bias in estimating the annual average NO_x, NO_2 and O_3 concentrations.

We next examine the performance of *LBM* in the San Joaquin Valley in more detail at two of the 19 monitoring sites: Site 5, which is located near Bakersfield, and Site 14, which is located in Shafter, a town 26 kilometers northwest of Bakersfield. Figure 4-14 compares the modeled daily averaged NO_x, NO_2, and O_3 concentrations to the corresponding observed concentrations at these two sites. The left panels of the figure show that the model provides an adequate description of the daily average NO_x, NO_2, and O_3 concentrations at Bakersfield, while it slightly underestimates and overestimates the NO_x and NO_2 concentrations in Shafter, respectively. More than 80% of the modeled NO_x and NO_2 concentrations are within a factor of two of the corresponding observed concentrations. Even though the correlation (r^2) between the modeled and observed daily average NO_x and NO_2 ranges from 0.25 to 0.4, the modeled daily average O_3 concentration correlates well with the observed O_3 concentration as seen in the lower panels of Figure 4-14 (r^2 is 0.58 and 0.79 at site 5 and 14, respectively).

Figure 4-14: Comparison of modeled daily-average concentrations with the corresponding observed concentrations

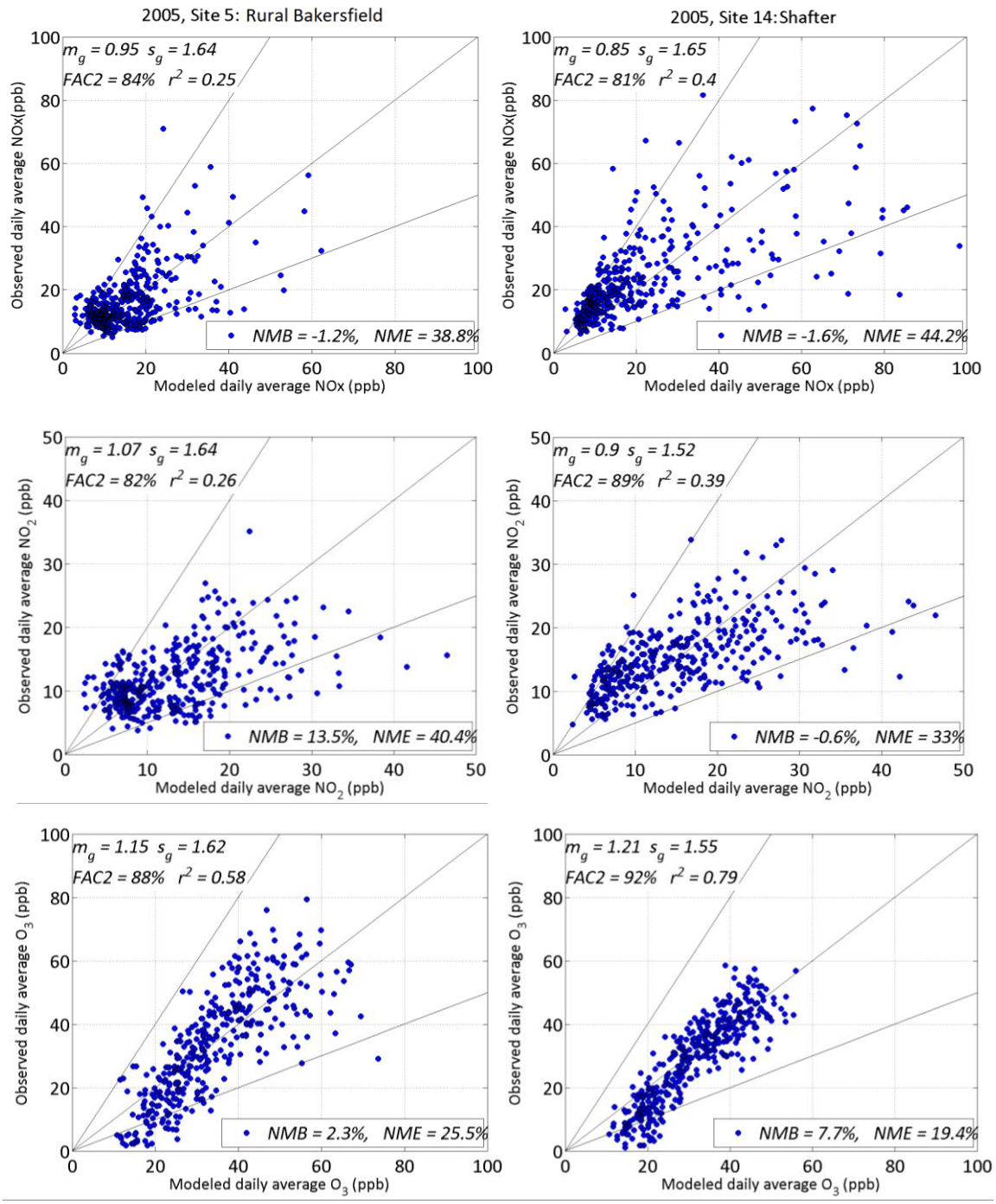

Upper Panels: NO_x, Middle Panels: NO_2, and Lower Panels: O_3. Left panels correspond to Site 5, and right panels correspond to Site 14

Figure 4-15 compares the modeled daily maximum NO_x, NO_2, and O_3 concentrations to the observed concentrations at sites 5 (Bakersfield) and site 14 (Shafter) for the whole year of 2005. The team sees that the model performs reasonably well at site 5 while at site 14 it

slightly under/overestimates NO_x and NO_2 concentrations, respectively. At both sites 5 and 14, about 90% of the modeled daily maximum O_3 concentrations are within a factor of two of the corresponding observed concentrations. Statistics of the model performance show that the scatter (s_g^2) of the predicted daily maximum O_3 is less than 2.3 (s_g^2 = 2.28 at site 5), and the bias (m_g) is 20% and 11% at site 5 and 14, respectively. The correlation of observed and predicted daily maximum O_3 is relatively high at site 14 (r^2 = 0.61) while it is 0.25 at site 5.

Figure 4-15: Comparison of modeled daily maximum concentrations with the observed concentrations for sites 5 and 14 from January – December 2005

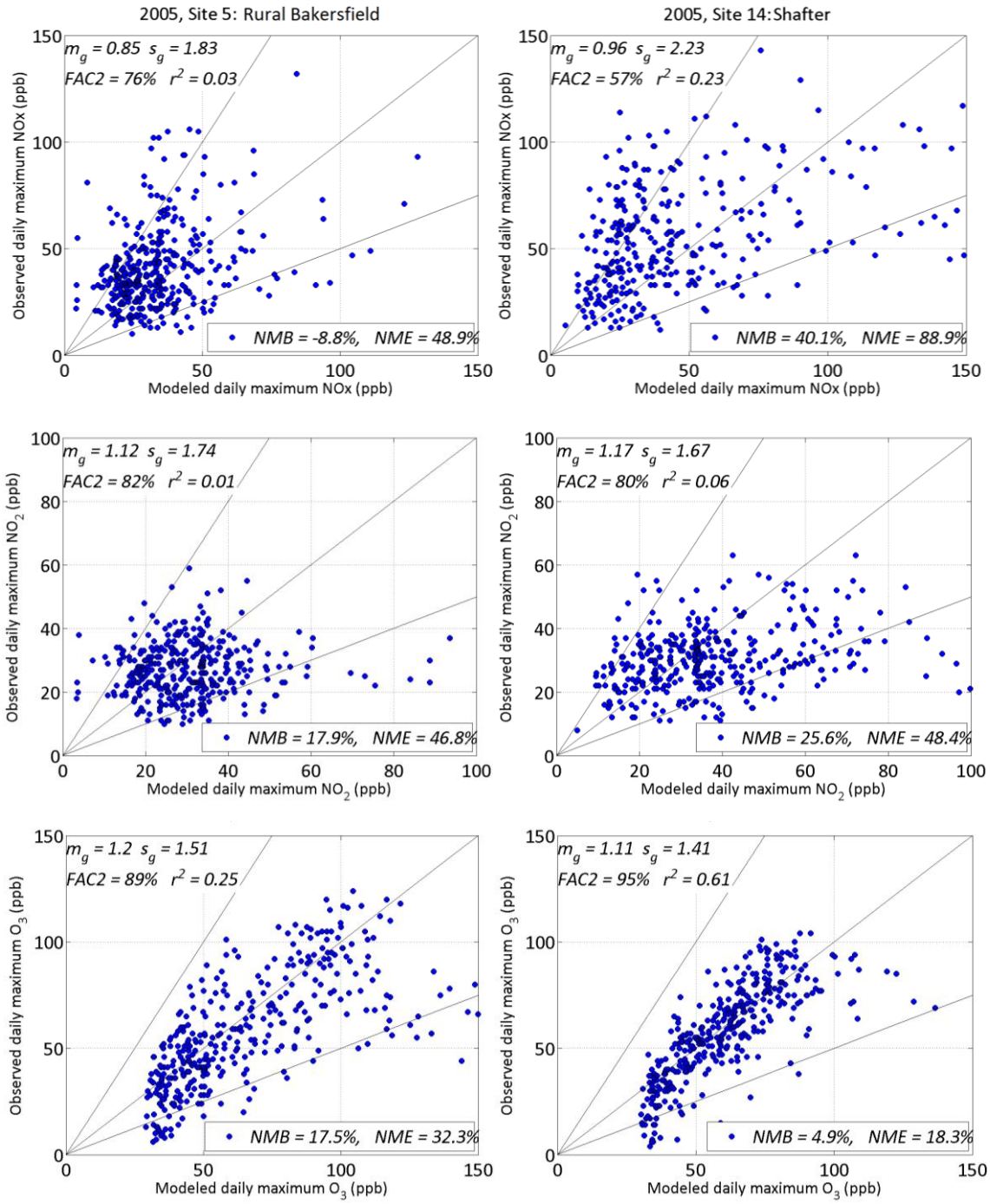

Upper Panels: NO_x, Middle Panels: NO_2, and Lower Panels: O_3. Left panels correspond to Site 5, and right panels correspond to Site 14.

The ability of *LBM* in reproducing the seasonal variations of NO_2, NO_x and O_3 concentrations is depicted in Figure 4-16. Table 4-3 provides performance measures of *LBM* in describing the daily average and maximum NO_2 and O_3 concentrations at two sites in the SJVAB.

Figure 4-16: Modeled monthly averaged concentration compared with corresponding observed concentration for each month of the year at site 5 and 14.

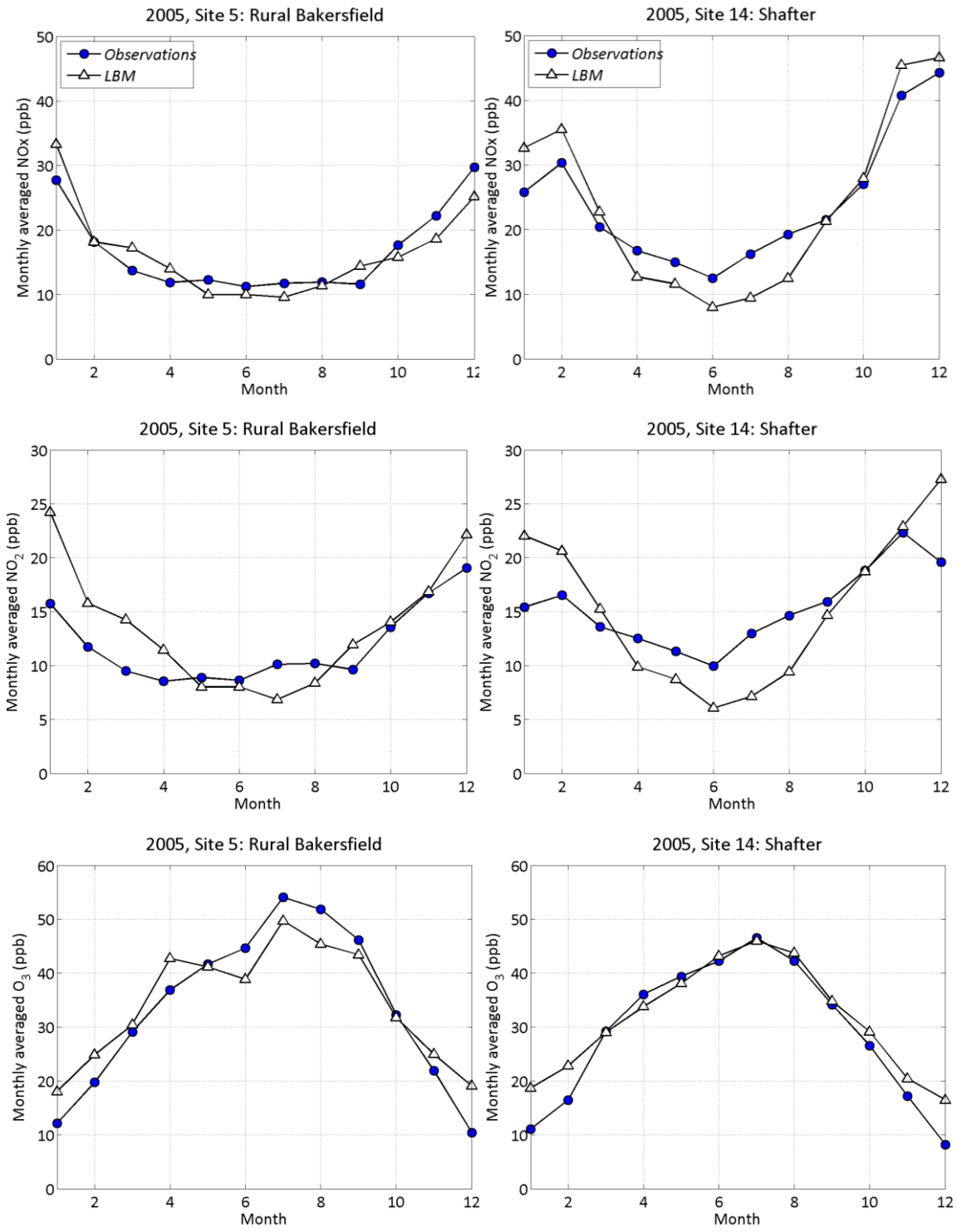

Upper Panels: NO_x, Middle Panels: NO_2, and Lower Panels: O_3. Left panels correspond to Site 5, and right panels correspond to Site 14

Table 4-3: Statistical performance measures of the *LBM* model for calendar year 2005 at two sites (Bakersfield and Shafter) in SJVAB.

Species		NMB [a] (%)		NME [b] (%)		r^2	
		Bakersfield	Shafter	Bakersfield	Shafter	Bakersfield	Shafter
NO_2	Daily Max	17.9	25.6	46.8	48.4	0.01	0.06
	Daily Averaged	13.5	-0.6	40.4	33	0.26	0.39
O_3	Daily Max	17.5	4.9	32.3	18.3	0.25	0.61
	Daily Averaged	2.3	7.7	25.5	19.4	0.58	0.79

a: Normalized Mean Bias

b: Normalized Mean Error

Figure 4-17 shows that the modeled daily variations averaged over a year correlate well with the corresponding observed variations. At site 5, the modeled NO_x concentrations clearly show a diurnal variation with the maximum occurring during rush hours, which differs slightly from the observed variations. At site 14, the model slightly overestimates NO_x concentration from midnight to 5am. The lower panels of Figure 4-17 show that the model can estimate the daytime O_3 concentration well, but that it slightly overestimates during nighttime. Although emissions are relatively low during nighttime, the high nighttime NO_x concentrations are related to the choice of the boundary layer height, the estimation of which is highly uncertain (Pournazeri et al., 2012b). The *LBM* program is implemented in MatLab, and the one year simulation of hourly concentrations at 28 receptors in the SJVAB took approximately 145 minutes to run on a machine with a 4 core Intel i7-920 2.67 GHz processor and 6 GB of ram.

Figure 4-17: Modeled annual averaged daily variation of NO_x, NO_2 and O_3 concentration compared with corresponding observations

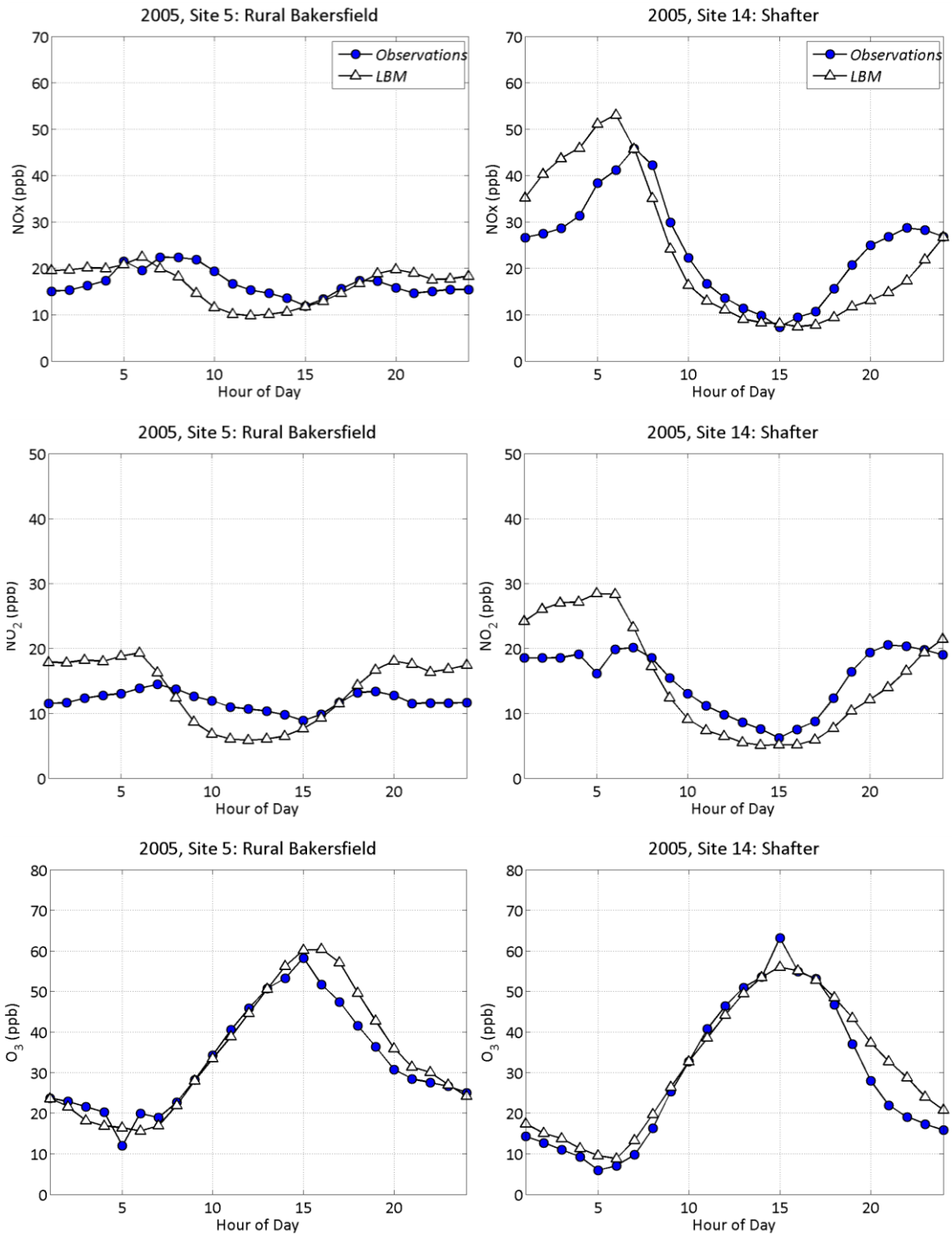

Upper Panels: NO_x, Middle Panels: NO_2, and Lower Panels: O_3. Left panels correspond to Site 5, and right panels correspond to Site 14.

4.3.3 Comparison of O_3 Time Series

As mentioned earlier, one of the main air pollution problems in California is the high levels of photochemical smog, which mostly consists of ozone (O_3) and particulate matter (PM). Hence, in this report, two O_3 episodes from the two studied air basins (SoCAB and SJVAB) were selected, and the estimated hourly averaged O_3 concentrations were compared with those from observations (Figure 4-18). The O_3 episode selected for the SoCAB occurred in the city of Azusa, located northeast of Los Angeles County, during September 1–4, 2007, where the maximum hourly averaged O_3 of 158 ppb was recorded. In the SJVAB, the selected O_3 episode refers to the city of Fresno, located in central California, where an hourly averaged O_3 concentration of 131 ppb occurred during the period of July 14–17, 2005.

Figure 4-18: *O_3* episodes during September 1 - 4, 2007 in Azusa in the SoCAB (upper panel) and July 14 - 17, 2005 in Fresno in the SJVAB (lower panel).

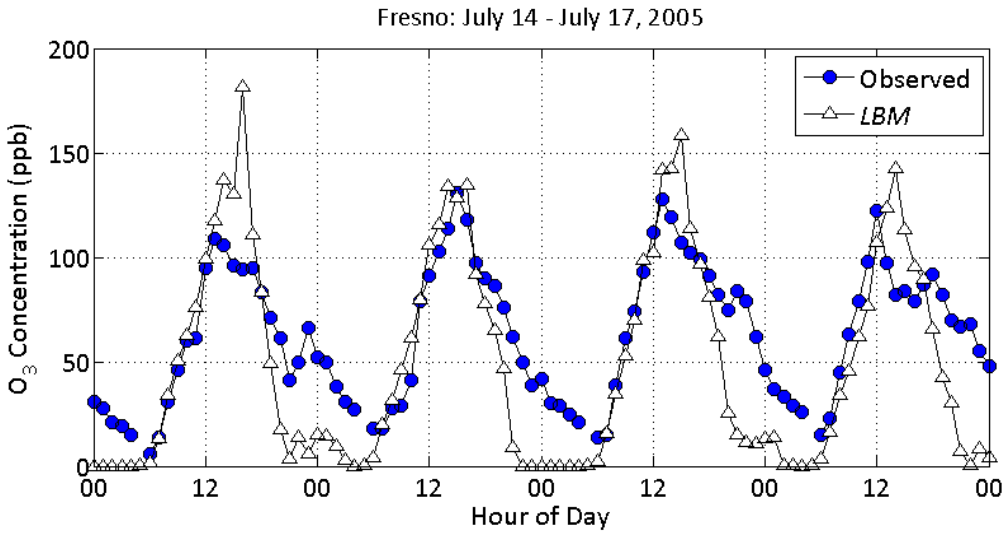

As shown in Figure 4-18, for the O_3 episode in the SoCAB, the modeled concentrations are in good agreement with the observed concentrations, except that the model slightly underestimated the maximum O_3 concentration that occurred on September 3 and 4. In the SJVAB, the estimated concentrations are well in agreement with the observed data during the daytime; however, the model fails to explain the relatively high O_3 concentrations during the nighttime. Estimated O_3 concentrations decreased rapidly to a value close to zero and stayed low throughout the night, while the observed O_3 concentrations decreased at a much slower rate throughout the entire night, to approximately 20 ppb right before sunrise. This again could be related to uncertainties in estimating the nighttime boundary height. The modeled boundary layer height decreased rapidly after sunset, which lead to an increase in NO concentrations and resulted in rapid destruction of O_3. In addition, the model slightly overestimated the daily peak O_3 concentrations on July 14, 16, and 17.

4.4 UCI-CIT Model

The University of California, Irvine - California Institute of Technology (UCI-CIT) model is a regional atmospheric transport model used to predict the air quality of Southern California. The UCI-CIT model solves numerically mass conservation equations for modeled species on a computational grid to obtain spatially and temporally resolved concentrations of gas and aerosol species of interest (Vutukuru and Dabdub 2008). Atmospheric gas-phase chemistry was modeled using the Caltech Atmospheric Chemical Mechanism (CACM) (Griffin et al. 2002).

Figure 4-19: Comparison of the UCI-CIT and Lagrangian (UCR) Models

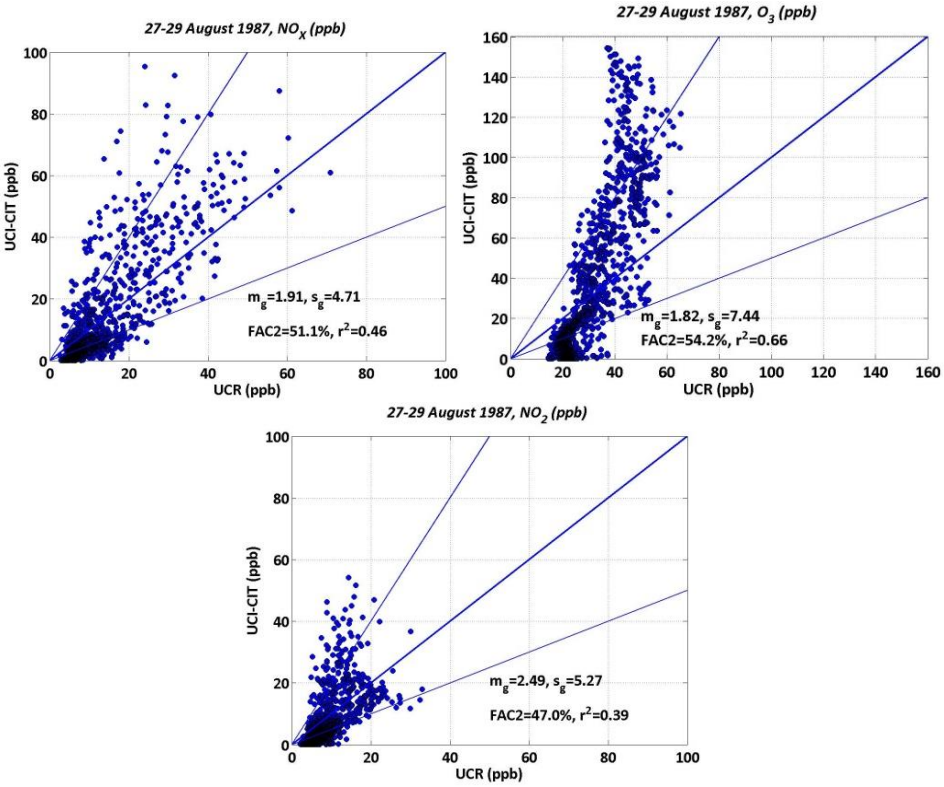

Averaged (72-hour) concentrations of NO_x, NO_2, and O_3 for 994 stations in the SoCAB, from August 27–29, 1987

In addition to the background model proposed in this report, the performance of UCI-CIT model was also evaluated for three consecutive days, from August 27–29, 1987. Results from the UCI-CIT model were obtained for 994 stations located in SoCAB. These results were compared with those obtained from the LBM (Figure 4-19). As seen in Figure 4-19, the UCI-CIT model tends to predict larger NO_x and NO_2 concentrations than the LBM. In addition, O_3 concentrations predicted by UCI-CIT vary from 0 to 160 ppb, while those predicted by UCR have a smaller variation, ranging from a minimum of 20 to a maximum of 60 ppb.

4.5 Generic Reaction Set (GRS) Chemistry

In addition to the Carbon Bond IV mechanism, which is a relative complex chemistry model, the team implemented a scheme referred to as the *GRS chemistry module.* GRS is an empirical approximation of all the processes that lead to production of radicals (RP) from the VOCs through photo oxidation. Using these radicals, NO is converted to NO_2 and causes the net production of O_3. GRS reduces the complicated chemistry reaction in the atmosphere to seven reactions among seven species, as follows:

$$ROC + h\nu \rightarrow RP + ROC \qquad \text{(R1)}$$

$$RP + NO \longrightarrow NO2 \qquad \text{(R2)}$$

$$NO_2 + h\nu \rightarrow NO + O_3 \qquad \text{(R3)}$$

$$NO + O_3 \rightarrow NO_2 \qquad \text{(R4)}$$

$$RP + RP \rightarrow RP \qquad \text{(R5)}$$

$$RP + NO_2 \rightarrow SGN \qquad \text{(R6)}$$

$$RP + NO_2 \rightarrow SNGN\ , \qquad \text{(R7)}$$

where

ROC = reactive organic compounds

RP = radical pool

SGN = stable gaseous nitrogen product

SNGN = stable non-gaseous nitrogen product

These reactions and the corresponding reaction rates are defined as:

R1. Radical production from photo-oxidation of ROC

$k_1 = 0.0067\ k_3\ f(T)$ where $f(T) = \exp\left(-1000\left[\frac{1}{T} - \frac{1}{316}\right]\right)$

R2. Oxidation of nitric oxide by radicals

$k_2 = 3.58\times10^6\ T^{-1}$

R3. Photolysis of nitrogen dioxide to nitric oxide

$k_3 = \exp\left(-\frac{0.575}{\sin(\theta)}\right)$, where θ is the sun elevation angle

R4. Nitric oxide-ozone titration reaction

$k_4 = 9.24 \times 10^5\, T^{-1} \exp\left(-\frac{1450}{T}\right)$

R5. Radical pool sink through recombination to stable products

$k_5 = 10200$

R6. Sink for nitrogen dioxide to stable gaseous nitrates

$k_6 = 120$

R7. Sink for nitrogen dioxide to stable non-gaseous nitrates

$k_7 = 120$

Reactions R3 and R4 represent chemically exact mechanisms, while the rest approximate reactions of generic chemical counterparts. Reaction R1 is a semi-empirical representation of all the processes that lead to radical production from *VOCs* through photo-oxidation. Notice that *ROC* is conserved in the reaction; thus, *ROC* becomes a surrogate for the products of the initial oxidation of the emitted *VOCs*. Reaction R2 represents the conversion of *NO* to NO_2 by radicals. Notice that, unlike the reactions in the actual mechanism, it leads to the termination of generic radicals, *RP*. Reaction R5 represents another sink for the radical pool. Reactions R6 and R7 lead to the formation of organic and inorganic nitrates. The rates of these "pseudo" reactions have been determined empirically by fitting the ozone obtained from the *GRS* to smog chamber data. Reaction R1 is the most important reaction in the semi-empirical *GRS*. The rate of this reaction has been calibrated against the rate at which radicals are produced by the different types of *VOCs*. The reactivity coefficient, 0.0067, in R1 was derived by Johnson (1984) for a mixture of *VOCs* dominated by automobile emissions, and is incorporated by Hurley et al (2003) in an Eulerian air pollution model. Venkatram et al. (1994) used a slightly different approach by converting *VOC* emissions to equivalent *ROC* by calibrating the *GRS* mechanism with a more complete chemical mechanism.

The team implemented this model into the Lagrangian background model by solving this set of stiff differential equations numerically. The team predicted the NO_x, NO_2, and O_3 concentration for 21 receptors in SoCAB for September 2007 (Figure 4-20).

Figure 4-20: Monthly Averaged Concentrations Predicted Using the GRS Chemistry Model for 21 Receptors in SoCAB (top panel) Comparison between the observations, transport model with GRS and CBM IV chemistry module (bottom panel)

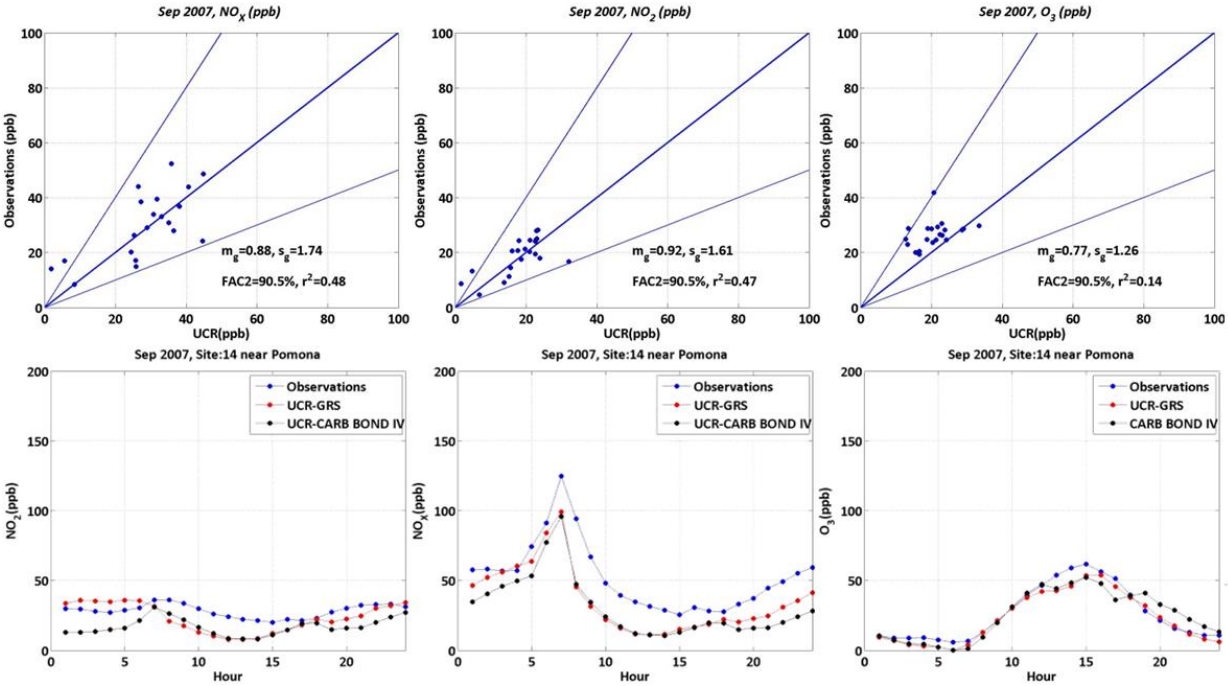

Despite the simplicity of the GRS chemistry module, it performs reasonably well compared with the Carbon Bond IV model, which the team used earlier. This suggests that the most important factor affecting the concentrations is the transport scheme rather than the chemistry.

4.6 Sensitivity Study

The comparison of model estimates with observations shows that the LBM, despite its simplicity, can adequately predict concentrations of NO_2 and ozone (O_3), which leads us to ask what elements of the model are the most important for producing these estimates. To answer this question the team performed sensitivity studies of the effect on the concentration estimates of the emission distribution, wind speed, wind direction, boundary layer height, species age, and back-trajectory tracing time. These variables were modified within the model and compared the resulting annual average NO_x, NO_2, and O_3 concentrations with the observed concentrations. The corresponding geometric mean (m_g) and geometric standard deviation (s_g) are shown in Table 4-4. The cases included in the table are: (1) the wind speed is doubled, (2) 90° is added to the wind direction, (3) the emissions are made spatially uniform, (4) the boundary layer height is set to a constant for each 24-hour period, (5) the species age is doubled, (6) the back-trajectory tracing time is increased to 48 hours and (7) 72 hours, and (8) the back-trajectory tracing time is increased to 48 hours,

and the boundary layer height is set to a constant. The team also compared the hourly concentration variation of cases 3, 4, 5, 6, and 8. Plots of the hourly concentration variation are shown in Figure 4-21, Figure 4-22, and Figure 4-23.

We also formulated a simple model where the concentration is calculated as:

$$C = \frac{QT}{z_i} \tag{4-8}$$

where T = 24 hr and Q and z_i are the emission rate and boundary layer height within the local grid square. The results of equation 4-8 are shown in Table 4-4 as Case 9.

Table 4-4: Comparison of m_g and s_g for the Different Cases of the Sensitivity Study

Case Number	Type of Sensitivity Study	m_g			s_g		
		NO_x	NO_2	O_3	NO_x	NO_2	O_3
0	Base Model (Original Met)	1.02	1.11	1.04	1.48	1.4	1.24
1	Wind Speed × 2	0.82	0.94	0.98	1.38	1.29	1.22
2	Wind Direction + 90°	0.85	0.97	1.04	1.44	1.36	1.2
3	Uniform Emission	0.42	0.53	0.84	3.86	4.79	3.08
4	Constant BL Height	1.18	1.37	1.2	1.4	1.36	1.26
5	Species Age × 2	1.02	1.27	1.66	1.48	1.55	1.42
6	48-hr Trajectory	1.07	1.27	1.41	1.47	1.48	1.39
7	72-hr Trajectory	1.08	1.29	1.61	1.47	1.5	1.49
8	48-hr + Constant BL Height	1.68	2.01	1.78	1.41	1.37	1.48
9	Simple Model ($C = Q \times T/z_i$)	2.37	--	--	3.02	--	--

Cases 1 and 2 do not significantly change the model estimates relative to the unmodified LBM. This is likely because the modified trajectory still passes through grid squares with emissions that are similar to those of the unmodified trajectory. The model sensitivity to wind speed and direction must depend on the emission distribution because the function of the trajectories is to select the grid squares from which emissions contribute to the predicted concentrations. If the emission distribution within the San Joaquin Valley were less homogeneous, then the model would likely be more sensitive to the wind speed and direction. This study also validates the team's choice of the surface winds, rather than the upper air winds, for calculating the trajectories in the SJVAB and SoCAB because the model estimates are not very sensitive to the wind speed in these domains.

Making the emissions within the San Joaquin Valley (center of Figure 4-12) spatially uniform causes the model to underestimate NO_x, NO_2, and O_3 concentrations significantly, which indicates that the emission distribution is a key element of the model. Figure 4-22 shows that the model does not predict the peak in NO_x, which occurs around 7 a.m. when the emissions are made uniform. The peak in concentration occurs due to the large emissions that occur in Bakersfield, Fresno, and Stockton during rush hour and are then transported to the surrounding sites. When the emissions are made uniform, the large emissions are no longer associated with these geographic locations, so the model underestimates concentrations at the surrounding sites.

The modeled boundary layer height has a significant effect on the predicted concentrations. The team found that replacing the boundary layer height with the 24-hour average value causes the model to underestimate concentrations during the day and overestimate them during the night, as shown in Figure 4-22. This shows that the boundary layer height formulation is important for predicting the daily concentration variation.

Doubling the species age (Case 5) resulted in an increase in the O_3 m_g from 1.04 to 1.66, and an increase in the NO_2 m_g from 1.11 to 1.27. Figure 4-21 shows that the prediction of the hourly variation of O_3 does not show the correct trend (peak during noon), and the NO_2 prediction shows an unrealistically large peak during the night, when the species age is doubled. This shows that the team's formulation of species age is useful for predicting the chemical processes separately from the transport.

Figure 4-21: Hourly Concentration Variation for the Base Case with No Changes to the LBM (left) and the Case When the Species Age is Doubled (right)

Species	Base Case	Species Age × 2
NO_x	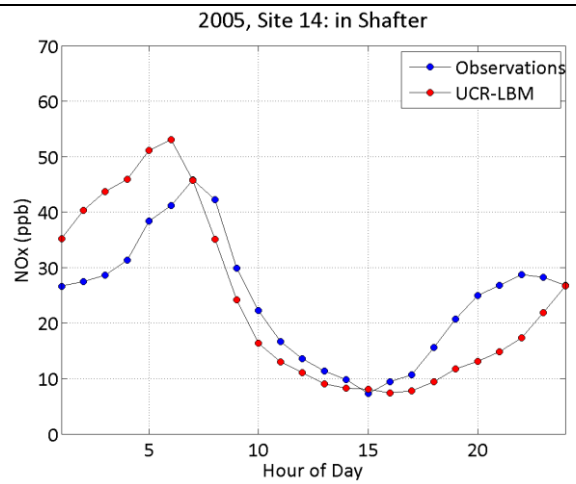	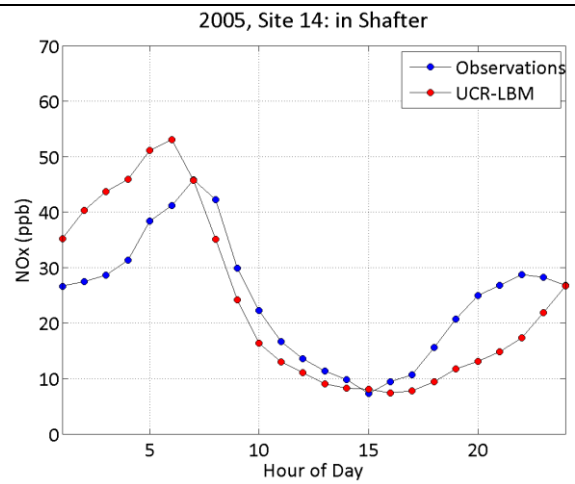
NO_2	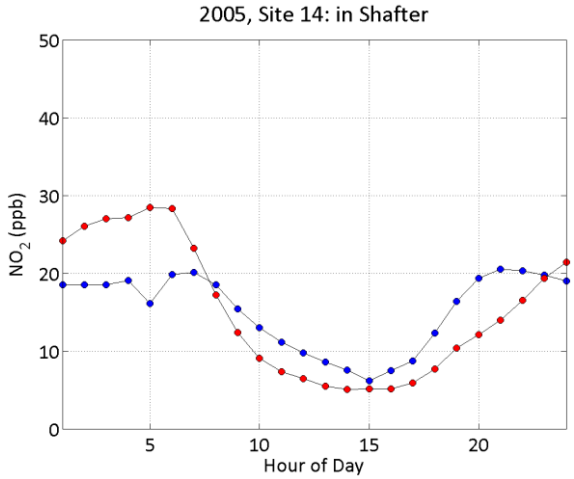	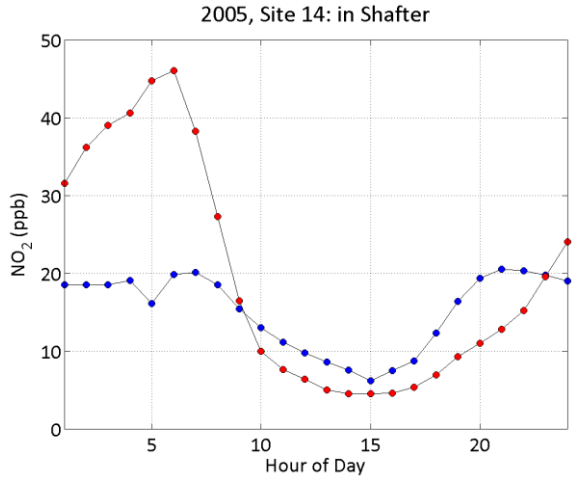
O_3	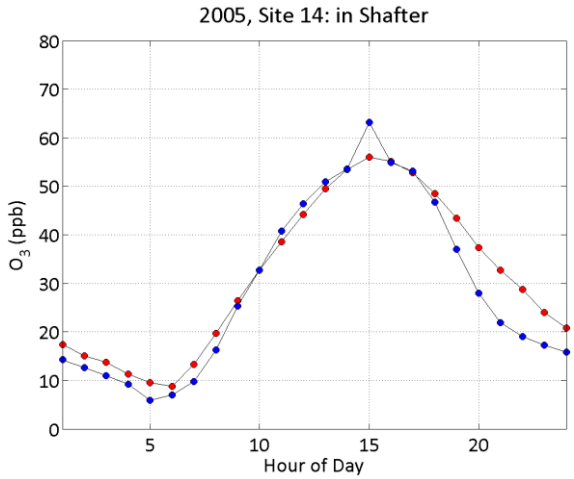	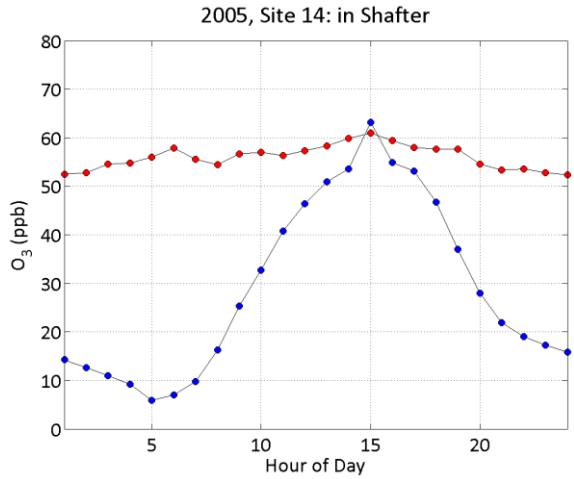

Figure 4-22: Hourly Concentration Variation for the Constant Boundary Layer Height Case (left) and the Uniform Emission Distribution Case (right)

Species	Constant Boundary Layer Height	Uniform Emission within the Valley Region
NO_x	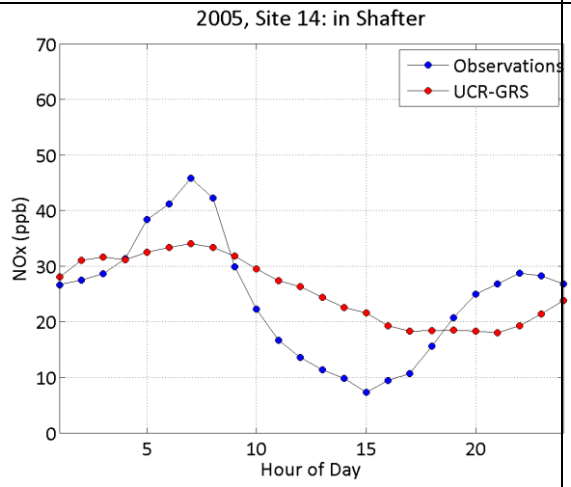	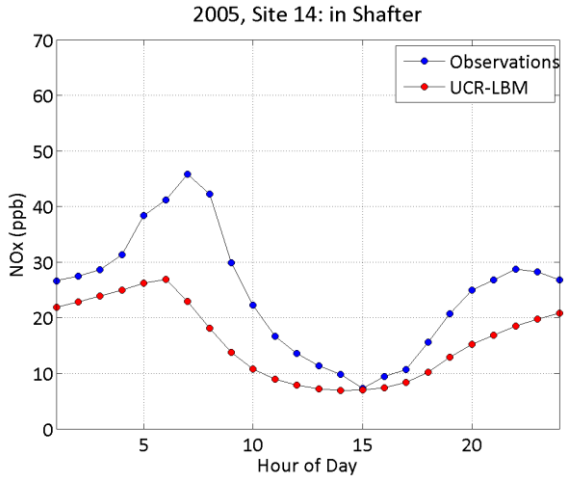
NO_2	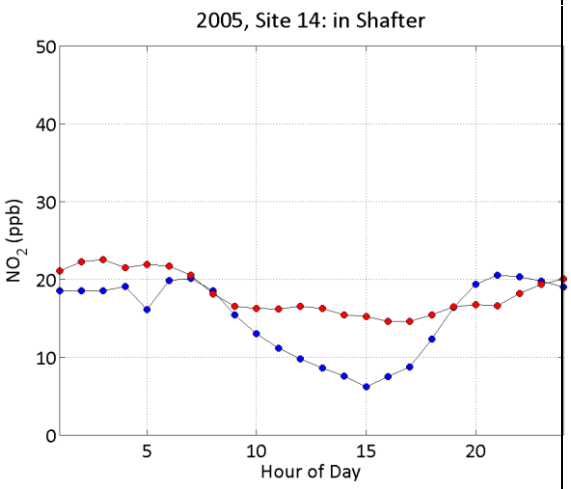	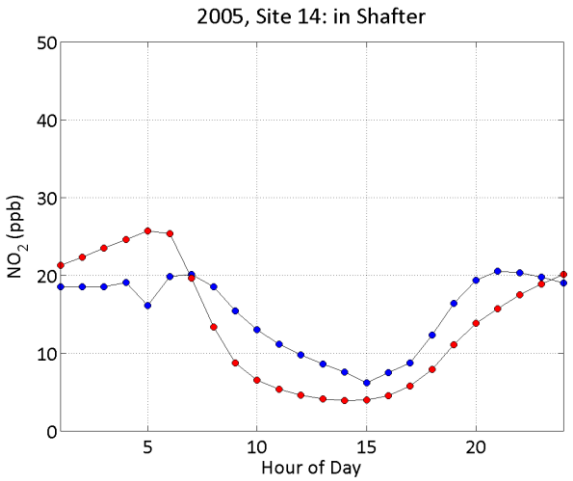
O_3	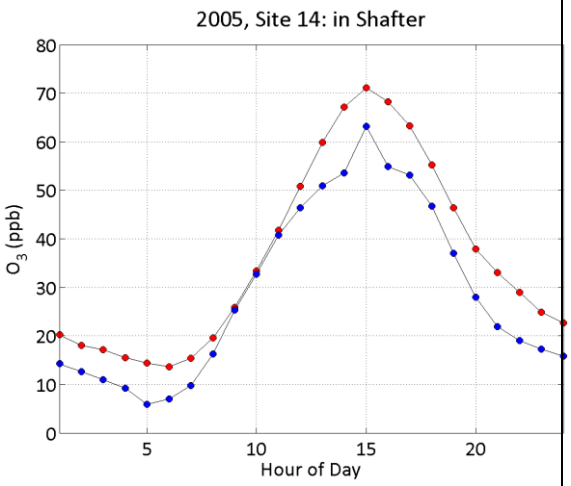	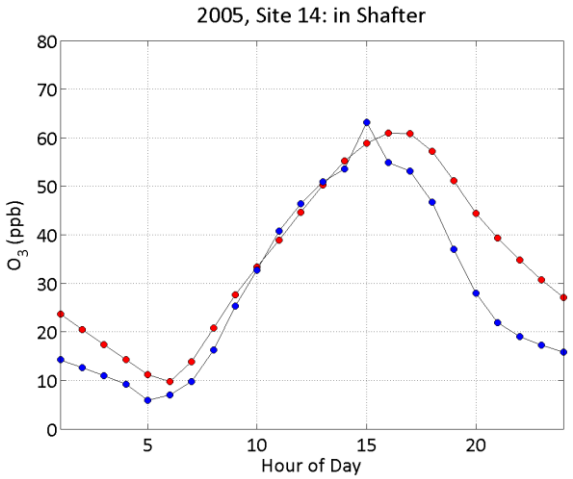

In this formulation of the LBM, trajectories were traced back over a 24-hour time period, but the choice of this time scale could alter concentration predictions. When the time period was

increased from 24 hours to 48 hours and 72 hours, the predicted NO_x concentrations did not change significantly, but the model overestimated the O_3 and NO_2 concentrations at night. The NO_x is unchanged because of the boundary layer height variation over a 24-hour period; when the boundary layer collapses at dusk, the pollutant mass above the nighttime boundary layer height is lost, which reduces the total mass that the model accumulates over a 24-hour period and limits the concentration increase over time periods greater than 24 hours. This can also be seen in the model sensitivity in Case 8, where the boundary layer height was set to a constant over each 24-hour day and the back trajectory was calculated over 48 hours. The model overestimated NO_x by about 70 percent in this case because the boundary layer height did not decrease at the beginning of each night, so the model could accumulate a larger pollutant mass.

Figure 4-23 shows the hourly concentration variation for these cases, which also shows the effect of holding the boundary layer height constant while increasing the back-trajectory time. The effect on NO_2 and O_3 of increasing the back-trajectory time is similar to that of increasing the species age (compare the right half of Figure 4-21 with the left half of Figure 4-23). This gives credence to the boundary layer height formulation used in the LBM, since it naturally limits the concentration from upwind sources in the same manner as could be expected to occur in nature.

Figure 4-23: Hourly Concentration Variation for the 48-hour Back Trajectory Case (left) and the 48-hour Back Trajectory and Constant Boundary Layer Height Case (right).

Species	48-Hr Trajectory	48-Hr Trajectory + Constant BL Height
NO_x	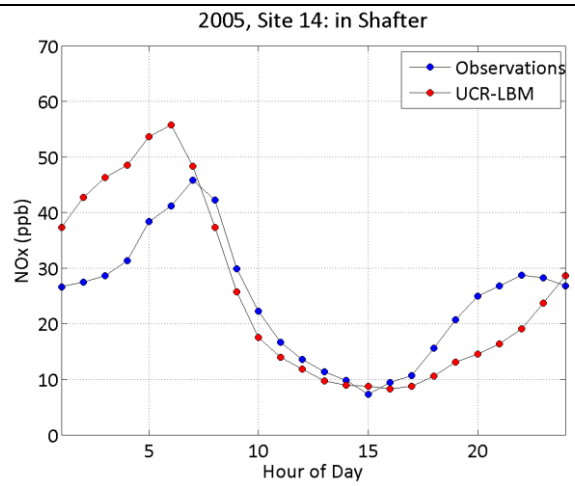	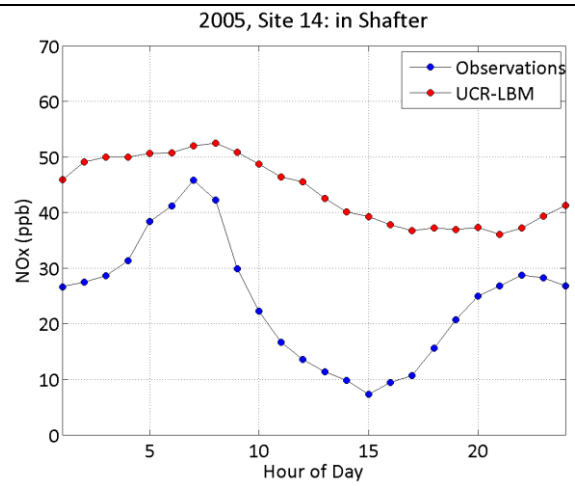
NO_2	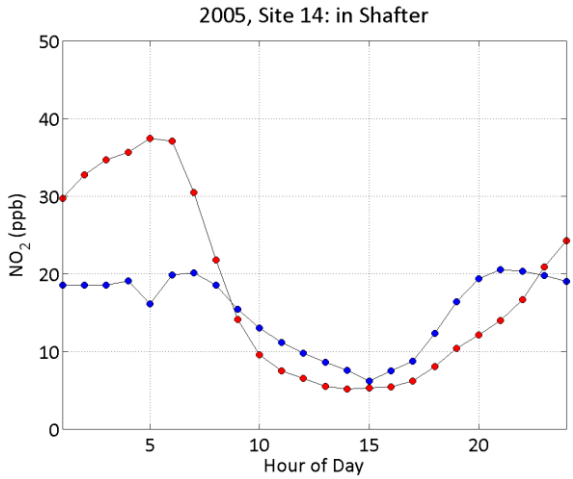	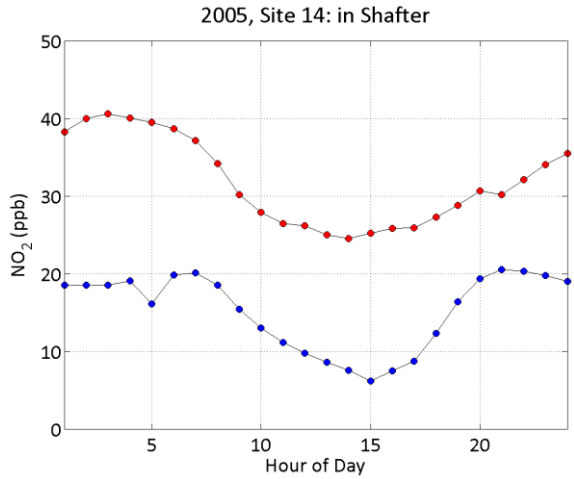
O_3	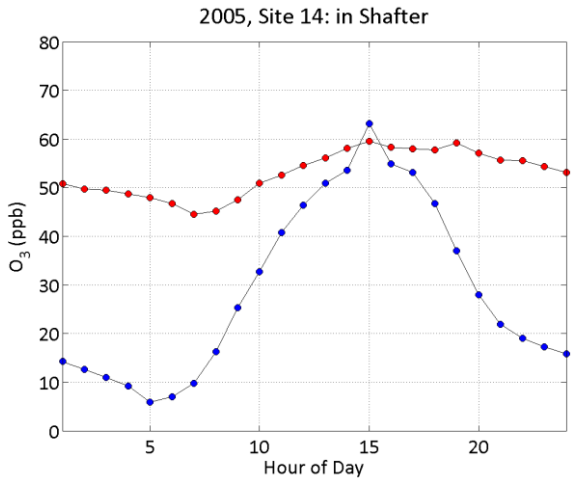	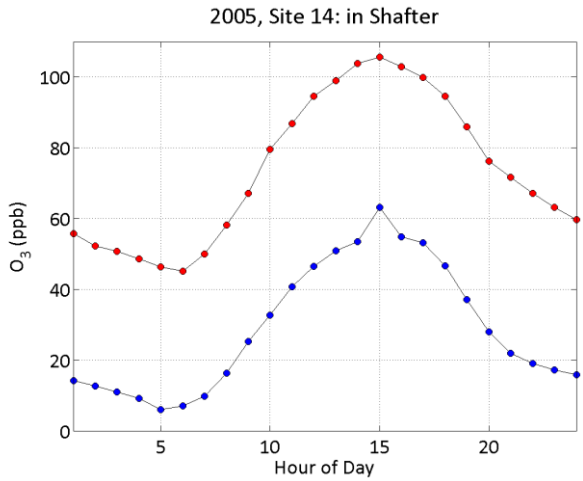

The simple model described by equation 4-8 overestimates NO_x by more than a factor of 2. This is because the emission rate in equation 4-8 is the local emission rate, which is larger

than the average emission rate the back trajectory would have encountered as it passed through the domain. This shows that the emissions from upwind locations must be taken into account when calculating concentrations, which justifies the team's use of the Lagrangian trajectory model.

4.7 The Air Quality Impact of a DG Deployment Relative to Background Sources in the SoCAB

This section compares the predicted air quality of a hypothetical DG deployment in the SoCAB to the sources described in Section 4.3 (referred to as "background sources") using the LBM. The team used NO_x as a surrogate for primary pollutants. In Section 5 the team uses the concentrations of NO_x, NO_2, and O_3 predicted in Section 4.3 as background concentrations for estimating concentrations of secondary pollutants due to the DG deployment.

Samuelson et al. (2005) developed several gridded DG emission inventories that describe likely future DG emissions in the SoCAB and San Joaquin Valley, as well as several extreme scenarios where the parameters used to generate the emissions are set to extreme values (see Section 5.2). The extra-high penetration (EHP) scenario developed for the South Coast air basin assumed that DGs would meet 20 percent of the total power demand of the SoCAB in 2010.

We predicted the concentrations of NO_x, NO_2, and O_3 under the EHP scenario using meteorology from August 27–29, 1987. The change in pollutant concentrations relative to the base emissions were calculated and compared with those obtained from the UCI-CIT model (Figure 4-24).

Figure 4-24: The Impact of DGs on the Concentrations of NO_x, NO_2, and O_3 under the EHP Scenario

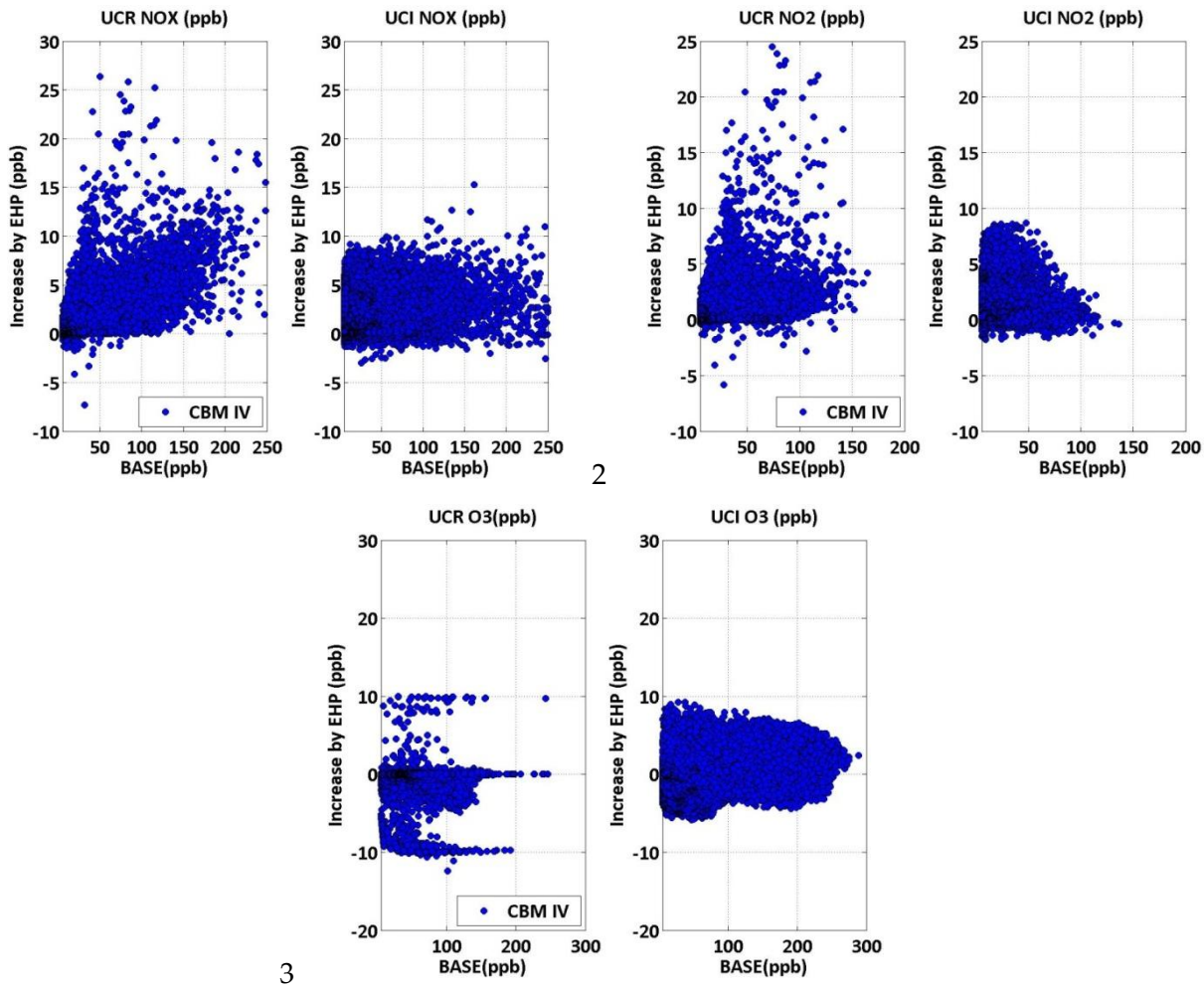

As shown in Figure 4-24, both models (UCR on the left panel and UCI-CIT on the right panel) show negligible increases (< 10 ppb for NO_x and O_3 and < 20 ppb for NO_x) in background concentrations associated with the EHP scenario. The predicted impact of DGs on NO_x and NO_2 by the UCI-CIT model is slightly lower than the UCR model. As shown in the bottom panel of Figure 4-24, the UCR model predicts that O_3 concentrations will substantially decrease, which illustrates the limitations on the production of NO_2 by the reaction of NO and O_3 due to the lack of available O_3. The impacts of DGs on concentrations at different locations are more clearly shown in Figure 4-25, Figure 4-26, and Figure 4-27. The emission color-map is added for better interpretations of concentration increase/decrease.

One of the main reasons for the extra-small impact of DGs is their relatively small emissions compared to base emissions. Figure 4-28 shows the comparison between base emissions and the increase in emissions. As shown, the average emissions increase is almost less than 40 grams per day for NO_x, and less than 10 grams per day for VOC emissions, which shows the negligible impact of DGs on total NO_x and VOC emission in the SoCAB.

Figure 4-25: Maximum Increase/Decrease in Ground-Level Concentrations of NO_x under the EHP Scenario, with CBM IV as the Chemistry Module

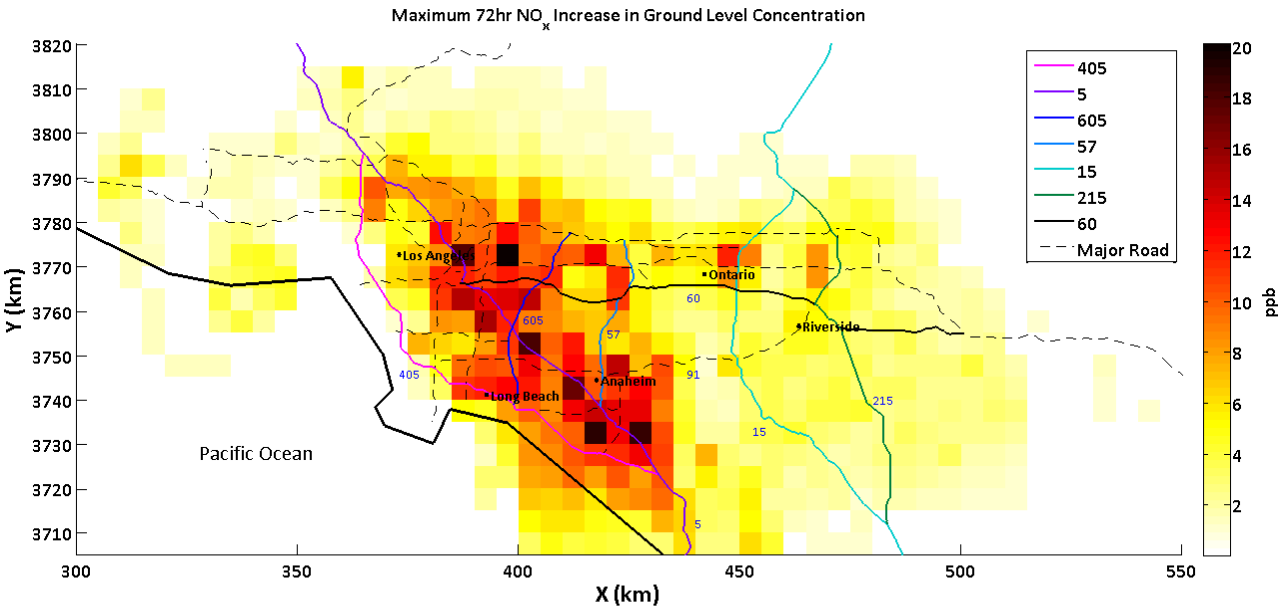

Figure 4-26: Maximum Increase/Decrease in Ground-Level Concentrations of NO_2 under the EHP Scenario, with CBM IV as the Chemistry Module

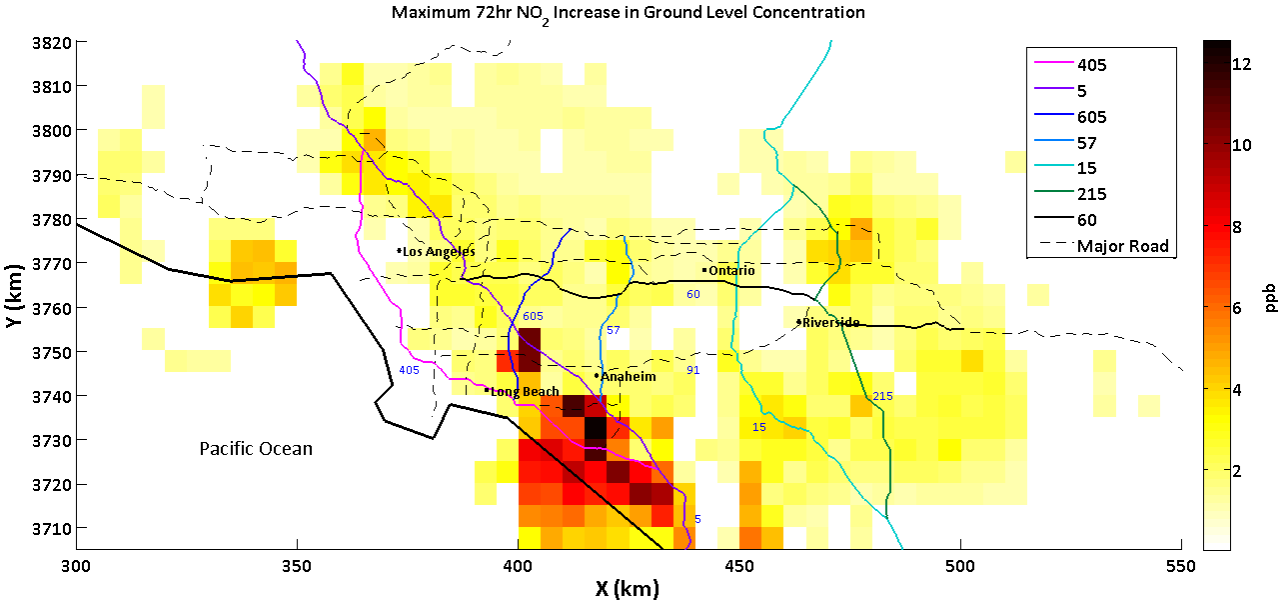

Figure 4-27: Maximum Increase/Decrease in Ground-Level Concentrations of O_3 under the EHP Scenario, with CBM IV as the Chemistry Module

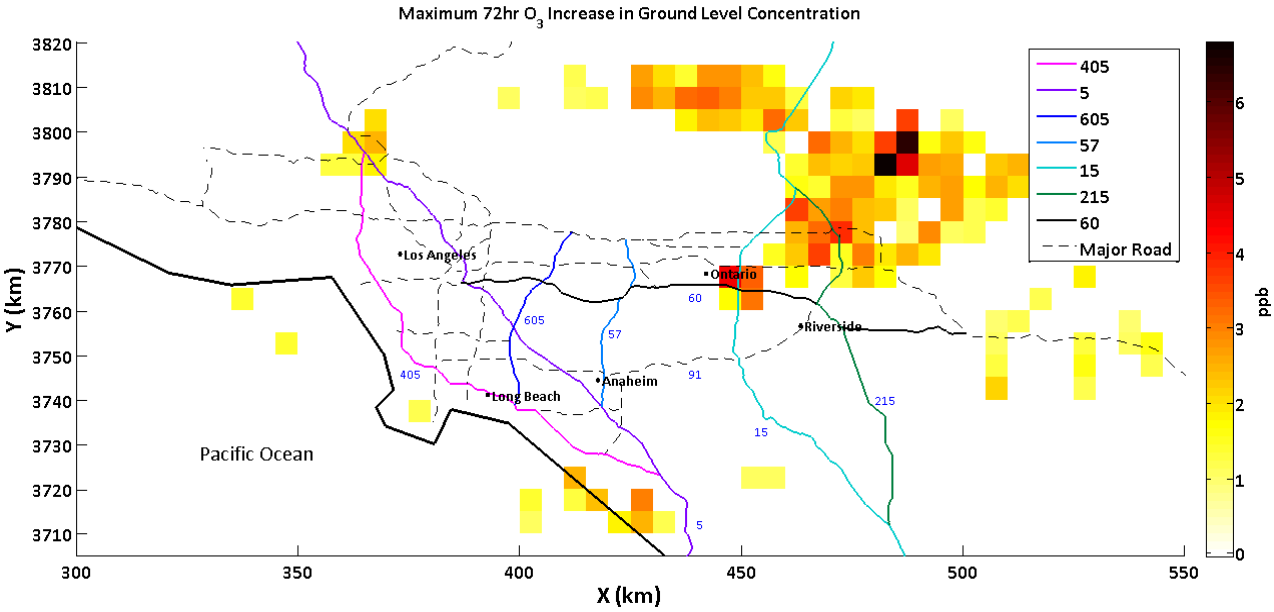

Figure 4-28: Increase in Total Daily Emissions Associated with Surface Sources and DGs (under the EHP scenario), Compared to the Background (base) Emissions for NO_x (left panel) and VOC (right panel)

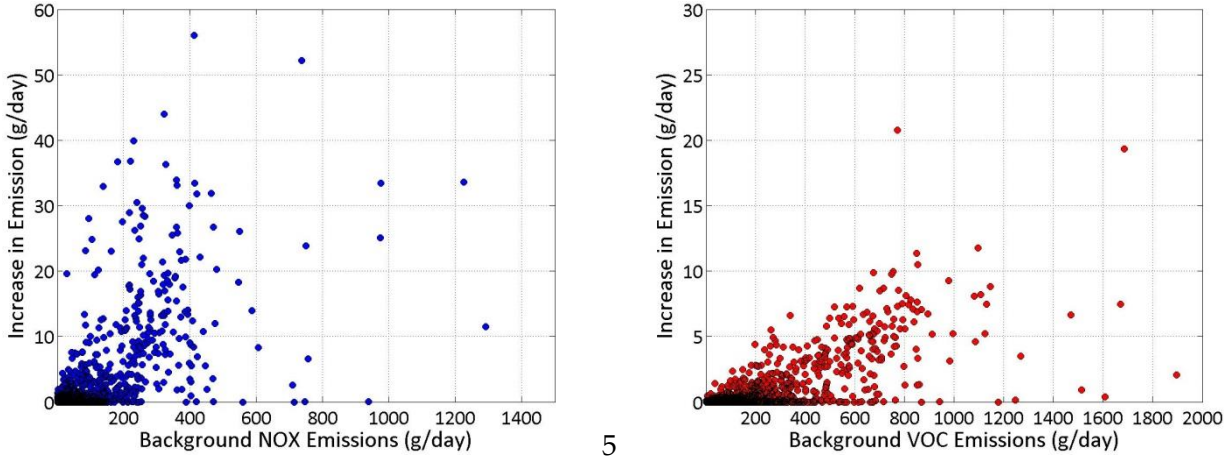

Although these models are showing the relatively small impact of DGs on background concentrations, the short-range impact of these sources are not considered in these predictions. The impacts of DGs on the background concentrations were also investigated using the GRS chemistry model, in order to examine the sensitivity of the calculated DG impacts to the chemistry method (CBM IV or GRS). Results from this analysis are shown in Figure 4-29.

Figure 4-29: The impact of DGs on the Concentrations of NO_x, NO_2, and O_3 under the EHP Scenario, using the GRS Chemistry Set

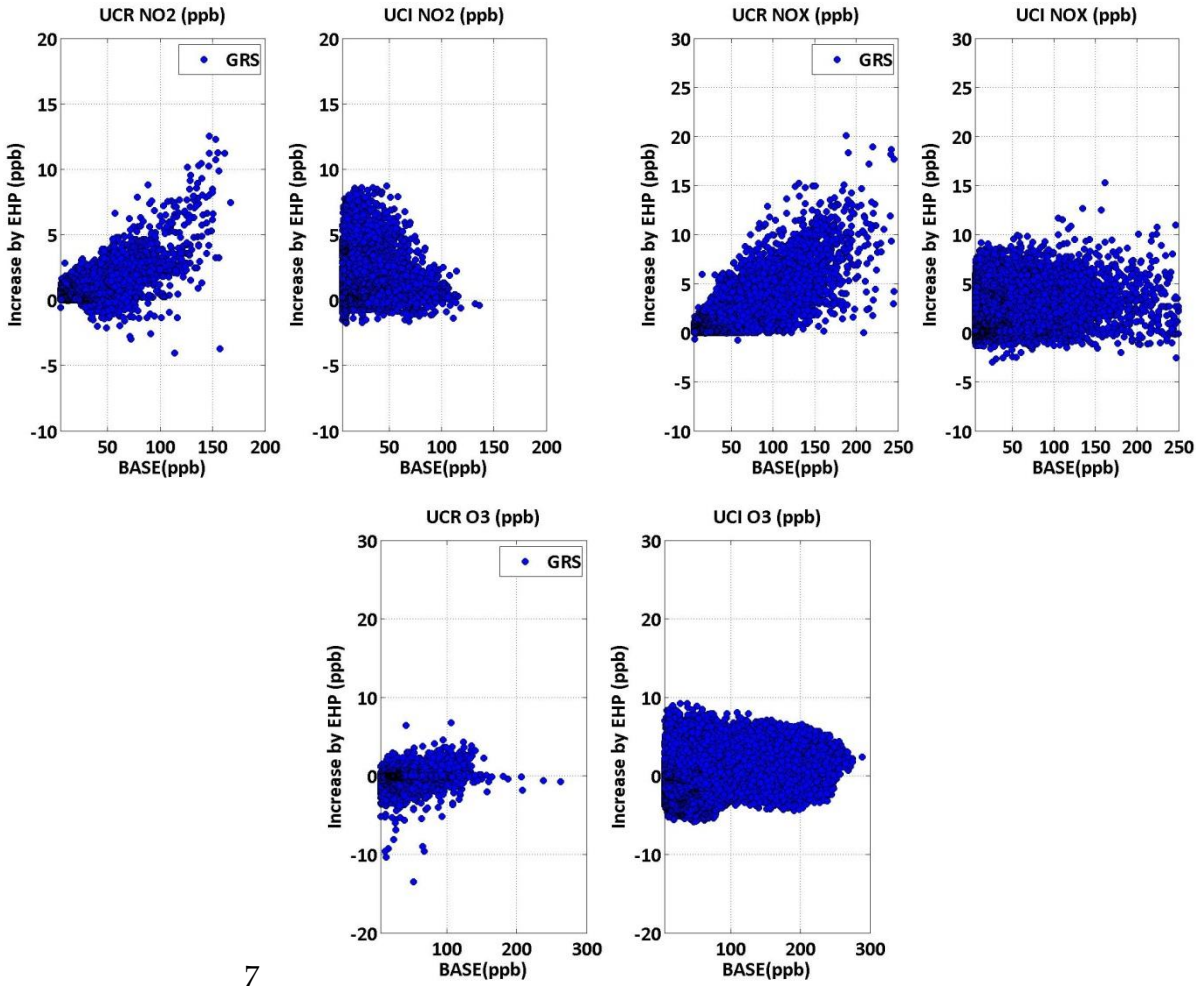

As can be seen, significant differences on the impact of DGs on O_3 concentrations can be seen when the chemistry module is changed from CBM IV to GRS , although the concentration prediction from both chemistry models are in good agreement (Figure 4-30). However, similar to CBM IV, the GRS chemistry model showed an increase in NO_2 concentrations that in most cases is higher than what the UCI-CIT model predicts. The reason for this higher impact can be explained by the higher impact of NO_x predicted by the LBM, which mainly goes back to the approach behind the transport model, which plays the major role in determining the NO_x concentrations.

Figure 4-30: Comparison of Different Chemistry Modules (GRS vs. CBM IV) in Predicting the Concentrations of NO_x, NO_2, and O_3 under the Base Scenario

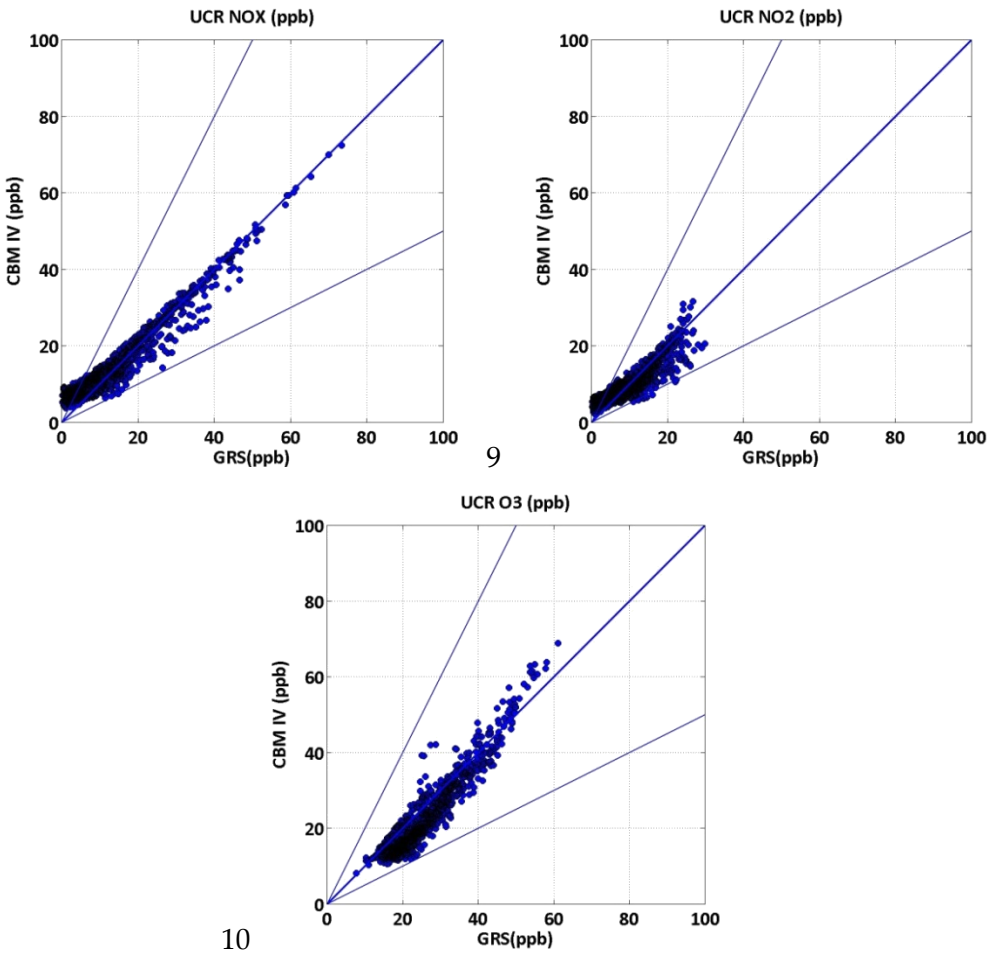

The upper panel of Figure 4-31 shows that the maximum hourly NO_x concentrations of the background sources at 21 sites are at least 30 times higher than those of the DG. The minimum hourly impacts of the background sources are just slightly lower than the maximum hourly impacts of the DG deployment at most sites, because the emission rate of background sources, 413 tons/day, is much higher than the emission rate of the DG deployment, 4.4 tons /day if DGs meet the California NO_x emission standard of 32 g/MWh for a new generation device. The lower panel of Figure 4-31 shows that the annually averaged NO_x concentrations of the background sources are at least 100 times higher than those of the DG.

Figure 4-31: Comparing NO_x Concentrations of the DG Deployment and the Background Sources. Upper panel: Hourly concentration; lower panel: annually averaged concentration.

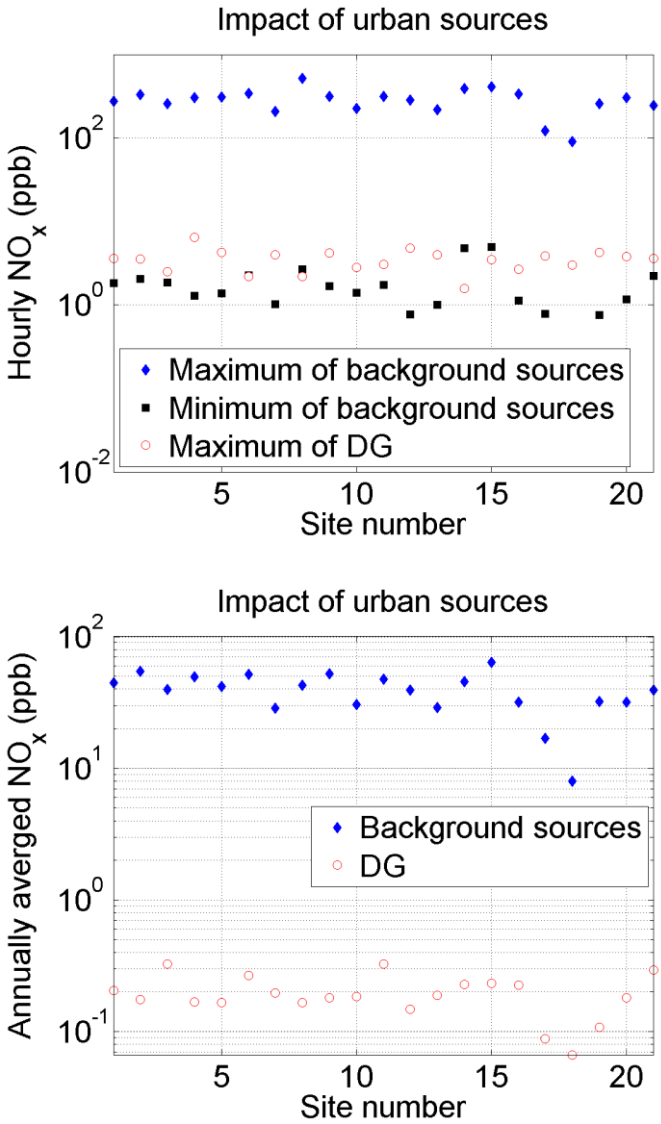

4.7 Conclusions

Air pollution in urban areas is affected by sources located both near to and far away from the receptor. This section's main focus was on the long-range impact of stationary sources, such as distributed power generators located inside an urban area. The effect of chemistry can be neglected during short-range dispersion because the species undergo relatively short travel times from source to receptor, but chemistry plays a major role in determining the concentration of major pollutants such as NO_2 and O_3 in long-range transport models.

We formulated a simple LBM that can be used to estimate background concentrations of NO, NO_2, and O_3 in an urban area. The model can provide hourly concentrations of these species over time periods of a year, which is required in exposure studies. The model

achieves its computational efficiency by separating transport and chemistry using the concept of species age. Evaluations with measurements made in the SoCAB during 2007 and in the San Joaquin Valley indicate that the model can provide adequate descriptions of the spatial and temporal behavior of NO_x and NO_2. Model estimates of maximum hourly ozone concentrations are unbiased relative to observations, but the 95 percent confidence interval$(\approx s_g^2)$ of the ratios of observed to estimated concentrations is over a factor of two.

This model has also been compared with the UCI-CIT grid model. The comparison shows that UCI-CIT model predicts substantially higher concentrations, and the variation of O_3 concentrations is unrealistically larger than that of the LBM. Unlike the LBM, the UCI-CIT model was not evaluated against the observations in SoCAB and the San Joaquin Valley due to the relatively high computational requirements for running this model over a one-year period. Therefore, this study mainly focused on the LBM rather than UCI-CIT model.

CHAPTER 5:

Hybrid Modeling

5.1 The Hybrid Model

The combined short-range and long-range impact of DG on ground-level concentrations can be predicted through a hybrid model consisting of AERMOD (Cimorelli et al. 2005) as a short-range dispersion model combined with the background model explained in previous section. This approach is known as *hybrid modeling,* where a combination of a short-range and long-range photochemical transport models is used to predict the relative impact of sources located at different length scales from the receptor. A schematic of this method is shown in Figure 5-1.

Figure 5-1: Schematic of the Hybrid Model

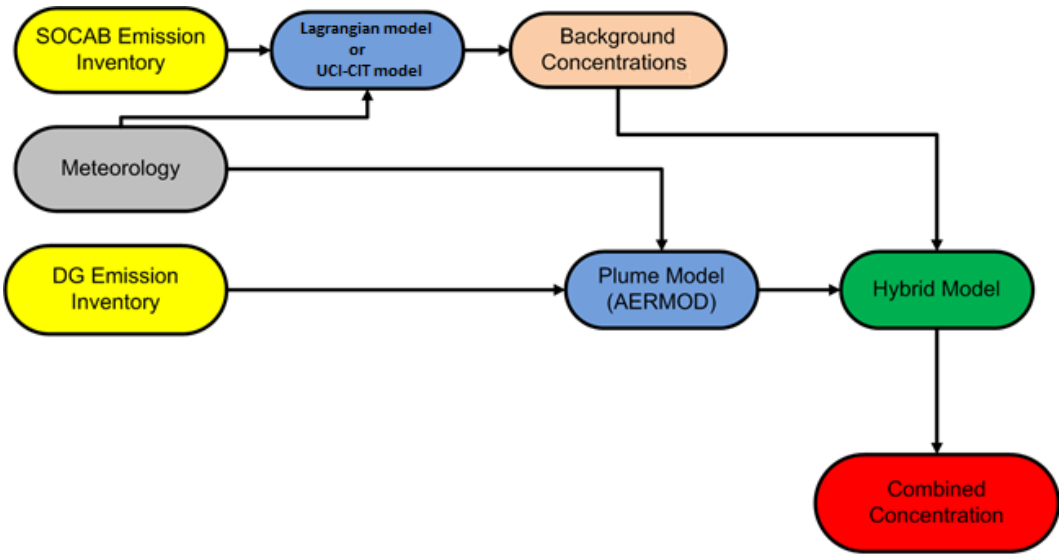

Using AERMOD, the hourly averaged ground-level concentrations associated with each receptor are calculated. In this set of calculations, the ground-level concentration is only affected by sources inside the grid of interest, and any source outside this grid does not have any impact.

Background concentrations are calculated using either the LBM or the UCI-CIT model. Using a sub-grid scale chemistry method proposed by Hess and Cope (1989) for photochemical modeling, O_3 and NO_2 concentrations are predicted using the previously calculated background concentrations. The resulting concentrations are then added to the background concentrations in that grid point.

The model suggested by Hess and Cope (1989) assumes that hydrocarbon impacts at the source are negligible. Thus, considering only NO_x and O_3, the chemistry can be simplified as,

$$NO_2 + h\nu \rightarrow^{k1} NO + O \quad \text{(R8)}$$

$$O + O_2 + M \rightarrow^{k2} O_3 + M \quad \text{(R9)}$$

$$O_3 + NO \rightarrow^{k3} NO_2 + O_2 \quad \text{(R10)}$$

where $h\nu$ is the solar radiation energy and k_1, k_2 and k_3 are the reaction rates. Assuming that O_2 , NO and O_3 are in photo-stationary equilibrium, one can write that,

$$[NO_2] = \left(\frac{k_3}{k_1}\right)[NO][O_3] \quad \text{(5-1)}$$

The total NO_x and O_x (= NO_2 + O_3) is conserved in these reactions. If the team assume that the species are well-mixed within the plume and neglect deposition at the ground, the team can write the mass conservation equations for NO_x and O_x by considering the infinitesimal control volume depicted inFigure 5-2.

Figure 5-2: Control Volume Used for the Mass Balance of NOx and Ox within the Plume

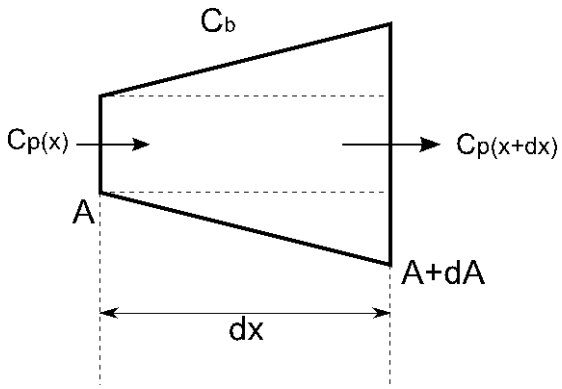

The concentration within the plume is C_p, the background concentration is C_b, and the cross-sectional area of the plume at x and $x+dx$ are A and $A+dA$, respectively. The mass balance for this control volume can be written as follows:

$$C_p(x)A + C_b dA = (C_p + dC_p)(A + dA) \quad \text{(5-2)}$$

Simplifying and dividing by dx results in:

$$\frac{dC_p}{dx}A + (C_p - C_b)\frac{dA}{dx} = 0 \quad \text{(5-3)}$$

$$\frac{d}{dx}\left[A(C_p - C_b)\right] = 0 \tag{5-4}$$

$$A(C_p - C_b) = constant = A_o(C_{po} - C_{bo}) \tag{5-5}$$

$$C_p = DC_{po} + (1 - D)C_b \tag{5-6}$$

where $D = \frac{A_o}{A}$ is the dilution.

Using equation 5-6, the team can write the NO_x and O_x balance as:

$$NO_x(t) = NO_2(t) + NO(t) = D(t)NO_x(0) + [1 - D(t)]NO_x^b \tag{5-7}$$

$$O_x(t) = NO_2(t) + O_3(t) = D(t)[NO_2(0) + O_3(0)] + [1 - D(t)](NO_2^b + O_3^b), \tag{5-8}$$

where $NO_x(0)$ is the concentration at the source, superscript *b* denotes the background values, and dilution $D(t)$ is:

$$D(t) = \pi r_s^2 / [4\pi\sigma_y\sigma_z], \tag{5-9}$$

where r_s is radius of the stack.

Solving equations5-7, 5-8, and 5-9 results in:

$$NO_2(t) = 0.5\left[\left(a + b + \frac{k_1}{k_3}\right)^2 - 4ab\right]^2 \tag{5-10}$$

$$NO(t) = a - NO_2(t) \tag{5-11}$$

$$O_3(t) = b - NO_2(t), \tag{5-12}$$

where:

$$a = D(t)NO_x(0) + [1 - D(t)]NO^b \tag{5-13}$$

$$b = D(t)NO_2(0) + [1 - D(t)](NO_2^b + O_3^b) \tag{5-14}$$

The main unknown in these expressions is the dilution. The σ_y and σ_z defined in equation 5-9 are instantaneous plume spreads, which can be modeled following the Plume Volume Molar Ratio Method (PVMRM) for modeling the conversion of NO_x to NO_2 in AERMOD:

$$\sigma_{ra} = \frac{a_1 \varepsilon^{\frac{1}{2}} t^{\frac{3}{2}}}{1 + a_2 t / T_{Lr}}, \tag{5-15}$$

where a_1 is a constant (= 0.57), a_2 = 0.62 a_1, t is the plume travel time (= x/U), and T_{Lr} is a Lagrangian time scale for relative dispersion, defined as:

$$T_{Lr} = a_{r1} \frac{z_i}{\sigma_w}, \tag{5-16}$$

where a_{r1} = 0.46, z_i is the mixing height, and σ_w is the standard deviation of vertical component of turbulent velocity. The turbulence dissipation rate, ε, is calculated as follows, based on Weil (1996):

$$\varepsilon = b\sigma_w^2 / T_{Lr}, \tag{5-17}$$

where b is a constant (= 0.78).

The Hess and Cope method is applicable when only a single source contributes to the concentration at each receptor. It must be modified when multiple sources are present because when multiple plumes "overlap" the mass balance is no longer valid. The team can modify the method for multiple sources by determining an average dilution for each receptor using the concept of species age. If the concentration due to source i at a receptor is C_i, and the age of the species released from source i when it reaches the receptor is A_i, then the species age at the receptor is:

$$A = \frac{\sum_i C_i A_i}{\sum_i C_i}. \tag{5-18}$$

We use equations (5-15) through (5-18) to calculate the instantaneous plume spread, where the travel time *t* equals the species age and $A_i = x_i/U$, where x_i is the downwind distance from source *i* to the receptor.

The method suggested by Hess and Cope (1989) provides the instantaneous concentrations, but to obtain the 1-hour average values, these concentrations had to be scaled. The team scaled the NO_2 obtained using the Hess and Cope method by the ratio of the NO_x concentration calculated with AERMOD to that calculated using the Hess and Cope method. This resulted in the NO_2 concentrations due to the local sources, which were then added to the values calculated with the background model. The team calculated 1-hour average O_3 similarly, except the team scaled the difference between the instantaneous O_3 (calculated using the Hess and Cope method) and the O_3 calculated using the background model, rather than the instantaneous O_3 itself. This procedure is described by equations 5-19 and 5-20:

$$NO_2^t = NO_2 \frac{NO_x^a}{NO_x} + NO_2^b \tag{5-19}$$

$$O_3^t = \left(O_3 - O_3^b\right) \frac{NO_x^a}{NO_x} + O_3^b, \tag{5-20}$$

where *t* refers to the total concentration, and *a* refers to the value calculated by AERMOD.

Following this method, the impact of sources in each grid on the NO_2 concentrations could be calculated. Note that the background concentration for each grid square is associated with all sources including DGs, except for the DG sources inside that specific grid. Thus, the short-range transport model prediction will add the concentrations associated with DGs inside that grid point.

5.2 Distributed Generation Scenario

We applied the hybrid model to estimate the effect of distributed generation under the extra-high penetration (EHP and SJV-EHP) scenarios developed by Samuelson et al. (2005) for the South Coast air basin and the San Joaquin Valley. Samuelson et al. developed several gridded DG emission inventories which describe likely future DG emissions as well as several extreme scenarios where the parameters used to generate the emissions are set to extreme values. The EHP scenario was developed by assuming that DGs will meet 20 percent of the total power demand of the SoCAB in 2010, and the SJV-EHP scenario was developed by assuming that DGs will meet 45 percent of the increased power demand in the San Joaquin Valley from 2007 to 2030. This means that DGs account for about 5.7 gigawatts (GW) of power generation in the SoCAB and about 1 GW in the San Joaquin Valley. Total DG NO_x emissions are about 4.4 tons/day in the SoCAB and 0.5 tons/day in the San Joaquin Valley.

The spatial resolution of the EHP scenario emission inventories is on the order of several kilometers, which is not fine enough for the hybrid model (because the goal of hybrid modeling is to resolve the concentration distribution at a scale of several meters). To meet the model input requirements, the team created a distribution of DGs with a spatial resolution of 50 m by using land use data obtained from the U.S. EPA and the total installed power capacity and NO_x emission rate of the EHP scenarios. The team distributed the total DG power by land use category, assuming that each land use category only contains DGs of one representative type (shown in Table 5-1).

Table 5-1: Representative DG Specifications Used to Generate the DG Distribution for EHP Scenarios with a 50-m Resolution

Land Use Code (Samuelson et al. 2005)	Capacity (kW)	Stack Height (m)	Exit Temperature (K)	Exit Velocity (m/s)	Stack diameter (m)
6	12,500	10	473	18.65	2.60
5	5,000	7	473	13.92	2.00
4	2,500	6.5	473	9.95	1.80
3	1,000	6	473	8.07	1.50
2	625	5	473	6.51	1.50
1	250	3	473	5.68	1.40

The total NO_x emission rate of the DG distribution equals that of the EHP scenarios developed by Samuelson et al. (2005), and the spatial distribution is generated in a similar manner (Samuelson et al. also used land use data to distribute the DGs).

Figure 5-3 shows the gridded DG emissions in the SoCAB for the EHP scenario. The emissions are distributed relatively uniformly around the major population centers in the SoCAB, with the maximum emission rate of about 50 g/day occurring near Los Angeles.

Figure 5-3: Gridded DG Emissions in the SoCAB

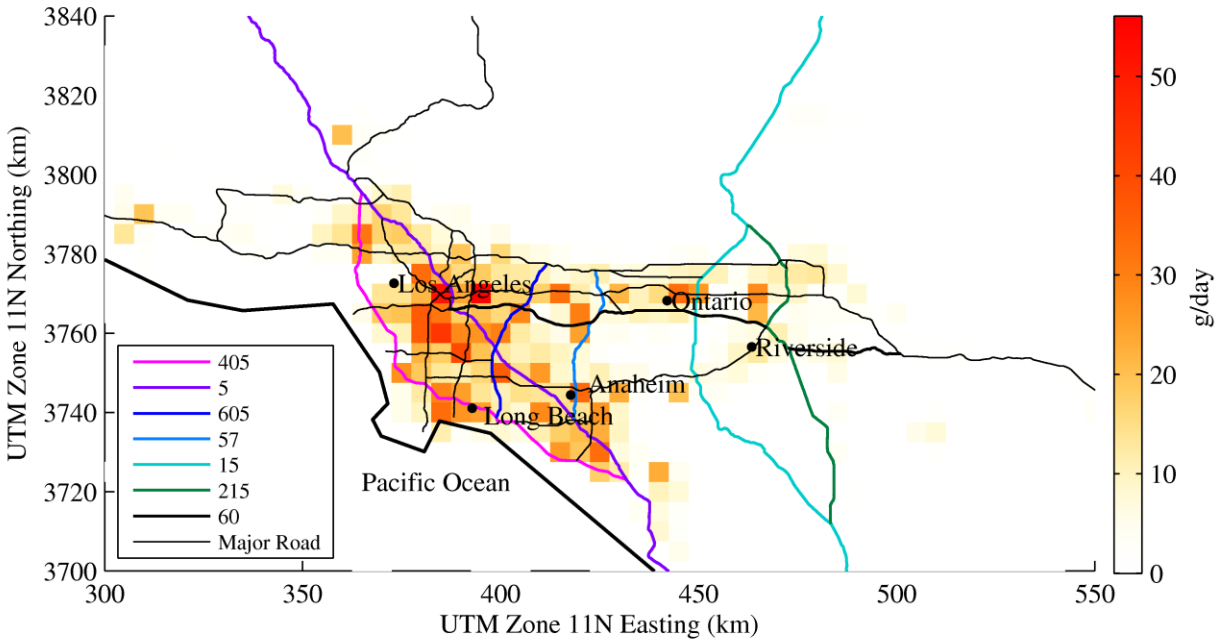

Grid sizes are 5 km by 5 km.

Figure 5-4 shows results from the short-range transport model without the chemistry (only NO_x concentrations) for the SoCAB. A spatial resolution of 50 m is used for prediction of ground-level concentrations in each grid point. Following these calculations, the maximum hourly concentration is selected in each grid point. As can be seen in Figure 5-3, the maximum 72-hour concentration is mostly about 3 ppb, while in one location it exceeds 5 ppb. Thus, as it was expected the impact of short-range dispersion on the ground-level concentration is almost negligible compared with the impact of DGs on the background concentration. The result from this analysis is shown in Figure 5-4. As shown, the NO_2 pattern is very similar to that of the NO_x contribution, since the NO_2 to NO_x ratios are close to 1.0 (Figure 5-5). The reason for this behavior is the significantly small values of dilution which entrain a high amount of background O_3 into the plume, causing fast conversion of NO to NO_2.

Figure 5-4: Maximum 72-hr NO_x Ground-Level Concentrations (ppb)

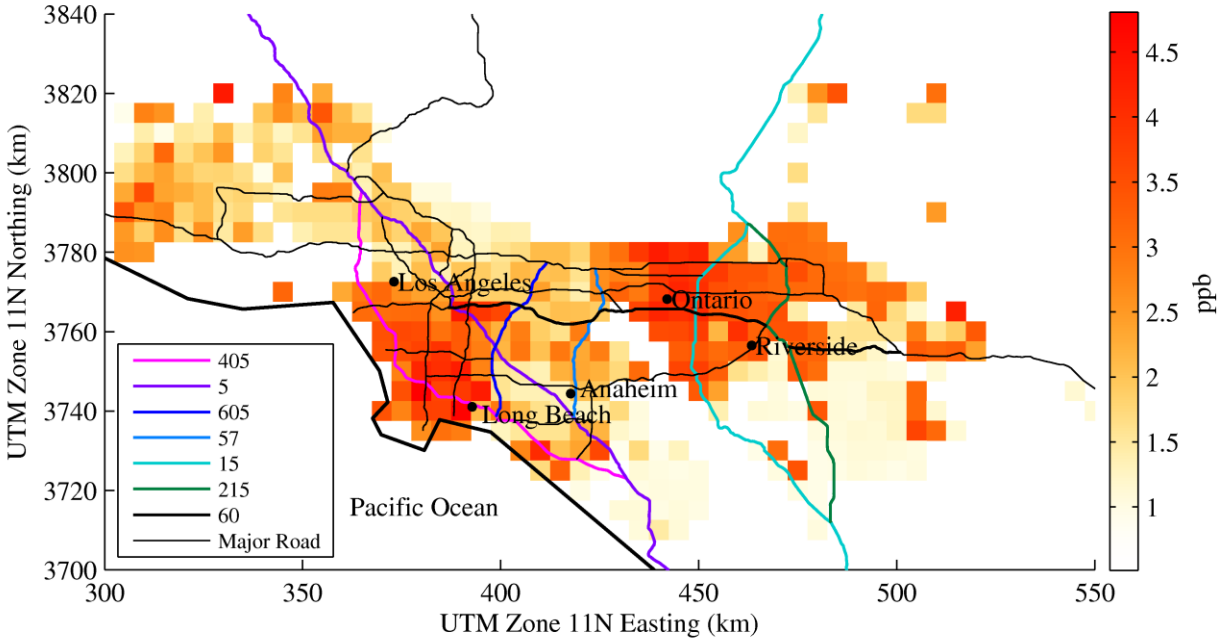

Figure 5-5: The Contribution of DGs to the Maximum Increase/Decrease in Ground-Level Concentrations of NO_2 at Each Grid Point

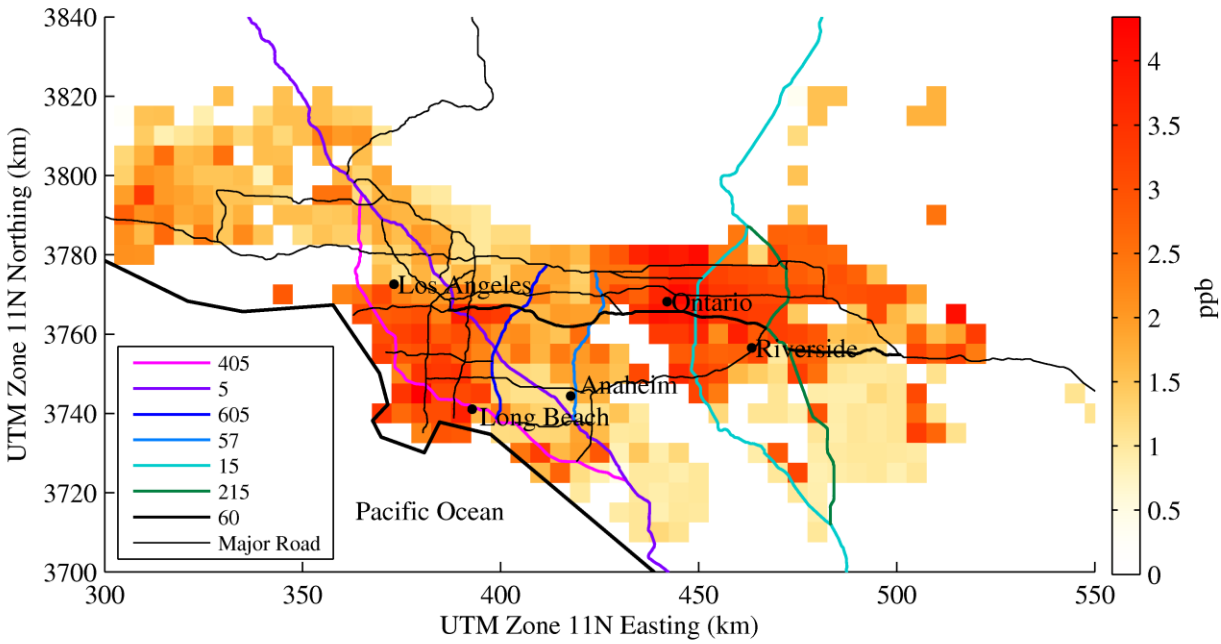

Figure 5-6: The Ratio of NO_2 to NOx from Hess and Cope (1989) model

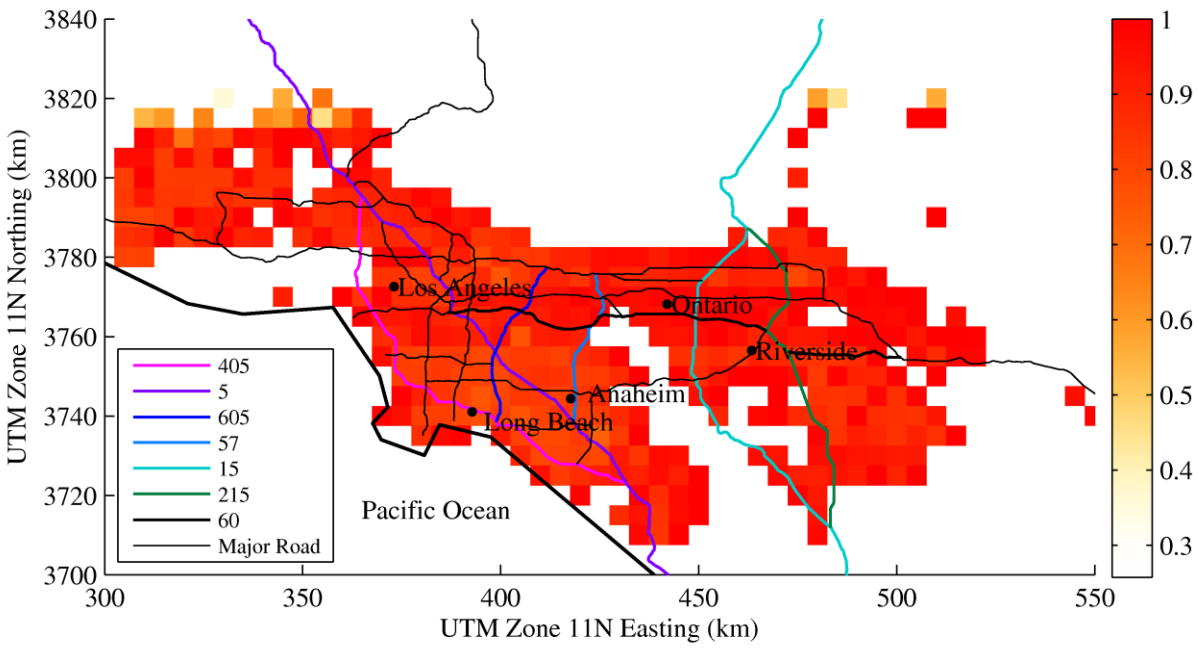

5.3 Impact of Distributed Generation in the South Coast Air Basin

Following this analysis, the team calculated the overall impact of DGs on ground-level concentrations of NO_x, NO_2, and O_3. Results from these analyses are shown in Figure 5-6, Figure 5-7, and Figure 5-8 in color-map, since the difference with those shown in Figure 4-18, Figure 4-19, and Figure 4-20 are relatively small, and it may be very difficult to recognize the difference through the scatter plots. To clarify this, Figure 5-9 shows a comparison on the impacts solely predicted by the LBM with GRS as the chemistry module, with those obtained from the hybrid model.

As shown in Figure 5-7, the hybrid model shows slightly higher NO_x increases than the LBM, because the short-range impact of DGs is larger than the impact of DGs on the background concentration. However, the predicted impacts on NO_2 using the hybrid model are slightly lower than those shown by the LBM. The reason that the hybrid model predicts a larger NO_x and smaller NO_2 concentration is because the plume model predicts a smaller conversion of NO to NO_2 (probably because less O_3 is available) compared to the LBM. Thus, despite the higher NO_x concentrations predicted by the hybrid model, less NO_2 contribution is observed. Since the focus of hybrid modeling is on the NO_2, this analysis does not include the impact on O_3 concentrations.

Figure 5-7: Maximum Increases/Decreases in Ground-Level Concentrations of NO_x under the EHP Scenario

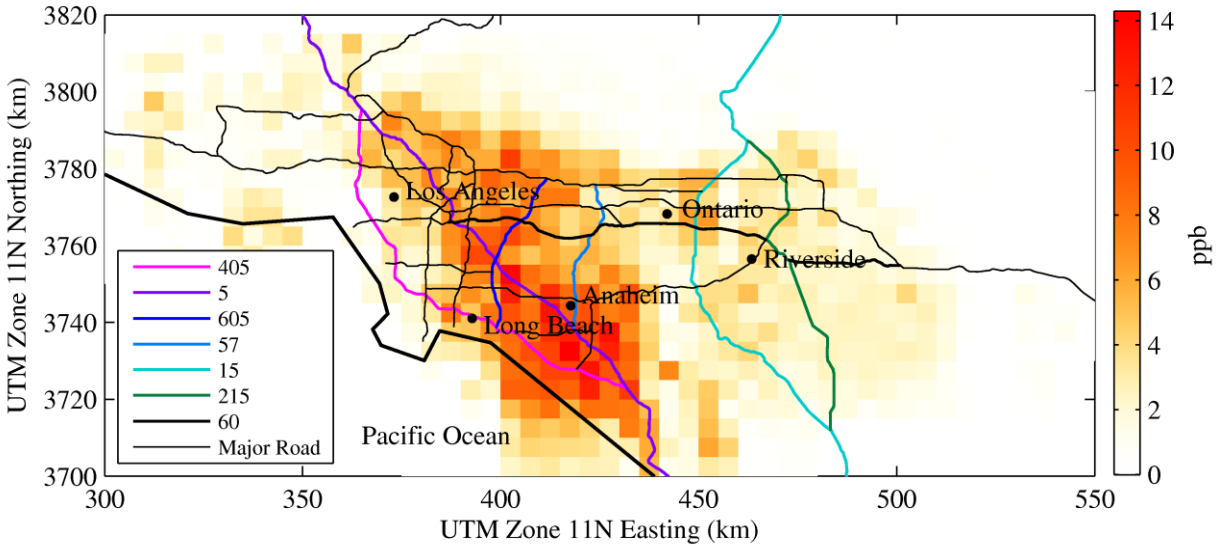

Calculated Using the Hybrid Model with GRS as the Base Chemistry Module for the Background Concentration Calculations

Figure 5-8: Maximum Increase/Decrease in Ground-Level Concentrations of NO_2 under the EHP Scenario

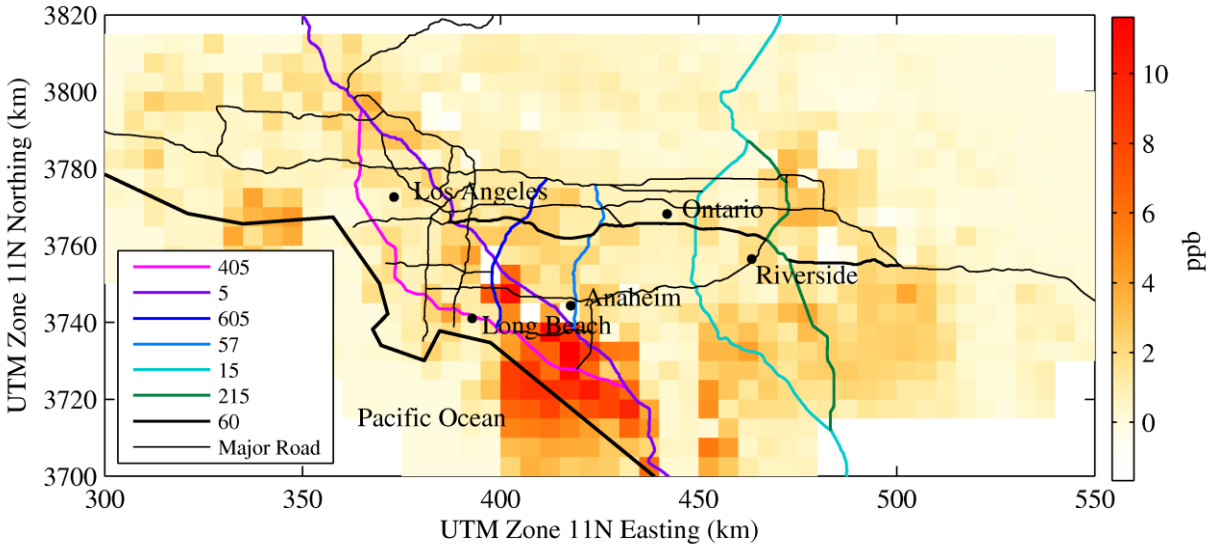

Calculated Using the Hybrid Model with GRS as the Base Chemistry Module for the Background Concentration Calculations

Figure 5-9: Maximum Increase/Decrease in Ground-Level Concentrations of O_3 under the EHP Scenario

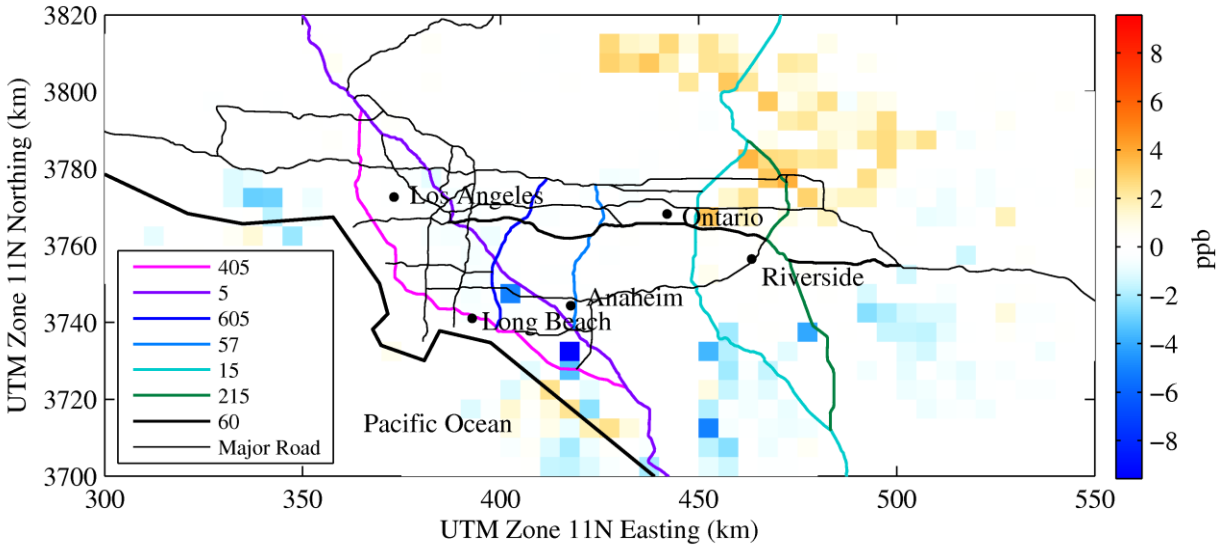

Calculated Using the Hybrid Model with GRS as the Base Chemistry Module for the Background Concentration Calculations

Figure 5-10: Comparison between the Impact on NO_x and NO_2 Predicted by the LBM to those Obtained from the Hybrid Model

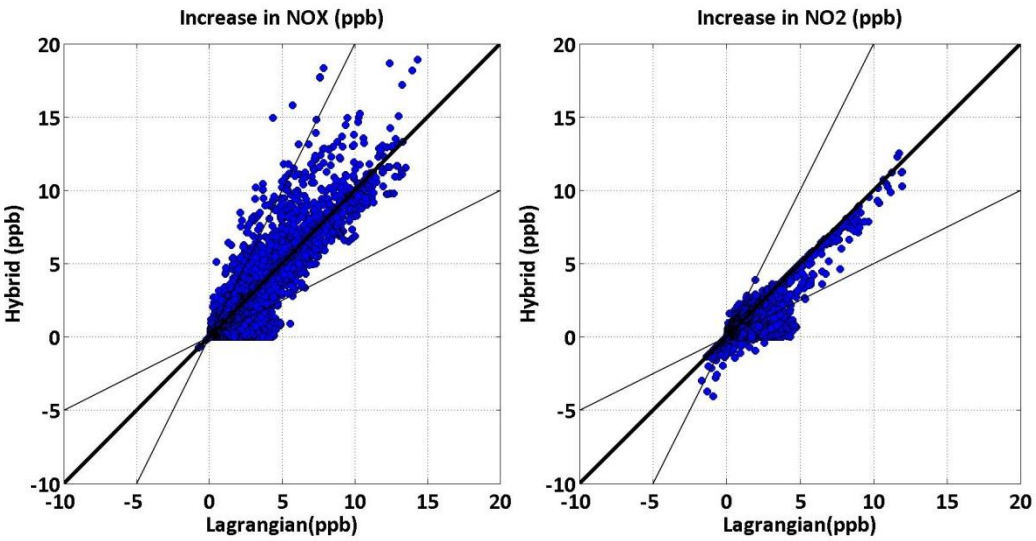

The contribution of DGs to the ground-level concentrations of NO_x, NO_2, and O_3 is less than 10 percent of the base concentrations, which is due to the relatively small increase in the total emissions associated with DGs under the EHP scenario.

5.4 Impact of Distributed Generation in the San Joaquin Valley

For the San Joaquin Valley domain, the team simulated both a base emission scenario without extra DGs and the SJV-EHP scenario developed by Samuelson et al. (2005). The base scenario emissions, obtained from the California Air Resource Board (ARB), were scaled so that the total NO_x emissions are 160 tons/day, matching the emissions used by Samuelson et al. for the year 2023. Apart for this change in the total emissions, the background model was run in the same manner as described in Section 4.3.2.

Figure 5-11 shows the locations of the DGs placed using the method described in Section5.2. Most of the DGs are located near major population centers such as Fresno, but some are also located in smaller cities and along major freeways in the San Joaquin Valley.

Figure 5-11: DG Locations for the San Joaquin Valley EHP Scenario (SJV-EHP)

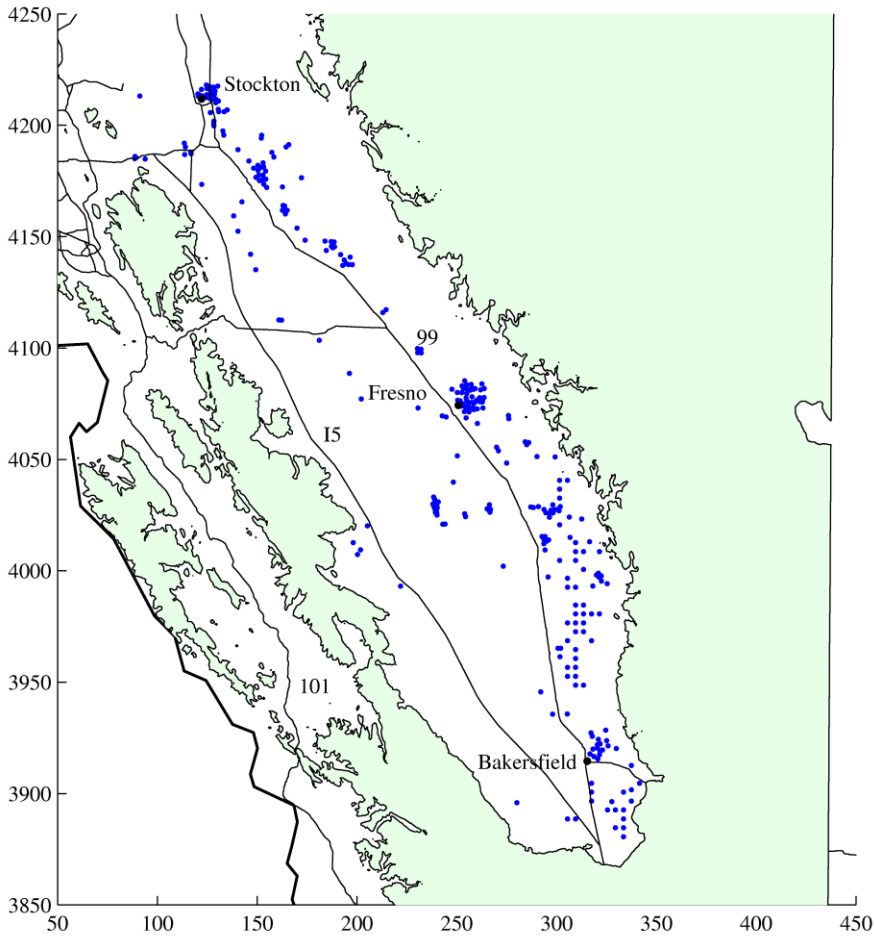

The 99, I5, and 101 freeways and the centers of Stockton, Fresno, and Bakersfield are also shown. The green-shaded area represents the mountain ranges around the San Joaquin Valley.

Figure 5-12 shows the total daily gridded DG emissions under the SJV-EHP scenario. Most of the emissions occur in large cities such as Bakersfield, Fresno, and Stockton. The maximum emission rate is about 400 g/day, which is about six times larger than the maximum gridded emission rate of the EHP scenario for the SoCAB. However, the total NOx emission rate is about 0.5 tons/day, less than the total emission rate of 4.4 tons/day for SoCAB. The DG emissions for the San Joaquin Valley are much more sharply concentrated around the large cities than those of the SoCAB because the SoCAB has a more uniform population distribution.

Figure 5-12: DG Emissions in the San Joaquin Valley

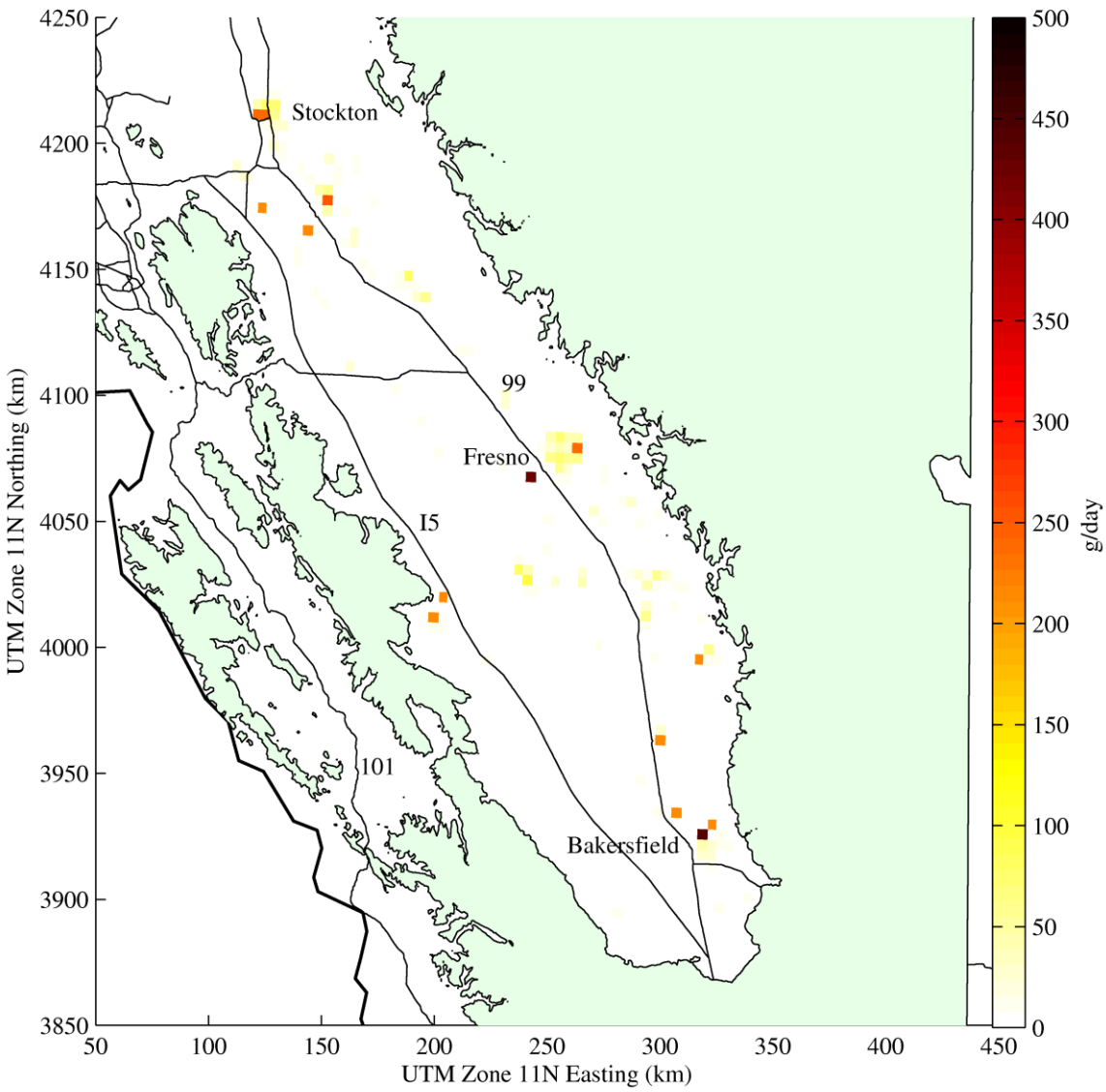

Most of the DG emissions are concentrated in large cities such as Bakersfield, Fresno, and Stockton

Figure 5-13 shows the change in the 24-hour maximum ground-level NOx concentrations between the base scenario and the SJV-EHP scenario for one simulation day. The maximum increase in NOx concentration is about 1 ppb. The maximum change occurs near the large cities, where most of the DG emissions are located.

Figure 5-13: Increase or Decrease in Ground-Level 24-hour Maximum NO_x Concentrations under the SJV-EHP Scenario

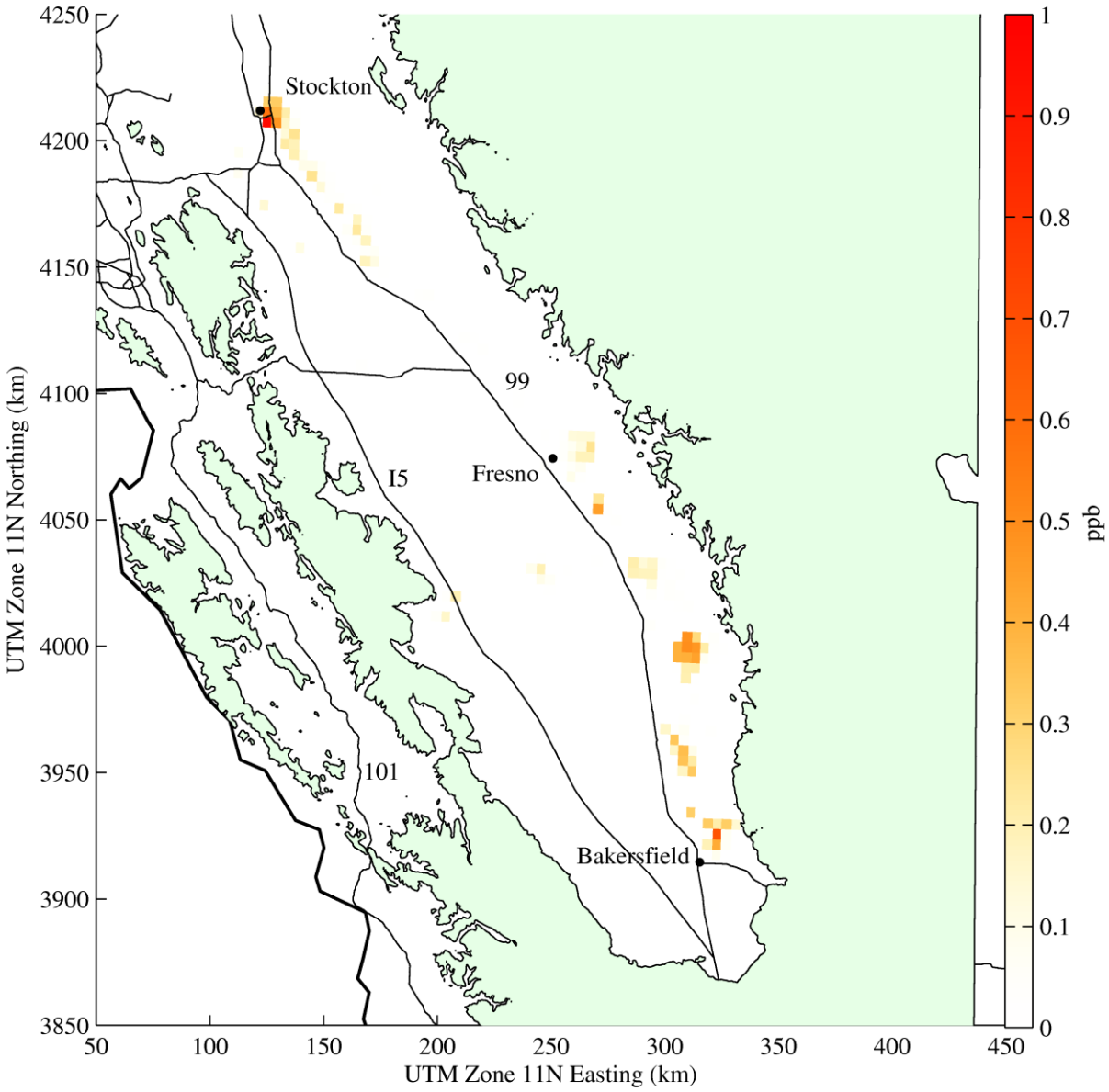

Calculated Using the Hybrid Model with GRS as the Base Chemistry Module for the Background Concentration Calculations

Figure 5-14 shows the change in the 24-hour maximum ground-level NO_2 concentrations between the base scenario and the SJV-EHP scenario for one simulation day. The maximum change in NO_2 concentration is about 1 ppb. The maximum increase occurs near Bakersfield and Stockton.

Figure 5-14: Increase or Decrease in Ground-Level 24-hour Maximum NO_2 Concentrations under the SJV-EHP Scenario

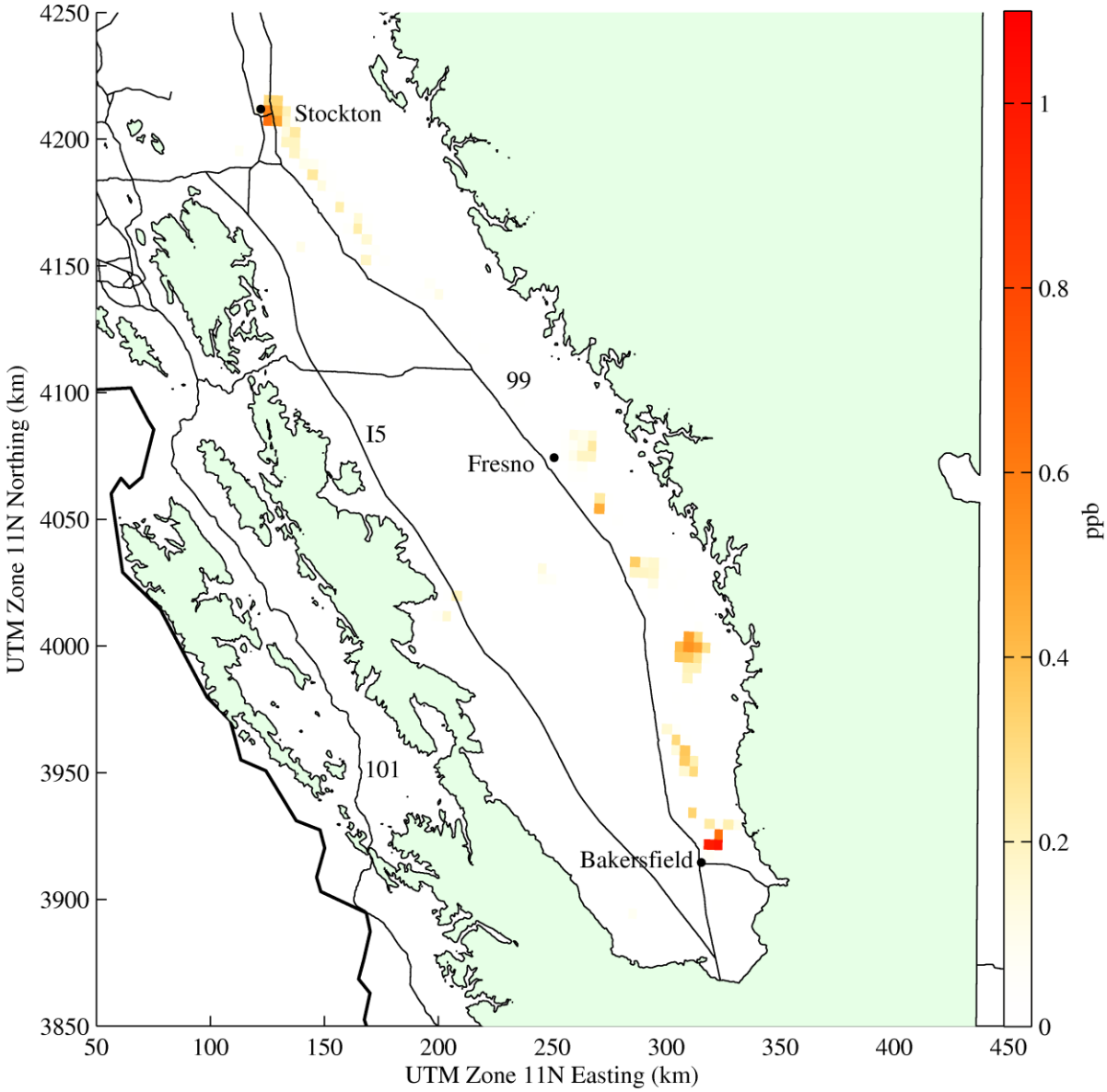

Calculated Using the Hybrid Model with GRS as the Base Chemistry Module for the Background Concentration Calculations

Figure 5-15 shows the change in the 24-hour maximum ground-level O_3 concentrations between the base scenario and the SJV-EHP scenario for one simulation day. The maximum increase in O_3 concentration is about 1 ppb near Fresno and along Highway 99. The maximum decrease is about -0.4 ppb, occurring north of Bakersfield.

Figure 5-15: Increase or Decrease in Ground-Level 24-hour Maximum O_3 Concentrations under the SJV-EHP Scenario

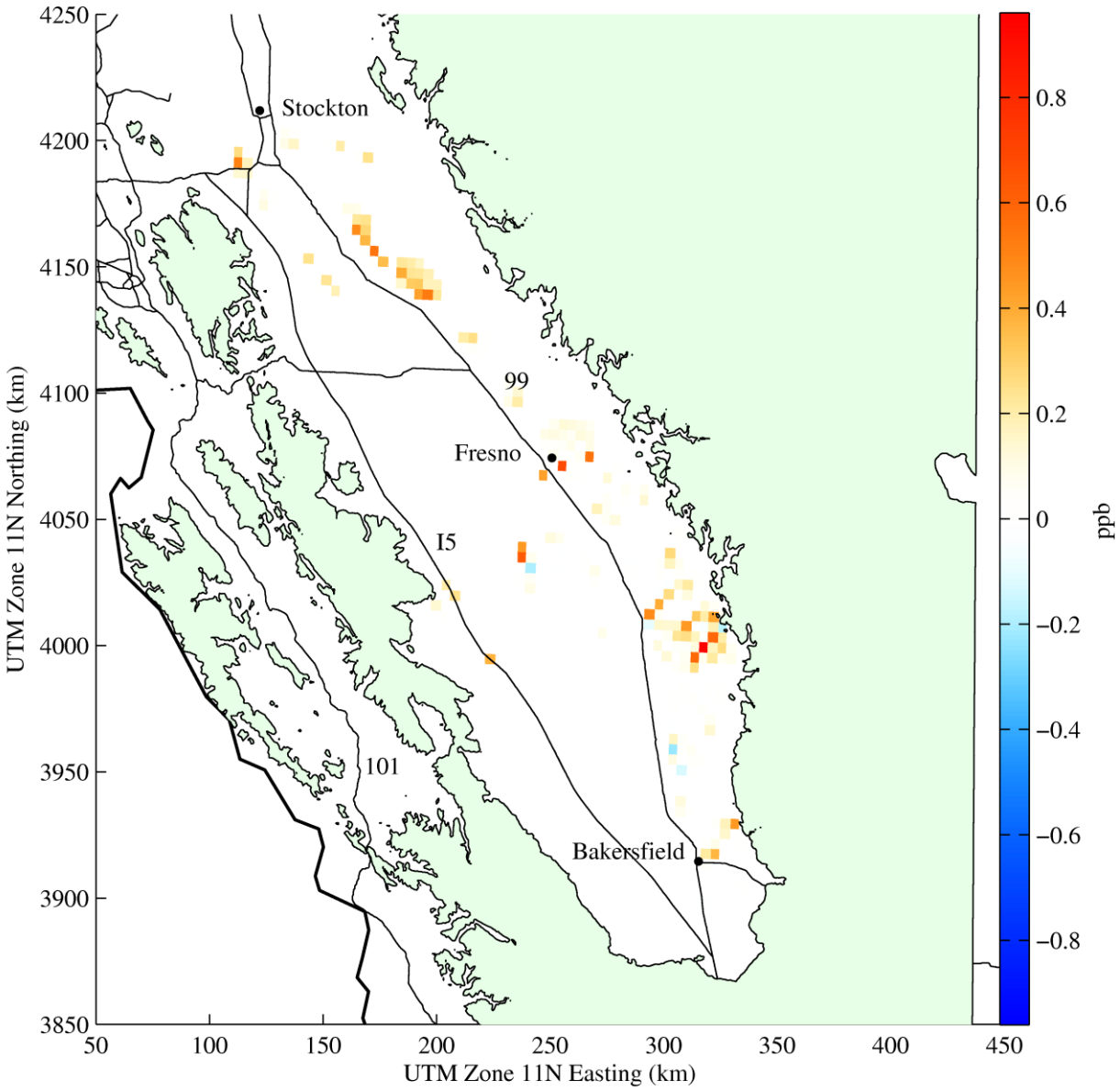

Calculated Using the Hybrid Model with GRS as the Base Chemistry Module for the Background Concentration Calculations

The hybrid model results for the San Joaquin Valley are similar to those of the SoCAB. The change in NO_x, NO_2, and O_3 concentrations is small because the DG emissions are small relative to the total emissions.

5.5 Summary and Conclusions

Air pollution in urban areas is affected by sources both near to and far away from the receptor. This section's main focus was on combining the short-range and long-range impact of stationary sources such as distributed power generators located inside urban areas. The LBM was combined with the short-range transport model AERMOD (Cimorelli et al. 2005) to understand the relative impact of DGs on the ground-level concentration of NO, NO_2 and O_3. This approach is known as *hybrid modeling,* where a combination of a short-range and long-range photochemical transport models are used to predict the relative impact of sources located at different multiple length scales from the receptor.

Using the emission inventory developed by Samuelson et al. (2005), the concentrations of NO, NO_2, and O_3 were estimated under both a "base" scenario and a hypothetical scenario in which DG accounts for 45 percent of the increased power demand from 2007 to 2030. The first scenario reflects the effect of basic ground-level sources (such as mobile sources) on the ground-level concentrations. The second scenario represents a possible future deployment of DG. Two methods were used to predict the impact of DGs on ground-level concentrations: in Chapter 4 the team used solely the LBM, and here in Chapter 5 the team combined the LBM with AERMOD. The team compared these methods and found that the hybrid model shows a higher impact of DGs on NO_x, with lower impact on NO_2, compared to the LBM.

The hybrid model uses the background concentrations from either the LBM or the UCI-CIT model to predict the conversion of NO_x to NO_2 inside the plume. The plume species concentrations obtained from this method are added to those from the background sources (both base and DGs) to predict the total concentration of species at the receptor. Results from these two approaches showed that the contribution of DGs to the ground-level concentrations of NO_x, NO_2, and O_3 is less than 10 percent of the base concentrations. The reason for this low impact is the relatively small increase in the total emissions associated with DGs under the EHP scenario.

Chapter 6:
Conclusions and Recommendations

6.1 Conclusions

The study of the effect of plume rise on ground level concentrations of pollutants emitted from DGs resulted in the following conclusions:

- Realistic modeling of plume rise from DGs plays a major role in determining the ground-level concentrations associated with these sources.
- The Briggs plume rise prediction is in good agreement with observations from the field study of plume rise from a DG in Palm Springs, USA. The relatively sparse and small buildings surrounding the DG do not have a significant impact on plume rise. The low wind speeds in Palm Springs allow the plume to rise high relative to the stack, avoiding possible trapping by the updrafts/downdrafts caused by DG and surrounding buildings. The higher the plume rise, the smaller the effects of the buildings on plume rise.
- The results from laboratory measurements show that, in most cases, the presence of surrounding buildings increases the plume rise as buildings reduce the wind speed close to the stack and induce updrafts in the region where the plume tends to rise.
- A numerical plume rise model which accounts for the effect of surrounding buildings is able to accurately predict the plume rise. To apply this plume rise model to the field case, measurements of building caused flows are needed; however, with the significant improvement in CFD models throughout the past decade, the future work will be to combine this plume rise model with a CFD model and evaluate it with field measurements.
- The Palm Springs field study showed that the highest concentrations occur during the night even though the emissions were highly buoyant. The ability to explain these concentrations through a model was limited by the uncertainty in describing the structure of the stable boundary layer (SBL) over an urban area.

The results of the team's measurement of the nighttime boundary layer height yields the following major conclusions:

- Our analysis of data from three field studies conducted in urban areas confirms earlier results that diagnostic models of the SBL provide poor estimates of the height of the SBL. One-dimensional prognostic models also fare poorly in estimating the SBL height.
- Our analysis indicates that observed boundary layer height correlates best with $\int u_* dt$ where time is counted from sunset; the constant multiplying the integral

might be site specific. An estimate of the boundary layer height based on the integrated surface friction velocity has practical value because the surface friction velocity can be estimated from a measured surface wind speed, and an estimate of the surface roughness length.

The development of the Lagrangian Background Model (LBM) and comparison with observations in the SoCAB and San Joaquin Valley resulted in the following conclusions:

- The model is computationally efficient and is capable of providing hourly concentrations of NO_x, NO_2, and O_3 over time periods of a year, which is required in exposure studies.
- Evaluations with measurements made in SoCAB during 2007 and in the San Joaquin Valley in 2005 indicate that the model can provides adequate descriptions of the spatial and temporal behavior of NO_x and NO_2. Model estimates of maximum hourly ozone concentrations are unbiased relative to observations but the 95 percent confidence interval of the ratios of observed to estimated concentrations is over a factor of two.

The sensitivity study of the LBM resulted in the following conclusions:

- The model is not sensitive to the wind speed and direction, likely because the trajectory, modified by changing the wind speed and direction, still passes through grid squares with emissions that are similar to those of the unmodified trajectory. The model sensitivity to wind speed and direction must depend on the emission distribution because the function of the trajectories is to select the grid squares from which emissions contribute to the predicted concentrations. If the emission distribution within the San Joaquin valley were less homogeneous then the model would likely be more sensitive to the wind speed and direction.
- Our choice of the surface winds, rather than the upper air winds, for calculating the trajectories in the SJV and SoCAB is validated because the model estimates are not very sensitive to the wind speed in these domains.
- The model is not sensitive to the time period over which the back-trajectory is calculated.
- The LBM is very sensitive to the emission distribution.
- The model is sensitive to the boundary layer height formulation, which is important to produce good estimates of the hourly concentration variation.
- Increasing the species age causes the model to overestimate NO_2 and O_3. This, along with the comparison with observations shows that the team's formulation of the species age accurately represents the chemical processes and is useful for decoupling the transport and chemical processes of the model.

The study on the impact of DG on concentrations of NO_x, NO_2, and O_3 under the EHP and SJV-EHP scenarios resulted in the following major conclusions:

- The hybrid model shows a higher impact of DGs on NO_x and a lower impact on NO_2 compared to the LBM alone.
- The contribution of DGs to the ground-level concentrations of NO_x, NO_2 and O_3 in the SoCAB is less than 10 percent of the base concentrations. Under the EHP scenario the maximum increase in NO_2 is about 10 ppb and the maximum decrease in O_3 is about 8 ppb. The reason for this low impact is the relatively small increase in the total emission associated with DGs under the EHP scenario. The team found similar results when comparing the base and EHP scenarios developed by Samuelson et al. (2005) for the San Joaquin Valley. In the San Joaquin Valley the maximum increase in NO_2 and O_3 are both about 1 ppb, relative to base concentrations of about 30 and 60 ppb, respectively. The maximum NO_2 change occurs near Stockton and Bakersfield, where most of the DG emissions are located.

This research helped to understand and address distributed generation knowledge gaps in an effort to identify mitigation measures for potential air quality and near-source exposure impacts from placement of distributed generator. Improved methods of emissions modeling for this particular source of electricity results in more accurate estimates of air pollution emissions and exposure. This modeling helped produce information needed to develop effective mitigation strategies for air quality and near-source exposure impacts. For California residents, this information can be used to improve air quality and reduced adverse health impacts associated with air pollution, including reduced health care costs.

6.2 Recommendations

We developed a hybrid model that combines short-range and long-range transport models, but the model performance has yet to be evaluated with observation data. The greater Detroit area is a suitable region for such a task because a detailed emission inventory, hourly observation data, and meteorology data are available; the team can not fully evaluate the hybrid model using the SoCAB and SJV data because the existing emission inventories are gridded on a scale of several kilometers, but the team can evaluate the model using data measured in Detroit because a highly spatially resolved emission inventory exists for the Detroit area. Note that the team was able to apply the hybrid model to the problem of estimating DG impact because the team generated the team's own fine scale emission inventory for the DG sources. The hybrid model should also be evaluated in many regions with different topographical features and different meteorology conditions to check the model's applicability under various conditions.

As shown in the sensitivity studies, the spatial emission distribution makes the most contribution to the performance of LBM model. Because of this sensitivity the team could probably improve the hybrid model by incorporating land use data and elevation data into the model. Land use data could be used to refine a coarse emission inventory when a fine scale emission inventory is not available, thereby allowing us to apply the hybrid model when no fine scale emission inventory exists. The model should be evaluated with data after incorporating land use data to examine the resulting increase in performance.

The hybrid model treats the entire study region as a flat surface, and the trajectories not confined by the topographical features of a study region. To simulate the SJV the team manually removed emissions from grid squares outside of the valley region because these emissions do not travel into the valley and should not affect the resulting concentrations. The LBM (and hybrid model) should incorporate elevation data so it may account for the effect of mountains by automatically discard inappropriate emissions.

GLOSSARY

Term	Definition
μg/L	micrograms per liter
ABL	atmospheric boundary layer
ADMS	Atmospheric Dispersion Modelling System
AERMET	AERMOD meteorological preprocessor
AERMOD	an atmospheric dispersion modeling system
AERMOD-PRIME	AERMOD Plume Rise Model Enhancements
AQMIS	Air Quality and Meteorological Information System
ARB	California Air Resources Board
CACM	Caltech Atmospheric Chemical Mechanism
CCD	charge coupled device
CBM IV	Carbon Bond IV mechanism
CE-CERT	College of Engineering's Center for Environmental Research and Technology
CFD	Computational Fluid Dynamics
CG	central generating
CIT	California Institute of Technology
CMAS	Community Modeling and Analysis System
CMAQ	Congestion Mitigation and Air Quality
DEOM	Danish Eulerian Operational Model
DG	distributed generation
DOY	Day of Year
EHP	extra high penetration
FB	fractional bias
GRS	Generic Reaction Set
GW	gigawatts
ISL	inertial sublayer

K	kelvin
km	kilometer
LBM	Lagrangian background model
LEFM	University of California Riverside, Laboratory for Environmental Flow Modeling
LIDAR	LIght Detection And Ranging
m	meter
m_g	geometric mean
mg/L	milligrams per liter
mJ	megajoule
mm	millimeter
MOST	Monin-Obukhov similarity theory
ms^{-1}	meters per second
MVK	Model Validation Kit
MWh	megawatt-hour
NAAQS	national ambient air quality standards
nm	nanometers
NMHC	non-methane hydrocarbons
NMB	Normalized Mean Bias
NME	Normalized Mean Error
NO	nitrogen monoxide
NO_2	nitrogen dioxide
NOx	nitrogen oxide
NSME	normalized mean square error
O_3	ozone
OSPM	Operational Street Pollutuion Model
PIER	Public Interest Energy Research Program
PIV	Particle Image Velocimetry
PLIF	planar laser-induced fluorescence
PM	particulate matter

$PM_{2.5}$	particulate matter with diameter less than 2.5 microns
PST	Pacific Standard Time
ppb	parts per billion
RASS	Radio Acoustic Sounding System
RMSE	root mean squared error
ROC	reactive organic compounds
RP	Radical pool
RSL	roughness sublayer
SBL	stable boundary layer
SCAQMD	South Coast Air Quality Management District
s_g	geometric standard deviation
SG	specific gravity
SGN	stable gaseous nitrogen product
SNGN	stable non-gaseous nitrogen product
SIP	state implementation plan
SJVAB	San Joaquin Valley Air Basin
SoCAB	South Coast Air Basin
SODAR	SOnic Detection And Ranging
TVA	Tennessee Valley Authority
UBM	urban background model
UC	University of California
UCI-CIT	University of California, Irvine - California Institute of Technology
UCR	University of California, Riverside
U.S. EPA	U.S. Environmental Protection Agency
VOC	voltaic organic compound
VTMX	Vertical Transport and Mixing
$W\ m^{-2}$	watts per square meter

REFERENCES

Adrian, R. J., 1988. Review of particle image velocimetry research. In: The symposium on optical methods in flow and particle diagnostics, 6th International Congress on Applications of Lasers and Electro-Optics. 9: 317–319, San Diego, California: Optics and Lasers in Engineering.

Adrian, R. J., 1991. "Particle-imaging techniques for experimental fluid-mechanics." *Ann. Rev. Fluid Mech.* 23: 261–304.

Adrian, R. J., 1997. "Dynamic ranges of velocity and spatial resolution of Particle Image Velocimetry." Meas. Sci. & Tech. 8(12): 1393–1398.

Allison, K. E., and J. Lents, 2002. "Encouraging distributed generation of power that improves air quality: Can we have our cake and eat it too?" J. Energy Policy 30: 737–752.

Allwine, K. J., and J. E. Flaherty, 2006. Joint Urban 2003: Study overview and instrument locations. PNNL-15967, Prepared for the U.S. Department of Homeland Security under a Related Services Agreement with the U.S. Department of Energy under contract DE-AC05-76RL01830. Pacific Northwest National Laboratory, Richland, Washington.

Arcoumanis, C., J. J. McGuirk, and J. Palma, 1990. "On the use of Fluorescent dyes for concentration measurements." Exp. Fluids 10: 171-180. doi: 10.1007/BF00215028.

Arya, S. P. S., 1981. "Parameterizing the height of the stable atmospheric boundary layer." J. App. Meteorol. 20: 1192–1202.

Arya, S. P. S., 1988. Introduction to Micrometeorology. San Diego: Academic Press. 307.

Arya, S. P. S., and J. F. Lape, 1990. "A comparative study of the different criteria for the physical modeling of buoyant plume rise in a neutral atmosphere." Atmos. Environ. 24A: 289–295.

Avissar, R., M. D. Moran, G. Wu, R. N. Meroney, and R. A. Pielke, 1990. "Operating ranges of mesoscale numerical models and meteorological wind tunnels for the simulation of sea and land breezes." Boundary-Layer Meteorol. 50: 227–275.

Bacci, P., G. Elisei, and A. Longhetto. 1974. "Lidar measurement of plume rise and dispersion at Ostiglia power station." Atmos. Environ. 8 (11): 1177–1186.

Baklanov, A., S. M. Joffre, M. Piringer, M. Deserti, D. R. Middleton, M. Tombrou, A. Karppinen, S. Emeis, V. Prior, M. W. Rotach, G. Bonafè, K. Baumann-Stanzer, and A. Kuchin, 2006. Towards estimating the mixing height in urban Areas. Recent experimental and modelling results from the COST-715 Action and FUMAPEX project. Scientific Report 06-06. Digital ISBN: 87-7478-540-0 ISSN: 1399–1949.

Barilla, P. A., 1968. Dependence of entrainment coefficients upon orifice conditions in model studies of a smoke plume in a laminar cross wind. M. S. Thesis, Massachusetts Institute of Technology, Cambridge, Massachusetts.

Benkley, C. W., and L. L. Schulman, 1979. „Estimation hourly mixing depth from historical meteorological data." J. App.Meteorol. 18: 772–780.

Berkowicz, R. 1999. OSPM - A parameterised street pollution model. 2nd International Conference on Urban Air Quality, Madrid.

Berkowicz, R., 2000. "A Simple Model for Urban Background Pollution." Environmental Monitoring and Assessment 65: 259–267.

Berlman, I. B., 1971. Handbook of fluorescence spectra of aromatic molecules, 2nd edition. New York: Academic Press.

Blackadar, K., 1962. "The vertical distribution of wind and turbulent exchange in a neutral atmosphere." J. geophys. Res. 67: 3095–3101.

Boarnet, M. G., R. Edwards, M. Princevac, J. Wu, H. Pan, C. Bartolome, et al., 2009. Near-Source Modeling of Transportation Emissions in Built Environments Surrounding Major Arterials. UC Berkeley: University of California Transportation Center. Research paper No. 886. Retrieved from: http://escholarship.org/uc/item/5w357946.

Bosanquet, C. H., 1957. "The rise of a hot waste gas plume." J. Inst. Fuel 30: 322–329. Brandt, J., J. H. Christensen, L. M. Frohn, and R. Berkowicz, 2003. "Air pollution forecasting from regional to urban street scale—implementation and validation for two cities in Denmark." Physics and Chemistry of the Earth, Parts A/B/C 28: 335–344.

Brandt, J., Christensen, J.H., Frohn, L.M., Geernaert, G.L., Berkowicz, R., 2000a. Development of a new operational air pollution forecast system on regional and urban scale. In: Schiermeier, G. (Ed.), Millennium NATO/CCMS International Technical Meeting on Air Pollution Modelling and its Application XIV, 15–19 May 2000, Boulder Colorado, USA. Kluwer Academic/Plenum Publishers, pp. 573–581.

Brandt, J., Christensen, J.H., Frohn, L.M., Berkowicz, R., Palmgren, F., 2000b. The DMU-ATMI THOR air pollution forecast system—system description. National Environmental Research Institute, Roskilde, Denmark, 60pp. NERI Technical Report No. 321.

Brandt, J., Christensen, J.H., Frohn, L.M., Palmgren, F., Berkowicz, R., Zlatev, Z. 2001a. Operational air pollution forecasts from European to local scale. Atmospheric Environment, 35(1) 91-98.

Brandt, J., Christensen, J.H., Frohn, L.M., Berkowicz, R., 2001b. Operational air pollution forecast from regional scale to urban street scale. Part 1: system description. Physics and Chemistry of the Earth (B), 26(10), 781-786.

Brandt, J., Christensen, J.H., Frohn, L.M., 2001c. Operational air pollution forecast from regional scale to urban street scale. Part 2: performance evaluation, Physics and Chemistry of the Earth (B), 26(10), 825-830.

Brandt, J., Christensen, J.H., Frohn, L.M., Zlatev, Z., 2001d. Operational air pollution forecast modelling by using the THOR system. Physics and Chemistry of the Earth (B) 26 (2), 117–122.

Brandt, J., Christensen, J.H., Frohn, L.M., 2001e. Traffic scenarios for the city of Aalborg using the DMU-ATMI THOR model system. Technical report. National Environmental Research Institute, Frederiksborgvej 399, P.O. Box 358, DK-4000 Roskilde, Denmark, p. 20.

Brandt, J., Christensen, J.H., Frohn, L.M., Berkowicz, R., 2003. Air pollution forecasting from regional to urban street scale - implementation and validation for two cities in Denmark. Physics and Chemistry of the Earth, 28, 335-344.

Briggs, G. A., 1969. Plume rise. U.S. Army Environmental Center Critical Review Series. Report Number TID-25075, USAEC Technical Information Center, Oak Ridge, Tennessee.

Briggs, G. A., 1984. Plume rise and buoyancy effects. In: Atmospheric Science and Power Production (D. Randerson, Ed.), Chapter 8, 327–366. DOE/TIC-27601, DE84005177. U.S. Dept. of Energy Office of Sci. and Tech. Information, Springfield, Virginia.

Bringfelt, B., 1968. "Plume rise measurements at industrial chimneys." Atmos. Environ. 2 (6): 575–598.

Britter, R. E. and S. R. Hanna, 2003. "Flow and dispersion in urban areas." Annual Review of Fluid Mechanics 469–496.

Businger, J. A., 1973. Turbulent transfer in the atmospheric surface layer. In: Haugen, D. H. (ed). Workshop on Micrometeorology. Am. Met. Soc., Boston, Massachusetts. 67–100.

Byun, D., and K. L. Schere, 2006. "Review of the Governing Equations, Computational Algorithms, and Other Components of the Models-3 Community Multiscale Air Quality (CMAQ) Modeling System." Applied Mechanics Reviews 59: 51–77.

CARB (California Air Resources Board), 2007. 2007 San Joaquin Valley 8-hour Ozone Plan. Air Resources Board, Sacramento, California. (http://www.arb.ca.gov/planning/sip/2007sip/sjv8hr/sjvozone.htm).

CARB, 2011. California air quality data for the years 1980–2009. Air Resources Board, Sacramento, California. www.arb.ca.gov/aqd/aqdcd/aqdcddld.htm.

CARB, 2012. California air quality data for the years 1980-2009. Air Resources Board, Sacramento, CA (http://www.arb.ca.gov/aqd/aqdcd/aqdcddld.htm).

Carlotti, P., and G. R. Hunt, 2005. "Analytical solutions for turbulent non-Boussinesq plumes." J. Fluid Mech. 538: 343–359.

Carpenter, S. B., J. A. Frizzola, M. E. Smith, J. M. Leavitt, and F. W. Thomas. 1968. "Full-Scale Study of Plume Rise at Large Electric Generating Stations." J. Air Pollut. Control Assoc. 18(7): 458–465.

Carreras-Sospedra, M., M. Medrano, G. S. Samuelsen, J. Brouwer, M. Rodriguez, and D. Dabdub, 2004. Urban air quality impacts of distributed generation, Proceedings of ASME Turbo Expo, 14–17 June, Vienna, Austria.

Carreras-Sospedra, M., D. Dabdub, J. Brouwer, E. Knipping, N. Kumar, K. Darrow, A. Hampson, and B. Hedman, 2008. "Air quality impacts of distributed energy resources implemented in the northeastern United States." J. Air & Waste Management Association 58(7): 902–912.

Carreras-Sospedra, M., Vutukuru, S., Brouwer, J., Dabdub, D., 2010. "Central power generation versus distributed generation–An air quality assessment in the South Coast Air Basin of California." Atmospheric Environment, 44(26), 3215-3223.

Carruthers, D. J., R. Holroyd, J. Hunt, W. S. Weng, A. G. Robins, D. Apsley, D. Thomson, and F. Smith, 1994. UK-ADMS: A new approach to modelling dispersion in the Earth's atmospheric boundary layer. J. Wind Eng. Ind. Aerodyn. 52: 139–153.

Carruthers, D. J., A. M. Mckeown, D. J. Hall, and S. Porter, 1999. "Validation of ADMS against wind tunnel data of dispersion from chemical warehouse fires." Atmos. Environ., 33: 1937–1953.

CERR, 2002. Consolidated Emission Reporting Rule, Federal Register: 10 June 2002, vol. 67, No. 111, Proposed Rules, pp. 39602–39616.

Cermak, J. E., A. G. Davenport, E. J. Plate, and D. X. Viegas, 1995. Wind Climate in Cities, Proceedings of a NATO Advanced Study Institute. NATO ASI Series E, 277, Kluwer Academic Publishers, Dordrecht, The Netherlands, 772 pp. ISBN 0-7923-3202-4.

Cimorelli, A. J., S. G. Perry, A. Venkatram, J. C. Weil, R. Paine, R. B. Wilson, R. F. Lee, W. D. Peters, and R. W. Brode, 2005. "AERMOD: A dispersion model for industrial source applications. Part I: general model formulation and boundary layer characterization." Journal of Applied Meteorology 44(5): 682–693.

Clarke, R. H., A. J. Dyer, R. R. Brook, D. G. Reid, and A. J. Troup, 1971. The Wangara Experiment: Boundary layer data. Tech. Paper No. 19, Div. Meteorol. Phys., CSIRO, Australia.

Cohan, A., Chang, W., Carreras-Sospedra, M., Dabdub, D., 2008. Influence of sea-salt activated chlorine and surface-mediated renoxification on the weekend effect in the South Coast Air Basin of California. Atmospheric Environment, 42(13), 3115-3129.

Contini, D., A. Donateo, D. Cesari, and A. G. Robins, 2011. "Comparison of plume rise models against water tank experimental data for neutral and stable crossflows." J. Wind Eng. Ind. Aerodyn. 99(5): 539–553.

Contini, D., and A. G. Robins, 2001. "Water tank measurements of buoyant plume rise and structure in neutral crossflows." Atmos. Environ. 35: 6105–6115.

Contini, D., and A. G. Robins, 2004. "Experiments on the rise and mixing in neutral crossflow of plumes from two identical sources for different wind directions." Atmos. Environ. 38: 3573–3583.

Cuxart, J., and coauthors, 2006. "Single-column model intercomparison for a stably stratified atmospheric boundary layer." Boundary-Layer Meteorol. 118: 273–303.

Davidson, G. A., and P. R. Slawson, 1967. "Effective source flux parameters for use in analytical plume rise models." Atmos. Environ. 16(2): 223–227.

Deardorff, J. W., 1972. Rate of growth of the nocturnal boundary layer. In H. W. Church and R. E. Luna (eds.) Proceeding of American Meteorological Society Conference on Air Pollution, Turbulence & Diffusion. Las Cruces, New Mexico, 183–190.

Doran, J. C., J. D. Fast, J. Horel, 2002. "The VTMX 2000 campaign." Bulletin of the Am. Met. Soc. 83:537–551.

Eder, B., Yu, S., 2006. A performance evaluation of the 2004 release of Models-3 CMAQ. Atmospheric Environment. 40, 4811-4824.

Eliassen, A., Saltbones, J., 1983. Modelling of long-range transport of sulphur over Europe: a two-year model run and some model experiments. Atmospheric Environment. 17(8), 1457-1473.

Ensberg, J. J., Carreras-Sospedra, M., Dabdub, D., 2010. Impacts of electronically photo-excited NO 2 on air pollution in the South Coast Air Basin of California. Atmospheric Chemistry and Physics, 10(3), 1171-1181.

EPA, 2008. AERSURFACE User's Guide. EPA-454/B-083-001. U.S. Environmental Protection Agency, Research Triangle Park, North Carolina.

Etling, D., and F. Wippermann, 1975. "The height of the planetary boundary layer and of the surface layer." Beitraege zur Physik der Atmosphaere 48: 250–254.

Fackrell, J. E., and J. E. Pearce, 1981. Parameters affecting dispersion in the near wake of buildings. Central Electricity Generating Board, Report RD/M/1179N81, Marchwood Engineering Laboratories, UK (1981), p. 41.

Fay, J. A., 1973. "Buoyant plumes and wakes." Ann. Rev. Fluid Mech. 5, 151–160. DOI: 10.1146/annurev.fl.05. 010173.001055.

Fay, J. A., M. P. Escudier, and D. Hoult, 1970. "A correlation of field observations of plume rise." J. Air Pollut. Control Ass. 20: 291–397.

Fujita, E. M., Stockwell, W. R., Campbell, D. E., Keislar, R. E., Lawson, D. R., 2003. Evolution of the magnitude and spatial extent of the weekend ozone effect in California's South Coast Air Basin, 1981–2000. Journal of the Air & Waste Management Association, 53(7), 802-815.

Gailis, R. M., and A. Hill, 2006. "A wind tunnel simulation of plume dispersion within a large array of obstacles." Boundary-Layer Meteorol. doi: 10.1007/s10546-005-9029-1.

Garratt, J. R., 1982. "Observations in the nocturnal boundary layer. Boundary-Layer Meteorol. 22: 21–48.

Garratt, J. R., 1992. The Atmospheric Boundary Layer. University Press: Cambridge. 316.

Gery, M. W., G. Z. Whitten, J. P. Killus, and M. C. Dodge, 1989. "A photochemical kinetics mechanism for urban and regional scale computer modeling." J. Geophys. Res. 94.

Griffin, R. J., D. Dabdub, and J. H. Seinfeld, 2002. "Secondary organic aerosol: 1. Atmospheric chemical mechanism for production of molecular constituents." J. Geophys. Res. 107(D17), 4332, DOI:10.1029/2001JD000541.

Grimmond, C. S. B., and T. R. Oke, 2002. "Turbulent heat fluxes in urban areas: Observations and a local-scale urban meteorological parameterization scheme (LUMPS)." J. App.Meteorol. 41(7): 792–810.

Guilbault, G. G., 1973. Practical Fluorescence: Theory, Methods and Techniques. Dekker: New York.

Halitsky, J., 1968. Gas diffusion near buildings. D. H. Slade, Editor, TID-24190, Meteorology and Atomic Energy, chapter 5-5, 221–231.

Halliday, E. C., 1968. "Measurements of the rise of hot plumes." Atmos. Environ. 2(5): 509–516.

Hamilton, P. M., 1967. "Paper III: Plume height measurements at Northfleet and Tilbury power stations." Atmos. Environ. 1(4): 379–387.

Hanna, S. R., 1969. "The thickness of the planetary boundary layer." Atmos. Environ. 3: 519–536.

Heath, G. A., P. W. Granvold, A. S. Hoats, and W. W. Nazaroff, 2006. "Intake fraction assessment of the air pollutant exposure implications of a shift toward distributed electricity generation." Atmos. Environ. 40: 7164–7177.

Hess, G. D., B. B. Hicks, and T. Yamada, 1981. "The Impact of the Wangara Experiment." Boundary-Layer Meteorol.

Hess, G. D., and M. E. Cope, 1989. "A Note on Subgrid-Scale Processes in Photochemical Modelling." Atmospheric Environment 23: 2857–2860.

Holtslag, A. A. M., E. I. F. De Bruin, and H. L. Pan, 1990. "A high resolution air mass transformation model for short range weather forecasting." Mon. Weather Rev. 118: 1561–1575.

Houcine, I., H. Vivier, E. Plasari, R. David, and J. Villermaux, 1996. "Planar laser induced Fluorescence technique for measurements of concentration fields in continuous stirred reactors." Exp. Fluids 22: 95–102.

Hoult, D. P., J. Fay, and L. Forney, 1969. "A theory of plume rise compared with field observations." J. Air Pollut. Control Assoc. 19: 585–590.

Hoult, D. P., and J. C. Weil, 1972. "Turbulent plume in a laminar cross flow." Atmos. Environ. 6(8): 513–530. DOI: 10.1016/0004-6981(72)90069-8.

Hughes, S. A., 1993. Physical models and laboratory techniques in coastal engineering. Advanced series on ocean engineering, v. 7. Singapore: World Scientific. pp. 568.

Hunter, G. C., 1992. The behavior of plumes from point sources in stratified flows. Ph.D. Dissertation, National Power Research and Technology Department. 275 pp. Available from British Library Document Supply Center DSC: DX172355.

Hurley, P., Manins, P., Lee, S., Boyle, R., Ng, Y. L., Dewundege, P., 2003. Year-long, high-resolution, urban airshed modelling: verification of TAPM predictions of smog and particles in Melbourne, Australia. Atmospheric Environment, 37(14), 1899-1910.

Isakov, V., A. Venkatram, J. S. Touma, D. Koracin, and T. L. Otte, 2007. "Evaluating the use of outputs from comprehensive meteorological models in air quality modeling applications." Atmos. Environ. 41(8): 1689–1705.

Isyumov, N., and H. Tanaka, 1979. Wind tunnel modelling of stack gas dispersion: Difficulties and approximations. In Wind Engineering (edited by Cermak, J. E.), 2, 987–1001. Pergamon Press: Oxford.

Jensen, M., 1958. "The Model Law for Phenomena in Natural Wind." Ingenioren, 2: 121–128.

Jin, L., Harley, R.A., Brown, N.J., 2011. Ozone pollution regimes modeled for a summer season in California's San Joaquin Valley: a cluster analysis. Atmospheric Environment. 45 (27), 4707-4718.

Jing Q., and A. Venkatram, 2011. "The relative impacts of distributed and centralized generation of electricity on local air quality in the South Coast Air Basin of California." Energy Policy 39(9): 4999–5007. doi: 10.1016/j.enpol.2011.05.056.

Jing, Q., 2011. Air Quality Impact of Distributed Generation of Electricity, Dissertation (PhD), University of California, Riverside.

Jing, Q., A. Venkatram, M. Princevac, D. Pankratz, and W. Qian, 2010. Modeling Dispersion of Buoyant Emissions from Low Level Sources in an Urban Area, 90th AMS Annual Meeting, 16th Conference on Air Pollution Meteorology, 90th Annual Meeting, Atlanta, Georgia. January 2010.

Johnson, G.M., 1984. A simple model for predicting the ozone concentration of ambient air. Proceedings of the Eighth International Clean Air and Environment Conference, Clean Air Society of Australia and New Zealand, New Zealand.

Kaimal, J. C., and J.J. Finnigan, 1994. Atmospheric Boundary Layer Flows: Their Structure and Measurement. New York- Oxford: University Press Inc.

Karasso, P. S., and M. G. Mungal, 1997. "PLIF measurements in aqueous flows using the Nd: YAG laser." Exp. Fluids 23(5): 382–387.

Klein, P., B. Leitl, and M. Schatzmann, 2011. "Concentration fluctuations in a downtown urban area—part II: Analysis of joint urban 2003 wind-tunnel measurements." Environ. Fluid Mech. 11(1): 43–60. doi:10.1007/s10652-010-9195-7.

Kobus, H., and G. Abraham, 1980. Hydraulic modelling. Hamburg, West Germany: Parey. pp. 323

Koracin, D., and R. Berkowicz. 1988. "Nocturnal boundary layer height: Observations by acoustic sounders and prediction in terms of surface layer parameters." Boundary-Layer Meteorol. 43: 65–83.

Kulchin Y. N., S. S. Voznesenskiy, E. L. Gamayunov, A. S. Gurin, A. A. Korotenko, and A. Y. Maior, 2007. "An Immersible Fiber-Optic Fluorometer." Instruments and Experimental Techniques 6: 117–122.

Kychakoff, G., R. D. Howe, and R. K. Hanson, 1984. "Quantitative Flow visualization technique for measurements in combustion gases." Applied Optics 23: 704–712.

Laikhtman, L., 1961. Physics of the Boundary Layer of the Atmosphere. Translated by the Israel Program for Scientific Translations, Jerusalem, 1964. Available from the office of Technical Services, U.S. Dept. of Commerce, Washington, D.C., 200.

Lawson, D.R., 1990. The Southern California Air Quality Study. Journal of the Air and Waste Management Association. 40, 156-165.

Lena, F., and F. Desiato, 1999. "Intercomparison of nocturnal mixing height estimate methods for urban air pollution modeling." Atmos. Environ. 33(15): 2385–2393.

Lettau, H. H., 1962. "Theoretical wind spirals in the boundary layer of a barotropic atmosphere." Beit. Phys. Atmos. 35: 195–212.

Li, S.M., 2004. A concerted effort to understand the ambient particulate matter in the Lower Fraser Valley: The Pacific 2001 Air Quality Study. Atmospheric Environment. 38, 5719–5731.

Liu, X.-H., Zhang, Y., Cheng, S.-H., Xing, J., Zhang, Q., Streets, D.G., Jang, C., Wang, W.-X., Hao, J.-M., 2010. Understanding of regional air pollution over China using CMAQ, part I performance evaluation and seasonal variation. Atmospheric Environment. 44, 2415-2426.

Lucas, D. H., D. J. Moore, and G. Spurr, 1963. "The rise of hot plumes from chimneys." Int. J. Air Wat. Pollut. 7: 473–500.

Luhar, A. K., A. Venkatram, and S. M. Lee, 2006. "On relationships between urban and rural near-surface meteorology for diffusion applications." Atmos. Environ. 40(34): 6541–6553.

Macdonald, R. W., R. F. Griffiths, and D. J. Hall, 1998. "A comparison of results from scaled field and wind tunnel modelling of dispersion in arrays of obstacles." Atmos. Environ. 32(22): 3845–3862.

Mahrt, L., 1981a. "Modeling the depth of the stable boundary layer." Bound-Layer Meteorol. 21: 3–19.

Mahrt, L., 1981b. "The early evening boundary layer transition." Quarterly. J. Roy. Met. Soc. 107: 329–343.

Mahrt, L., 1998. "Stratified atmospheric boundary layer." Boundary-Layer Meteorology 90: 375–396.

Mahrt, L., J. C. Andre, and R. C. Heald, 1982. "On the depth of the nocturnal boundary layer." J. App.Meteorol. 21, 90–92.

McNair, L.A., Harley, R.A., Russell, A.G., 1996. Spatial inhomogeneity in pollutant concentrations, and their implications for air quality model evaluation. Atmospheric Environment. 30, 4291-4301.

Melgarejo, J. W., and J. W. Deardorff, 1974. "Stability functions for the boundary layer resistance laws based upon observed boundary layer heights." J. Atmos. Sci., 31: 1324–1333.

Meroney, R. N., 1982. "Wind tunnel experiments on dense gas dispersion." Special Issue J. of Hazardous Materials 6: 85–106.

Meroney, R. N., 1986a. Guideline for fluid modeling of liquefied natural gas cloud dispersion - Vol. I: Instruction Guide. Final Report for Gas Research Institute, Contract No. 5083-252-0962, Report GRI86/0102.1, May 1986, pp. 57.

Meroney, R. N., 1986b. Guideline for fluid modeling of liquefied natural gas cloud dispersion - Vol. II: Technical Support Document. Final Report for Gas Research Institute, Contract No. 5083-252-0962, Report GRI86/0102.2, May 1986, pp. 262.

Meroney, R. N., 1987. "Validation of fluid modeling techniques for assessing hazards of dense gas cloud dispersion." Journal of Hazardous Materials 15: 377–417.

Meroney, R. N., 1998. Wind tunnel simulation of convective boundary layer phenomena: Simulation criteria and operating ranges of laboratory facilities. Buoyant Convection in Geophysical Flows, E. J. Plate et al., Eds., Kluwer, 313–326.

Meroney, R. N., J. E. Cermak, and B. T. Yang. 1975. "Modeling of atmospheric transport and fumigation at shoreline site." Boundary-Layer Meteorol. 9: 69–90.

Meroney, R. N., and W. H. Melbourne, 1992. "Operating Ranges of Meteorological Wind Tunnels for the Simulation of Convective Boundary Layer (CBL) Phenomena." Boundary-Layer Meteorol. 61: 145–174.

Mery, P., 1969. "Reproduction en Similitude de la Diffusion dans la Couche Limite Atmospherique." la Houille Blanche 4: 327–343.

Morton, B. R., G. I. Taylor, and J. S. Turner, 1956. "Turbulent gravitational convection from maintained and instantaneous sources." Proc. R. Soc. Lond. A 234: 1–23.

Neff, D. E., and R. N. Meroney, 1981. The behavior of LNG vapor clouds: Wind-tunnel simulation of 40 m3 LNG spill tests at China lake Naval Weapons Center, California. Final Report for Gas Research Institute, Report GRI 80/0094, pp. 155

Nieuwstadt, F. T. M., 1984. "Some aspects of the turbulent stable boundary layer." Boundary-Layer Meteorol. 30: 31–55.

Nieuwstadt, F. T. M., and H. Tennekes, 1981. "A rate equation for the nocturnal boundary layer height." J. Atmos. Sci. 38: 1418–1428.

Obasaju, E. D., and A. G. Robins, 1998. "Simulation of pollution dispersion using small scale physical models - an assessment of scaling options." Environ. Monitoring Assessment 52(1–2): 239–254.

Ohba, R., S. Kakishima, and S. Ito, 1990. "Water tank study of plume rise and diffusion in a stably stratified layer under calm conditions." Il Nuovo Cimento C 13(6): 1017–1028.

Oke, T. R. 1987. Boundary Layer Climates. 2nd ed. Routledge: London, 435 pp. ISBN 0-415-04319-0.

Olesen, H. R., 2005. User's guide to the Model Validation Kit. Initiative on harmonisation within atmospheric dispersion modeling for regulatory purposes. Available at http://www.harmo.org/kit/Download/Kit_UsersGuide.pdf.

Plate, E. J., 1999. "Methods of Investigating Urban Wind Fields–Physical Models." Atmos. Environ 33: 3981–3989.

Poreh, M., M. Rau, and E. J. Plate, 1991. "Design considerations for wind tunnel simulations of diffusion within the convective boundary layer." Atmos. Environ. 25A: 1250–1257.

Pournazeri, S., M. Princevac, and A. Venkatram, 2012a." Rise of Buoyant Emissions from Low-Level Sources in the Presence of Upstream and Downstream Obstacles." Boundary-Layer Meteorology 144(2): 287–308.

Pournazeri, S., A. Venkatram, M. Princevac, S. Tan, and N. Schulte, 2012b. "Estimating the height of the nocturnal urban boundary layer for dispersion applications." Atmospheric Environment 54: 611–623.

Prasad, A. K., R. J. Adrian, C. C. Landreth, and P. W. Offutt, 1992. "Effect of resolution on the speed and accuracy of Particle Image Velocimetry interrogation." Exp. Fluids 13(2-3): 105–116.

Priestly, C. H. B., 1956. "A working theory of the bent-over plume of hot gas." Q. J. Roy. Meteorol. Soc. 82(352): 165–176. DOI: 10.1002/qj.49708235203.

Princevac, M., J. Baik, X. Li, H. Pan, and S. Park, 2010. "Lateral channeling within rectangular arrays of cubical obstacles." J. Wind Eng. Ind. Aerodyn. 98: 377–385. DOI: 10.1016/j.jweia.2009.11.001.

Princevac, M., and A. Venkatram, 2007. Estimating micrometeorological inputs for modeling dispersion in urban areas during stable conditions, Atmos. Environ. 41(26): 5345–5356.

Pringsheim, P., 1949. Flourescence and Phosphorescence. Interscience: New York.

Qian, W., M. Princevac, and A. Venkatram, 2010. "Using temperature fluctuation measurements to estimate meteorological inputs for modelling dispersion during convective conditions in urban areas." Boundary-Layer Meteorology 135: 269–289.

Qian, W., and A. Venkatram, 2011. "Performance of Steady-State Dispersion Models Under Low Wind-Speed Conditions." Boundary-Layer Meteorol. 138: 475–491.

Rau, M., W. Bachlin, and E. J. Plate, 1991. "Detailed design features of a new wind tunnel for studying the effects of thermal stratification." Atmos. Environ. 25(7): 1257–1262. DOI: 10.1016/0960-1686(91)90236-Z.

Ricou, F. P., and D. B. Spalding, 1961. "Measurements of entrainment by axisymmetrical turbulent jets." J. Fluid Mech. 8: 21–32.

Robins, A. G., D. D. Apsley, D. J. Carruthers, C. A. McHugh, and S. J. Dyster, 2005. Plume rise model specification. ADMS 3 documentation (P11/02N/05), Cambridge Environmental Research Consultants Ltd.

Robins, A. G., and C. McHugh, 2001. "Development and Evaluation of the ADMS Building Effects Module." Int. J. Environ. and Poll. 16(1-6): 161–174.

Robins, A. G., 1980. Wind Tunnel Modelling of Buoyant Emissions, In: Michel M. Benarie, Editor(s), Studies in Environmental Science, 8, 117–124. ISSN 0166-1116, ISBN 9780444418890.

Robins, A. G., 2003. "Wind-tunnel modelling some recent and not so recent achievements." J. Wind Eng. Ind. Aerodyn. 91: 1777–1790.

Robins, A. G., D. J. Carruthers, and C. A. McHugh, 1997a. "The ADMS building effects module." Int. J. Environ. and Poll. 8: 708–717.

Robins, A. G., C. A. McHugh, and D. J. Carruthers, 1997b. "Testing and evaluating the ADMS building effects module." Int. J. Environ. and Poll. 8(3-6): 708–717.

Rodriguez, M.A. , Carreras-Sospedra , M. , Medrano., M., Brouwer, J., Samuelsen, G.S., Dabdub, D., 2006. "Air quality impacts of distributed power generation in the South Coast Air Basin of California 1: Scenario development and modeling analysis." Atmos. Environ., 40(2006), 5508-5521.

Rotach, M. W., 1993. "Turbulence Close to a Rough Urban Surface Part I: Reynolds Stress." Boundary-Layer Meteorol. 65: 1–28.

Rotach, M. W., 2001. "Simulation of urban-scale dispersion using a lagrangian stochastic dispersion model." Boundary-Layer Meteorol 99: 379–410.

Rotach, M. W., S. E. Gryning, E. Batchvarova, A. Christen, and R. Vogt, 2004. "Pollutant dispersion close to an urban surface—the BUBBLE tracer experiment." Meteorol. Atmos. Phys. 87(1-3): 39–56.

Samuelsen, S., D. Dabdub, J. Brouwer, M. Medrano, M. Rodriguez, and M. Carreras-Sosedra, 2005. Air quality impacts of distributed generation. California Energy Commission, PIER Energy-Related Environmental Research, CEC-500-2005-069-F.

Samuelsen, S., Dabdub, D., Brouwer, J., Carreras-Sospedra, M., Vutukuru, S., 2010. Air quality impacts of distributed generation in the South Coast air basin and the San Joaquin Valley. California Energy Commission, PIER Energy-Related Environmental Research, CEC-500-2009-070.

SCAQMD, 2009. 26 Sites with AERMOD-Ready Meteorological Data, South Coast Air Quality Management District, Diamond Bar, California (www.aqmd.gov/ smog/metdata/AERMOD_Table2.html).

Schulman, L. L., D. G. Strimaitis, and J. S. Scire, 2000. "Development and evaluation of the PRIME plume rise and building downwash model." J. Air Waste Manag. Assoc. 50: 378–390.

Seibert, P., F. Beyrich, S. E. Gryning, S. Joffre, A. Rasmussen, and P. Tercier, 1998. Mixing layer depth determination for dispersion modelling. European Commission. In: Fisher, B. E. A., J. J. Erbrink, S. Finardi, P. Jeannet, S. Joffre, M. G. Morselli, U. Pechinger, P. Seibert, and D. J. Thomson, eds. COST Action 710-Final Report. Harmonisation of the pre-processing of meteorological data for atmospheric dispersion models. L-2985 Luxembourg: European Commission, EUR 18195 EN (ISBN 92- 828-3302-X).

Seibert, P., F. Beyrich, S. E. Gryning, S. Joffre, A. Rasmussen, and P. Tercier, 2000. "Review and intercomparison of operational methods for the determination of the mixing height." Atmos. Environ. 34: 1001–1027.

Snyder, W. H., 1972. "Similarity criteria for the application of fluid models to the study of air pollution meteorology." Boundary-Layer Meteorol. 3: 113.

Snyder, W. H., 1981. Guidelines for fluid modeling of atmospheric diffusion. Report Number EPA-600/8-81-009, Environmental Protection Agency, Research Triangle Park, North Carolina. 200 pp.

Snyder, W. H., 1985. "Fluid modeling of pollutant transport and diffusion in stably stratified flows over complex terrain." Annu. Rev. Fluid Mech. 17: 239–266.

Snyder, W. H., and R. E. Lawson, 1991. "Fluid modelling simulation of stack-tip downwash for neutrally buoyant plumes." Atmos. Environ., 25A, 2837–2850.

Sorbjan, Z., 1989. Structure of atmospheric boundary layer, London: Prentice Hall, 317.

Steeneveld, G.J., B. J. H. Van de Wiel, and A. A. M. Holtslag, 2007. "Diagnostic equations for the stable boundary layer height: Evaluation and dimensional analysis." J. Appl.Meteor. Climate 46: 212–225.

Stein, A. F., V. Isakov, J. Godowitch, and R. R. Draxler, 2007. "A hybrid modeling approach to resolve pollutant concentrations in an urban area." Atmos. Environ. 41: 9410–9426.

Stull, R. B., 1983. "A heat-flux history length scale for the nocturnal boundary layer." Tellus 35A: 219–230.

Stull, R. B., 1988. An Introduction to Boundary Layer Meteorology. Kluwer Academic Publisher: Boston.

Sutton, O. G., 1947. "The problem of diffusion in the lower atmosphere." QJRMS 73: 257–281.

Smyth, S.C., Jiang, W., Yin, D., Roth, H., Giroux, É., 2006. Evaluation of CMAQ O3 and PM2.5 performance using Pacific 2001 measurement data. Atmospheric Environment. 40, 2735-2749.

Taylor, G. I., 1931. "Effects of Variation in Density on the Stability of Superimposed Streams of Fluids." Proc. Roy. Soc. (Lond.), Ser. A 132: 499–523.

Thompson, R. S., 1993. "Building amplification factors for sources near buildings: A wind tunnel study." Atmos. Environ. 15: 2313–2325.

Townsend, A. A., 1956. "The Structure of Turbulent Shear Flow." Cambridge University Press: Cambridge, England. pp. 315.

Venkatram, A., 1980. "Estimating the Monin-Obukhov length in the stable boundary layer for dispersion calculations." Boundary-Layer Meteorol. 19: 481–485.

Venkatram, A., and R. Paine, 1985. "A model to estimate dispersion of elevated releases into a shear-dominated boundary layer." Atmos. Environ. 19(11) 1797-1805. doi: 10.1016/0004-6981(85)90006-X.

Venkatram, A., P. Karamchandani, P. Pai, and R. Goldstein, 1994. "The development and application of a simplified ozone modeling system (SOMS)." Atmos. Environ. 28: 3665–3678.

Venkatram, A., S. Du, R. Hariharan, W. Carter, and R. Goldstein, 1998. "The concept of species age in photochemical modeling." Atmos. Environ. 32: 3403–3413.

Venkatram, A., V. Isakov, J. Yuan, and D. Pankratz, 2004a. "Modeling Dispersion at Distances of Meters from Urban Sources." Atmos. Environ. 38(28): 4633–4641.

Venkatram, A., V. Isakov, D. Pankratz, J. Heumann, and J. Yuan, 2004b. "The analysis of data from an urban dispersion experiment." Atmos. Environ. 38(22): 3647–3659.

Venkatram, A., V. Isakov, D. Pankratz, and J. Yuan, 2005. "Relating plume spread to meteorology in urban areas." Atmos. Environ. 39(2): 371–380.

Venkatram, A., and A. J. Cimorelli, 2007. "On the role of nighttime meteorology in modeling dispersion of near surface emissions in urban areas." Atmos. Environ. 41(4): 692–704.

Venkatram, A., 2008. "Computing and displaying model performance statistics." Atmos. Environ. 24: 6862–6868.

Venkatram, A., and M. Princevac, 2008. "Using measurements in urban areas to estimate turbulent velocities for modeling dispersion." Atmos. Environ. 42(16): 3833–3841.

Vijayaraghavan, K., Karamchandani, P., Seigneur, C., 2006. Plume-in-grid modeling of summer air pollution in central California. Atmospheric Environment. 40, 5097–5109.

Vutukuru, S., and D. Dabdub, 2008. "Modeling the effects of ship emissions on coastal air quality: A case study of southern California." Atmospheric Environment 42(16): 3751–3764.

Walker, D. A., 1987. "A fluorescence technique for measurement of concentration in mixing liquids." Journal of Physics 20: 217–224.

Weil, J. C., 1988. Plume Rise, In: Venkatram, A. and J. C. Wyngaard, editors. "Lectures in Air Pollution Modeling." Am. Met. Soc. Boston, Massachusetts, 119–166.

Woods, A. W., 1997. "A note on non-Boussinesq plumes in an incompressible stratified environment." J. Fluid Mech. 345: 347–356.

Yamada, T., 1979. "Prediction of the nocturnal surface inversion height." J. Appl.Meteor. 18: 226–531.

Yee, E., R. M. Gailis, A. Hill, T. Hilderman, and D. Kiel, 2006. "Comparison of wind-tunnel and water-channel simulations of plume dispersion through a large array of obstacles with a scaled field experiment." Boundary-Layer Meteorol. 121: 389–432.

Yu, T. W., 1978. "Determining height of the nocturnal boundary layer." J. Appl.Meteor. 17: 28–33.

Zhang, Y., Vijayaraghavan, K., Wen, X.-Y., Snell, H.E., Jacobson, M.Z., 2009. Probing into regional ozone and particulate matter pollution in the United States: 1. A 1 year CMAQ simulation and evaluation using surface and satellite data. Journal of Geophysical Research. 114, D22304.

Zilitinkevich, S. S., 1972. "On the Determination of the Height of the Ekman Boundary Layer." Boundary-Layer Meteorol. 3: 141–145.

Zilitinkevich, S. S., and A. Baklanov, 2002. "Calculation of the Height of the Stable Boundary Layer in Practical Applications." Boundary-Layer Meteorol. 105: 389–409.

Zilitinkevich, S. S., A. Baklanov, J. Rost, A. S. Smedman, V. Lykosov, and P. Calanca, 2002. "Diagnostic and Prognostic Equations for the Depth of the Stably Stratified Ekman Boundary Layer." QJRMS 128(579): 25–46.

APPENDIX A:

IMPROVING UNDERSTANDING OF REGIONAL AND NEAR-SOURCE AIR QUALITY IMPACTS OF DISTRIBUTED GENERATION SOURCES

Alexander Cohan

Department of Mechanical & Aerospace Engineering

University of California, Irvine

Table of Contents

1 Executive Summary 5

2 Introduction 5

3 Emissions.....6

4 Metereology ..... **Error! Bookmark not defined.**

5 Single Point Model Results 11

6 Distributed Power Generation Results 16

7 NO_X to VOC Ratio.....21

8 UCI-CIT model and AERMOD Results 23

9 Box Model 25

9.1 Box Model Description.....25

9.2 Test Case 1.....28

9.3 Test Case 2.....28

10 Development and Evaluation of Chemistry Methods in AERMOD 29

10.1 Background.....30

10.2 A Highly Resolved Eulerian Model 31

10.3 AERMOD 34

10.4 Plume Chemistry- OLM.....36

10.5 Plume Chemistry- PVMRM.....36

10.6 Plume Chemistry- Hess' Method.....37

10.7 Plume Chemistry – VA.....37

10.8 Scenarios.....39

10.9 Results.....41

10.10 Discussion 46

11 Acknowledgements ..... **Error! Bookmark not defined.**

12 References 48

13 Appendix A: Species List 56

Table of Figures

Figure 1. Daily NO_X emissions (g/s) . ..... **Error! Bookmark not defined.**

Figure 2. Daily VOC emissions (g/s). 102

Figure 3. Flow chart of methodology structure. UCI modules are shown in orange, UCR modules are shown in blue, shared modules are shown in green.**Error! Bookmark not defined.**

Figure 4. UCI-CIT model 24Hr NO (ppb) difference without chemistry (a) no background emissions, (b) with background emissions..... **Error! Bookmark not defined.**

Figure 5. UCI-CIT model 24Hr NO_2 (ppb) difference without chemistry (a) no background emissions, (b) with background emissions..... **Error! Bookmark not defined.**

Figure 6. UCI-CIT model 24Hr NO (ppb) difference (a) no background emissions, (b) with background emissions..... **Error! Bookmark not defined.**

Figure 7. UCI-CIT model 24Hr NO_2 (ppb) difference (a) no background emissions, (b) with background emissions..... **Error! Bookmark not defined.**

Figure 8. UCI-CIT model transport only 24Hr NO (ppb) results; Base line August 27(a), 28(b) and 29(c), EHP area sources minus baseline August 27(d), 28(e) and 29(f), EHP point sources minus baseline August 27(g), 28(h) and 29(i)..... **Error! Bookmark not defined.**

Figure 9. UCI-CIT model transport only 24Hr NO_2 (ppb) results; Base line August 27(a), 28(b) and 29(c), EHP area sources minus baseline August 27(d), 28(e) and 29(f), EHP point sources minus baseline August 27(g), 28(h) and 29(i). .. **Error! Bookmark not defined.**

Figure 10. UCI-CIT model 24Hr NO (ppb) results; Base line August 27(a), 28(b) and 29(c), EHP area sources minus baseline August 27(d), 28(e) and 29(f), EHP point sources minus baseline August 27(g), 28(h) and 29(i)..... **Error! Bookmark not defined.**

Figure 11. UCI-CIT model 24Hr NO_2 (ppb) results; Base line August 27(a), 28(b) and 29(c), EHP area sources minus baseline August 27(d), 28(e) and 29(f), EHP point sources minus baseline August 27(g), 28(h) and 29(i)..... **Error! Bookmark not defined.**

Figure 12. UCI-CIT model transport only 24Hr NO_X to VOC ratio; Base line August 27(a), 28(d) and 29(g), EHP area sources minus baseline August 27(c), 28(f) and 29(i), EHP point sources minus baseline August 27(b), 28(e) and 29(h)... **Error! Bookmark not defined.**

Figure 13. UCI-CIT model 24Hr NO_X to VOC ratio; Base line August 27(a), 28(d) and 29(g), EHP area sources minus baseline August 27(c), 28(f) and 29(i), EHP point sources minus baseline August 27(b), 28(e) and 29(h)..... **Error! Bookmark not defined.**

Figure 14. One day simulation results of NO and NO_2 from initial mixture of NO, NO_2 and O_3 at 10 PPM each. ..... **Error! Bookmark not defined.**

Figure 15. One day simulation results of NO and NO_2 from constant NO_2 source of 10 PPM*m/min..... **Error! Bookmark not defined.**

Figure 16. Steady state NO_2 concentration from transport of NO_X point source at origin. **Error! Bookmark not defined.**

Figure 17. Steady state NO_2 concentration from transport and chemistry of NO_X point source at origin..... **Error! Bookmark not defined.**

EXECUTIVE SUMMARY

This paper outlines the research conducted at the University of California, Irvine (UCI) Computational and Environmental Science Laboratory in collaboration with researchers at the University of California, Riverside (UCR) sponsored by the California Energy Commission. This work is motivated to examine high-spatial air pollution impact of distributed power generation (DG) using state-of-the-art numerical methods. The University of California, Irvine - California Institute of Technology (UCI-CIT) model is a regional atmospheric transport model used to predict the air quality of Southern California. Small scale impacts of DG are examined at UCR with the plume model AERMOD. Consist meteorology is used for both AERMOD and the UCI-CIT model. The effects of modeling sources using either a regional or plume model is examined with a single plume scenario. DG scenarios are modeled with both regional and local scale models. A box model that considers photochemical gas phase and aerosol reactions has been created to serve as a new computational tool. Additionally, the treatment of small scale chemistry is examined.

1 Introduction

Several studies have examined the impact of distributed generation (DG) on air quality at urban and regional scales. Allison and Lents (2002) investigated the tradeoff between the increase in emissions associated with urban DG emissions and the decrease in emissions by replacing heating plants with waste heat generated from DG plants. They found that realistic DG scenarios were likely to lead to net increases in emissions in urban areas. Their relatively simple analysis focused on aggregated emissions and did not relate these emission changes to air quality.

Heath et al. (2003) examined the air quality impact of DG units relative to central generating stations. They found that the air quality impact of DG units, quantified in terms of intake factors, could be several times that of central generating (CG) stations because a) the ground-level concentrations from the elevated emissions of a CG plant are much smaller than those associated with the near surface emissions from DG units, such as microturbines, and b) CG plants are likely to be located far from urban centers, while DG units are located in urban areas close to energy consumers. These conclusions are based on a simple Gaussian model applied to idealized emission scenarios that do not account for existing emissions. Thus, the results from Heath et al. (2003) do not directly address the impact of DG emissions on ambient concentrations under realistic emission scenarios.

Carreras et al. (2004) performed a detailed examination of the impact of DG emissions on ambient concentrations of both primary and secondary pollutants in the South Coast Air Basin (SoCAB). A major part of their effort was the construction of detailed emission inventories for the year 2010. These inventories accounted for growth in energy demand as well as various DG penetration scenarios. The DG emissions were spatially allocated in the SoCAB using demographic and land-use information. The air quality impacts of DG were examined by running a comprehensive photochemical model using these emission scenarios as inputs. Because DG emissions contribute to less than 3 percent of the total projected NO_x

and VOC emissions in SoCAB, ambient concentrations of ozone, NO_2, and PM are changed by relatively small amounts. The 1Hr daily peak concentrations show almost no change, while the largest changes of about 5 percent occur during the nighttime. These results show that DG penetration, amounting to as much as 20 percent of energy growth until 2010, has little effect on secondary pollutants such as ozone and $PM_{2.5}$ concentrations. However, this study did not provide results on the impact of primary DG emissions on scales of less than 5 km because the comprehensive air quality model uses a 5 km by 5 km grid resolution. Thus, emissions are uniformly mixed through a box that is 5 km by 5 km by 38.5 m. While this approximation might be valid for estimating secondary pollutants, it cannot provide realistic concentration estimates of primary pollutants at neighborhood scales of meters to kilometers.

Over the past years, methods have been developed to estimate the air quality impact at source-receptor distances of hundreds of meters (Venkatram 2008; Venkatram at al. 2004) within urban areas. These methods are currently being evaluated with field observations corresponding to distributed generators.

A realistic assessment of the air quality impact of urban sources, such as DG, requires a model that can estimate concentrations at the required scale of interest. In principle, an Eulerian grid model could satisfy this requirement if the grid size is small enough, but such a model would be impractical from a computational viewpoint. Furthermore, at scales of meters, dispersion parameterizations in grid based models are inadequate for resolving the horizontal and vertical structure of plumes.

This investigation takes advantage of two studies conducted at University of California, Riverside (UCR) and Univserity of California, Irvine (UCI) to examine the impact of DG penetration in the SoCAB. The UCR study (Venkatram et. al., 2010) applied AERMOD to estimate PM and NO_2 concentrations at scales ranging from tens of meters to kilometers from the DG sources. Chemical reactions were not included in the study. On the other hand, the UCI study included the relevant chemical reactions in the CIT model to examine the impact of DG sources on both primary and secondary pollutants, such as ozone. However, the grid resolution of the CIT model results in concentrations averaged over a horizontal scale of 5 km by 5 km, and a vertical scale determined by the vertical grid spacing. This grid volume averaging reduces the concentration gradients of primary pollutants associated with plumes originating from DG units within a grid square.

2 Emissions

South Coast Air Quality Management District (SCAQMD) and California Air Resources Board (ARB) created a projected emissions inventory of 2010 for the purpose of evaluating control measures. This emissions scenario serves as a baseline which accounts for population increase as well as power and transportation demands increases, but does not consider contributions due to DG power. Table 1: summarizes the baseline emission inventory.

Table 1: Summary of Basin-wide baseline emissions for 2010 Species tons/day

Anthropogenic NMHC*	659
Biogenic NMHC	232
NO_X	407
CO	3268
PM	580
SO_X	88
NH_3	168

*NMHC = Non-Methane Hydrocarbons

The spatial distribution of NO_X and VOCs in SoCAB for the baseline emissions are shown in Figures 1 and 2.

Figure 1: Daily NOX emissions (g/s)

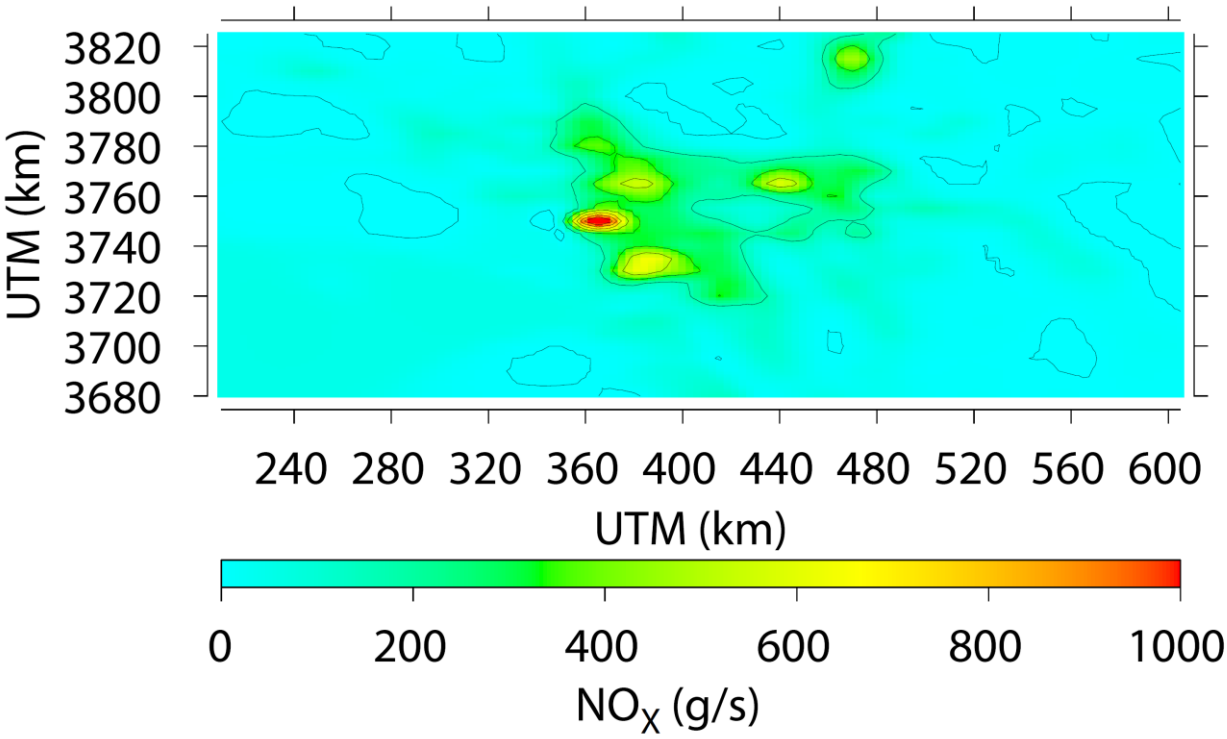

Figure 2: Daily VOC emissions (g/s)

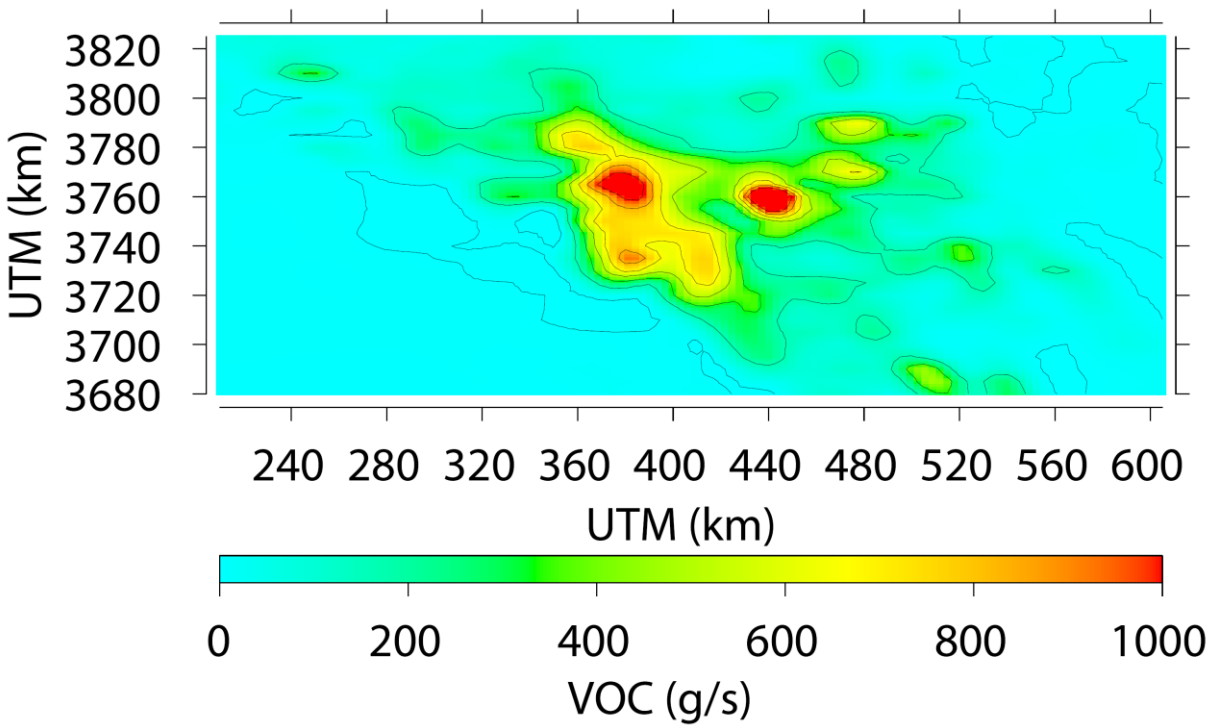

Carreras et al. (2004) developed over a dozen additional emissions episodes which account for influences of DG considering both realistic and spanning scenarios. This study will examine two of the DG scenarios as a basis for comparing the University of California, Irvine - California Institute of Technology (UCI-CIT) model and AERMOD results;

1) PW2010 – These emissions represent a low DG penetration scenario that uses population-weighted spatial emissions.

2) EHP – These emissions represent an extremely high DG penetration scenario where DG accounts for 20 percent of the total power requirements.

3 Meteorology

The meteorological data was developed as part of the Southern California Air Quality Study (SCAQS). The SCAQS was a comprehensive campaign of atmospheric measurements in the SoCAB, during August 27–29, 1987. The study collected an extensive set of meteorological and air quality data that has been used widely to validate air quality models (Meng et al., 1998; Griffin et al.,2002a; Pun et al. 2002; Griffin et al. 2002b, Moya et al. 2002; Knipping and Dabdub 2002). Zeldin et al. (1990) stated that August 28, 1987 is representative of the meteorological conditions in the SoCAB, which makes it suitable for modeling. In addition, the August 27–28, 1987 episode is statistically within the top 10 percent of severe ozone-forming meteorological conditions. The 1987 episode is characterized by a weak onshore pressure gradient and warming temperatures aloft. The wind flow is characterized by a sea breeze during the day and a weak land-mountain breeze at night. The presence of a well-defined diurnal inversion layer at the top of neutral and unstable layers near the surface,

along with a slightly stable nocturnal boundary layer, facilitate the accumulation of pollutants in the SoCAB, which lead to a high ozone concentration occurrence.

While meteorological measurements include observations of mixing height, mixing height information generated by AERMET is used in this study instead in order to be consistent with the AERMOD modeling. The recorded mixing heights range between 300 and 400 m on average, while the AERMET mixing heights range between 750 and 900 m on average. While this is a large increase in mixing height magnitude, this study is focused on examining ground layer results (0 – 38.5 m), where such impact on UCI-CIT modeling results is relatively small. Upper layers which are below the AERMET mixing heights will see a bigger impact from this change.

outlines the general methodology employed.

Figure 3: Flow chart of methodology structure. UCI modules are shown in orange, UCR modules are shown in blue, shared modules are shown in green.

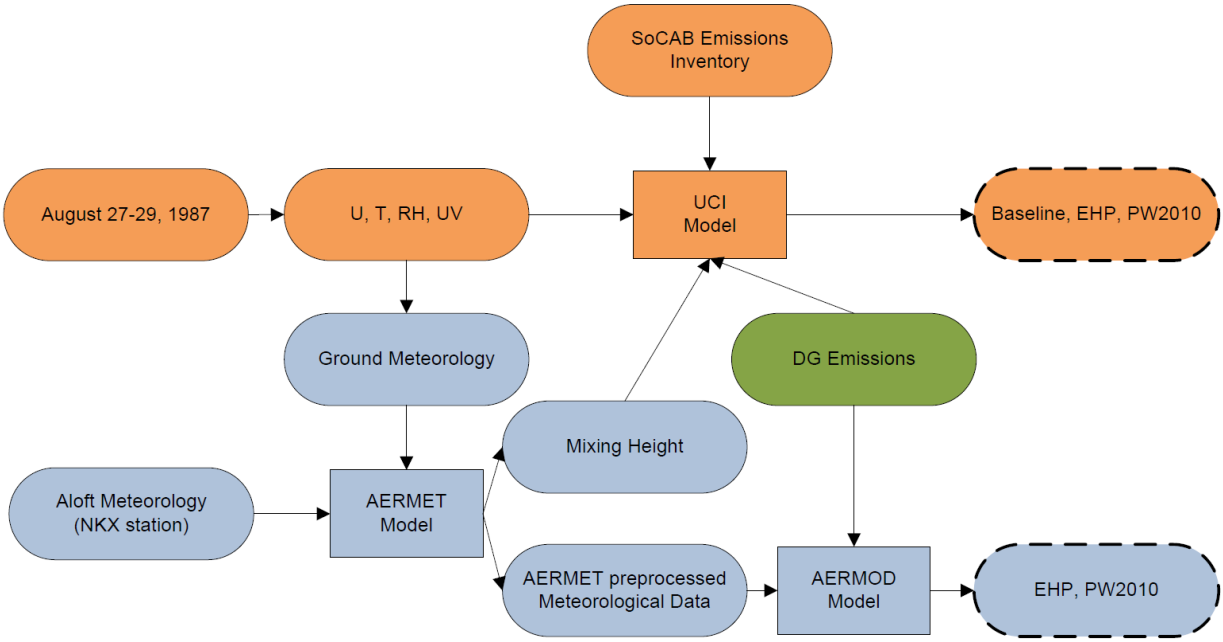

4 Single Point Model Results

A single point source simulation is conducted to examine differences in the UCI and UCR model treatment of sources. The single point run will allow the models to be compared without the influence of multiple plumes. The single point characteristics are summarized in Table 2.

Table 2: Characteristics of single point emission source.

Specifications		Emissions (g/s)	
Stack Height (m)	10.3	CO	0.3632
Stack Diameter (m)	1.8	NO_X	0.0833
Exit Temperature (k)	450	PM	0.0174
Exit Velocity (m/s)	8.32	SO_X	0.0028
Location	Riverside	NH_3	0.0132

The single point is modeled in the UCI-CIT model with and without chemistry. The speciation of emissions follows Samuelsen et al. (2005).

A special set of cases for the single point emissions is examined where there are no background emissions to isolate the effect of the single point source. The no background emission cases are examined with and without chemistry, for a total of 4 cases examining the single point. For each case, a different baseline is used to model the background without the single point source. The results presented are differences calculated by taking single point case minus the corresponding baseline case. This way, results focus on the impact of the source.

Figure 5**: UCI-CIT model 24Hr NO2 (ppb) difference without chemistry (a) no background emissions, (b) with background emissions.** and **Error! Reference source not found.** show the 24Hr NO and NO_2 difference results, respectively, for the scenarios which do not consider chemistry. This simplifies the UCI-CIT model to simulate only transport.

Figure 4: UCI-CIT model 24Hr NO (ppb) difference without chemistry (a) no background emissions, (b) with background emissions.

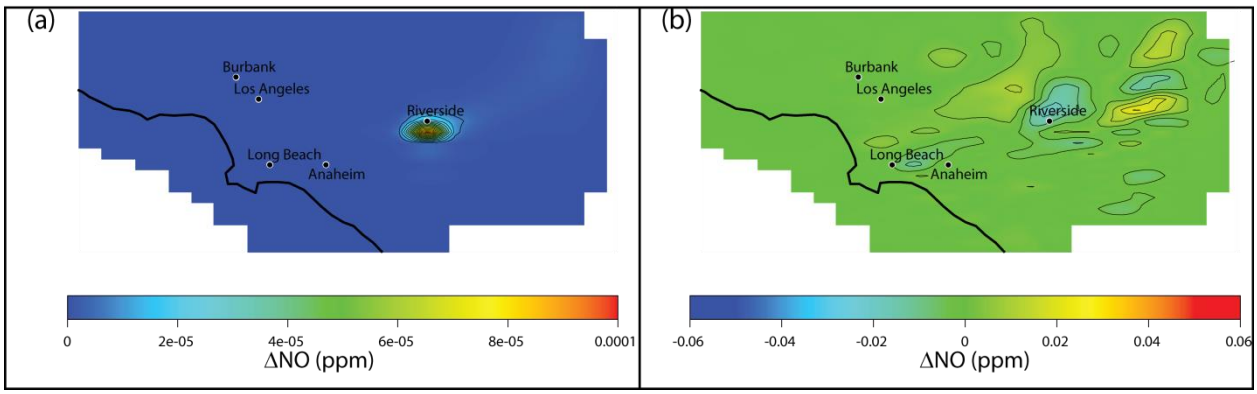

Figure 5: UCI-CIT model 24Hr NO2 (ppb) difference without chemistry (a) no background emissions, (b) with background emissions.

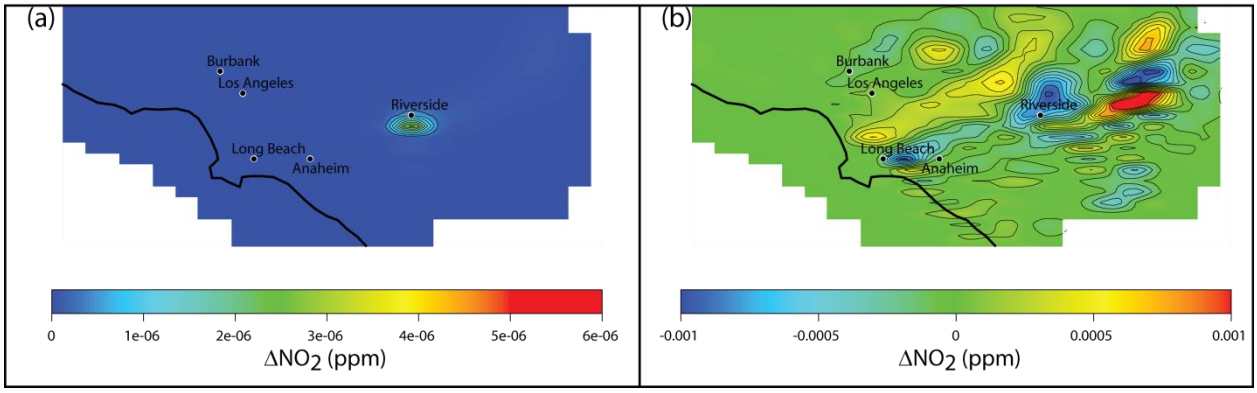

These results clearly correlate with the source when background emissions are not considered and the single point is the only emission source. NO and NO_2 peak at the source location for the case without background emissions. When background emissions are considered the peak is moved ~80 km east and increased by a factor of 1000. Differences in peak location and magnitude can be attributed to differences in the scale of the background emissions and the single point source. The single point source only contributes 0.002 percent of total NO_x emissions when background emissions are considered. NO_x concentrations are high in Riverside, so the impact of the single source is pushed to a lower NO_x concentration site 80 km west of the source. With background emissions, the NO_x peak magnitude is increased in absolute terms, however the percentage increase from the baseline is less, but this not a fair comparison because baseline NO_x without background emissions are zero.

The cases that consider background emissions exhibits resonance behavior around the peak which causes ripples. Resonance is a natural phenomenon that occurs in this case due to the interaction of the continuous source with the system. The resonance causes areas of alternating negative and positive influence expanding from the peak with decreasing

magnitude. The negative areas surrounding the peak increase the magnitude of the peak by conservation of mass.

Figures 6 and 7 show the 24Hr NO and NO_2 difference results, respectively, for the scenarios which consider chemistry.

Figure 6: UCI-CIT model 24Hr NO (ppb) difference (a) no background emissions, (b) with background emissions.

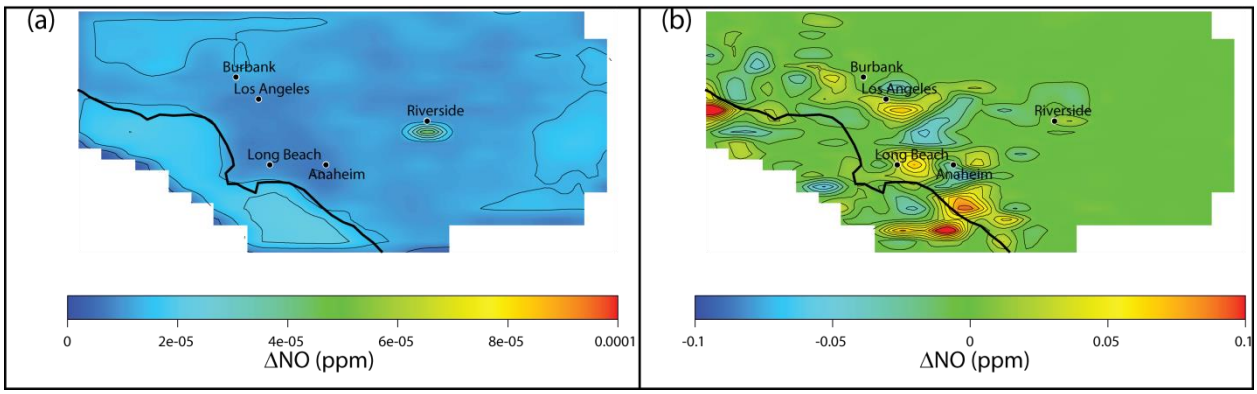

Figure 7: UCI-CIT model 24Hr NO2 (ppb) difference (a) no background emissions, (b) with background emissions.

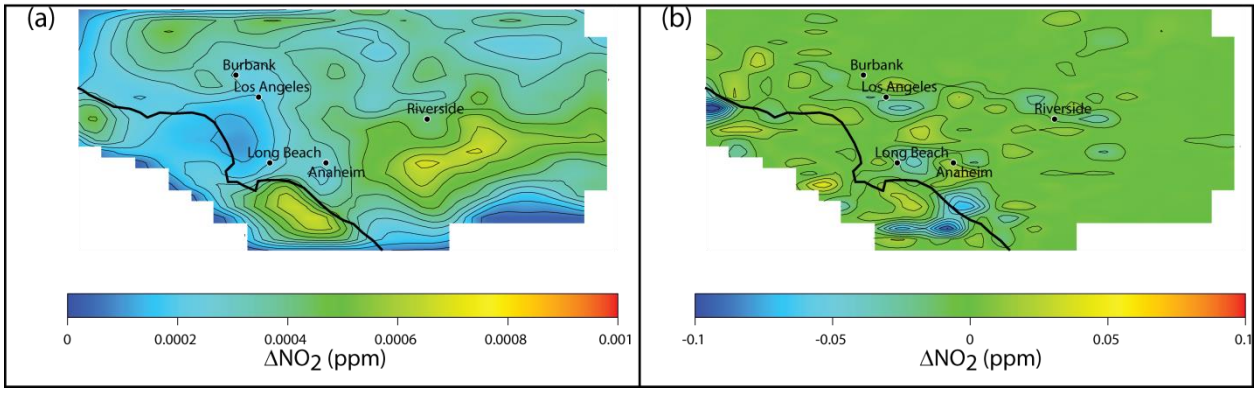

Without background emissions, NO closely resembles a direct source impact even when chemistry is considered, as shown in Figure 7**: UCI-CIT model 24Hr NO2 (ppb) difference (a) no background emissions, (b) with background emissions.**(a). NO near the sea-side boundary to the west is increased due the influences of chemical reactions and transport. NO can be reserved as HONO

$$NO + OH \rightarrow HONO \qquad \text{(R1)}$$

HONO generated from the source is transported downwideast past Riverside where it photolyzes to produce NO

$$HONO \xrightarrow{h\nu} NO + OH \qquad \text{(R2)}$$

Reaction 2 accounts for the increase of NO present around the coast in Figure 7**: UCI-CIT model 24Hr NO2 (ppb) difference (a) no background emissions, (b) with background emissions.**(a).

NO_2 does not resemble a direct source impact even without background emissions when chemistry is considered due to photolysis.

$$NO_2 \xrightarrow{h\nu} NO + O \tag{R3}$$

The majority of the impact shown in **Error! Reference source not found.**(b) can better be explained by the oxidation of NO than by the direct source contribution because NO_2 emitted is only 5 percent by mass of the total NO_X emitted. NO can be oxidized by ozone

$$NO + O_3 \rightarrow NO_2 + O_2 \tag{R4}$$

and the daytime radical HO_2

$$NO + HO_2 \rightarrow NO_2 + OH \tag{R5}$$

Reactions 4 and 5 explain the unique NO_2 spatial distribution shown in **Error! Reference source not found.**(b).

When both background emissions and chemistry are considered, as shown in Figure 7**: UCI-CIT model 24Hr NO2 (ppb) difference (a) no background emissions, (b) with background emissions.**(b) and **Error! Reference source not found.**(b), the influences are combined. Background emissions create a fully populated air quality episode representative of SoCAB. High NO_X locations tend to favor more photochemical pathways which can result in a net loss of NO and NO_2. Reactions 1, 4, and 5 all present NO oxidation pathways. Also, NO can be removed by oxidation with VOCs and the self reaction

$$NO + NO \rightarrow NO_2 + O_2 \tag{R6}$$

Reaction 3 presents a daytime NO_2 reduction pathway. Additionally, NO_2 can be react with oxygen

$$NO_2 + O \rightarrow NO + O_2 \tag{R7}$$

NO_2 can be reserved as HONO

$$NO_2 + H_2O \rightarrow HONO + OH \tag{R8}$$

The OH radical can be a NO_2 sink

$$NO_2 + OH \rightarrow HNO_3 \quad \text{(R9)}$$

During the night when NO_3 is not photolyzed, the NO_2 reaction with ozone can be important

$$NO_2 + O_3 \rightarrow NO_3 + O_2 \quad \text{(R10)}$$

These photochemical pathways of NO and NO_2 loss are only prevalent when there are pollutants in the air to react with.

These pathways create situations where despite adding NO and NO_2 to the system, there are locations and times where the net effect is an overall reduction in NO and/or NO_2. This impact is magnified from the negative values caused by resonance, shown in Figure 7**: UCI-CIT model 24Hr NO2 (ppb) difference (a) no background emissions, (b) with background emissions.**(b) and **Error! Reference source not found.**(b).

5 Distributed Power Generation Results

The point source data concerning the EHP emissions collected from UCR is used to construct the point-source emissions inventory for the UCI-CIT model. Additionally, the EHP emissions are also modeled as area sources similar to Carreras et al. (2004). These two EHP scenarios, point and area sources, are simulated using the UCI-CIT model with and without chemistry. **Error! Reference source not found.** and **Error! Reference source not found.** show 24Hr results of NO and NO_2, respectively, for cases without chemistry.

Figure 8: UCI-CIT model transport only 24Hr NO (ppb) results; Base line August 27(a), 28(b) and 29(c), EHP area sources minus baseline August 27(d), 28(e) and 29(f), EHP point sources minus baseline August 27(g), 28(h) and 29(i).

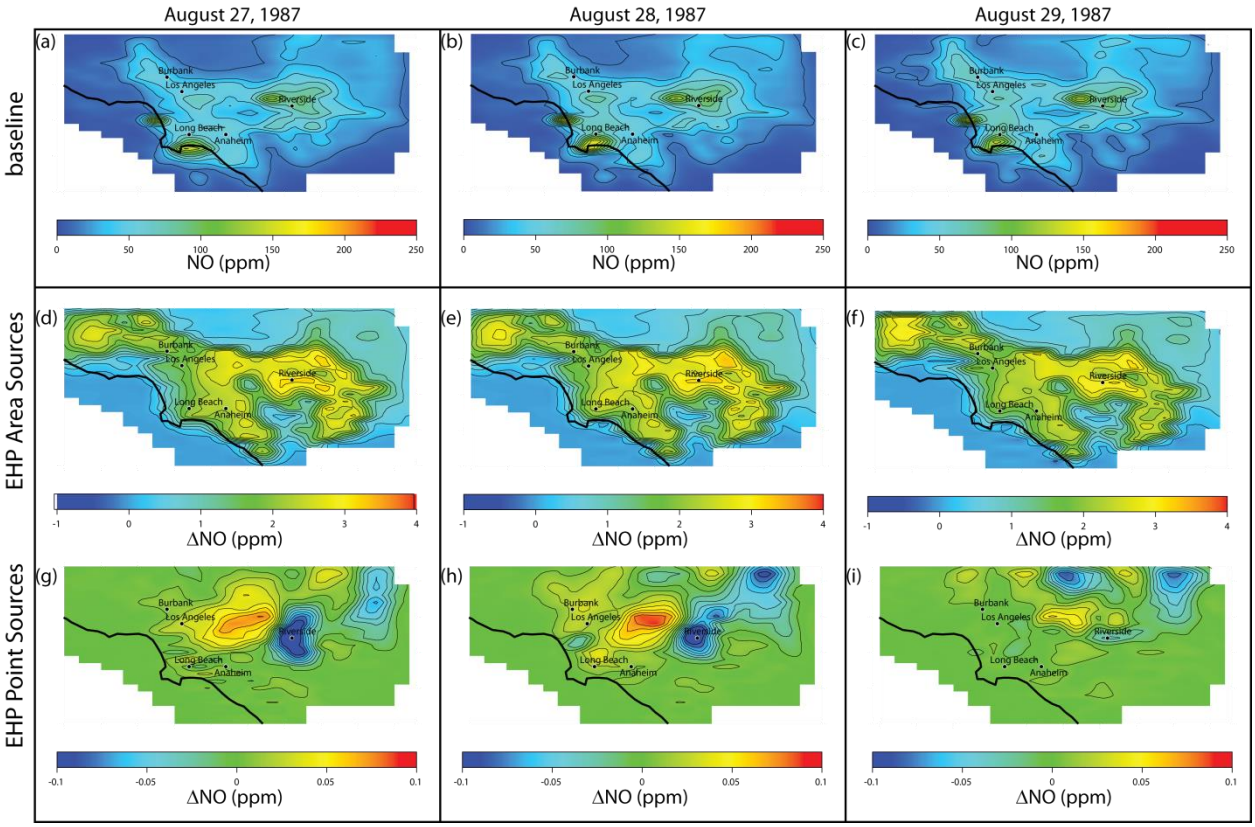

Figure 9: UCI-CIT model transport only 24Hr NO2 (ppb) results; Base line August 27(a), 28(b) and 29(c), EHP area sources minus baseline August 27(d), 28(e) and 29(f), EHP point sources minus baseline August 27(g), 28(h) and 29(i).

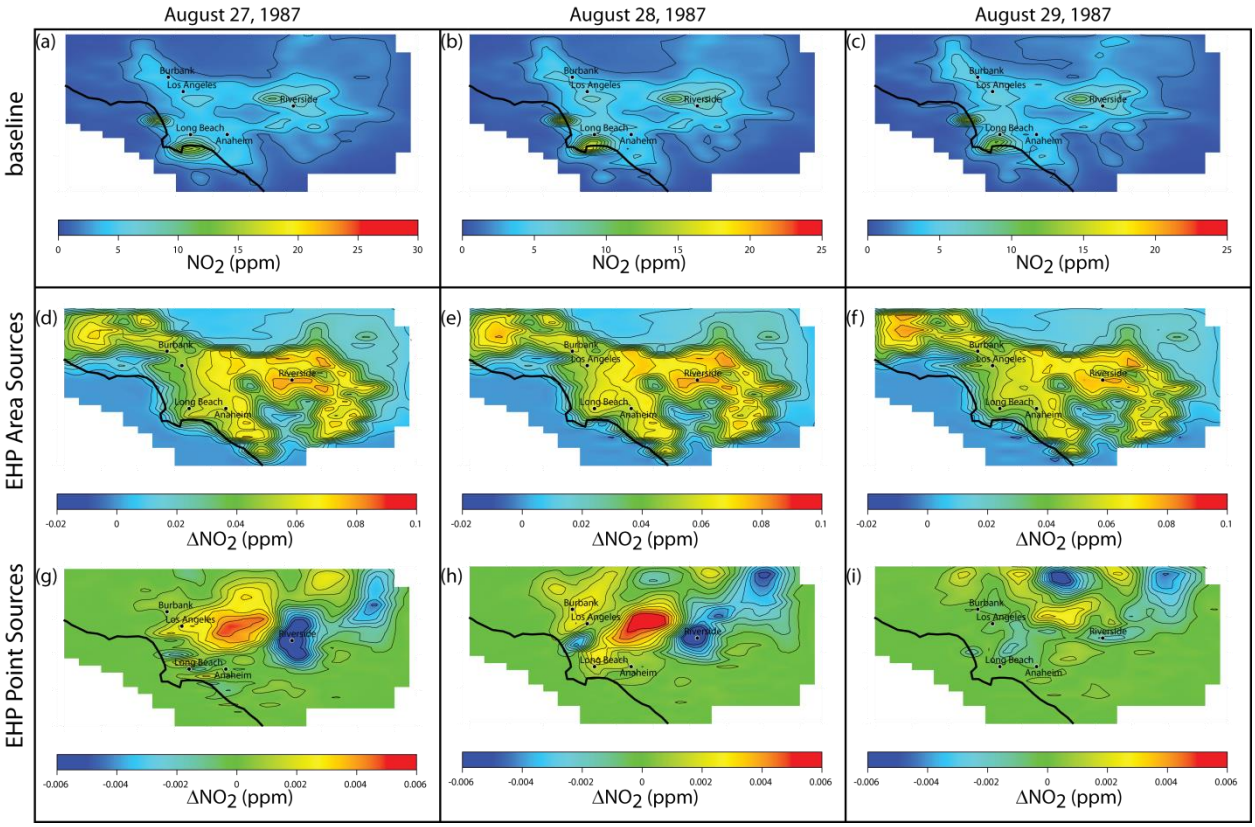

Error! Reference source not found. and **Error! Reference source not found.** show UCI-CIT model results from transport only, for the ground layer (0-38.5 m). The baseline concentrations are characteristic of a 2010 air quality episode in SoCAB with high NO_x levels around Riverside and Long Beach areas.

EHP modeled as area sources has a more prominent impact on the ground layer compared to EHP modeled as elevated point sources. While the emissions rates for area and point sources are the same, area sources are always released in the ground layer, where point sources can be released in aloft layers depending on the plume rise and stack height. The impact of EHP modeled as point sources is distributed among the first few layers of the UCI-CIT model, while the impact of EHP modeled as area sources is mainly localized to the ground layer. As a result, the ground layer NO_x impact of EHP are sources coincides with the source locations.

Figure **11: UCI-CIT model 24Hr NO2 (ppb) results; Base line August 27(a), 28(b) and 29(c), EHP area sources minus baseline August 27(d), 28(e) and 29(f), EHP point sources minus baseline August 27(g), 28(h) and 29(i).** and **Error! Reference source not found.** show 24Hr results of NO and NO_2, respectively, for cases that do consider chemistry.

Figure 10: UCI-CIT model 24Hr NO (ppb) results; Base line August 27(a), 28(b) and 29(c), EHP area sources minus baseline August 27(d), 28(e) and 29(f), EHP point sources minus baseline August 27(g), 28(h) and 29(i).

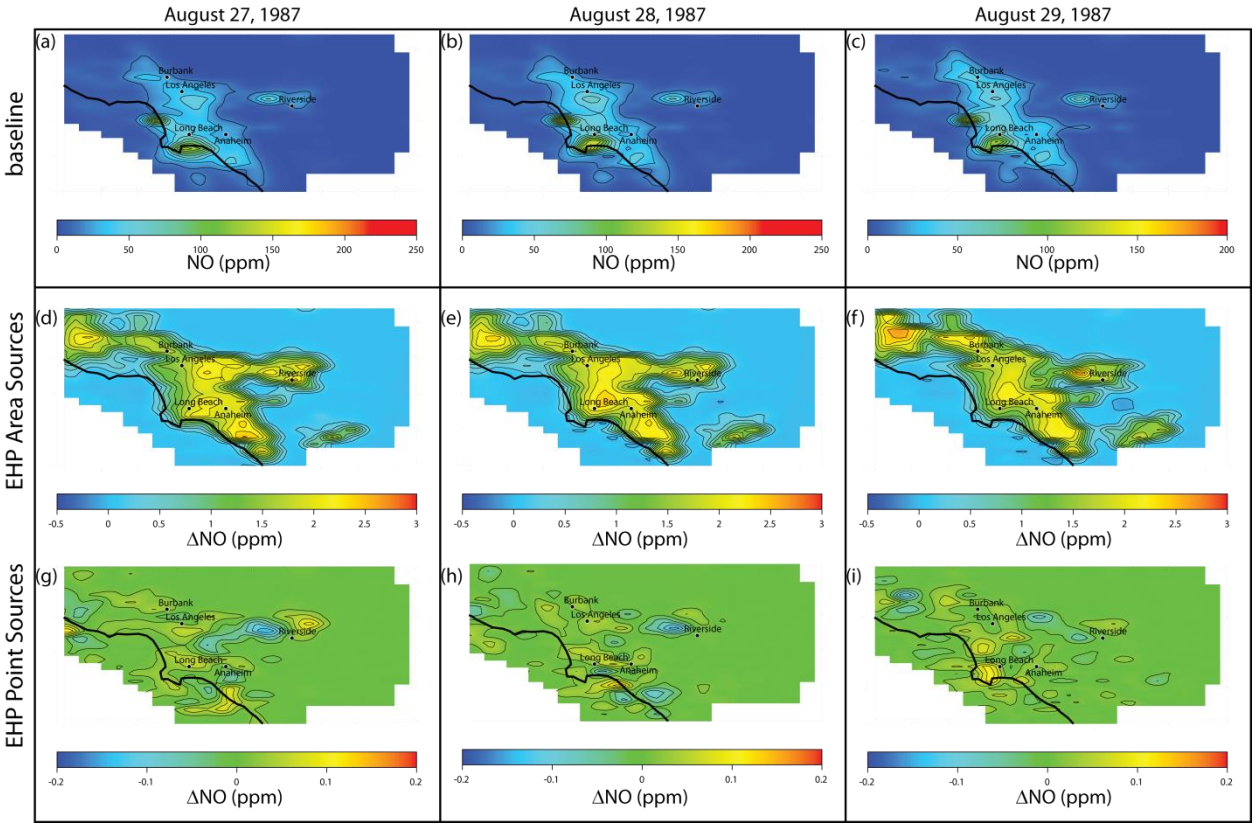

Figure 11: UCI-CIT model 24Hr NO2 (ppb) results; Base line August 27(a), 28(b) and 29(c), EHP area sources minus baseline August 27(d), 28(e) and 29(f), EHP point sources minus baseline August 27(g), 28(h) and 29(i).

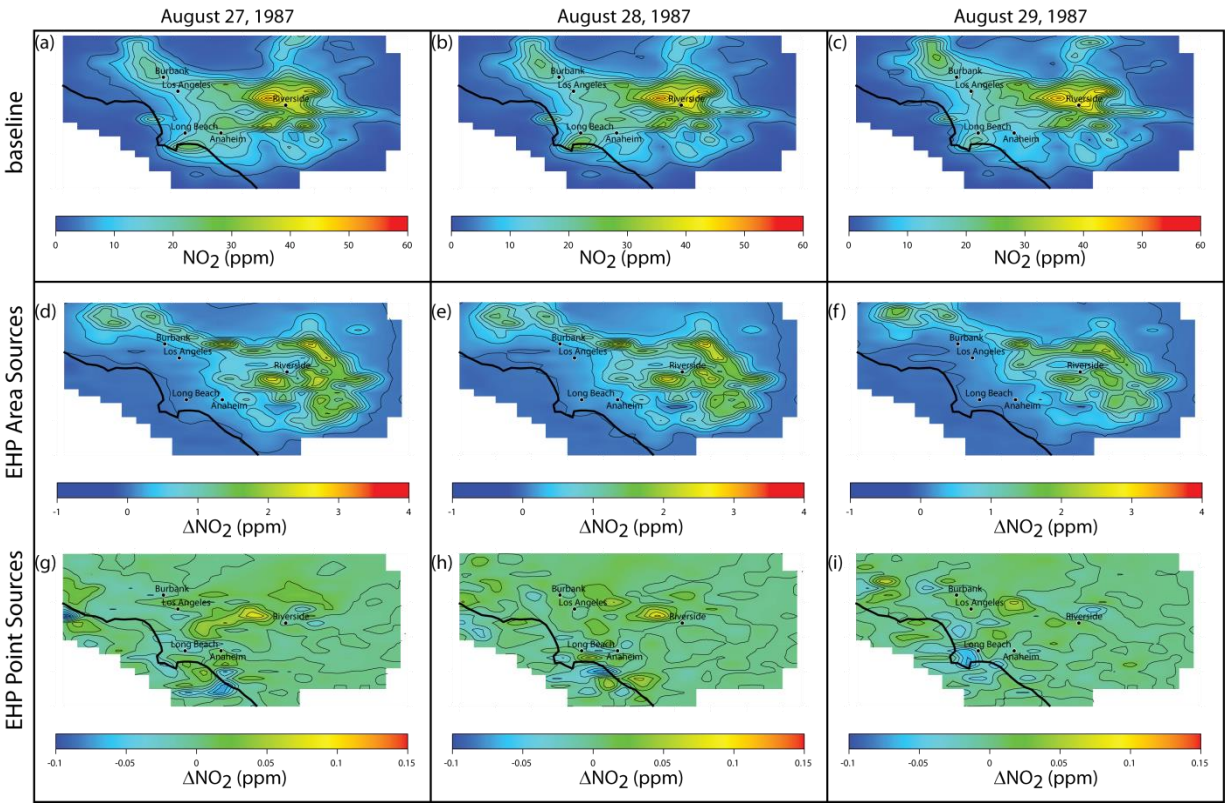

When chemistry is considered, the impact of NO is diminished compared with transport only cases. The modeled air quality episode tends to favor more photochemical NO removal than production, which is typical for SoCAB. NO can be reserved as HONO (R1) and quickly reacts with ozone to produce NO_2 (R4). Alternatively, the impact of NO_2 is increased when chemistry is considered. More NO_2 is produced by photochemical reactions (R4) than by direct source emissions.

Cases that consider chemistry tend to have more negatively impacted areas due the photochemical loss pathways, where transport only cases have less negative areas caused by resonance.

6 NO_X to VOC Ratio

The VOC to NO_X ratio has been related to the potential ozone production from a NO_X or VOC emission source. Because VOC and NO_X compete for ozone production, the impact of a source to peak ozone depends strongly on the background ratio of VOC to NO_X. Often, emission controls are evaluated by examining a two dimensional isopleth showing the impact to peak ozone with varying levels of VOC and NO_X emissions (Finlayson-Pitts and Pitts 1993; Milford et al. 1989). However, no one representative VOC to NO_X ratio exists for a single air basin. This ratio varies significantly from day to day and changes with location (Altshuller 1989; Wolff and Korsog 1992) .

Daily average VOC to NOx results for the 2010 baseline and EHP scenarios are presented in **Error! Reference source not found.** and **Error! Reference source not found.**. These results are consistent with those presented by Dabdub et al. (2008).

Figure 12: UCI-CIT model transport only 24Hr NOX to VOC ratio; Base line August 27(a), 28(d) and 29(g), EHP area sources minus baseline August 27(c), 28(f) and 29(i), EHP point sources minus baseline August 27(b), 28(e) and 29(h).

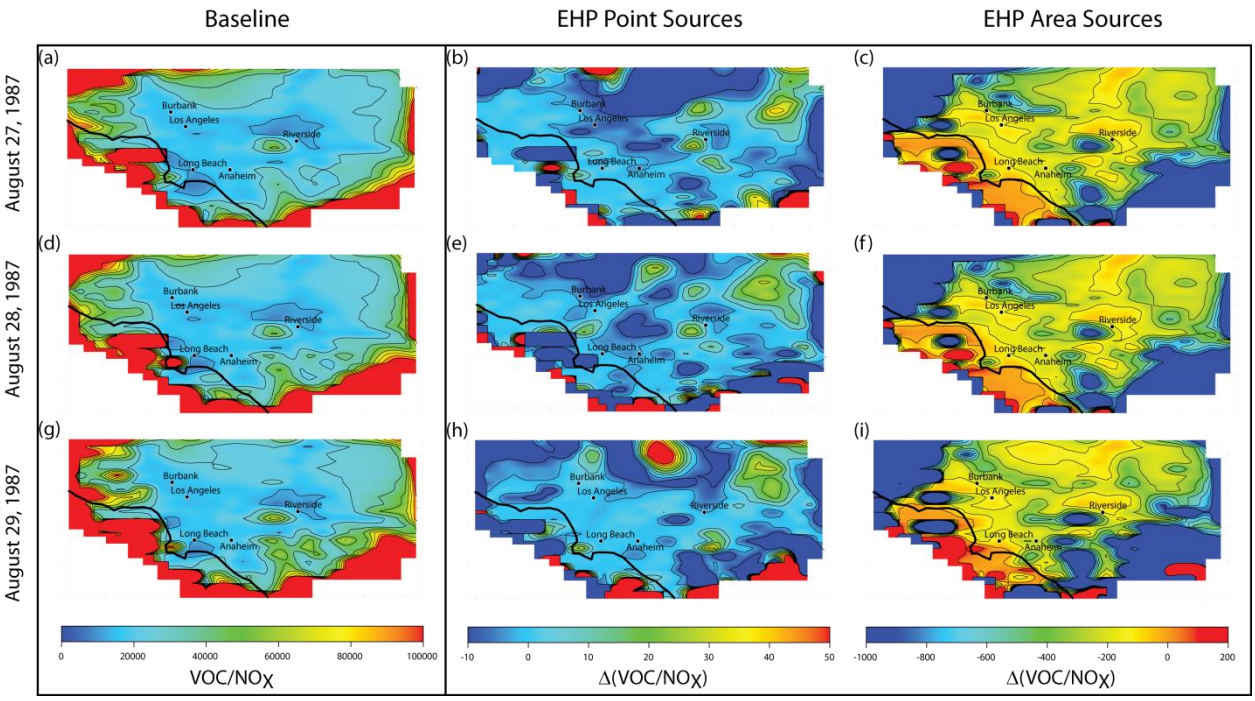

Figure 13: UCI-CIT model 24Hr NOX to VOC ratio; Base line August 27(a), 28(d) and 29(g), EHP area sources minus baseline August 27(c), 28(f) and 29(i), EHP point sources minus baseline August 27(b), 28(e) and 29(h).

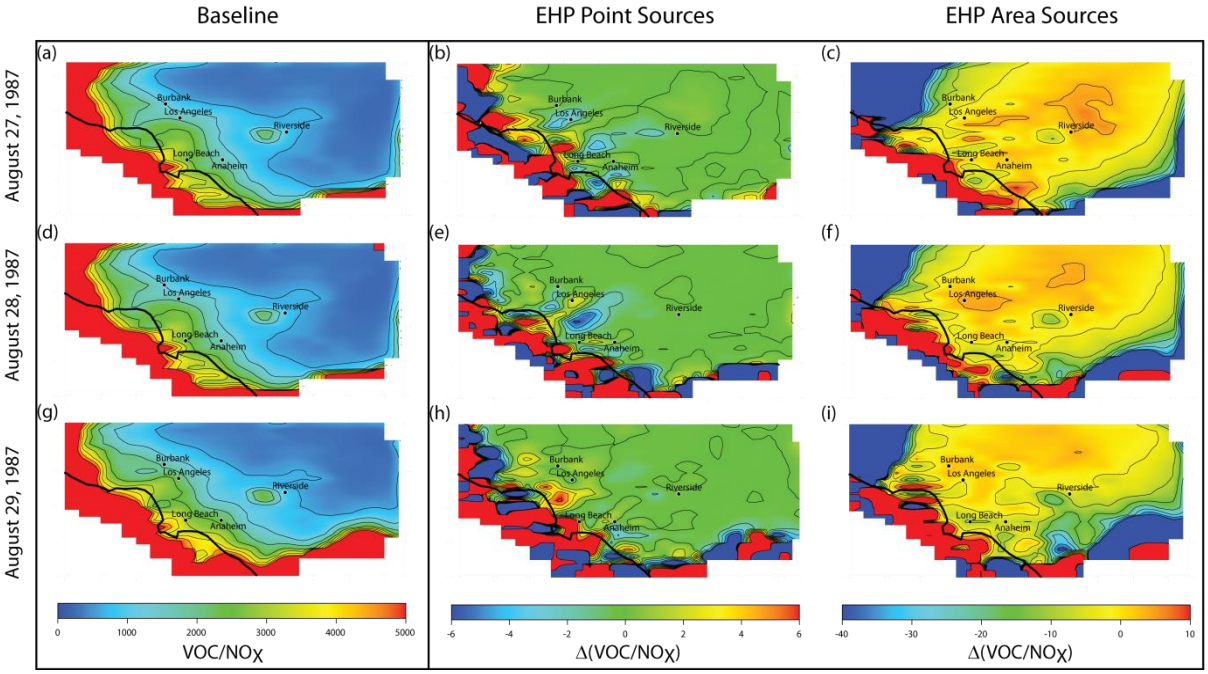

The highest values of NOx to VOC are found along the west and southern boundary where there are trace amounts of NOx. The ratio is lowest to the east and north of Riverside. The influence of chemistry drives the NOx to VOC ratio down as NOx is removed through reactions with OH and VOCs. Generally, the EHP emissions lower the NOx to VOC ratio because more NOx is emitted than VOCs. Modeling EHP as area sources has a bigger impact to the NOx to VOC ratio than modeling as point sources due to the larger change in peak NOx.

7 UCI-CIT Model and AERMOD Results

The UCI-CIT model results of the increase from the EHP scenario over the Baseline are compared with UCR AERMOD results of the EHP scenario in

Table 3.

Table 3: Peak NO_2 and NO_X from UCI and UCR models

Model	Aug., 27							
	NO2				NOx			
	Conc.	Hour	UtmX	UtmY	Conc.	Hour	UtmX	UtmY
UCI (Volume-averaged Conc.; Area source released from ground w/ Chemistry)	8.60	6	485	3770	13.97	6	465	3765
UCI (Volume-averaged Conc.; Area source released from ground w/o Chemistry)	0.22	6	460	3760	9.72	6	460	3760
UCI (Volume-averaged Conc.; Elevated point source w/ Chemistry)	0.91	1	400	3725	0.47	23	415	3720
UCI (Volume-averaged Conc.; Elevated point source w/o Chemistry)	0.05	12	400	3735	0.65	12	400	3735
UCR (Surface-averaged Conc.; Point source with Plume rise)	6.30	4	410	3740	7.70	7	390	3740
UCR (Volume-averaged Conc. 0-15.4 m ; Point source with Plume rise)	5.50	4	410	3740	6.90	7	390	3740
UCR (Surface-averaged Conc.; Point source without Plume rise)	41.90	2	410	3770	62.10	23	325	3800
UCR (Surface-avearged Conc.; Area source released from ground)	43.10	6	415	3700	60.40	7	420	3725

Model	Aug., 28							
	NO2				NOx			
	Conc.	Hour	UtmX	UtmY	Conc.	Hour	UtmX	UtmY
UCI (Volume-averaged Conc.; Area source released from ground w/ Chemistry)	8.72	2	475	3760	15.08	6	465	3770
UCI (Volume-averaged Conc.; Area source released from ground w/o Chemistry)	0.27	6	465	3765	12.07	6	465	3765
UCI (Volume-averaged Conc.; Elevated point source w/ Chemistry)	0.76	3	410	3715	0.34	24	400	3730
UCI (Volume-averaged Conc.; Elevated point source w/o Chemistry)	0.04	12	470	3770	0.64	12	470	3770
UCR (Surface-averaged Conc.; Point source with Plume rise)	6.70	6	410	3750	7.40	7	395	3760
UCR (Volume-averaged Conc. 0-15.4 m ; Point source with Plume rise)	5.90	6	410	3750	6.60	7	395	3760
UCR (Surface-averaged Conc.; Point source without Plume rise)	46.40	21	465	3770	49.60	20	390	3760
UCR (Surface-avearged Conc.; Area source released from ground)	51.40	6	455	3730	62.10	5	445	3720

Model	Aug., 29							
	NO2				NOx			
	Conc.	Hour	UtmX	UtmY	Conc.	Hour	UtmX	UtmY
UCI (Volume-averaged Conc.; Area source released from ground w/ Chemistry)	8.55	6	480	3745	12.20	5	465	3765
UCI (Volume-averaged Conc.; Area source released from ground w/o Chemistry)	0.24	6	440	3760	9.84	6	440	3760
UCI (Volume-averaged Conc.; Elevated point source w/ Chemistry)	0.54	4	405	3720	0.44	24	405	3720
UCI (Volume-averaged Conc.; Elevated point source w/o Chemistry)	0.03	12	415	3775	0.44	12	465	3770
UCR (Surface-averaged Conc.; Point source with Plume rise)	7.90	3	405	3760	9.40	3	385	3745
UCR (Volume-averaged Conc. 0-15.4 m ; Point source with Plume rise)	7.20	3	405	3760	8.70	3	385	3745
UCR (Surface-averaged Conc.; Point source without Plume rise)	56.90	23	340	3800	58.20	23	465	3770
UCR (Surface-avearged Conc.; Area source released from ground)	54.60	5	435	3785	68.20	3	410	3770

For the UCI-CIT model, area sources predict greater influence than point sources because the area sources are exclusively released on the ground layer. When chemistry is considered, NO_2 peaks increase dramatically from NO_2 photochemical production (R4-6). Chemistry opens pathways where NO_X can be isolated through reservoir species like HONO (R1, R8) and removed by HNO_3 deposition (R9), resulting in a net loss of peak NO_X compared to similar cases without chemistry.

AERMOD results are averaged over the ground surface area and a volume average from the ground to 15 m, with minor variations between the two averages. Peaks reported with plume rise are considerably lower than peaks reported without plume rise. All models and variations predict peaks located inland around Riverside.

8 Box Model

A photochemical box model is a very simple approximation of atmospheric chemical evolution. While this model is able to efficiently account for photochemical effects, it does not consider the dynamic impact from advection and dispersion. Instead, the box model focuses on a comprehensive treatment of gas phase photochemical processes. The box model is intended for use in a surrogate global or regional transport model to account for photochemistry.

8.1 Box Model Description

The box model is based on the same formulation as the University of California, Irvine (UCI) regional photochemical model (Dabdub and Seinfeld 1994). However, the box model does not consider diffusion, advection or deposition. The chemistry of the box model is based on

the mechanism described by Griffin et al. (2002). The mechanism includes 124 gas-phase and 296 aerosol-phase species (shown in Appendix A:
Species List) and 361 chemical reactions. The box model stores gas-phase species in PPM and aerosol-phase species in $\mu g/m^3$.

Aerosols are split into organic and inorganic groups using the module Simulating the Composition of Atmospheric Particles at Equilibrium 2 (SCAPE2) (Kim et al. 1993; Meng et al. 1995). SCAPE2 considers the liquid water content, $[H^+]$, nitric acid, sulfuric acid and ammonia. Aerosols are lumped into 8 size bins shown in Table 4.

Table 4: Aerosols size bins

Bin	Diameter Range (um)
1	5 - 10
2	2.5 - 5
3	1.25 - 2.5
4	1.125 - 1.25
5	0.563 - 1.125
6	0.281 - 0.141
7	0.141 - 0.070
8	0.070 - 0.035

The chemistry mechanism predicts the oxidation of organic compounds which are capable of forming secondary organic aerosols (SOA). The chemistry mechanism includes 10 species used a surrogates to simulate SOA formation. The Model to Predict the Multiphase Partitioning of Organics (MPMPO) module (Griffin et al. 2003; Griffin et al. 2005) is used to predict organic aerosol formation from the surrogate species. MPMPO assumes aerosols are either in a organic or liquid phase.

The main model variables are listed in Table 5 along with the lines they can be edited in the main code.

Table 5: Model variables and description

Variable	Line Number	Description
UVFAC(1)	37	Ultra violet light scaling factor (1 for clear sky)
TEMP	40	Temperature in degrees Celsius
AHE	43	Absolute humidity of water in ppth
ID	46	Start day of month
IM	47	Start month
IYR	48	Start year
TSTART	49	Start time in minutes past midnight
IDE	53	End day of month
IME	54	End month
IYRE	55	End year
TEND	56	End time in minutes past midnight
SLA	61	Latitude in degrees
SLO	62	Longitude in degrees
TZ	63	Time zone
DTT	73	Time step between updating reaction rates
TIME	-	Current model time in minutes past midnight
CNT	-	Array of chemical species concentrations (PPM) at the current time step
SCDOTA	-	Array of chemical sources (PPM*m/min)

The box model can be used to analyze a time period ranging from days to years. Additionally, the code could be simply modified to account for leap years so that multiple years could be considered.

Sources and initial conditions are read in from separate input files. Initial conditions are read from file *IC.DAT* and sources are read from file *SOURCES.DAT*. Both files have the same formatting of [*integer*, *real*], where *integer* is the species order number (see appendix A), and *real* is the concentration (PPM) for the initial conditions file and source rate (PPM*m/min) for the sources file. The sample input files provided have zero initial conditions and a NO_2 source of 10 PPM*m/min.

The model is setup to create an output file *RESULTS.DAT* which contains concentrations (PPM) of NO, NO_2 and O_3. Results are written to *RESULTS.DAT* each half hour. Additionally, the model requires the *parameter.h* file which contains model constants.

8.2 Test Case 1

The first test case represents a puff of initial pollutants without any sources. The initial concentrations are 10 PPM of NO, NO_2 and O_3. One day simulation results of NO and NO_2 are shown in **Error! Reference source not found.**.

Figure 14: One day simulation results of NO and NO2 from initial mixture of NO, NO2 and O3 at 10 PPM each

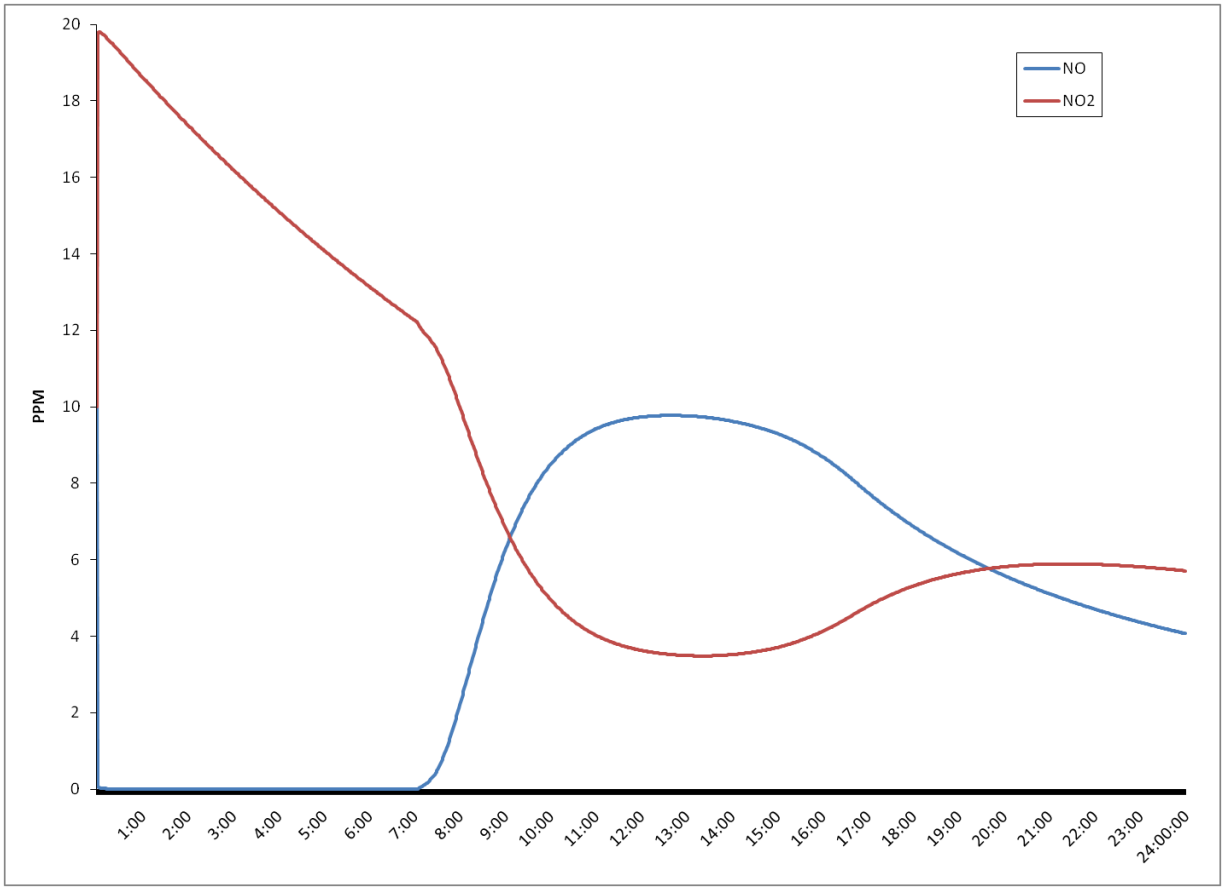

Once the simulation begins, all the NO and O_3 are converted to NO_2 by titration which doubles the NO_2 concentration. NO_2 is also titrated by ozone, but at a much slower rate. Around 6:00 a.m., NO_2 begins to photolyze into NO. By 2:00 p.m., NO is being lost to ozone titration faster than NO_2 is photolyzing NO, resulting in an increase of NO_2 and decrease of NO.

8.3 Test Case 2

The second test case represents a constant source in initially clean air. The source emits NO_2 at a constant rate of 10 PPM*m/min. One day simulation results of NO and NO_2 are shown in **Error! Reference source not found.**.

Figure 15: One day simulation results of NO and NO2 from constant NO2 source of 10 PPM*m/min

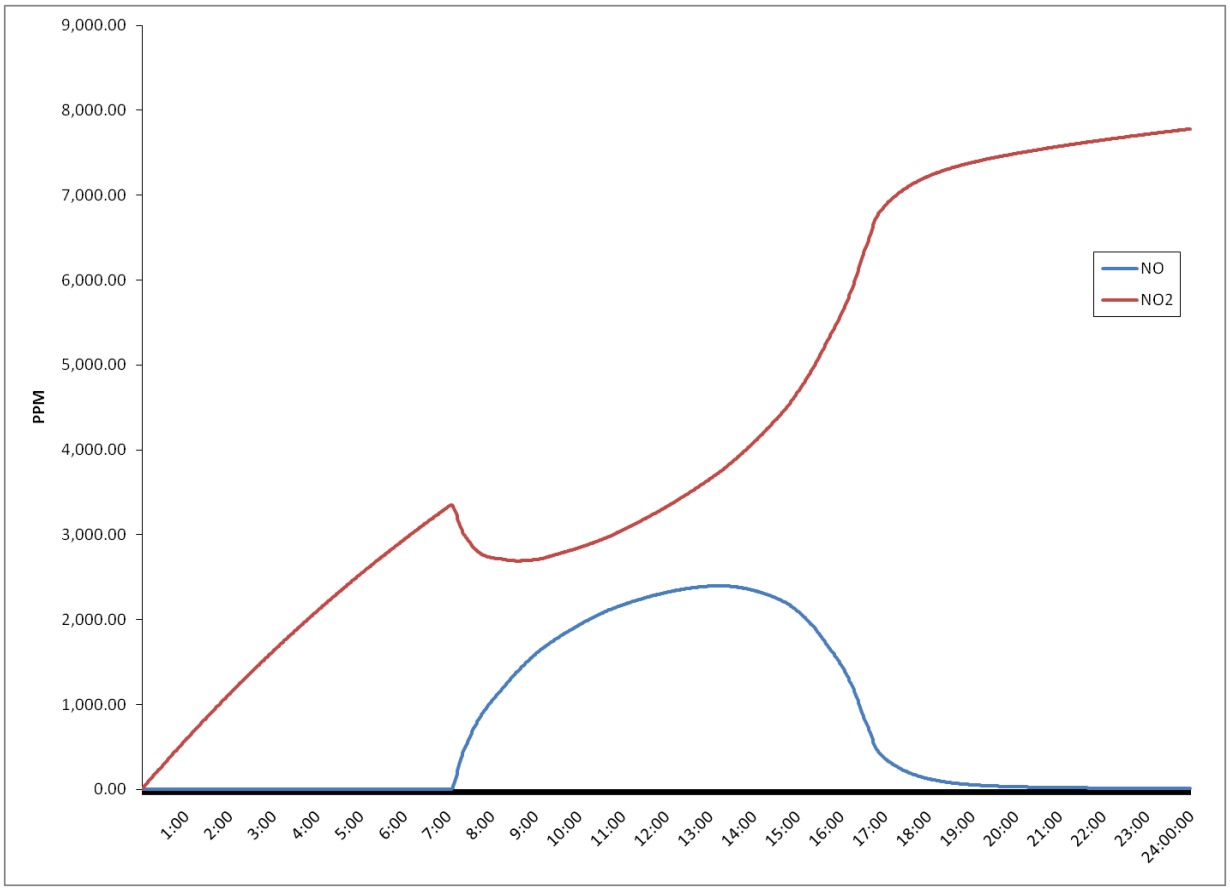

The concentration of NO_2 increases steadily before daylight. There are no nighttime losses of NO_2 because the air is initially clean. During the day NO_2 photolysis produces NO and a radical oxygen which leads to ozone production. The NO titrates back into NO_2, which drastically increases the NO_2 production until all the NO is consumed.

9 Development and Evaluation of Chemistry Methods in AERMOD

AERMOD is the current Environmental Protection Agency (EPA) recommended plume dispersion model. AERMOD includes two options to account for gas phase NO_X ($NO_X = NO + NO_2$) chemistry; the plume volume molar ratio method (PVMRM) and the ozone limiting method (OLM). However, there is little discussion about these chemistry processing methods and other methods currently available. A new method to account for photochemical effects in plume transport is developed based on a mass conservation equation of concentration variations (VA). The photochemical methods VA, OLM, PMVMRM, Hess and Bagney are evaluated with a highly resolved Eulerian photochemical transport model. A sensitivity to wind speed and background pollutants is presented. Significant differences are reported among the chemical methods with OLM consistently under-predicting and Bagney over-predicting peak NO_2. Hess' method performs best considering NO-O_3-NO_2 chemistry. The new method introduced, VA, performs well and, unlike Hess' method, has the flexibility to consider additional photochemical pathways.

9.1 Background

Plume dispersion models are better than conventional regional atmospheric transport models at examining local-scale impacts of specific sources. These models provide high spatial-resolution that considers the micro-terrain and meteorology. Plume models were first developed to study the dynamics of SO_2 emissions from power plants (Schlunzen 2002). Today plume models are used for a variety of applications, including modeling the emissions from stone crushing (Sivacoumar et al. 2009), pharmaceutical plants (Chang et al. 2009), pesticide use (Schleier et al. 2008) and roadway traffic (Wu et al. 2009). Plume dispersions models have many practical applications involving the control and regulation of pollutants. The U.S. Environmental Protection Agency (EPA) recommends using plumes models to test for compliance of air quality regulations such as the National Ambient Air Quality Standards. The current recommended model for State Implementation Plans is AERMOD (EPA 2004).

Like all plume dispersion models, AERMOD is limited because of the inability of plume models to consider complex photochemical processes (Schlunzen 2002). The work examining the chemistry of plume dispersion has branched into models investigating plume transport within an atmospheric boundary layer (ABL) and reactive plume models. ABL models have been used to analyze both isotropic (Fabregat et al. 2010) and non-isotropic (Alessandrini and Ferrero 2009) atmospheres. Reactive plume models include chemical treatment using second-order enclosure schemes (Galmarini et al. 1995; Karamchandani et al. 2000), Lagrangian Gaussian models (Bottenheim and Strausz 1982; Joos et al. 1987; Stewart and Liu 1981), Large Eddy Simulations (LES) (Sykes et al. 1992; Vilà-Guerau de Arellano et al. 2004), Direct Numerical Simulations (Fabregat et al. 2010) and Stochastic Fields method (Garmony et al. 2006).

Validation of high-resolution chemical mechanisms from direct measurements is impractical because it would require measurements of multiple pollutants within a high-resolution monitoring grid with samples obtained on an hourly or more frequent basis. Local meteorology would need to be accurately defined with both surface and aloft observations. Additionally, device and human errors would be cumbersome. Thus, instead of direct observations, studies have relied on multiple plane measurements (Joos et al. 1987), wind tunnel testing (Garmony et al. 2006), and smog chamber data (Bottenheim and Strausz 1982). Specific modeled episodes are compared with an aggregate of observational data, and only a qualitative comparison of results has been presented up to now.

Several studies have noted the importance of chemical segregation within the plume, which can affect reaction rates (Galmarini et al. 1995; Hilst 1998; Pagnini 2009; Rubio et al. 2008). Chemical reactions rates are measured in homogenous mixtures where reaction is uniform. However, turbulent eddies in the atmosphere can generate an inhomogeneous composition that slows down biomolecular reaction rates compared with a homogenous composition. Chemical segregation can hinder chemical activity of a reactive plume (Hilst 1998; Paginini 2009). This effect is particularly important when the photochemical time-scale is of similar magnitude as the characteristic turbulent time-scale (Vinuesa and Vilà-Guerau de Arellano 2005). The intensity of segregation has been related to the Damköhler number (ratio of

turbulent time scale to reactive time scale), the distance from the centerline and the standard deviation in the horizontal crosswind direction (Pagnini et al. 2009; Fabregat et al. 2010).

As a first step to quantitatively comparing available chemistry methods on a diffusion model, this study investigates the steady-state transport of a single plume centerline under idealized conditions. The first section describes a new computational tool developed to examine the transport and chemistry. The second section explores the host diffusion model examined, followed by a thorough description of the chemical methods applied. Neutral and stable atmospheric scenarios for a variety of background pollutant conditions are presented in the results section. Finally, a discussion is presented.

9.2 A Highly Resolved Eulerian Model

Plume models solve a specific form of the atmospheric transport equation, shown here for one dimension:

$$\frac{\partial C_i}{\partial t} + U\frac{\partial C_i}{\partial x} = K\frac{\partial^2 C_i}{\partial x^2} + S_{Chem}(C_i) + S_{Emiss}(C_i) \qquad (1)$$

where C_i is the concentration of chemical species *i*, *x* is the distance downwind, *K* is eddy diffusivity, S_{Chem} is the contribution of chemical reactions and S_{Emiss} are emission contributions. Often a slender plume approximation is made where diffusion parallel to the wind is neglected compared with advection.

Eulerian models are not typically used to model plume transport because they have difficulty modeling turbulence, and their spatial resolution is typically inadequate to capture the fine-scale plume variations without high computational cost. However, several studies have applied finite volume methods to investigate equation 1 (Geiser 2009; Yudianto and Xie 2010). At this phase, the investigation is focused on the non-turbulent atmosphere where a highly resolved one dimensional Eulerian (HRE) model is suitable for examining the transport down a plume centerline. HRE is applied to characterize transport from advection and diffusion with and without photochemical reactions.

HRE uses the same formulation as the California Institute of Technology (CIT) regional atmospheric transport model (Dabdub and Seinfield. 1996) but on a smaller scale and much higher resolution. Advection is solved using a two-level time-marching scheme quintic spline (Nguyen and Dabdub 2001). Diffusion is solved explicitly with a forward in time, centered in space finite difference. Chemistry and sources are solved with a 4th order Runge-Kutta time integrator. HRE uses a simple chemical mechanism which considers 10 gas phase species (Table 6) and 10 reactions (Table 7) which represent a simple NO-O_3-NO_2 mechanism. Kumar and Russell (1996) showed that a simple NO-O_3-NO_2 mechanism compares well with a detailed organic chemistry mechanism when examining the influence of NO_x point sources. Hence, a more detailed chemical mechanism is not required for this investigation.

Table 6: Chemical species considered in NO-O_3-NO_2 system

Abbreviation	Name	Comment
O	Oxygen radical	PSSA*
O_2	Oxygen	Constant
O_3	Ozone	Constant
OH	Hydroxyl radical	PSSA*
HO_2	Hydroperoxyl radical	PSSA*
H_2O	Water	Constant
NO	Nitrogen oxide	
NO_2	Nitrogen dioxide	
NO_3	Nitrate Radical	
HNO_3	Nitric Acid	

*Pseudo-steady-state assumption (PSSA)

Table 7: Chemical reactions and rates

Reaction		K (PPM, Mins)
1	$NO_2 \xrightarrow{hv} NO + O$	K_1
2	$O + O_2 \rightarrow O_3$	22
3	$O_3 + NO \rightarrow NO_2 + O_2$	27
4	$HO_2 + NO \rightarrow NO_2 + OH$	$1.2 * 10^4$
5	$OH + NO_2 \rightarrow HNO_3$	$1.6 * 10^4$
6	$NO_3 + NO \rightarrow 2NO_2$	$2.8 * 10^4$
7	$H_2O + NO_3 + NO_2 \rightarrow 2HNO_3$	$1.4 * 10^{-35}$
8	$NO_3 \xrightarrow{hv} NO + O_2$	$K_1/1.5$
9	$NO_3 \xrightarrow{hv} NO_2 + O$	$K_1/308$
10	$O_3 + NO_2 \rightarrow NO_3 + O_2$	$4.8 * 10^{-2}$
11	$NO_3 + NO_3 \rightarrow 2NO_2 + O_2$	.34

*K_1 is .51 mins^{-1} during the day and 0 at night

Special care needs to be taken to ensure the HRE model produces a transport solution consistent with a diffusion model. Diffusion for HRE is specified to be in a power-law expression (Bange et al. 1991), a common assumption for plume models.

$$K = ax^b \tag{2}$$

Where *a* and *b* are empirical constants. Values for a and b reported vary widely for different atmospheric stabilities and averaging times (Turner 1969; Martin 1976; Klug 1969). These values may be determined while validating a specific method, and hence are primarily appropriate for their original purpose. Similarly, this study determines diffusion parameters ideal for the scenarios presented. PEST (Doherty 2007) is used to find optimum parameters for *a* and *b* by minimizing the root mean square error between the normalized solutions of the HRE model run without chemistry and a normalized analytical solution. This step ensures the HRE model produces a Gaussian solution. Values for *a* and *b* are shown in Table 8**Error! Reference source not found.** for each meteorology case examined.

Table 8: Diffusion parameters for HRE calculated by PEST. $K = ax^b \ [m^2/min]$

	Neutral	Stable
a	3044	2.48
b	2528	2.50

Several studies have noted the importance of proper handling of ozone penetrating into the plume (Alessandrini and Ferrero 2009; Peters and Richards 1979). As the primary oxidant of NO, the available ozone is a strong indicator of the rate at which NO can convert to NO_2. Alessandrini and Ferrero (2009) noted that a constant ozone assumption produced similar results to a non-constant ozone case when considering plume transport in three dimensions. Hence, ozone is held constant for the one dimensional HRE model.

Yudianto and Xie (2010) showed that a one dimensional finite difference method compared well with other computational methods when a small step size is used. HRE uses a size resolution of 10 cm with a time step of 1 ns. Model steady state is achieved within 0.1 s. Hence, for a one-hour time resolution, like that used in plume dispersion models, HRE is effectively constant. The steady state solution of HRE is presented for discussion.

An ideal one dimensional source has no clear correlation with a real source which has a specific mass flow rate. This study chooses the source emission rate for the HRE model so that the HRE model's value matches AERMOD's value at AERMOD's peak location when only transport is considered. This ensures coherent model results between HRE and AERMOD in absolute terms. A description of the source characteristics is shown in Table 9.

Table 9: Point source characteristics

NO_X Emission Rate (g/s)	0.1
NO_2/NO_X Emitted	0.05
Diameter (m)	0.1
Height (m)	0
Temperature	Ambient
Exit Velocity (m/s)	0

A real world scenario that considers three dimensional local meteorology and surface characteristics would be difficult and computationally expensive with an Eulerian model. Real world problems require more specialized plume models, but for the ideal problem presented HRE poses a novel basis to examine a simple non-turbulent reactive plume.

9.3 AERMOD

Plume dispersion modeling has advanced in recent years with the state-of-the-art AERMOD that incorporates air dispersion based on planetary boundary layer turbulence structure and scaling concepts, including treatment of both surface and elevated sources, and both simple

and complex terrain (EPA 2004; Cimorelli et al. 2005). AERMOD has been applied to a wide variety of pollutant sources, such as NO_X, SO_X, and particulate matter (Jampana et al. 2004; Kumar et al. 2006; Sivacoumar et al. 2009).

AERMOD predicts distinctively different behavior for night and day time because of the urban formulation, which applies only to nighttime. AERMOD enhances turbulence at night to simulate the influence of the urban heat island. The smallest time scale of AERMOD is one hour. This investigation found that given constant meteorology and a fixed source, AERMOD's predictions are the same between the hours of 6 a.m. and 4 p.m., daytime, and hours 6 p.m. to 4 a.m., nighttime. The steady-state day and night time behaviors are examined to evaluate the diurnal changes.

AERMOD does not predict the ultra-near field concentration within 1 m of the source, so the predicted peak concentration is 1 m downwind of the source instead of directly over the source. All results based on AERMOD inherent this quality.

A tiered approach has been recommended for modeling NO_X point emissions in AERMOD (EPA 1996). Here, dispersion model results are post-processed by a parameterized chemistry method to account for photochemical impacts. Early methods to parameterize the NO_2-O_3-NO in-plume chemistry include Partial Conversion, where a constant ratio of NO_2/NO_X ($NO_X = NO_2+NO$) is assumed, and Exponential Decay, where half of all NO is converted to NO_2 every 10 minutes (Cole and Summerhays 1979). Newer methods assume a dynamic equilibrium between NO, NO_2 and O_3 (Bange et al. 1991; Chu and Meyer 1991; Hanrahan 1999A). With conservation of NO_X and O_X ($O_X = NO_2 + O_3$), these assumptions allow the use of simple algebraic expression in calculating the combined effect of dispersion and chemical transformations. AERMOD includes two options for simply treating local NO_X chemistry. The discussion of these methods is limited to a single study (Hanrahan 1999B) which only considered the two default NO_X treatments options and a third older method which did not perform well. Additionally, this study only presented a relative comparison of results. There is a need for better characterization of the chemical methods available for incorporation into plume model results (Schlunzen 2002). This study examines five chemical methods summarized in Table 10.

Table 10: Description of chemical methods

Name	Description	Dependence	Reference
Bange's Method	Dynamic equilibrium considering daytime NO-O_3-NO_2 cycle	Receptor NO and NO_2, background O_3	Bange et al. 1991
Hess' Method	Dynamic equilibrium considering NO-O_3-NO_2 cycle and the plume parameterization from McRae et al. (1982)	Receptor NO and NO_2, background O_3	Hess and Cope 1989
Ozone Limiting Method (OLM)	Background ozone controls the rate of O_3 titrating NO	Receptor NO and NO_2, background O_3	Cole and Summerhays 1979
Plume Volume Molar Ratio Method (PVMRM)	Titration of NO from O_3 as the plume segment expands traveling downwind	Background NO_2/NO_X, Receptor NO and NO_2	Hanrahan 1999A
Variational Analysis (VA)	Reynolds averaging of mass balance from Bottenheim and Strausz (1982)	All species at all receptors, background species	This work

9.4 Plume Chemistry- OLM

The Ozone Limiting Method (OLM) is based on the theory that background ozone controls the rate of ozone penetrating into the plume, and the rate at which ozone titrates NO (Tikvart 1996). OLM is based on the Ambient Ratio Method (ARM) which uses the background NO_2 to NO_X ratio to estimate partial conversion of NO to NO_2 (Chu and Meyer 1991). OLM assume partial to full conversion of NO to NO_2 depending on the ratio of the background O_3 to the plume NO_X (Cole and Summerhays 1979). OLM is dependent on the physical size of the plume and the background ozone concentration.

9.5 Plume Chemistry- PVMRM

Plume Volume Molar Ratio Method (PVMRM) was introduced by Hanrahan (1999A). PVMRM method examines the titration NO from O_3 as a plume segment expands traveling downwind. PVMRM was validated with observational data and large eddy simulations (Hanrahan 1999B). However, comparison of observations was sparse and the comparison with large eddy simulations was only relative. Hanrahan (1999B) noted that PVMRM tends to over predict the NO_2 to NO_X ratio. Lui et al. (2007) applied PVMRM to Gaussian dispersion model results in a pollution exposure study of Switzerland.

The PVMRM method is primarily dependent on the background NO_2 to NO_X ratio. There is no clear choice for this ratio because the ideal scenario examined here has no background NO_X. The AERMOD default ratio for background NO_2 to NO_X of 0.9 is used for all PVMRM

calculations. A technical description of the implementation of PVMRM in AERMOD is presented by Cimorelli et al. (2002).

Plume Chemistry - Bange's Method

Bange et al. (1991) developed a technique combining a photostationary state with conservation of NO_X and O_X, a practical application of the methodology outlined by Peters and Richards (1979). NO_2 is calculated directly based on NO_X and O_X concentrations derived from the dispersion model.

$$0 = (NO_2)^2 - NO_2(NO_X + O_X + \propto) + NO_X + O_X \qquad (3)$$

where $\propto$ is the ratio of the kinetic rate constants for titration of NO (R3) to photolysis of NO_2 (R1). $\propto$ is undefined (∞) at night because photolysis only occurs during the daytime. Hence, this method is limited to daytime applications.

9.6 Plume Chemistry- Hess' Method

Hess and Cope (1989) developed a parameterized chemical and plume transport equation based on the work of McRae et al. (1982). They considered the chemistry of NO_2-O_3-NO. Similar to the parameterization created by Bange et al. (1991), a photostationary state is combined with conservation of NO_X and O_X. However, Hess and Cope assume that ozone is diluted within the plume. The parameterization from Hess and Cope (1989) is considerably simplified for this investigation because AERMOD is used to calculate plume transport. The calculation of NO_2 is shown here:

$$NO_2 = {}^1/_2\left\{NO_X + O_X + {}^1/_\propto - \sqrt{\left(NO_X + O_X + {}^1/_\propto\right)^2 - 4NO_X O_X}\right\} \qquad (4)$$

Because (4) depends on ${}^1/_\propto$ which is 0 at night, Hess' method can be applied to night as well as day time predictions.

9.7 Plume Chemistry – VA

Schlunzen (2002) noted the need for improved methods to account for atmospheric reactions in plume models. The chemical techniques described previously are formulated based on closed systems of chemical reactions and specific plume approximations. However, an ideal chemical method should be adaptable to the newest understanding in atmospheric chemical mechanisms.

Several Lagrangian based advection-diffusion-reaction models have been developed which incorporate NO-NO_2-O_3 chemical systems (Bottenheim and Strausz 1982; Vilà-Guerau de Arellano et al. 1990). These particle models use concentric rings of equal volume. Variations

within the rings are related with chemistry considering a mass balance. The expression from Bottenheim and Strausz (1982) is presented for a fixed reference frame

$$\frac{\partial C_i}{\partial t} = \varepsilon U(\alpha_i C_{i-1} + \beta_i C_i + \gamma_i C_{i+1}) + S_{Chem}(C_i) \tag{5}$$

where i is the number of cells away from the source $(x = i\Delta x)$ and U is the mean wind velocity. ε depends on the dispersion coefficients, while α_i, β_i and γ_i depend on the location and averaging area. Expressions for ε, α_i, β_i and γ_i can found in Vilà-Guerau de Arellano et al. (1990), shown here assuming equal areas (A)

$$\alpha_i = \frac{A(i-1)}{A-1} \tag{6}$$

$$\gamma_i = \frac{Ai}{A-1} \tag{7}$$

$$\beta_i = \frac{A(1-2i)}{A-1} \tag{8}$$

$$\varepsilon = \frac{b}{x} \tag{9}$$

Additional discussion of these parameters is presented in Lusis (1976).

The concentration term is split into an average ($\overline{C_i}$) and fluctuation (C_i')

$$C_i = C_i' + \overline{C_i} \tag{10}$$

Here the average term refers to a transport only scenario and the fluctuation term represents a variation due to chemistry. For plume model applications, the plume transport model will compute the 1hr average concentration. Hence within a 1hr average, the average concentration can be treated as constant in time. (5) and (10) can be used to solve for the fluctuation term

$$\frac{\partial C_i'}{\partial t} = \varepsilon U[\alpha_i(C_{i-1}' + \overline{C_{i-1}}) + \beta_i(C_i' + \overline{C_i}) + \gamma_i(C_{i+1}' + \overline{C_{i+1}})] + S_{Chem}(C_i' + \overline{C_i}) \tag{11}$$

(11) is integrated in time to achieve a new steady state solution that accounts for plume transport and chemical impacts. Finally, a Forester filter (Forester 1977) is applied to smooth the solution. The system is constrained so total concentration is non-negative.

This method is referenced the Variation Analysis (VA) method because it is based on a mass balance on variations of concentrations (Bottenheim and Strausz 1982; Vilà-Guerau de Arellano et al. 1990). The steady state solution from VA presented is achieved within 1s using a time step of 60 μs and an initial profile of zero for the fluctuation.

The previous chemical methods are all direct calculations, whereas VA is a gridded method. Discontinuities in initial conditions can cause numerical resonance and should be avoided in the application of VA. Since AERMOD is undefined within 1 m of the source, this region is linearly interpolated for $\bar{C}_i$.

Because this study focuses on examining a NO_x point source, this application of the VA method is limited to a simple NO_2-O_3-NO mechanism. However, the VA method is generalized to easily incorporate new chemical mechanisms. Future work should examine other sources such as SO_x and particulate matter. Chemical segregation could be considered with a parameterization similar to that presented by Alessandrini and Ferrero (2009) or Pagnini (2009).

9.8 Scenarios

The comparison is based on the protocol developed by Hall et al. (2002) which examined transport of plume models. However, the current investigation focuses on a more idealized scenario in order be more exact for the comparison. The present problem considers a fixed ground point source on an infinite plane under steady horizontal wind where surface effects are negligible. The source emits NO_x and has characteristics shown in Table 9. This study focuses on the 1D plume centerline. Auger and Legras (2007) report similar results for 1D and 3D simulations examining advection-diffusion-chemistry of plume centerline. This initial value problem presents a simple test case to examine the various methods which account for photochemical activity. The analytical solution of the plume centerline from a continuous homogenous point source, q, at the origin is shown here assuming a power-law expression for the horizontal and vertical diffusion (Seinfeld and Pandis 1998)

$$C(x) = \frac{q}{\pi U R_y R_z} x^{-(r_y + r_z)} \tag{12}$$

where q is the point source emission rate, U is the wind velocity, and R_y, R_z, r_y and r_z are empirically derived diffusion constants dependent on the stability class and averaging time (ASME 1973).

While both the analytical solution and AERMOD are based on solutions of equation (1), the analytical solution does not consider planetary boundary layer turbulence structure and

scaling concepts like AERMOD. Additionally, AERMOD also has different treatment for night and day transport while the analytical solution does not consider time of day. Hence, AERMOD and the analytical solution produce highly correlated solutions of different magnitude. The analytical solution is used only to evaluate HRE and AERMOD model predictions of plume transport without photochemistry. For discussion purposes, the analytical solution presented has been modified so that the analytical peak concentration of the study region matches the peak predicted by HRE and AERMOD. This is accomplished by changing the source term, q, used in (12) for each case presented.

Several studies have noted the importance of chemical segregation within the plume, which can affect reaction rates (Galmarini et al. 1995; Hilst 1998; Pagnini 2009; Rubio et al. 2008). Chemical reactions rates are measured in homogenous mixtures where reaction is uniform. However, turbulent eddies in the atmosphere can generate an inhomogeneous composition that slows down biomolecular reaction rates compared with a homogenous composition. Chemical segregation can hinder chemical activity of a reactive plume (Hilst 1998; Paginini 2009). This effect is particularly important when the photochemical time-scale is of similar magnitude as the characteristic turbulent time scale (Vinuesa and Vilà-Guerau de Arellano 2005). The intensity of segregation has been related to the Damköhler number (ratio of turbulent time scale to reactive time scale), the distance from the centerline and the standard deviation in the horizontal crosswind direction (Fabregat et al. 2010; Pagnini et al. 2009).

At this initial stage, the investigation examines an ideal non-turbulent point source where there is no chemical segregation. Instead, neutral and stable meteorology cases are examined. Vilà-Guerau de Arellano et al. (2004) note the key scaling factors for this problem is the Damköhler number and the ratios of the concentrations in the species. Two meteorology scenarios are selected from different ranges of Damköhler number; 1) stable atmospheric conditions with a wind velocity of 1 m/s and a Pasquill-Gifford (P-G) stability class of F, and 2) neutral atmospheric conditions with a wind velocity of 5 m/s and a P-G stability class of D. Each meteorology is examined with 0, 1 and 1000 ppb of the primary background NO_X oxidant, ozone. These background ozone scenarios represent none, very low and very high levels of ozone. A total of six scenarios examining chemical effects on plume transport are presented. There are several assumptions that are made for this ideal case including very low surface roughness and no sensible heat flux. The micro-environment characteristics used in this study are shown in Table 11.

Table 11: Local meteorology characteristics

Meteorological Parameters	Day/Night
Surface Roughness Length (m)	.1 / .1
Sensible Heat Flux	0 / 0
Surface Friction Velocity (m/s)	.164 / .102
Convective Velocity Scale (m/s)	.516 / .385
Convectively Generated Boundary Layer (m)	100 / 100
Mechanically Generated Boundary Layer (m)	100 / 100
Monin-Obukhov Length (m)	-8 / 50
Bowen Ratio	0 / 0
Surface Albedo	0 / 0
Temperature (K)	293.15 / 293.15

Several of the chemical methods examined predict the chemical impact for multiple pollutant species. However, only NO_2 is predicted by all the chemical methods. Hence, only the impact to NO_2 is examined for consistency.

9.9 Results

AERMOD is used to model a single continuous area source with characteristics shown in Table 9. Typically meteorology examined is shown in Table 11. For the scenarios examined, the concentration predicted by AERMOD transport is over two orders of magnitude lower than the predicted peak concentration at 20 m down-wind of the source due to the exponential nature of plume transport. Hence, the present investigation is focused on plume behavior within 20 m of the source. Receptors are placed evenly down the plume centerline every 10 cm.

The steady-state transport solution from HRE, AERMOD and the analytical solution are shown in **Error! Reference source not found.**.

Figure 16: Steady state NO2 concentration from transport of NOX point source at origin

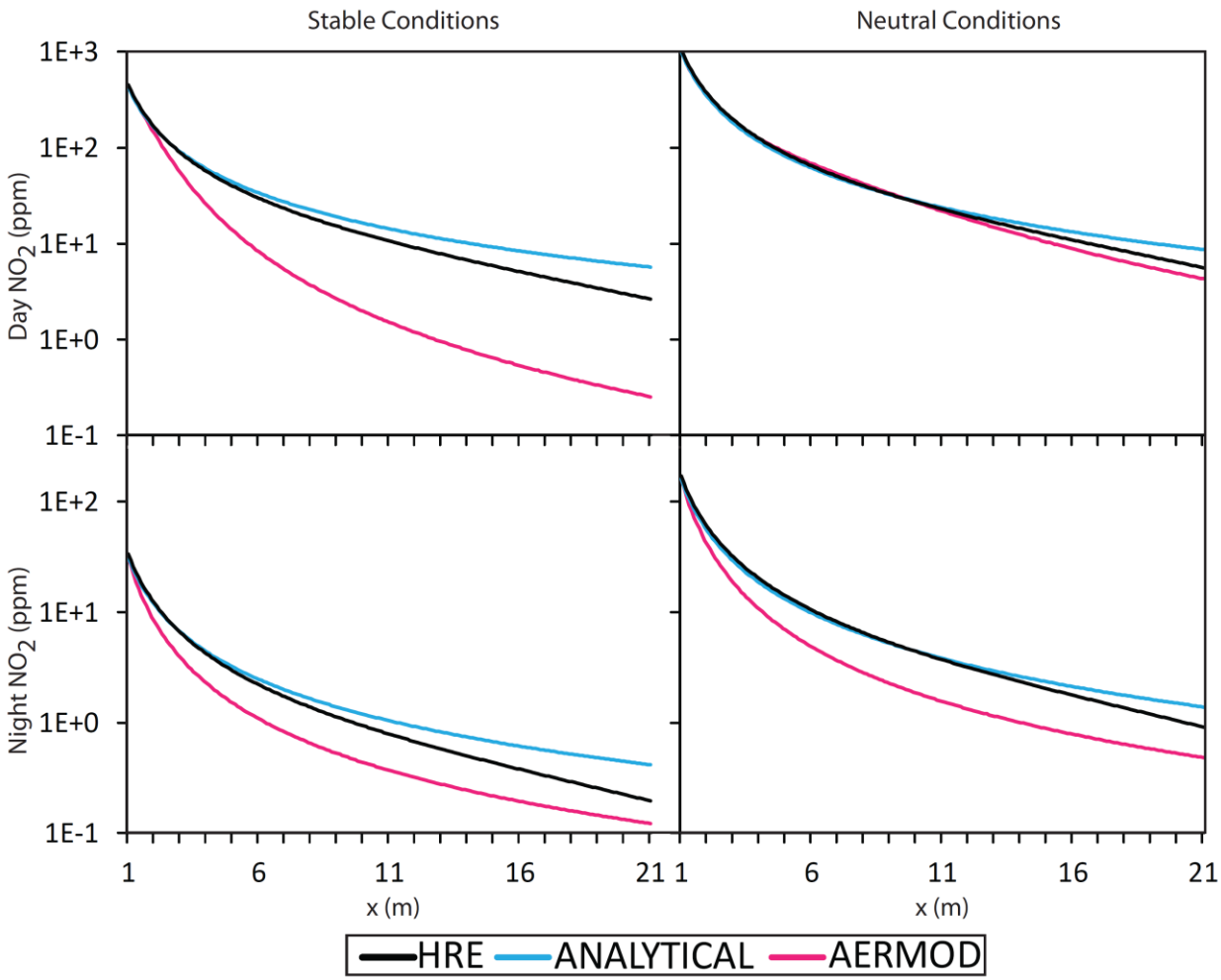

HRE and the analytical solution are both normalized to match AERMOD 1 m downwind. A statistical comparison is presented in Table 12 and Table 13.

Table 12: Statistical comparison considering stable atmospheric conditions results with HRE model results

	Scenario	Method	Pearson Correlation Coefficient	Fractional Bias	Root Mean Square Error	Mean Normalized Bias
Day	TRANSPORT	AERMOD	0.99	1.30	12.20	569.22
		Analytical	1.00	-0.70	3.97	-46.08
	NO OZONE	VA	0.99	1.24	9.45	494.03
		Hess	0.99	1.24	9.44	495.63
		OLM	0.99	1.94	49.48	11782.10
		Bangey	0.99	-1.82	1573.48	-95.17
	1 PPB O_3	VA	0.99	1.19	9.20	445.95
		Hess	0.99	1.19	9.20	445.22
		OLM	0.99	1.93	46.57	10019.28
		Bangey	0.99	-1.83	1576.29	-95.55
		PVMRM	0.99	1.60	28.87	1257.81
	1 PPM O_3	VA	0.99	1.64	88.80	1420.49
		Hess	0.99	1.03	91.58	431.52
		OLM	1.00	1.78	139.52	2602.76
		Bangey	0.99	-1.56	1484.72	-86.99
Night	TRANSPORT	AERMOD	0.99	0.24	1.07	48.39
		Analytical	1.00	-0.69	0.32	-45.33
	NO OZONE	VA	0.99	-0.02	0.53	10.96
		Hess	0.99	-0.02	0.53	10.96
		OLM	0.99	1.72	3.08	2119.83
	1 PPB O_3	VA	0.99	-0.10	0.58	2.20
		Hess	0.99	-0.10	0.58	1.69
		OLM	0.99	1.66	2.90	1763.68
		PVMRM	0.99	0.81	1.90	196.20
	1 PPM O_3	VA	0.99	0.77	5.11	180.14
		Hess	0.99	-0.56	5.01	-14.21
		OLM	0.84	0.89	8.21	315.58

Table 13: Statistical comparison considering neutral atmospheric conditions results with HRE model results

	Scenario	Method	Pearson Correlation Coefficient	Fractional Bias	Root Mean Square Error	Mean Normalized Bias
Day	TRANSPORT	AERMOD	1.00	-0.04	7.15	1.22
		Analytical	1.00	-0.48	8.48	-31.21
	NO OZONE	VA	1.00	0.05	17.02	11.52
		Hess	1.00	0.05	17.01	11.55
		OLM	1.00	1.78	135.96	2130.67
		Bangey	1.00	-1.89	3783.06	-97.19
	1 PPB O_3	VA	1.00	0.05	17.02	11.52
		Hess	1.00	0.05	17.01	11.52
		OLM	1.00	1.78	135.96	2121.37
		Bangey	1.00	-1.89	3783.06	-97.19
		PVMRM	1.00	0.15	29.44	23.92
	1 PPM O_3	VA	1.00	0.06	15.63	12.73
		Hess	1.00	-0.11	16.85	-3.28
		OLM	1.00	1.15	135.78	742.54
		Bangey	1.00	-1.89	3783.25	-97.14
Night	TRANSPORT	AERMOD	0.99	0.36	5.21	67.28
		Analytical	1.00	-0.46	1.64	-30.25
	NO OZONE	VA	0.99	0.30	3.98	57.39
		Hess	0.99	0.30	3.97	57.39
		OLM	0.99	1.80	18.88	3047.94
	1 PPB O_3	VA	0.99	0.30	3.98	57.39
		Hess	0.99	0.30	3.97	57.17
		OLM	0.99	1.79	18.88	2965.96
		PVMRM	0.99	0.40	5.12	74.87
	1 PPM O_3	VA	0.99	0.36	4.11	67.00
		Hess	0.99	-0.36	3.79	-11.56
		OLM	0.97	0.64	18.72	302.70

AERMOD matches the analytical solution best for day neutral conditions, moderately at night for stable and neutral conditions, and poorly for day stable conditions. The poor correlation between AERMOD and the analytical solution during day stable conditions is due to AERMOD inability process low wind speeds. AERMOD does not handle wind speeds less than 0.5 m/s and the case of stable conditions requires a wind speed of 1 m/s, close to the cutoff. Still, there is reasonably good agreement in all cases between AERMOD and the analytical solution. HRE matches the analytical solution quite well for all cases.

Results considering photochemically reactive transport are shown in **Error! Reference source not found.**, with statistical analysis shown in Table 12 and Table 13.

Figure 17: Steady state NO2 concentration from transport and chemistry of NOX point source at origin

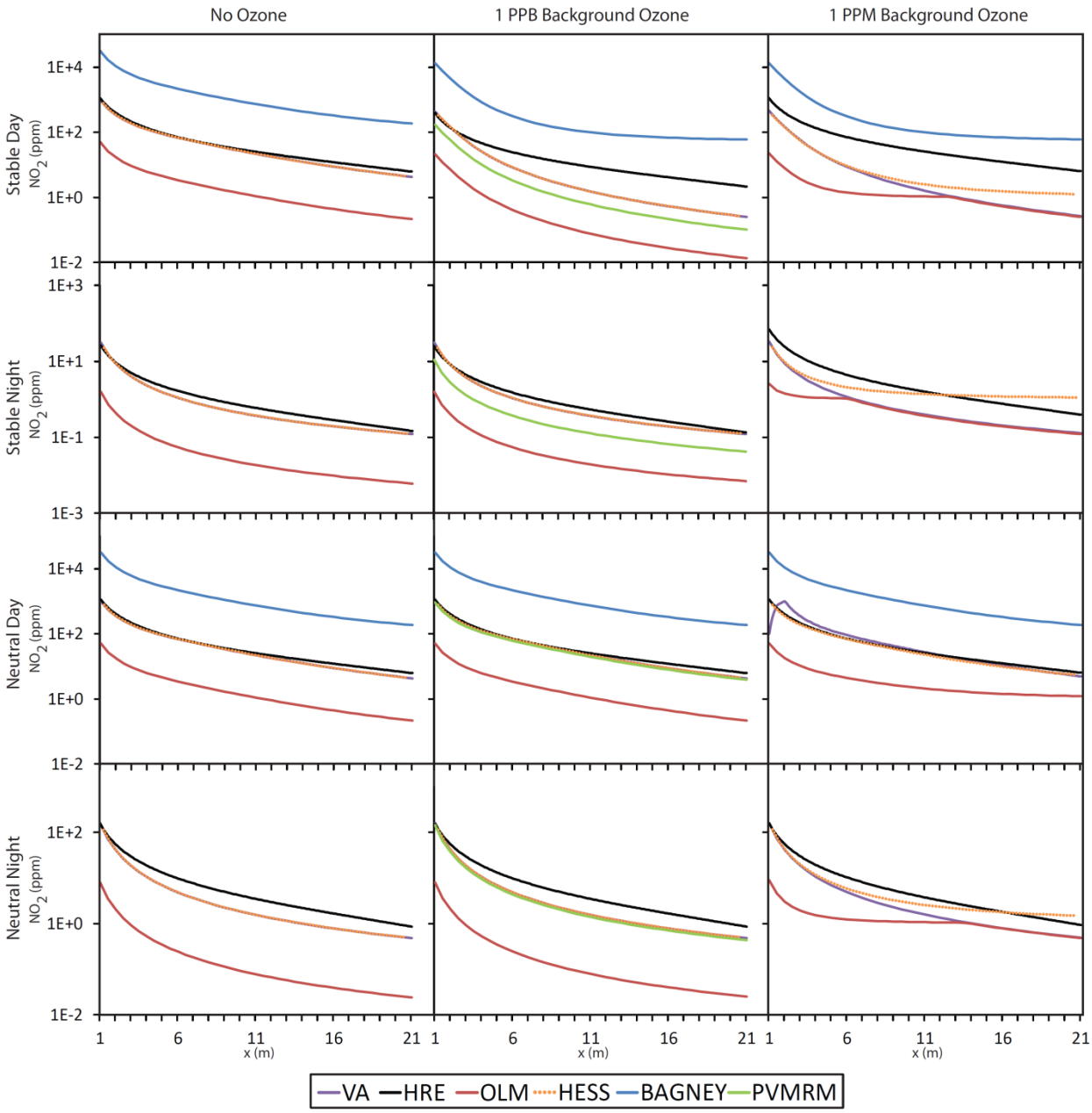

Since the source produces both NO and NO_2, there is conversion of NO to NO_2 from NO_3 (R6) and O_3 (R3). NO_3 is produced from ozone titration NO_2 (R10). During the day NO_3 photolyzes mostly into NO (R8), a small amount is removed through deposition (R7). At night NO_3 is more abundant and presents a significant pathway to convert NO to NO_2 (reaction 6). Several studies have noted the importance of NO_3 on the NO_2-O_3-NO cycle at nighttime (Chang et al. 2011; Finlayson-Pitts and Pitts 1986; Finlayson-Pitts and Pitts 2000; Russell et al. 1985; Weschler 1992). During the day, NO_2 photolysis is balanced mainly by NO titration. HRE predicts little distinction between scenarios with 1 and 0 ppb background O_3, and higher NO_2 concentrations for the 1 ppm scenarios. The increase in NO_2 from 1 ppb

background O_3 to 1 ppm is greater for stable meteorology than neutral meteorology where the transport time scale is larger.

The chemical methods examined vary widely in their predictions, but they all correlate well with HRE. OLM consistently under-predicts NO_2 production compared with HRE and shows the highest mean normalized bias. Additionally, for several of the 1 ppm background O_3 scenarios OLM produces an inflection point where the NO_X concentration meets background O_3. This inflection is not replicated in HRE and can lead to reduced correlation.

Bagney's method consistently over-predicts NO_2 production compared with HRE by at least an order of magnitude and shows the highest root mean square error. The comparison of Bagney's method is rather limited because the method is restricted to daytime application.

PVMRM is only applied to the 1 ppb background O_3 scenario because the method does not consider background ozone in its formulation and this scenario is the closest to normal conditions. PVMRM predicts a solution similar to VA and Hess for neutral conditions, and under-predicts HRE for stable conditions. PVMRM performs reasonably well for the scenario it is applied to, but not as well as VA or Hess.

VA and Hess' method produce virtually identical predictions for low and no background O_3, which is unexpected considering they have such different formulations. Additionally, the prediction for low and no background O_3 matches HRE well. For high background O_3, Hess' method performs better than VA.

VA exhibits resonance from the initial step of AERMOD's peak which is most notable for the high background ozone neutral day scenario. VA is the only method to exhibit resonance behavior, but it is not substantial.

9.10 Discussion

Without using a second-order enclosure scheme (Karamchandani et al. 2000) or entirely different transport model such as LES (Sykes et al. 1992; Vilà-Guerau de Arellano et al. 2004), there are no other present options to account for chemical reactions in a plume than a chemical method. While the implication of chemical methods may not be ideal, it is the most practical and convenient solution at the current state-of-the-science. This study is intended to foster the discussion of plume chemical methods with a comprehensive comparison of available methods. Eventually, the problem of finding a chemical treatment method for dispersion transport models maybe entirely circumvented if AERMOD is succeeded with a reactive plume model. This is perhaps the ideal solution, but at the present time the application of a modular chemistry mechanism is recommended (EPA 2004).

The application of modular chemical mechanisms on plume model results has been limited up to now due to lack of discussion. Numerical schemes to solve for chemistry need to be improved (Schlunzen 2002). This study presents a first step to quantitatively comparing available chemistry methods on a diffusion model under neutral and stable atmospheric conditions for a variety of background pollutant conditions. Suggested modular chemical mechanisms are presented with a newly-derived mechanism (VA). A highly-resolved

Eulerian model is developed to match the transport of AERMOD. Chemical impacts from the Eulerian model are compared with results from chemical methods applied to AERMOD's transport. This study illustrates that a relative comparison alone is not enough to characterize the performance of the chemical methods.

Furthermore, this study focuses on the ground level near field reactive plume centerline. Previous work has been unclear on the chemical activity in the reactive plume down the ground centerline with some studies indicating no chemical activity (Galmarini et al. 1995; Komori et al. 1991) and other studies indicating full chemical treatment (Auger and Legras 2007; Vilà-Guerau de Arellano et al. 2004; Pagnini 2009). HRE model results show that the chemical impact is sensitive to the meteorology, a result consistent with past work (Vilà-Guerau de Arellano et al. 2004; Meeders and Nieuwstadt 2000).

Venkatram and Cimorelli (2007) discuss how even low wind speeds can be governed by large turbulent eddies. Hence, a comparison with observational data would require turbulent modeling such as LES. However, these models have only been evaluated with a relative comparison (Alessandrini and Ferrero 2009; Vilà-Guerau de Arellano et al. 2004; Sykes et al. 1992). This study has shown that considering only relative statistical indicators is inadequate to effectively compare the chemistry methods because it disregards significant absolute differences. The chemical methods presented differ in their predictions of NO_2 by several orders of magnitude (Fig. 2).

The methods examined in this study assume homogenous mixing occurs at the molecular level and that local chemistry is in equilibrium (Cole and Summerhays 1979). However, this equilibrium can be perturbed by flow separating species and by insufficient mixing (Vilà-Guerau de Arellano 2003). Chemical segregation could be considered with VA, while it is not clear how a chemical segregation parameterization could be applied to the other chemical methods. Future work should examine the influence of turbulent meteorology scenarios with possible validation from LES (Vilà-Guerau de Arellano et al. 2004) and second-order closure schemes (Karamchandani et al. 2000). However, the influence of turbulent induced chemical segregation has been shown to only decrease the effective chemical reaction rate (Alessandrini and Ferrero 2009; Pagnini 2009).

OLM and Bagney's methods compare the worst of the chemical methods presented. OLM over-predicts and Bagney under-predicts NO_2 by at least an order of magnitude. PVMRM performs better than OLM and is the best choice of the built-in AERMOD photochemical processing options.

Overall, Hess and VA outperform the other methods. VA and Hess produce indistinguishable predictions for low and no background ozone. Only for high background ozone does Hess' method perform better than VA. However, VA is the only method which does not make any assumptions about the chemical mechanisms and can be adapted to include new photochemical pathways. Hess' method is limited to examining NO_2-O_3-NO chemistry. Several studies have noted the importance of plume chemistry for sources emitting aerosols (Joos 1987) and SO_X ($SO_X = SO_2 + SO_3$) (Bottenheim and Strausz 1982). Future work will evaluate the performance VA with different chemical mechanisms.

REFERENCES

Alessandrini, S., Ferrero, E., 2009. A hybrid Lagrangian-Eulerian particle model for reacting pollutant dispersion in non-homogeneous non-isotropic turbulence. Physica A 388(8), 1375-1387.

Altshuller, A.P., 1989. Nonmethane Organic Compound to Nitrogen Oxide Ratios and Organic Composition in Cities and Rural Areas. Journal of Air Pollution Control Association 39, 936-943.

American Society of Mechanical Engineers, 1973. Recommended Guide for the Prediction of the dispersion of airborne effluents, 2nd ed. AMSE, New York.

Auger, L., Legras, B., 2007. Chemical segregation by heterogeneous emissions. Atmospheric Environment 41, 2303-2318.

Bange, P, Janssen, L.H.J.M., Nieuwstadt, F.T.M., Visser, H., Erbrink, J.J., 1991. Improvement of the modeling of daytime nitrogen-oxide oxidation in plumes by using instantaneous plume dispersion parameters. Atmospheric Environment 25(10), 2321-2328.

Bange, P., 1993. Modeling NO conversion by using probability density-functions. Boundary-Layer Meteorology 62(1-4), 303-311.

Bottenheim, J.W., Strausz, O.P., 1982. Modeling study of a chemically reactive power plant plume. Atmospheric Environment 16(1), 85-97.

Briggs, G. A. (ed) (1984) Plume Rise and Buoyancy Effects. D., U. S. Dept. of Energy, 327-366.

Byun, D.W., Ching, J.K.S. (1999) Science Algorithms of the EPA Models-3 Community Multiscale Air Quality (CMAQ) Modeling System. EPA/600/R-99/030.

Chang, W., Bhave, P., Brown, S., Riemer, N., Stutz, J., Dabdub, D., 2011. Heterogeneous atmospheric chemistry, ambient measurements, and model calculations of N2O5: a review. Aerosol Science and Technology 45, 655-685.

Chang, W.S., Chen, S.S., Chang, J.H., Tang, C.H., Chang, T.C., 2009. Odor load investigation for a pharmaceutical plant by open path Fourier transform infrared (OP-FTIR)/Environmental Protection Agency Regulatory Dispersion Model (AERMOD). Environmental Forensics 10, 82-91.

Ching, J., Herwehe, J., Swall, J., 2006. On joint deterministic grid modeling and sub-grid variability conceptual framework for model evaluation. Atmospheric Environment. 40(26):4935-4945.

Chu, Shao-Hang, Meyer, E.L., 1991. Use of Ambient Ratios to Estimate Impact of NOX

Sources on Annual NO Concentrations. Air and Waste Management Association 84th Annual Meeting, June 1991. (AWMA Document Number 91-180.6).

Cimorelli, A.J., Perry, S.G., Venkatram, A., Weil, J.C., Paine, R.J., Wilson, R.B., Lee, R.F., Peters, W.D., Brode, R.W., Paumier, J.O., 2002. AERMOD: description of model formulation (Version 02222). EPA 454/R-02-002d. U. S. Environmental Protection Agency, Research Triangle Park, NC.

Cimorelli, A.J., Perry, S.G., Venkatram, A., Weil, J.C., Paine, R.J., Wilson, R.B., Lee, R.F., Peters, W.D., Brode, R.W., 2005. AERMOD: a dispersion model for industrial source applications. Part I: general model formulation and boundary layer characterization. Journal of Applied Meteorology 44, 682-693.

Cohan, A., Chang W., Carreras-Sospedra, M., Dabdub, D., 2008. How new chemistry findings affect our understanding of the weekend effect - A modeling study. Final report to the California Air Resources Board. ARB Contract 04-333.

Cole, H., Summerhays, J., 1979. Review of techniques available for estimating short-term NO2 Concentrations. Journal of the Air Pollution Control Association 29(8), 812-817.

Crone, G.C., Dinar, N., Van Dop, H., Verver, G.H.L., 1999. A Lagrangian approach for modeling turbulent transport and chemistry. Atmospheric Environment 33(29), 4919-4934.

Dabdub, D. and Seinfeld, J.H. (1994) Air quality modeling on massively parallel computers, Atmospheric Environment. 28:1679– 1687.

Doherty, J., 2007. PEST user manual. 5th ed. Brisbane, Queensland, Australia: Watermark Numerical Computing.

Draxler, R.R. and Hess, G.D. (1998) An overview of the Hysplit4 modeling system for trajectories, dispersion, and deposition, Australian Meteorological Magazine. 47:295–308.

EPA. (1995) User's Guide for the Industrial Source Complex (ISC3) Dispersion Models, 1-2. EPA-454/B-95-003a and b; Office of Air Quality Planning and Standards: Research Triangle Park, NC.

EPA, 1996. Guideline on air quality models (Revised). EPA Document Number EPA-450/2-78-027R, 40 CFR 51, Appendix W.

EPA. (2000) User's guide for the Assessment System for Population Exposure Nationwide (ASPEN, version 1.1) Model. Office of Air Quality Planning and Standards Rep. EPA-454/R-00-017, 108 pp.

EPA, 2004. User's Guide for the AMS/EPA regulatory model – AERMOD. EPA - 454/B - 03 - 001.

EPA. (2005) The HEPEM user's guide - Hazardous Air Pollutant Exposure Model, Version 5 [Available online at http://www.epa.gov/ttn/fera/human_hapem.html.]

Fabregat, A., Pallares, J., Cuesta, I., Grau, F.X., 2010. Numerical simulations of a second-order chemical reaction in a plane turbulent channel flow. International Journal of Heat and Mass Transfer 53(19-20), 4248-4263.

Finlayson-Pitts, B.J., Pitts, J.N., 1986. Atmospheric chemistry: fundamentals and experimental techniques. New York: John Wiley and Sons Inc.

Finlayson-Pitts, B.J., Pitts, J.N., 1993. Volatile organic compounds: ozone formation, alternative fuels and toxics. Chemistry and Industry 20, 796-800.

Finlayson-Pitts, B.J., Pitts, J.N., 2000. Chemistry of the upper and lower atmosphere: theory, experiments, and applications. San Diego: Academic Press.

Forester, C.K., 1977. Higher order monotonic convective difference schemes. Journal of Computational Physics, 23:1–22.

Galmarini, S., Dearellano, J., Duynkerke, P., 1995. The effect of microscale turbulence on the reaction-rate in a chemically reactive plume. Atmospheric Environment 29(1), 87-95.

Garmory, A., Richardson, E., Mastorakos, E., 2006. Micromixing effects in a reacting plume by the Stochastic Fields method. Atmospheric Environment 40(6), 1078-1091.

Geiser, J., 2009. Discretization methods with analytical characteristic methods for advection-diffusion-reaction equations and 2D applications. Modélisation Mathématique et Analyse Numérique 43(6), 1157-83

Griffin, R. J., Dabdub, D., Seinfeld, J. H. (2002) Secondary organic aerosol: 1. Atmospheric chemical mechanism for production of molecular constituents, J. Geophys. Res. 107:4332.

Griffin, R.J., Dabdub, D., Seinfeld, J.H., 2005. Development and initial evaluation of a dynamic species-resolved model for gas phase chemistry and size-resolved gas/particle partitioning associated with secondary organic aerosol formation. J Geophys Res doi:10.1029/2004JD005219.

Griffin, R.J., Nguyen, K., Dabdub, D., Seinfeld, J.H., 2003. A combined hydrophobic–hydrophilic module for predicting secondary organic aerosol formation. J Atmos Chem 44:171–190.

Hall, D.J., Spanton, A.M., Dunkerley, F., Bennett, M., Griffiths, R.F., 2000. An inter-comparison of the AERMOD, ADMS and ISC Dispersion Models for Regulatory Applications. Environment Agency Technical Report P353.

Hanrahan, P., 1999A. The plume volume molar ratio method for determining NO2/NOx ratios in modeling - part I: methodology. Journal of the Air and Waste Management Association 49(11), 1324-1331.

Hanrahan, P.,1999B. The plume volume molar ratio method for determining NO2/NOx ratios in modeling - part II: evaluation studies. Journal of the Air and Waste Management Association 49(11), 1332-1338.

Herwehe, J. (2000) A numerical study of the effects of large eddies on the trace gas measurements and photochemistry in the convective boundary layer. Ph. D. Dissertation, Department of Atmospheric Science, University of Alabama in Huntsville.

Herwehe, J., Ching, J., Swall, J. (2004) Quantifying subgrid pollutant variability in Eulerian air quality models. Extended Abstract, American Meteorological Society, Thirteenth Conference on Applications of Air Pollution Meteorology. 23–27 August, Vancouver, BC, Canada.

Hess, G.D., Cope, M.E., 1989. A note on subgrid-scale processes in photochemical modeling. Atmospheric Enviroment 23(9), 2857-2860.

Hilst, G., 1998. Segregation and chemical reaction rates in air quality models. Atmospheric Environment 32(22), 3891-3895.

Isakov, V. and Venkatram, A. (2006) Resolving Neighborhood Scale in Air Toxics Modeling: A Case Study in Wilmington, CA. J. Air & Waste Manage. Assoc. 56:559-568.

Isakov, V., Irwin, J. S. and Ching, J. (2007) Using CMAQ for Exposure Modeling and Characterizing the Subgrid Variability for Exposure Estimates. Journal of Applied Meteorology and Climatology. 46(9):1354-1371.

Jampana, S.S., Kumar, A., Varadarajan, C., 2004. Application of the United States Environmental Protection Agency's AERMOD model to an industrial area. Environmental Progress 23(1), 12-18.

Jing, Q., Pankratz, D., Princevac, M. and Venkatram, A. (2009) Modeling Dispersion of Buoyant Releases in an Urban Area. 11th Conference on Atmospheric Chemistry in the 89th American Meteorological Society Annual Meeting, Phoenix, AZ.

Joos, E., Mendonca, A., Seigneur, C., 1987. Evaluation of a reactive plume model with power plant plume data – application to the sensitivity analysis of sulfate and nitrate formation. Atmospheric Enviroment 21(6), 1331-1343.

Karamchandani, P., Koo, A., Seigneur, C., 1998. Reduced Gas-Phase Kinetic Mechanism for Atmospheric Plume Chemistry. Environmental Science & Technology. 32(11):1709-1720.

Karamchandani, P., Santos, L., Sykes, I., Zhang, Y., Tonne, C. and Seigneur, C., 2000. Development and Evaluation of a State-of-the-Science Reactive Plume Model. Environmental Science & Technology. 34(5):870-880.

Karamchandani, P., Seigneur, C., Vijayaraghavan, K., Wu, S. Y., 2002. Development and application of a state-of-the-science plume-in-grid model. Journal of Geophysical Research D: Atmospheres. 107(19).

Karamchandani, P., Vijayaraghavan, K., Chen, S.-Y., Seigneur, C., Edgerton, E. S., 2006. Plume-in-grid modeling for particulate matter. Atmospheric Environment. 40(38):7280-7297.

Kim, Y.P., Seinfeld, J.H., Saxena, P., 1993. Atmospheric gas-aerosol equilibrium I. Thermodynamic model. Aerosol Sci Technol 19:157–181.

Klug, W., 1969. A method for determining diffusion conditions from synoptic observations. Staub-Reinhalt Luft 29, 14-20.

Komori S., Hunt J. C. R., Kanzaki, T., Murakami, Y., 1991. The effects of the turbulent mixing on the correlation between two species and concentration fluctuations in non-premixed reacting flows. J. Fluid Mech 228, 629-659.

Kumar, A., Dixit,S., Varadarajan, C., Vijayan, A., Masuraha, A., 2006. Evaluation of the AERMOD dispersion model as a function of atmospheric stability for an urban area. Environmental Progress 25(2), 141-151.

Kumar, N., Russell, A.G., 1996. Development of a computationally efficient, reactive subgid-scale plume model and the impact in the northeastern United States using increasing levels of chemical detail. Journal of Geophysical Research 101(D11), 16737-16744.

Liu, L.J.S., Curjuric, I., Keidel, D., Heldstab, J., Kunzli, N., Bayer-Oglesby, L., Ackermann-Liebrich, U., Schindler, C., 2007. Characterization of source-specific air pollution exposure for a large population-based swiss cohort (SAPALDIA). Environmental Health Perspectives 115(11), 1638-1645.

Martin, D.O., 1976. Comment on the change of concentration standard deviations with distance. Journal of Air Pollution Control Association 26, 145-146.

Meeder, J., Nieuwstadt, F., 2000. Large-eddy simulation of the turbulent dispersion of a reactive plume from a point source into a neutral atmospheric boundary layer. Atmospheric Environment 34(21), 3563-3573.

Meng, Z., Seinfeld, J.H., Saxena, P., Kim, Y.P., 1995. Atmospheric gas aerosol equilibrium 4.Thermodynamics of carbonates. Aerosol Sci Technol 23:131–154.

Milford, J.B., Russell, A.G, McRae, G.J., 1989. A New Approach to Photochemical Pollution Control: Implications of Spatial Patterns in Pollutant Responses to Reductions in Nitrogen Oxides and Reactive Organic Gas Emissions. Environmental Science and Technology 23, 1290-1301.

Nguyen, K., Dabdub, D., 2001. Two-level time-marching scheme using splines for solving the advection equation. Atmospheric Environment 35, 1627-1637.

Pagnini, G., 2009. The kernel method to compute the intensity of segregation for reactive pollutants: mathematical formulation. Atmospheric Environment 43(24), 3691-3698.

Peters, L., Richards, L., 1979. Extension of atmospheric dispersions to incorporate fast and reversible reactions. Atmospheric Environment 11, 101-108.

Russell, A.G., McRae, G.J., Cass, G.R., 1985. The dynamics of nitric acid production and the fate of nitrogen oxides. Atmospheric Environment 19(6), 893-903.

Rubio, A., Zalts, A., El Hasi, C., 2008. Numerical solution of the advection-reaction-diffusion equation at different scales. Environmental Modeling and Software 23(1), 90-95.

Samuelsen, S., D. Dabdub, J. Brouwer, M. Medrano, M. Rodriguez, and M. Carreras-Sosedra. 2005. Air quality impacts of distributed generation. California Energy Commission, PIER Energy-Related Environmental Research. CEC-500-2005-069-F.

Sax, T., Isakov, V. (2003) A case study for assessing uncertainty in local-scale regulatory air quality modeling applications. Atmospheric Environment, 37 (25), pp. 3481-3489.

Scire, Joseph S., Strimaitis, David G., Yamartino, Robert J. (2000) A user's guide for the CALPUFF dispersion model (Version 5). Earth Tech. Inc., Concord, MA.

Schleier, J.J., Davis, R.S., Shama, L.M., Macedo, P.A., Peterson, R., 2008. Equine risk assessment of insecticides used in adult mosquito management. Human and Ecological Risk Assessment 14, 392-407.

Schlunzen, K.H.. 2002. Simulation of transport and chemical transformations in the atmospheric boundary layer review on the past 20 years developments in science and practice. Meteorologische Zeitschrift 11(4), 303-313.

Seinfield, J.H., Pandis, S.N., 1998. Atmospheric chemistry and physics. John Wiley and Sons, New York, NY.

Sivacoumar, R., Raj, S.M., Chinnadurai, S.J., Jayabalou, R., 2009. Modeling of fugitive dust emission and control measures in stone crushing industry. Journal of Environmental Monitoring 11(5), 987-997.

Stein, A. F., Isakov, V., Godowitch, J., Draxler, R.R., 2007. A hybrid modeling approach to resolve pollutant concentrations in an urban area. Atmospheric Environment. 41(40):9410-9426.

Stewart, D.A., Liu, M.K., 1981. Development and application of a reactive plume model. Atmospheric Enviroment 15(10-11), 2377-2393.

Sykes, R.I., Henn, D.S., Parker, S.F., Lewellen, W.S., 1992. Large-eddy simulation of a turbulent reacting plume. Atmospheric Environment 26(14), 2565-2574.

Sykes, R. I., Lewellen, W. S., Parker, S. F., Henn, D.S., 1989. A hierarchy of dynamic plume models incorporating uncertainty: Volume 4, Second-order closure integrated puff: Final report. EPRI-EA-6095-Vol.4.

Tikvart, J.A., 1996. Application of ozone limiting method. Model Clearinghouse Memorandum #107 U.S. Environmental Protection Agency, August 15.

Turner, D.B., 1969. Workbook of atmospheric diffusion estimates. US EPA 999-AP-26. U.S. Environmental Protection Agency, Washington, DC.

Venkatram, A., Cimorelli, A.J., 2007. On the role of nighttime meteorology in modeling dispersion of near surface emissions in urban areas. Atmospheric Environment 41(4), 692-704.

Venkatram, A. (2009) Evaluation of the Near Source Air Quality Impact of Distributed Generation. California Energy Commission, PIER Energy-Related Environmental Research. CEC-500-02-004.

Vijayaraghavan, K., Karamchandani, P. and Seigneur, C. (2006) Plume-in-grid modeling of summer air pollution in Central California. Atmospheric Environment. 40(26):5097-5109.

Vijayaraghavan, K., Karamchandani, P., Seigneur, C., Balmori, R. and Chen, S.-Y. (2008) Plume-in-grid modeling of atmospheric mercury. J. Geophys. Res. 113.

Vijayaraghavan, K., Zhang, Y., Seigneur, C., Karamchandani, P. and Snell, H. E. (2009) Export of reactive nitrogen from coal-fired power plants in the U.S.: Estimates from a plume-in-grid modeling study. J. Geophys. Res. 114.

Vilà-Guerau de Arellano, J., Talmon, A., Builtjes, P., 1990. A chemically reactive plume model for the NO-NO2-O3 system. Atmospheric Environment 24(8), 2237-2246.

Vilà-Guerau de Arellano, J., Dosio, A., Vinuesa, J.F., Holtslag, A.A.M., Galmarini, S., 2004. The dispersion of chemically reactive species in the atmospheric boundary layer. Meteorology and Atmospheric Physics 87, 23-28.

Vinuesa, J, Vilà-Guerau de Arellano, J., 2005. Introducing effective reaction rates to account for the inefficient mixing of the convective boundary layer. Atmospheric Environment 39(3), 445-461.

Weil, J., C. (1988) Plume Rise. In Lectures on Air Pollution Modeling, American Meteorological Society, Boston, Venkatram, A., and Wyngaard, J., Editors.

Wolff, G.T., Korsog, P.E., 1992. Ozone Control Strategies based on the Ratio of Volatile Organic Compounds to Nitrogen Oxides. Journal of Air and Waste Management Association 42, 1173-1177.

Wu, J., Houston, D., Lurmann, F., Ong, P., Winer, A., 2009. Exposure of PM2.5 and EC from diesel and gasoline vehicles in communities near the ports of Los Angeles and Long Beach, California. Atmospheric Environment 43, 1962-1971.

Weschler, C.J., 1992. Indoor ozone and nitrogen dioxide: a potential pathway to the generation of ntirate radicals, dinitrogen pentoxide, and nitric acid indoors. Environ Sci Technol 26(1): 179-184.

Yamartino, R. J., Scire, J. S., Carmichael, G.R., Chang, Y.S., 1992. The CALGRID mesoscale photochemical grid model--I. Model formulation. Atmospheric Environment. Part A. General Topics. 26(8):1493-1512.

Yudianto, D., Xie, Y., 2010. A comparison of some numerical methods in solving 1-D steady-state advection dispersion reaction equation. Civil Engineering and Environmental Systems 27(2), 155-172.

Appendix A:

Species List

This section contains the ordered list of chemical specials held in the main data array *CNT*. All atmospheric species are identified by their order number for the both the initial condition and sources input files.

Table 14: Gas phase chemical species listed in order

Species Number	Species Abbreviation	Molecular Weight (g/mol)	Description
1	NO	30	NITRIC OXIDE
2	NO2	46	NITROGEN DIOXIDE
3	O3	48	OZONE
4	HONO	47	NITROUS ACID
5	HNO3	63	NITRIC ACID
6	HNO4	79	PERNITRIC ACID
7	N2O5	108	NITROGEN PENTOXIDE
8	NO3	62	NITRATE RADICAL
9	HO2	33	HYDROPEROXY RADICAL
10	CO	28	CARBON MONOXIDE
11	CO2	44	CARBON DIOXIDE
12	H2O2	34	HYDROGEN PEROXIDE

13	NH3	17	AMMONIA
14	NIT	N/A	AEROSOL NITRATE
15	SO2	64.1	SULFUR DIOXIDE
16	SO3	80.1	SULFUR TRIOXIDE (RAPIDLY FORMS H2SO4)
17	ETHE	28	ETHENE
18	OLEL	70	LUMPED ALKENES C3-C6
19	OLEH	126	LUMPED ALKENES >C6
20	ALKL	72	LUMPED ALKANES C3-C6
21	ALKM	128	LUMPED ALKANES C6-C12
22	ALKH	226	LUMPED ALKANES >C12
23	AROH	134	LUMPED AROMATICS WITH HI SOA Y (a la Odum et al)
24	AROL	120	LUMPED AROMATICS WITH LO SOA Y
25	PHEN	122	LUMPED OXYGENATED AROMATICS (phenols)
26	BALD	120	LUMPED AROMATIC MONOALDEHYDES
27	ARAC	136	LUMPED AROMATIC MONOACIDS
28	ADAC	166	LUMPED AROMATIC DIACIDS
29	PAH	156	LUMPED PAH
30	HCHO	30	FORMALDEHYDE
31	ALD2	86	LUMPED ALDEHYDES
32	MEK	86	LUMPED KETONES C3-C6

33	KETO	114	LUMPED KETONES >C6
34	MEOH	32	METHANOL
35	ETOH	46	ETHANOL
36	ALCH	102	LUMPED HIGHER ALCOHOLS
37	ISOP	68.1	ISOPRENE
38	BIOL	154.2	LUMPED MONOTERPENES WITH LO SOA Y (a la Griffin et al)
39	BIOH	136.2	LUMPED MONOTERPENES WITH HI SOA Y
40	ACID	88	LUMPED ORGANIC ACIDS WITH <C6
41	MGLY	72	METHYL GLYOXAL
42	MVK	70	METHYL VINYL KETONE
43	MCR	70	METHACROLEIN
44	PAN1	163	PEROXY PENTIONYL NITRATE
45	PAN2	121	PAN
46	PAN3	133	UNSATURATED PPN
47	PAN4	149	KETO PPN
48	PAN5	147	METHYLENE-PPN
49	PAN6	135	PAN FROM GLYOXAL
50	PAN7	205	PEROXY 3-METHYL-HEPTIONYL NITRATE
51	PAN8	263	PEROXY 2-HYDROXY-3-ISOPROPYL-6-OXO-HEPTIONYL NITRATE
52	PAN9	205	PEROXY 3-ISOPROPYL-4-HYDROXY-2-BUTENIONYL NITRATE

53	PN10	137	PAN FROM GLYOXALIC ACID
54	RPR1	128	3-METHYL HEPTANAL
55	RPR2	136	3-HYDROXY-4-METHYL-BENZALDEHYDE
56	RPR3	186	2-HYDROXY-3-ISOPROPYL-6-OXO-HEPTANAL
57	RPR4	167	2,6-DIMETHYL-4-NITRO-PHENOL
58	RPR5	165	2-NITRO-4-METHYL-BENZALDEHYDE
59	RPR6	134	1,4-DIBENZALDEHYDE
60	RPR7	150	1-FORMYL-4-CARBOXY-BENZENE
61	RPR8	128	3-ISOPROPYL-4-HYDROXY-2-BUTENAL
62	RPR9	154	4-HYDROXY-3,5-DIMETHYL-2,4-HEXADIENDIAL
63	RP10	114	2-METHYL-BUTENALIC ACID
64	RP11	152	4,5-DIMETHYL-6-OXO-2,4-HEPTADIENAL
65	RP12	152	2-METHYL-5-FORMYL-2,4-HEXADIENDIAL
66	RP13	168	2-CARBOXYL-5-METHYL-2,4-HEXADIENDIAL
67	RP14	188	2-(DIMETHYL-PROPENAL)-BENZALDEHYDE
68	RP15	148	2-FORMYL-ACETOPHENONE
69	RP16	74	GLYOXALIC ACID
70	RP17	170	4-HYDROXY-3,5-DIMETHYL-2,4-HEXADIENALIC ACID
71	RP18	184	2-METHYL-5-FORMYL-2,4-HEXADIENDIOIC ACID
72	RP19	204	2-(DIMETHYL-PROPENAL)-BENZOIC ACID

73	AP1	183	2-NITRATOMETHYL-6-METHYL-PHENOL
74	AP2	191	2-METHYL-2-HYDROXY-5-HEPTYLNITRATE
75	AP3	175	3-METHYL-4-HEPTYLNITRATE
76	AP4	181	1,2-DIMETHYL-3-METHYLNITRATO-BENZENE
77	AP5	181	4-METHYLNITRATO-BENZALDEHYDE
78	AP6	197	4-METHYLNITRATO BENZOIC ACID
79	AP7	233	1-METHYL-1-NITRATO-2,3-DIHYDROXY-4-ISOPROPYL-CYCLOHEXANE
80	AP8	215	1-METHYL-4-NITRATO-4-ISOPROPYL-5-HYDROXY-CYCLOHEXENE
81	AP9	201	5-ISOPROPYL-6-NITRATO-4-HEXEN-2-ONE
82	AP10	217	1-METHYL-2-METHYLNITRATO-NAPHTHALENE
83	AP11	287	8-HEXADECYLNITRATE
84	AP12	303	8-HYDROXY-11-HEXADECYLNITRATE
85	UR1	144	3-METHYL-HEPTANOIC ACID
86	UR2	152	3-HYDROXY-4-METHYL BENZOIC ACID
87	UR3	202	2-HYDROXY-3-ISOPROPYL-6-OXO-HEPTANOIC ACID
88	UR4	156	2-ISOPROPYL-5-OXO-HEXANAL
89	UR5	170	1-METHYL-3-HYDROXY-4-ISOPROPYL-1,2-CYCLOHEXANE EPOXIDE
90	UR6	170	2-HYDROXY-3-ISOPROPYL-6-METHYL-CYCLOHEXANONE

91	UR7	168	3,7-DIMETHYL-6-OXO-3-OCTENAL
92	UR8	184	3-ISOPROPYL-6-OXO-3-HEPTENOIC ACID
93	UR9	152.2	1-METHYL-4-ISOPROPYL-1,2CYCLO-4-HEXENE EPOXIDE
94	UR10	152.2	3-ISOPROPYL-6-METHYL-3-CYCLOHEXENONE
95	UR11	172	1,2-DIMETHYL-3-HYDROXY-NAPHTHALENE
96	UR12	165	1,2,3-TRIMETHYL-5-NITRO-BENZENE
97	UR13	179	3-n-PROPYL-4-NITRO-TOLUENE
98	UR14	181	2-NITRO-4-METHYL-BENZOIC ACID
99	UR15	201	1,2-DIMETHYL-3-NITRO-NAPHTHALENE
100	UR16	144	2-METHYL-2-HYDROXY-5-HEPTANONE
101	UR17	172	2-HYDROXY-3-ISOPROPYL-HEXADIAL
102	UR18	140	3-ISOPROPYL-2-PENTENDIAL
103	UR19	170	1-METHYL-2-FORMYL-NAPTHALENE
104	UR20	256	11-HYDROXY-8-HEXADECANONE
105	UR21	88	KETO-PROPANOIC ACID
106	UR22	212	2,6-DIMETHYL-3,4-DINITRO-PHENOL
107	UR23	144	3-ISOPROPYL-4-HYDROXY-2-BUTENOIC ACID
108	UR24	98	MALEIC ANHYDRIDE
109	UR25	84	3H-FURAN-2-ONE
110	UR26	168	4,5-DIMETHYL-6-OXO-2,4-HEPTADIENOIC ACID

111	UR27	164	2-CARBOXY-ACETOPHENONE
112	UR28	90	OXALIC ACID
113	UR29	186	4-HYDROXY-3,5-DIMETHYL-2,4-HEXADIENDIOIC ACID
114	UR30	200	2-METHYL-5-CARBOXY-2,4-HEXADIENDIOIC ACID
115	UR31	220	2-(DIMETHYL-PROPENOIC ACID)-BENZOIC ACID
116	UR32	128	3-METHYL-4-HEPTANONE
117	UR33	154	2-ISOPROPYL-5-OXO-2-HEXENAL
118	UR34	240	8-HEXADECANONE
119	MTBE	88	METHYL TERT-BUTYL ETHER
120	RO2T		TOTAL RO2 ('SUM' OF RO21 THROUGH RO249)
121	RO28	75	ACYL PEROXY <C6 FROM ALD2,ISOP,BIOH,MEK,KETO,BIOL (2C)
122	OH	17	HYDROXYL RADICAL
123	HCL	36.5	HYDROCHLORIC ACID
124	UR35	128	

Table 15: Aerosol species listed in order

Species Number	Species Abbreviation	Description	Bin
125	Na	Soduim	1
126	Sf	Sulfates	1
127	Am	Amonium	1
128	Nt	Nitrogens	1
129	Cl	Chlorine	1
130	K	Potassuim	1
131	Ca	Calcuim	1
132	Mg	Magnesuim	1
133	Cb	Carbonate	1
134	Wa	Water	1
135	OI	Other inorganics	1
136	EC	Elemental carbon	1
137	AK	Alkane	1
138	DA	Di-acids	1
139	OX	Oxygenated PAH	1
140	PH	Poly cyclic aromatic hydrocarbon	1
141	CY	Other cyclic products	1
142	SA	Substituted aromatics	1
143	AA	Alphatic acids	1
144	OC	Other organics	1
145	B1		1
146	V1		1
147	B2		1
148	V2		1
149	B3		1
150	B4		1

151	B5		1
152	A1		1
153	M1		1
154	D1		1
155	A2		1
156	M2		1
157	D2		1
158	A3		1
159	A4		1
160	M4		1
161	A5		1
162	Na	Soduim	2
163	Sf	Sulfates	2
164	Am	Amonium	2
165	Nt	Nitrogens	2
166	Cl	Chlorine	2
167	K	Potassuim	2
168	Ca	Calcuim	2
169	Mg	Magnesuim	2
170	Cb	Carbonate	2
171	Wa	Water	2
172	OI	Other inorganics	2
173	EC	Elemental carbon	2
174	AK	Alkane	2
175	DA	Di-acids	2
176	OX	Oxygenated PAH	2
177	PH	Poly cyclic aromatic hydrocarbon	2
178	CY	Other cyclic products	2
179	SA	Substituted aromatics	2

180	AA	Alphatic acids	2
181	OC	Other organics	2
182	B1		2
183	V1		2
184	B2		2
185	V2		2
186	B3		2
187	B4		2
188	B5		2
189	A1		2
190	M1		2
191	D1		2
192	A2		2
193	M2		2
194	D2		2
195	A3		2
196	A4		2
197	M4		2
198	A5		2
199	Na	Soduim	3
200	Sf	Sulfates	3
201	Am	Amonium	3
202	Nt	Nitrogens	3
203	Cl	Chlorine	3
204	K	Potassuim	3
205	Ca	Calcuim	3
206	Mg	Magnesuim	3
207	Cb	Carbonate	3
208	Wa	Water	3
209	OI	Other inorganics	3

210	EC	Elemental carbon	3
211	AK	Alkane	3
212	DA	Di-acids	3
213	OX	Oxygenated PAH	3
214	PH	Poly cyclic aromatic hydrocarbon	3
215	CY	Other cyclic products	3
216	SA	Substituted aromatics	3
217	AA	Alphatic acids	3
218	OC	Other organics	3
219	B1		3
220	V1		3
221	B2		3
222	V2		3
223	B3		3
224	B4		3
225	B5		3
226	A1		3
227	M1		3
228	D1		3
229	A2		3
230	M2		3
231	D2		3
232	A3		3
233	A4		3
234	M4		3
235	A5		3
236	Na	Soduim	4
237	Sf	Sulfates	4
238	Am	Amonium	4

239	Nt	Nitrogens	4
240	Cl	Chlorine	4
241	K	Potassuim	4
242	Ca	Calcuim	4
243	Mg	Magnesuim	4
244	Cb	Carbonate	4
245	Wa	Water	4
246	OI	Other inorganics	4
247	EC	Elemental carbon	4
248	AK	Alkane	4
249	DA	Di-acids	4
250	OX	Oxygenated PAH	4
251	PH	Poly cyclic aromatic hydrocarbon	4
252	CY	Other cyclic products	4
253	SA	Substituted aromatics	4
254	AA	Alphatic acids	4
255	OC	Other organics	4
256	B1		4
257	V1		4
258	B2		4
259	V2		4
260	B3		4
261	B4		4
262	B5		4
263	A1		4
264	M1		4
265	D1		4
266	A2		4
267	M2		4

268	D2		4
269	A3		4
270	A4		4
271	M4		4
272	A5		4
273	Na	Soduim	5
274	Sf	Sulfates	5
275	Am	Amonium	5
276	Nt	Nitrogens	5
277	Cl	Chlorine	5
278	K	Potassuim	5
279	Ca	Calcuim	5
280	Mg	Magnesuim	5
281	Cb	Carbonate	5
282	Wa	Water	5
283	OI	Other inorganics	5
284	EC	Elemental carbon	5
285	AK	Alkane	5
286	DA	Di-acids	5
287	OX	Oxygenated PAH	5
288	PH	Poly cyclic aromatic hydrocarbon	5
289	CY	Other cyclic products	5
290	SA	Substituted aromatics	5
291	AA	Alphatic acids	5
292	OC	Other organics	5
293	B1		5
294	V1		5
295	B2		5
296	V2		5

297	B3		5
298	B4		5
299	B5		5
300	A1		5
301	M1		5
302	D1		5
303	A2		5
304	M2		5
305	D2		5
306	A3		5
307	A4		5
308	M4		5
309	A5		5
310	Na	Soduim	6
311	Sf	Sulfates	6
312	Am	Amonium	6
313	Nt	Nitrogens	6
314	Cl	Chlorine	6
315	K	Potassuim	6
316	Ca	Calcuim	6
317	Mg	Magnesuim	6
318	Cb	Carbonate	6
319	Wa	Water	6
320	OI	Other inorganics	6
321	EC	Elemental carbon	6
322	AK	Alkane	6
323	DA	Di-acids	6
324	OX	Oxygenated PAH	6
325	PH	Poly cyclic aromatic hydrocarbon	6

326	CY	Other cyclic products	6
327	SA	Substituted aromatics	6
328	AA	Alphatic acids	6
329	OC	Other organics	6
330	B1		6
331	V1		6
332	B2		6
333	V2		6
334	B3		6
335	B4		6
336	B5		6
337	A1		6
338	M1		6
339	D1		6
340	A2		6
341	M2		6
342	D2		6
343	A3		6
344	A4		6
345	M4		6
346	A5		6
347	Na	Soduim	7
348	Sf	Sulfates	7
349	Am	Amonium	7
350	Nt	Nitrogens	7
351	Cl	Chlorine	7
352	K	Potassuim	7
353	Ca	Calcuim	7
354	Mg	Magnesuim	7
355	Cb	Carbonate	7

356	Wa	Water	7
357	OI	Other inorganics	7
358	EC	Elemental carbon	7
359	AK	Alkane	7
360	DA	Di-acids	7
361	OX	Oxygenated PAH	7
362	PH	Poly cyclic aromatic hydrocarbon	7
363	CY	Other cyclic products	7
364	SA	Substituted aromatics	7
365	AA	Alphatic acids	7
366	OC	Other organics	7
367	B1		7
368	V1		7
369	B2		7
370	V2		7
371	B3		7
372	B4		7
373	B5		7
374	A1		7
375	M1		7
376	D1		7
377	A2		7
378	M2		7
379	D2		7
380	A3		7
381	A4		7
382	M4		7
383	A5		7
384	Na	Soduim	8

385	Sf	Sulfates	8
386	Am	Amonium	8
387	Nt	Nitrogens	8
388	Cl	Chlorine	8
389	K	Potassuim	8
390	Ca	Calcuim	8
391	Mg	Magnesuim	8
392	Cb	Carbonate	8
393	Wa	Water	8
394	OI	Other inorganics	8
395	EC	Elemental carbon	8
396	AK	Alkane	8
397	DA	Di-acids	8
398	OX	Oxygenated PAH	8
399	PH	Poly cyclic aromatic hydrocarbon	8
400	CY	Other cyclic products	8
401	SA	Substituted aromatics	8
402	AA	Alphatic acids	8
403	OC	Other organics	8
404	B1		8
405	V1		8
406	B2		8
407	V2		8
408	B3		8
409	B4		8
410	B5		8
411	A1		8
412	M1		8
413	D1		8

414	A2	8
415	M2	8
416	D2	8
417	A3	8
418	A4	8
419	M4	8
420	A5	8